AN EXPERIMENTAL STUDY OF THE AFT GUIDE VANES OF AN ENGINE BYPASS NACELLE FOR LOW-BOOM SUPERSONIC FLIGHT

BY

RUBEN HORTENSIUS

THESIS

Submitted in partial fulfillment of the requirements
for the degree of Master of Science in Aerospace Engineering
in the Graduate College of the
University of Illinois at Urbana-Champaign, 2011

Urbana, Illinois

Advisers:

Professor Michael B. Bragg
Professor Gregory S. Elliott

Abstract

Due to the large disturbance created by the sonic boom, supersonic flight is strictly controlled by the FAA. One way in which to minimize the sonic boom is through shape-tailoring of the aircraft body and of the propulsion system. To this end, a new supersonic engine concept has been proposed, wherein a core turbofan engine, which has a non-axisymmetric external profile due to a protruding gearbox, has been circularized. A new, secondary, bypass with a highly complex internal geometry is created during this process. The high-flow nacelle bypass geometry includes a forward and aft fairing to direct the flow around the gearbox, a set of thin forward guide vanes, and a set of thick, strut-like aft guide vanes. The aft guide vanes, which also serve structural purposes, are used to direct the flow such that the exhaust is a uniform, nearly-full annular cross-section, and to choke and then accelerate the flow to supersonic freestream conditions upon exit. A supersonic wind tunnel facility at the University of Illinois was modified and used to simulate the flow through the aft bypass at approximately 6% scale. In order to aid in understanding the effect of the aft vanes, two models, one with and one without guide vanes, are studied. Due to facility limitations, the design operating condition could not be achieved; a series of off-design operating conditions are tested instead.

Radial pressure surveys are conducted at several azimuthal stations at the inlet to the aft bypass in order to establish in-flow conditions. Static pressure taps on the model surface provide insight into the nature of the flow through the bypass on a per channel basis. An isentropic-case comparison, an estimate of total pressure losses, and mass flow rate calculations were performed. Pressure data were supplemented with schlieren imagery and surface oil flow visualization. Results indicate the flow through the aft bypass is highly three-dimensional and contains a large amount of flow separation in the off-design conditions tested.

Acknowledgements

I would like to thank all of those who were involved with and aided me in conducting and completing this research project. Thank you to Professor Michael Bragg and Professor Gregory Elliott for allowing me to come onboard as, first, a summer REU student, and then for inviting me to continue as the graduate assistant on this exciting project. Your tremendous knowledge and support are greatly appreciated. This project was supported by both Gulfstream Aerospace Corporation and Rolls-Royce plc. Thank you to Tim Conners, Tom Wayman, and Robbie Cowart from Gulfstream and John Whurr from Rolls-Royce for their assistance on this project. Thank you to Greg Milner from the Department of Aerospace Engineering Machine Shop and Robert Coverdill of the Ford Concurrent Design and Manufacture Lab in the Department of Mechanical Science and Engineering for their assistance in facility component and test model fabrication, respectively. I would also like to thank my friends and fellow group members for their help, advice, and support as this research was conducted.

I also want to thank my family. Rebecca, my soon wife-to-be, did not let the fact that we had live in opposite corners of the Midwest stop her from being a truly invaluable support to me during these past several years through her encouragement and love. I would also like to specially thank our parents for having always been supportive of my goals and for providing their support.

Table of Contents

List of Tables

List of Figures

Page

Nomenclature

Symbols

A	Local normal area within channel
c	Speed of sound
C_1	Sutherland's empirical constant
$Ch^{\#}$	Channel number
M	Mach number
$\dot{m}$	Mass flow rate
P	Pressure
PR	Pressure ratio; typically static-to-total
PRF	Pressure recovery factor
R	Radial position
$\mathcal{R}$	Universal gas constant
Re	Reynolds number
S	Sutherland's empirical constant
T	Temperature
t	Time
U	Velocity, streamwise direction
u	Measurement uncertainty
x	Axial position along model

Greek Symbols

μ	Viscosity
γ	Ratio of specific heats, 1.4 for air
δ	Boundary-layer thickness
Δ	Change
δ^*	Displacement thickness
θ	Azimuthal angle
Θ	Momentum thickness
λ	Thwaites correlation parameter
ν	Kinematic viscosity
ρ	Density
σ	Standard deviation

Superscripts

$*$	Normalized radial position -or- Sonic condition
Pre	Pre-processing
$Post$	Post-processing

Subscripts

0	Approximate inlet plane total pressure
amb	Ambient
ave	Average
chamber	Stagnation chamber (stagnation conditions)
core	Within the core flow; typically $0.35 \leq R^* \leq 0.65$
cowl	Position of cowling trailing edge
empty	Empty tunnel run, no probe present
exp	Experimental
inner	Inner wall radius
isen	Isentropic case calculation
local	Function of axial position within channel, for channel flow analyses
non-dim	Non-dimensional quantity
outer	Outer wall radius
ref	Reference
st	Static pressure
throat	Conditions at channel throat
Thw	Thwaites method adjusted value
total	Probe measured total pressure
tunnel	Conditions within core of Ch $^{\#}1$, operating reference condition

Acronyms

BC	Bottom-center azimuthal position
CADD	Computer aided drafting and design
CV	Coefficient of variance
EDM	Electrical discharge machine
FAA	Federal Aviation Administration
FS	Full scale
GAC	Gulfstream Aerospace Corporation
MFR	Mass flow rate
OP	Operating condition
QSBJ	Quiet Supersonic Business Jet
RR	Rolls Royce plc.
SAE	Society of Automotive Engineers
SLA	Stereolithography
TC	Top-center azimuthal position
UIUC	University of Illinois at Urbana-Champaign
UV	Ultra violet

Chapter 1

Introduction

1.1 Background

Throughout the history of aviation, the desire to increase flight speed has continually grown. The desire for increased speed, and hence, decreased flight time, was successfully met until flight speeds began to approach the speed of sound. Seen by some as a limit which could not be surpassed, the sound barrier was officially broken on October 14, 1947 in the Bell X-1.[1] Although supersonic flight has been within the limit of human attainability for more than sixty years, it has been, with one notable civilian transport exception, nearly entirely relegated to use by military organizations.

Only one civilian aircraft has regularly flown supersonically; the reason is driven by the presence of a sonic boom which accompanies supersonic flight. The sonic boom is an extremely loud, conical pressure wave generated by the supersonic body.[2] At supersonic conditions, the body moves faster than the speed of sound and the forward emanating pressure waves, which travel at the speed of sound, crowd each other. A Mach cone, which bounds the forward-most extent of the pressure waves, is formed. The Mach cone is tangent to the time discrete circular waves and its angle can be related to the Mach number of the body (Fig. 1.1). By coalescing on the Mach cone, a wave front, or shockwave, known as a sonic boom is formed. No evidence of the coming body is propagated upstream, but when the sonic boom reaches a listener, the shockwave can be strongly heard and felt as it passes.

Due to the disturbance it causes, Federal Aviation Administration (FAA) regulations explicitly forbid the generation of a sonic boom in the vicinity of populated areas.[3] For this reason, flight speeds greater than Mach one are rarely exceeded by any civilian or commercial aircraft in US airspace, and it is only in times of emergency that the military has permission to exceed this boundary. The Concorde did fly supersonically

on its transoceanic flights, but the specific areas where it was allowed to do so were strictly controlled to avoid populated areas.[4]

The sonic boom can be described, in terms of pressure by an "N wave" as shown in Fig. 1.2. The first peak is known as the "overpressure" and is experienced when the Mach cone is encountered. The pressure then decreases to negative values along the length of the aircraft. At the tail, the negative pressure jumps back to normal conditions, forming the characteristic "N" shape.[5] Part of the wave front reaches the ground; it is known as the primary sonic boom. The primary sonic boom's characteristic shape is very predictable, while the pressure disturbance that is deflected upward, known as the "over-the-top" boom, is not quite as predictable or as well understood.[5] It is the primary boom which is of most interest since it is the most likely to directly affect populated regions of the Earth.

Before overland supersonic flight can become a reality, the sonic boom must be greatly reduced to acceptable levels. Research efforts conducted on several fronts have shown that careful shaping of the supersonic body (aircraft) can greatly reduce the peaks of the "N" wave, thereby greatly reducing the sonic boom. Seebass and George[6] were able to greatly decrease sonic boom signature parameters by tailoring the area development of the equivalent body of revolution. Later, ground pressure signatures were recorded of a modified F-5E aircraft. The Shaped Sonic Boom Demonstrator,[7] as it was called, proved that low-boom supersonic flight was attainable by greatly reducing the overpressure signature so that it had a "flat top" instead of a peak.

It is clear that the physical shape of aircraft bodies and features can directly affect the sonic boom as the overpressure and expansion signatures due to geometry and body-to-body interactions vary.[8] Therefore, technologies such as variable airframe and wing geometries or other options relating to the propulsive systems or the empennage were developed and employed.

One particular part of the aircraft that influences sonic boom is the propulsion system. Many of today's engines, especially those used for civil and commercial aircraft, have a series of non-axisymmetric protuberances which extend below the primary nacelle (Fig. 1.3 a). These protuberances include a gearbox, various electric, hydraulic, and pneumatic lines, and structural components. Engines with a circular profile gearbox,

such as that shown in Fig. 1.3 b, have been shown to contribute less towards the sonic boom. These engines have a smaller frontal profile which decreases the contribution to nacelle pressure drag, the nacelle to remainder of aircraft interference drag, and generally contribute less to the overpressures and expansions around the gearbox.

The engine inlet is another large source of drag and sonic boom noise, especially for supersonic engines. The supersonic inlets' purpose is to slow the freestream flow so that it can be safely ingested by the engine turbomachinery in a relatively clean, that is, uniform, state. It accomplishes this through the use of shocks and expansions that form about the inlet cone, as shown in Fig. 1.4. The largest source of drag and boom contribution arising from supersonic inlets stems from the problem of flow spillage. If the shock arising from the tip of the inlet cone does not properly intersect the engine cowling, then some of the flow is spilled and is not ingested. This leads to greatly increased drag and sonic boom contribution.

Minimizing the amount of flow spillage at the inlet of a supersonic engine is a critical aspect of maximizing performance and minimizing the sonic boom. Spillage can only be avoided if the shock cone originating from the tip of the inlet cone can be captured by the inlet. Critical operation is achieved if the shock cone can be held to intersect with the leading edge tip of the inlet cowling. However, this state is very difficult to maintain during operation and adverse effects arise from operation in a supercritical state – that is, when the cone shock radius is less than that of the cowling leading edge tip. In this state, flow distortions near the cowling leading edge are ingested by the engine. These "tip–radial" distortions contain high pressure losses which negatively affect the stability of the engine's turbomachinery.[9,10]

1.2 Gulfstream Quiet Supersonic Business Jet Concept

Recently, Gulfstream Aerospace Corporation (GAC) has developed a concept aircraft that combines multiple technological advancements to minimize the sonic boom.[11] Known as the Gulfstream Quiet Supersonic Business Jet (QSBJ), it incorporates both airframe-based and propulsion-system advancements (Fig. 1.5).

Two key airframe-based technologies included are variable geometry wings and the Gulfstream Quiet Spike™. The use of variable geometry wings allows for more efficient flight operation across a subsonic to supersonic flight envelope as the wing sweep angle can be optimized based on current operating conditions. The Quiet Spike™,[12-15] is an extendable nose spike which decreases the sonic boom by breaking the single strong shock into a series of parallel weak shocks. Due to their parallel orientation, the Quiet Spike™'s weak shocks were prevented from coalescing and forming a single strong (and loud) shock. Morphing the forward fuselage into a needle-like shape has been proven, analytically and experimentally by both wind tunnel[16] and flight testing,[17] to greatly decrease noise characteristics. Both of these changes improve upon the noise signature of the aircraft, but the engines and other bodies on the airplane also contribute significantly to noise.

Gulfstream has also conducted a great deal of developmental work on an alternative supersonic inlet. Dubbed a "relaxed isentropic external compression" inlet,[18,19] it reshapes the inlet terminal shock which allows for the reduction of the cowl angle and slope. The reduced frontal profile leads to decreased cowl pressure drag and a reduced sonic boom. However, the relaxed isentropic external compression supersonic inlet may suffer from the same disadvantages that a conventionally designed supersonic inlet encounters – namely, the negative effects arising from spillage, as previously discussed.

GAC proposed a novel feature that was extremely beneficial to engine performance and sonic boom signature in several ways, including with the spillage problem. In an effort to minimize the boom signature effects generated by the turbofan's gearbox protuberances, a proposal to wrap a secondary nacelle around the engine to circularize it was offered. Circularizing the engine increased the proportion of its frontal area that was blocked, thereby leading to increased drag. However, by placing a fairing around the gearbox and allowing flow to pass between the core engine and the new cowling, thereby creating a secondary bypass, the frontal area was again reduced to acceptable levels. Additionally, the outer cowling's construction at the leading and trailing edges was more cylindrical in nature than that of the core engine nacelle. With less radial variation at the leading and trailing edges, the cowling angle and slope were

effectively reduced, which also contributed to the circularized engine's smaller frontal blockage proportion as compared to the original design.

The secondary benefit that circularizing the engine provided was that, by extending the new shroud upstream towards the supersonic inlet, it effectively became a flow splitting mechanism. The shroud was therefore able to swallow the tip-radial flow defects ingested by the supersonic inlet. Instead of passing through the turbomachinery of the core engine, this flow could be routed through the bypass instead. This concept is known as the High-Flow Bypass Nacelle.[11]

The core engine proposed for use in this new concept engine is the Rolls Royce Tay turbofan (Fig. 1.6). It has a maximum takeoff thrust of about 15,000 lbf, a bypass ratio of about 3, and a fan diameter of approximately 45 inches.[i] Although not designed for supersonic operation, this engine is well suited for the application given its proven reliability and narrow frontal external cowling profile.

In order to most accurately determine the azimuthal extent of the gearbox, plumbing, and other protuberances, a laser scan of the engine was conducted. A single large fairing, centered about bottom-center (BC), and blocking 160° of the annulus, shields the turbofan protuberances, as shown in Fig. 1.7. Upstream and downstream of the fully blocked region, forward and aft close out fairings are used to streamline the flow around the blockage. Nine, equally distributed, thin-walled vanes guide the flow into the fully blocked region. A second set of nine vanes, these being thicker strut-type structures, are used to redistribute the flow around the entire annulus at through the aft section of the bypass. An unwrapped view of the bypass geometry is shown in Fig. 1.8. A CAD image of the bypass can be found in Fig. 1.9, where the large gearbox fairing, guide vanes, supersonic inlet, and exhaust are all clearly evident.

The aft vanes serve several purposes.[20] They redistribute the flow from the fully blocked region to the complete annulus. Second, they provide a choke plane, and then reaccelerate the flow to supersonic freestream conditions upon passing the cowling trailing edge (end plane), x_{cowl}. The aft vanes transition into wedge type structures past x_{cowl} to aid in the expansion of the flow. Lastly, the aft struts serve structural purposes.

[i] http://www.rolls-royce.com/civil/products/smallaircraft/tay/index.jsp [retrieved 18 July 2011].

An early concept image is found in Fig. 1.10, where the supersonic inlet, outer cowling, upstream extension of the turbofan circularization shroud (splitter) used to extract the tip-radial defected flow, bypass duct, and plug nozzle can be seen. A comprehensive summary of the high-flow bypass concept, its feasibility, and research to-date is provided by Conners and Wayman.[20]

1.3 Motivation and Objectives

One critical element to the success of the new concept was to ensure that the flow through the bypass was of sufficient quality and only suffered reasonable losses. To this end, several experimental and computational studies have been carried out.

Yeong[21,22] conducted an approximately $1/6^{th}$ scale experimental investigation of the first generation bypass geometry (that without guide vanes) at the University of Illinois. A concurrent study, conducted by Chiles,[23,24] completed a CFD comparison to the experimental results. Both studies found that the gearbox blockage contributed greatly to increased pressure losses, especially as there was heavy flow separation at the fairing closing. Chiles also concluded that the forward fairing geometry did a good job of diverting the flow around the gearbox.

Since the addition of the guide vanes, additional studies have been carried out. Herrera[25,26] conducted an experimental assessment on the effect of the forward (thin) guide vanes of the bypass after modifying the facility that Yeong designed to allow for additional measurements and model updates. A second study, conducted at the University of Illinois and the focus of this work, was a similar assessment of the flow through the aft guide vanes.

A concurrent computational fluid dynamics (CFD) study is being conducted by Jian,[27,28] of the same experimental (wind tunnel based) geometry. Kim, et al.[29] conducted a CFD simulation of the full engine including the bypass duct with fore and aft fans. In this study, boundary conditions at the core turbofan inlet and exit were applied from an embedded solver to reflect the core engine performance characteristics. They found that the flow through the highly complex bypass duct greatly influenced the performance of the supersonic inlet by varying the axial position of the terminal normal shock. The

current work employs the same vane geometry as that used in Ref. 29. In a second study, Kim, et al.[30] explored the optimization of the aft vane geometry to minimize losses through the bypass such that it achieved design specifications.

This study is a small-scale (approximately 6%) experimental investigation of the flow through the aft bypass; that is, from within the fully blocked region, through the aft strut-like guide vanes, past the cowling trailing edge, and terminating at the nozzle shroud trailing edge. The purpose is to provide an experimental 'proof-of-concept' of the overall configuration. Specific objectives for this work are defined below:

1. Determine flow quality and defining characteristics at the model "inlet plane" within the fully blocked region.
2. Investigate the overall effect the presence of the aft vanes has on the flow quality by testing two models: one with the aft fairing and another with the aft fairing and the aft vanes.
3. Investigate the nature and characteristics of the flow through each channel at design and off-design operating conditions.
4. Provide adequate experimental data to allow for comparison between experimental study and the computational (CFD) studies.[27,28]

Figures

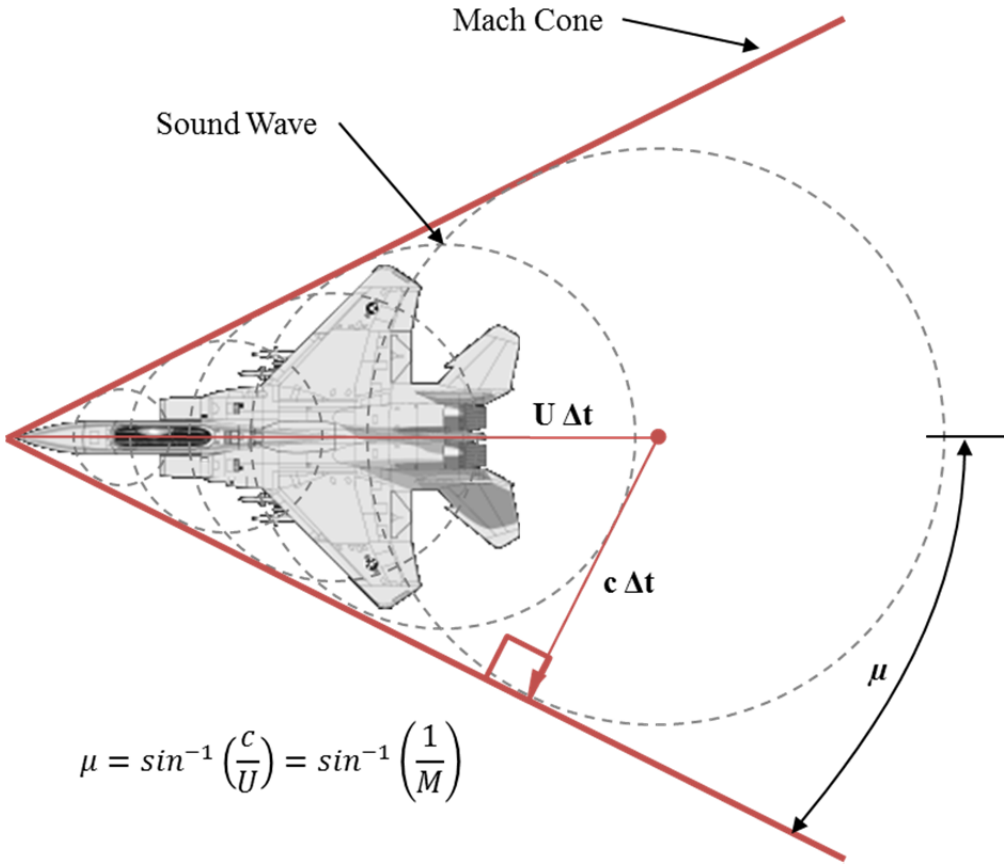

Fig. 1.1. The formation of the Mach cone. The shape of the Mach cone (angle) is related to Mach number.

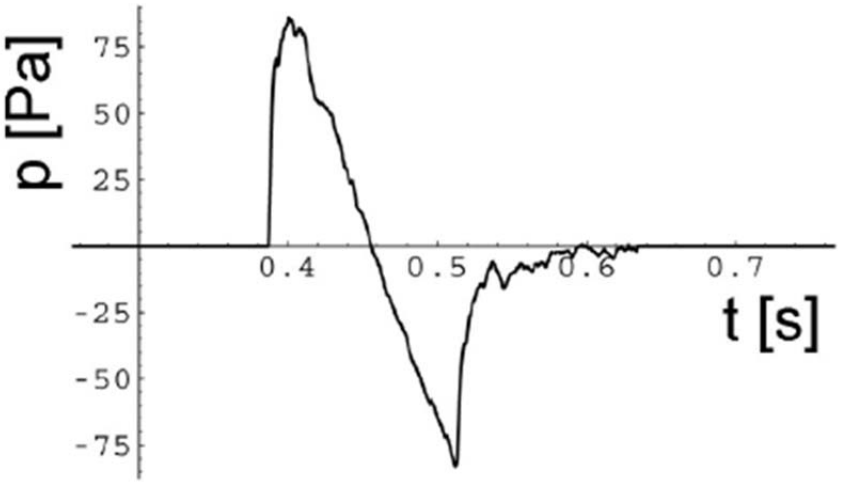

Fig. 1.2. Measured "N" wave pressure signature of a sonic boom from an F-15.[5]

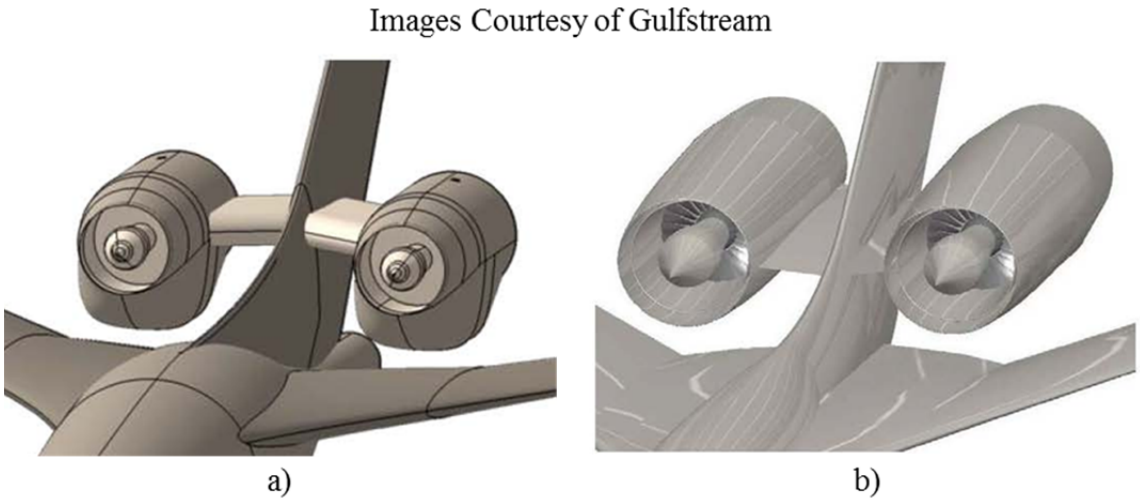

Fig. 1.3. Today's typical propulsive systems have a a) gearbox protuberance on the underside of the nacelles generating additional drag and contributing to sonic boom, while b) ideal models have circular profiles.[20]

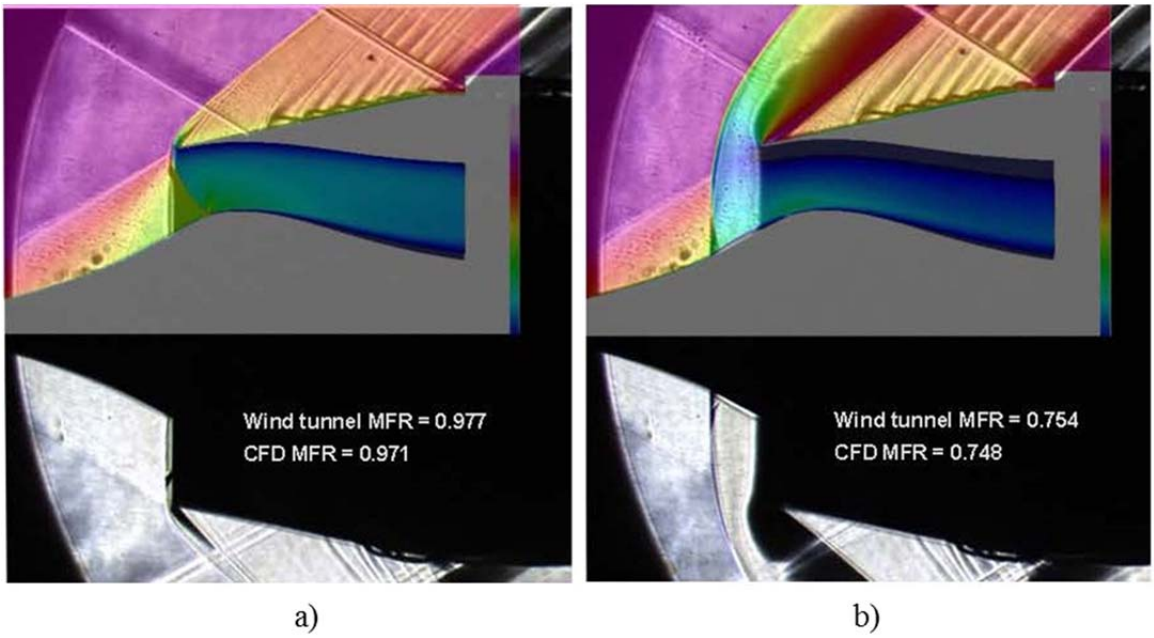

Fig. 1.4. Imagery of a supersonic inlet where a) the shock originating from the inlet cone tip intersects with the leading edge of the cowling, leading to no spillage, while b) the shock does not intersect correctly and spillage occurs. Flow is left to right. Top image is CFD Mach field, while lower image is Schlieren imagery.[16]

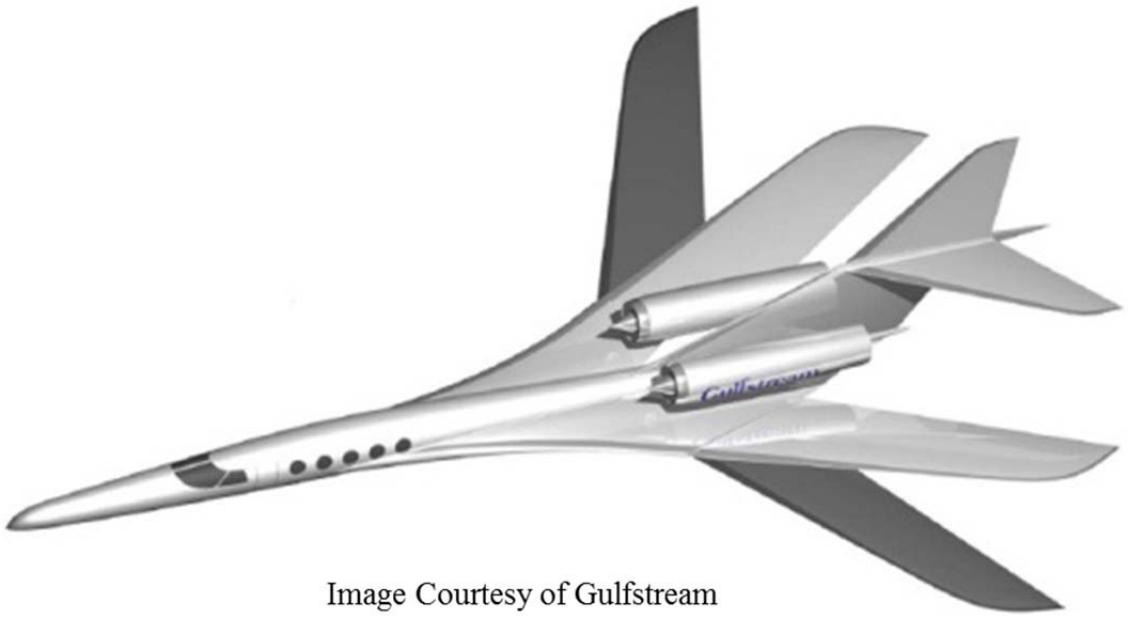

Fig. 1.5. Concept image of Gulfstream's Quiet Supersonic Business Jet (QSBJ) which utilizes airframe technologies such as morphing and propulsion system advanced technologies.[31]

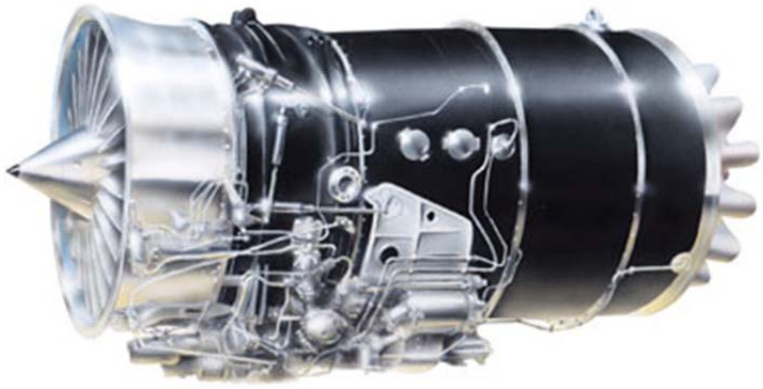

Fig. 1.6. The Rolls Royce Tay turbofan. Courtesy of RR.

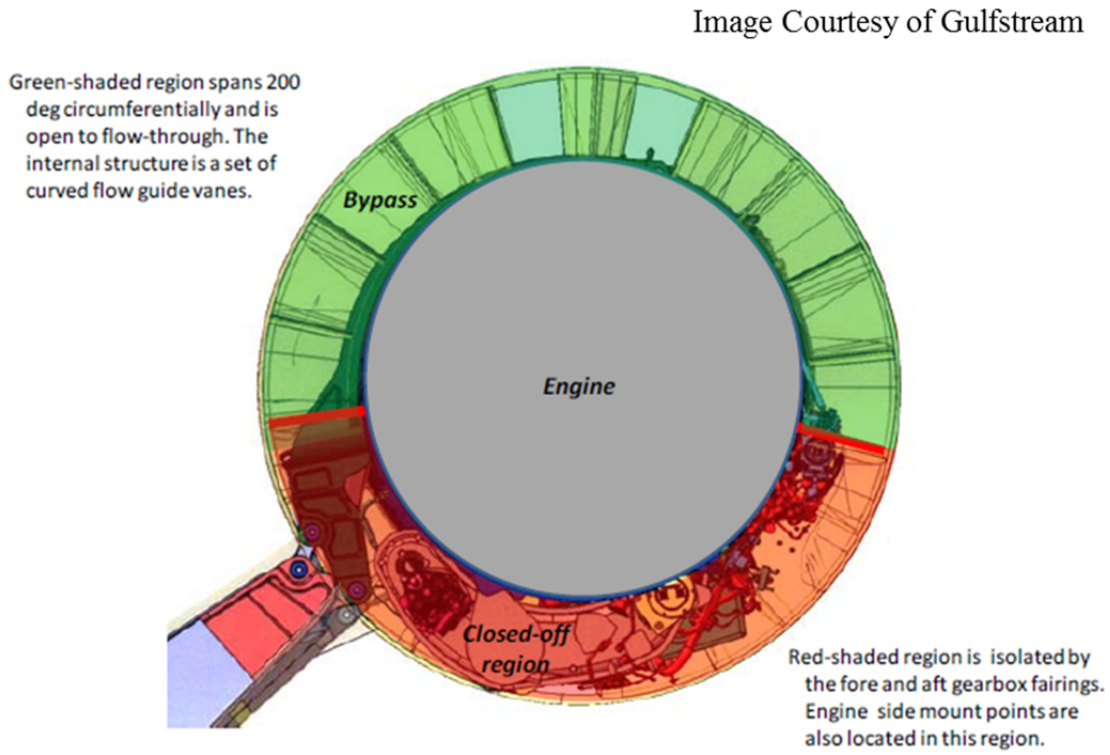

Fig. 1.7. Cross-sectional view of the Tay engine illustrating the extent of the blocked region due to the gearbox protuberances.[20]

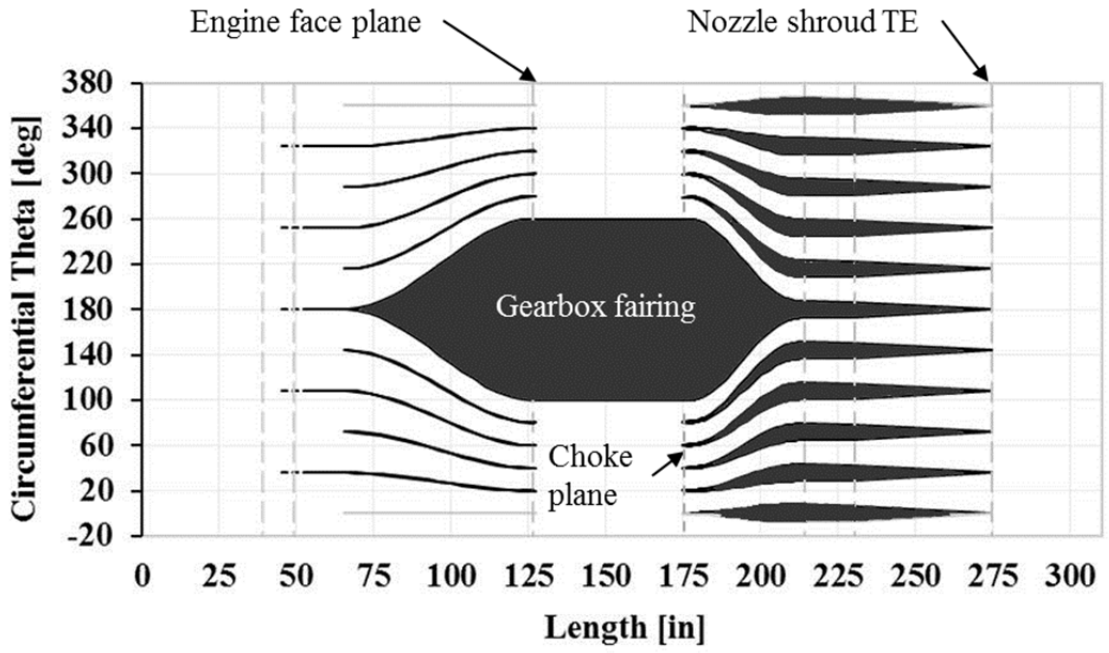

Fig. 1.8. Unwrapped view of the bypass geometry. Flow is from left to right. Courtesy of GAC.

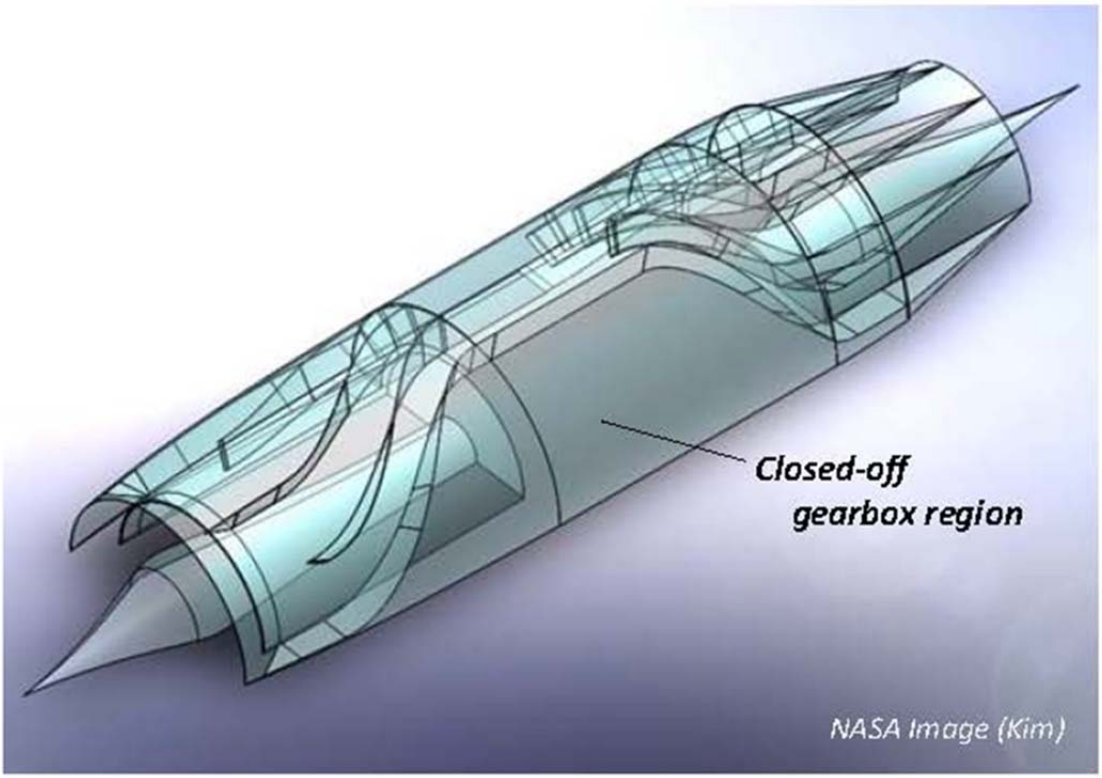

Fig. 1.9. Cross-sectional CAD representation of the bypass region with fore and aft guide vanes. Supersonic inlet centerbody and nozzle are also visible. Flow is from left to right.[20]

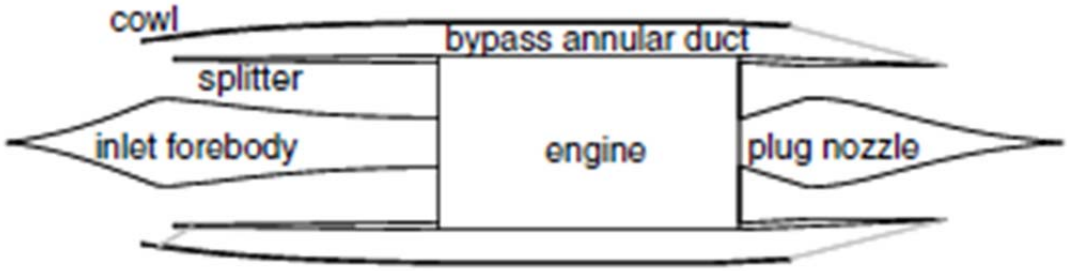

Fig. 1.10. Concept image of the proposed high-flow nacelle bypass supersonic engine. Flow is from left to right. Courtesy of GAC.

Chapter 2

Experimental Methodology

2.1 Aft Bypass Facility

2.1.1 Pre-Existing Facility

An existing wind tunnel, built in the late 1980's at the University of Illinois, was modified for use with the aft bypass project. Designed by Sauter[32], it is a unique blowdown type, supersonic wind tunnel capable of attaining design Mach numbers of up to 2.5. Originally designed to conduct experiments to study the flow behind bodies of revolution, the wind tunnel has an annular, axisymmetric, profile and contains a cylindrical central sting.

A schematic of the wind tunnel air supply system, control and safety features, and exhaust is shown in Fig. 2.1. High pressure air is stored in a tank farm located outside the building and is filled by two compressors located within the basement of the Mechanical Engineering Laboratory. A six inch pipe brings air from the tank farm to Aerospace Laboratory A, wherein the facility is located. A manually operated control value is used to regulate the flow through a six inch supply pipe. A second valve, an electrically operated, LabVIEW controlled, Valtek Mark One spring-cylinder actuated FlowServe valve, is located downstream of the manual valve for exact control of stagnation chamber conditions. The Valtek valve is supplied with house air to supply pressure. The supply pipe enters the stagnation chamber from the top at a 45° angle to cause the flow to impinge against the back wall of the stagnation chamber to facilitate nearly stagnation conditions.

The wind tunnel was originally designed for a stagnation chamber pressure of 60 psia, but for the purposes of this study, the maximum stagnation chamber pressure required was less than 22 psia. Therefore, it was not anticipated that any strength related

structural modifications of the original wind tunnel components would be required. Total temperature, $T_{chamber}$, and stagnation chamber pressure, $P_{chamber}$, are monitored within the chamber using a thermocouple and a pressure transducer, respectively.

The facility stagnation chamber is actually a schedule 40 standard flanged pipe cross with a 12 inch inner diameter, as shown in Fig. 2.2. Flow enters the stagnation chamber from above, while the bottom is closed off and sealed with a flat flange. A taper lock, centrally located within a rear flange is used to constrain the stainless steel central sting, which has a nominal diameter of 2.500 inches. Additional support for the sting is provided by a flow conditioning assembly mounted inside the stagnation chamber.

The flow conditioning assembly is functionally composed of a three-spoked central sting support and honeycomb flow straighteners. The spoked sting support has a tight clearance hole to allow the sting sleeve to pass through, yet still provide it with structural support. It is located 1 inch upstream of the honeycomb. The stainless steel honeycomb is 3 inches thick, and its cells are 0.0625 inches wide by 0.125 inches high. A last, tubular, component is used to fix the flow straightening and sting support devices within the stagnation chamber. All components were machined together so as to ensure that they share the same central axis. The sting support was designed to ensure that, due to the smaller stagnation chamber cross-sectional area due to its presence, the chamber Mach number did not exceed suggested limits. Additionally, Sauter[32] also ensured that the honeycomb would produce laminar, fully developed flow at the honeycomb exit for the tunnel design operating conditions.

A flange, to which the converging nozzle is then mounted, is bolted on the downstream end of the stagnation chamber. The main bolt clearance holes were allowed to be a little oversized so that four pins, located at 90° increments, could be used to manually centrally locate the converging nozzle. A separate diverging section is mounted downstream of the converging section. The entire nozzle was designed using the method of characteristics for irrotational supersonic axisymmetric flow.

The central sting extends fully through the length of the stagnation chamber, flow conditioners, and ends just beyond the end of the converging-diverging nozzle. The sting can slide axially several inches to align the end of the sting with a specific axial station. It protrudes several inches out of the taper lock to allow access through its hollow core.

The throat diameter of the converging-diverging nozzle is 4 inches, while the central sting has an outer diameter of 2.5 inches.

The viewing chamber, mounted downstream of the diverging nozzle, has an internal diameter of approximately 14 inches and is 12.25 inches long as measured from the inside. There are two 7 inch square windows on either side to allow for optical access and a third, 7.25 inches long by 4.25 inches wide, is located on the bottom of the chamber. The fused silica window panes are 0.5 inches thick and are of acceptable optical quality for use with Schlieren photography, surface oil flow visualization, or other optical diagnostics.

The viewing chamber is supported by a 1.50 inch thick support ring on the downstream end. An eye-hook located at top-center (TC) of the ring allows the viewing chamber to be hung from an overhead rail and trolley system, whose axis is directly above and parallel to the wind tunnel axis.

A constant area diffuser with a 7.25 inch inner diameter is located downstream of the viewing chamber. A second diffuser, this one with an increasing diameter, follows and is connected to the exhaust ducting. The exhaust ducting is shared with that of an adjacent supersonic wind tunnel[33]. To ensure that the exhaust from one wind tunnel does not enter the other wind tunnel, gate flanges were installed at the end of the diffusers in both tunnels. Electronic keys were added to the gates to ensure that neither tunnel could operate without the appropriate gates installed in both facilities. The air is exhausted out of the building within aluminum ducting and is directed out a window and then upwards in a chimney.

The rail and trolley system also supports both diffuser elements to the wind tunnel. Use of the rail and trolley aids in tunnel alignment, as all components must, when hanging, be oriented vertically. When chain hoists are employed, the rail can be used to more easily disassemble the facility and affords great flexibility to the system.

2.1.2 Adaptations for Aft Bypass Use

The existing axisymmetric supersonic wind tunnel was well suited for use with the aft bypass project. This is primarily due to its annular profile which corresponds well

with the bypass inner and outer surfaces by simple modification. By replacing the diverging nozzle with a constant area section and scaling the central sting diameter appropriately, the correct bypass annular proportions were generated. Second, the central sting provides a support system for the inner surface of the bypass, gearbox, fairing, and guide vanes, and, it also allows for convenient passage of any pressure lines. Whenever possible, the original wind tunnel components were used for this project.

2.1.3 Design Concept

The facility used in this study was designed to test the aft portion of the bypass region. The aft bypass facility, therefore, was unconcerned with the details of the engine geometry prior to the fully blocked region. This allowed for a simplified wind tunnel design, where uniform flow at the aft bypass inlet was desired.

The overarching concept behind the aft bypass facility design was to extend the full gearbox blockage as far upstream as possible so as to simulate the flow from the fully blocked region and onward only. The central sting concept of the original facility was retained and used as a support structure for all centerbody (inner bypass surface) features including the full gearbox blockage. This structure was extended upstream through the converging nozzle, along its profile, and then up to the flow conditioning devices mounted within the stagnation chamber. The diverging nozzle was removed and a constant area section, hereon referred to as the nacelle component, was placed in its stead to simulate the bypass surface of the outer cowling.

The nacelle component extends into the viewing chamber by approximately one inch. The lengths of the centerbody components were specifically chosen to align the model appropriately with the cowling trailing edge represented by the trailing edge (TE) of the nacelle component. A partial cutaway view of the aft bypass facility depicted in Fig. 2.3 illustrates how several key aft bypass axial-station planes of the full engine configuration concept are simulated within the experimental facility. The approximate location of the aft bypass inlet plane, the cowling TE plane, and the core engine exhaust plane are clearly designated within the figure.

2.2 Assembly Overview

The following section outlines the key wind tunnel components and subassemblies used in this study. A partial cross-sectional view of the entire facility with vaned model installed is shown in Fig. 2.4. The facility assembly process is outlined in Appendix A, complete with figures. A complete collection of wind tunnel component drawings and subassemblies can be found in Appendix B, to which the reader is referenced for more detail.

When possible, original components were used. The design of new components, especially with regards to the placement and size of O-ring grooves and other safety features, was modeled based the original design. When appropriate, calculations were performed to ensure that the components were over-designed. For instance, a worst case area-distributed (tunnel cross section) 100 psi axial load was used to determine the factors of safety of all fasteners.

2.2.1 Central Sting

A new sting, 50.50 inches long, was fabricated. The design concept called for the use of sleeve-type wind tunnel centerbody components representing the inner bypass surfaces. Accordingly, the sting diameter of 2.000 inches was chosen to provide sufficient wall thicknesses to the sleeve components. The sting support and flow straighteners within the stagnation chamber were not altered so the portion of the sting within these structures had to be enlarged so that it could be supported by them. An 8 inch long, 2.500 inch diameter sleeve was fastened to the sting with four cap screws to increase the local diameter so allow for the receipt of support within the stagnation chamber.

2.2.2 Blockage Assembly and Converging Nozzle

One of the most challenging aspects of extending the gearbox blockage upstream was to successfully separate the blocked and unblocked flow streams through the rapidly changing (radially) converging nozzle. A blockage assembly was therefore designed to

fit downstream of the flow conditioners and within the converging nozzle for this purpose.

The blockage assembly is shown in Fig. 2.5. A blockage flange component is mounted directly downstream of the flow conditioners and blocks any flow from passing through the honeycomb within the fully blocked region. A sleeve is mounted downstream of the flange on the central sting and represents the full configuration's centerbody (that is, the core engine). Within the converging nozzle, the upper surfaces of two plates, which are fastened to the blockage flange and the centerbody sleeve, simulate the gearbox.

Instead of machining the plates to exactly fit the complex curvature of the converging nozzle profile, a new converging nozzle with two slots was fabricated. The oversized plates were then fitted inside the slots. In this manner, the vertical alignment of the blockage assembly could be enforced. The slots and plates were machined in steps, thereby allowing for axial load transfer from the blockage assembly into the over-designed converging nozzle. The entire gearbox blockage design is shown in Fig. 2.6 where the converging nozzle is displayed transparently to aid in visualization.

In order to ensure that the new converging nozzle had the same profile as the original, its contour was measured. This was completed using a coordinate measuring machine located in the Metrology Lab of the Department of Mechanical Science and Engineering at UIUC. The measured profile was subsequently used in the new nozzle design and fabrication. The contours of both the converging and diverging nozzle can be found in Appendix C.

The core engine sleeve component extends into the nacelle component. Within the nacelle component, beyond the extent of the blockage plates within the converging nozzle, the gearbox is simulated with a partial sleeve that is fastened to the underside of the centerbody sleeve. The partial sleeve's outer diameter closely matches the inner diameter of the nacelle component to entirely close the blocked region flow path. This completes the blockage assembly and the aft bypass model is then mounted in the familiar sleeve-type configuration. The exact length of blockage assembly extension into the nacelle component is driven by the need to align the model and nacelle TE plane appropriately, as previously outlined in Fig. 2.3.

2.2.3 Nacelle Component

The nacelle component has a constant inner circular diameter equivalent to that of the converging nozzle throat diameter of 4.000 inches. The nacelle is in actuality composed of three components. The first component is a flange-type component and allows for the mounting against and alignment with the converging nozzle. The second component comprises of the majority of the outer wall, or cowling, of the bypass. The third component allows for mounting to and alignment with the viewing chamber. Alignment pins between components were used to ensure proper alignment and bolt hole orientations. The components were fastened together using eight equally spaced socket cap screws on both ends. The inner diameter bore was machined with the components fully assembled to ensure that they shared the same center and that inner surface was continuous.

As explained in Section 2.5.1.2 total pressure probe data was taken at an axial plane located upstream of the aft bypass model. The nacelle therefore had five 1.000 inch circular through holes located at the inlet plane to allow for the insertion of interchangeable wall plugs. Flats were machined into the nacelle at the location of the wall plugs to aid in their alignment and to ensure that the inner cowling wall was uniform at the plugs. Four 0.25 inch deep, threaded holes were placed around each hole so that the wall plugs could be secured. Fig. 2.7 shows how the nacelle wall plugs fitted into the nacelle. A more detailed description of the nacelle wall plugs can be found in Section 2.2.4.

Additionally, 0.040 inch diameter through hole was machined upstream of each wall plug location to serve as an outer wall static pressure tap. The static pressure taps were located approximately 1.5 total pressure probe diameters upstream of the probe tip so as to minimize any probe presence effects from being recorded in the static pressures. An outer nacelle counterbore allowed for the insertion of 0.0625 inch outer diameter stainless steel tubing, which was then epoxied in place. The stainless steel tubing was then used as tubulations for Nylon pneumatic tubing purchased from ScaniValve Corporation which was then plumbed to the pressure transducers.

The total pressure probe traverse was mounted to the outer wall of the nacelle components as well. Two threaded holes were therefore machined into the nacelle

component in line with each of the five nacelle wall plugs. These holes were used to align and hold the traverse and its mounting fixture in place.

Since it is known that the inlet plane through holes would be areas of stress concentration, the aluminum 7075 walls of the nacelle component were made overly thick – 0.725 inches. A load and stress analysis was then conducted on the nacelle assembly to assess its structural strength. Using Autodesk® Inventor, material properties of a weaker material were specified, and a grossly over-estimated 100 psid load applied across the inner and outer walls of the nacelle. The stress analysis report indicated that the maximum expected material displacement was only 1.04E-4 inches. Similarly, the maximum expected stresses were so small as to provide no concern for structural integrity under the expected loads.

2.2.4 Nacelle Wall Plugs

The nacelle wall plugs have a 1.00 inch circular cylindrical component that is then affixed to a 1.25 inch square cap. The flats machined on the outer wall of the nacelle component aided in aligning the square wall plugs. Socket cap screws were used to fix them in place. The wall plugs were inserted into the nacelle component and then the inside was machined to ensure that the inner nacelle wall was smooth and that all components shared the same center.

Five blank nacelle wall plugs were machined to close the facility in the event that no pressure probes were installed in the tunnel. Another wall plug was machined in such a manner to allow for the insertion of the total pressure probe into the facility. A 1/8 inch NPT mounting chuck mounted in the probe wall plug is used to secure the probe and seal the tunnel. The wall plugs are interchangeable so the probe wall plug could be installed in any one of the five nacelle probe holes.

2.2.5 Downstream Components

Since only approximately 0.75 inches of the sting remains uncovered once the model is installed, it could no longer be used to easily support components downstream of the model. This provided a new design challenge as it was important that a centerbody

and diffuser be located downstream of the model substituting for the hot core engine exhaust flow that was not simulated in this study. The centerbody served a secondary purpose of providing an enclosed space in which the pressure lines from the model's static pressure taps could be reversed and then allowed to exit through the central hollow sting. Following the pressure line reversal cavity, a centerbody diffusive cone was placed to ease the flow transition back to a circular cross section within the constant area diffuser. These centerbody structures could not be supported structurally by the central sting and so a new method had to be employed. Fig. 2.8 provides a CAD representation of the aft centerbody components, their physical arrangement, and how they were supported within the aft bypass facility.

Support for the centerbody pressure line reversal cavity cap and the diffusive cone was provided by the same ring-type component that supports the viewing chamber (by hanging). A central component of three spokes was utilized to support the diffusive cone on both the up and downstream sides of the new flange. The pressure line reversal cavity cap was also supported by this new, downstream centerbody support structure.

During wind tunnel facility assembly, the downstream assembly consisting of the components depicted in Fig. 2.8 was hung from the rail and trolley system. Once positioned to the correct height, it was moved upstream and was simultaneously aligned to fit the pressure line reversal cavity cap over the end of the sting and to fit the nacelle component into the viewing chamber. The simultaneous fitting over the sting and nacelle components is illustrated in Fig. 2.9. This was a delicate procedure as great care was necessary to ensure that no components or pressure lines were damaged during this process. Much effort was also placed in ensuring that the assembly settled evenly and tightly with its upstream components as the screws securing it in place were tightened. If needed, shims were added at the diffusive cone support to shift the centerbody assembly upstream to fill the gap between it and the model.

2.2.5.1 Pressure Line Reversal Cavity Cap

The static pressure taps located on the model surface exit the model on the downstream face. Stainless steel tubing is used to turn the lines inwards and then reverse them so that they can exit the facility through the central sting. When the model is

mounted on the sting, approximately 0.75 inches of the sting remains unused, so the stainless steel tubing must extend beyond the end of the sting before it can turn inwards. A cylindrical cap with outer diameter to match that of the inner bypass surface is used to cover and protect the pressure line reversal system. In addition, it also serves to simulate the core engine streamwise extension since the hot core engine exhaust was not simulated in this study.

The pressure line reversal cap, shown in Fig. 2.10, has a constant outer diameter to match that of the model. The cavity is 2.00 inches deep. Since there were multiple rows of pressure lines exiting the downstream face of the model, the walls of the reversal cap were kept to a minimum in order to provide the most space within the cavity. Four, approximately 15° wide segments of thicker walls, were retained in key locations that did not coincide with pressure lines. These segments were machined to slip fit around the last portion of the sting to ensure alignment with the sting and other centerbody components. These segments also added additional structural integrity to the cavity.

The reversal cap is not physically fastened to the model or any other upstream components – it simply uses them for alignment purposes. Instead, it is supported from the downstream direction by the centerbody diffusive cone. Support was provided by cap screws which utilized through holes and counterbores within the four greater wall thickness segments. Alignment pins were used to ensure that the pressure line reversal cap was oriented in the appropriate direction and that the thick segments did not impinge upon the model pressure lines.

2.2.5.2 Diffusive Cone

The diffusive cone was split into two components, one of which was located on either side of the downstream facility support ring. Both components had a half angle of 3°. This angle was chosen to minimize flow separation which would have very quickly rendered the cone ineffective. A side view of the aft centerbody components, including the diffusive cone, is shown in Fig. 2.11.

The first inch of the diffusive cone had a constant diameter, afterwhich, the conical section of the diffuser began. The upstream face of the first diffusive cone component had four threaded holes to allow the fastening of the pressure line reversal

cap. A centrally located threaded hole was located on its downstream end face, into which a male stem from the downstream component was threaded. In this manner, the downstream facility support ring was clamped down upon and thereby caused to support the diffusive cone. A set screw was used to stop the threaded stem from backing out during tunnel operation due to vibration. A short male circular stem and matching female counterbore on the support ring were used to ensure proper axial alignment with the support ring.

The downstream diffusive cone component also had a 3° half angle. When the diameter of the cone reached one inch, it was rounded off with a 0.5 inch radius. The downstream cone was approximately 13.2 inches long, bringing the entire length of the diffusive cone to approximately 20.3 inches. A 2.25 inch long threaded stem protruded from the upstream end to allow the diffusive cone components to be fastened to the downstream facility support ring.

2.2.5.3 Downstream Facility Support Ring

The ring-type component used to hang the viewing chamber from the overhead rail was also used to provide support for the downstream centerbody components of the aft bypass facility. Eight equally spaced screws were used to mount the downstream facility support ring to the viewing chamber and an O-ring provided the sealant. An additional eight screws were used to fasten and align the constant area diffuser, which was sealed with a large rubber gasket, as shown in Fig. 2.12.

The flange's centerbody was held in place by three spokes in a manner very similar to that of the spoked sting support in the stagnation chamber. The diameter of the central ring was chosen to match that of the downstream end of the upstream diffusive cone component. The spokes were 0.25 inches thick and approximately 2.5 inches long. Both the upstream and downstream ends of the spokes were streamlined by machining 15° chamfers to each end.

2.3 Aft Bypass Nomenclature Conventions

Channel and vane naming conventions were used in an identical manner to those established by Kim, et al.,[34] as shown in Fig. 2.13. The channels are numbered 1-5 by increasing curvature so that Ch #1 is the channel with the straightest flow path (near the top of the annulus). Ch #5 is directly adjacent to the highly curved gearbox fairing such that it comprises one wall of the channel. Since the model is symmetric, only five channels need be uniquely identified. The symmetric channels follow the same naming scheme, but are distinguished from the primary side by the subscript "s". The primary side of the model was arbitrarily defined, but generally is the same side of the model that contains the majority of the instrumentation used in this experiment.

The azimuthal angle, θ, is measured from the top-center location. Positive θ is assigned to the primary side of the model, whereas negative θ is on the complementary side. At the forward tips of the aft vanes, each channel encompasses approximately 20°. In this manner, all ten channels encompass the total 200° of the unblocked annulus. Although θ is primarily used with reference to the inlet plane, it is also used to describe the specific location of model surface static pressure taps when needed.

The vanes are also numbered 1-5. Vane numbers are assigned according to the adjacent channel in the increasing θ direction. The first vane is that which splits the symmetry plane, either wall of which make up the smaller θ channel wall. Vane #2 is the upper wall of Ch #2 and the lower wall of Ch #1. Similarly, Vane #5 is the upper wall of Ch #5. The gearbox fairing makes up the last channel walls. Vane numbering conventions follow those used in the channel naming convention with regards to the use of subscripts on the symmetric, or complementary, side of the model.

2.4 Model Design and Fabrication

Two aft bypass models were used in this study. The first, known as the 'clean' model, is devoid of the aft guide vanes and consists of the inner surface of the bypass region, that is, the core engine body, the gearbox blockage and the aft fairing. The second model, known as the 'vaned' model, also incorporates the aft bypass vanes. Fig.

2.14 shows CAD representations of both the clean and vaned models, while the images shown in Fig. 2.15 and Fig. 2.16 depict the final clean and vaned models, respectively.

The models were designed with the computer aided drafting and design (CADD) software Pro/Engineer. Exact model and vane geometry was provided by Gulfstream Aerospace Corporation and then scaled down appropriately for this study (approximately 6%).

The model's length extends 0.280 inches upstream of the plane marking the start of the gearbox closing fairing (and vane tips) to provide a short length of model within the fully blocked region. The model terminates at the trailing end of the fairing and vanes such that the overall length of the each model is 6.120 inches. The inner surface diameter is 2.920 inches, while the gearbox's diameter is 3.997 inches. Each model has an inner diameter of 2.002 inches so they fit tightly over the central sting.

Two cap screw clearance holes are located down the length of the model; one is located at bottom-center, while the other is positioned 35° from TC so that it is roughly aligned with the Vane $^{\#}2$. The cap screws ensure that the model is fixed axially and that it cannot rotate; thereby ensuring gearbox alignment to the upstream blockage components.

The models were fabricated at the Ford Concurrent Design and Manufacture Lab at the University of Illinois at Urbana-Champaign using a stereo lithography apparatus (SLA). The model surface static pressure taps and internal plumbing required to route the pressure readings to pressure lines connected to the pressure transducers were also incorporated into the models.

2.4.1 Model Surface Static Pressure Tap Internal Plumbing

All model surface static pressure taps had a tap diameter of 0.045 inches. The internal lines, of the same diameter, were directed into the model interior in the local normal direction by varying depths and then turned in the downstream direction with a 0.0625 inch turning radius. They then ran the length of the model in the streamwise direction to exit at the end face. A 0.5 inch deep, 0.067 inch diameter counterbore was

placed at each pressure line exit to allow for the insertion of stainless steel tubing. A cross section of the internal pressure line plumbing is shown in Fig. 2.17.

A minimum separation distance between internal pressures lines of 0.050 inches was enforced. In order to ensure that the internal pressure lines did not encroach upon each other at any point within the model, the depth at which the lines ran down the model's length was carefully controlled. Internal pressure lines that traveled the majority of the length of the model were plumbed deeper than those that did not. In this way, an internal line near the downstream end of the model that was plumbed deeper did not pass a shallow line that was already traveling down the model.

2.4.2 Model Fabrication

With guidance from the Ford Lab, it was decided to fabricate the models on a 3D Systems Viper SI Stereo Lithography Apparatus. This particular machine has a build platform size of 250 mm^3 (~10 in^3), comfortably fitting either model. Stereolithography is a rapid prototyping process where a laser is used to partially cure liquid photopolymer resin, thereby causing it to solidify. The resin is cured by the ultra violet (UV) light emitted by the laser, and in this manner, the additive process is continued to build a part. Once built, the part is placed in a UV oven to complete the curing process. The selected material was Somos ProtoGen O-XT 18420, a general purpose, ABS-like photopolymer[35]. Known as ProtoGen White, it is an opaque material commonly used in rapid prototyping. Table 2.1 provides a summary of the material specifications post cure.

Table 2.1 Post-Cure Somos ProtoGen O-XT 18420 Material Properties[35]

Tensile Strength	6.1 – 6.4 ksi
Tensile Modulus	316 – 336 ksi
Elongation at Break	8 – 16 %
Poisson's Ratio	0.43 – 0.45
Flexural Strength	9.7 – 10.2 ksi
Flexural Modulus	289 – 309 ksi
Hardness (Shore D)	87 - 88

Before building an entire model, a test part, consisting of the downstream 0.5 inches of the clean model, was built to conduct several tests. First, the dimensional precision of the SLA machine was tested since tolerances, particularly in the radial direction, were of great importance. Second, the pressure tap exit counterbore diameters could be tested to ensure a tight fit with the stainless steel tubing. Lastly, the relative spacing between pressure tap exits could also be evaluated. Several test rings were built as it was found that the radial accuracy was not as good as expected until a consistently accurate part could be built.

The part build orientation was selected so that uncured resin within the internal pressure lines would drain from the part due to gravity. Even after taking this precaution, it was found that much resin remained within the part's plumbing and so each line was individually cleaned prior to UV curing. This was accomplished by inserting a thin piece of wire into each line and then rinsing with isopropyl alcohol which was forced into each line with a hypodermic syringe with an appropriately sized needle tip. After all internal pressure lines had been cleaned, the part was allowed to fully cure in the UV oven. The models were sanded by hand with successively finer and finer sandpaper to improve surface smoothness to acceptable levels for wind tunnel testing.

2.5 Data Acquisition

2.5.1 Pressure Data

Pressure data were taken in two forms. First, a total pressure probe was traversed radially at five azimuthal locations within the fully blocked region at the inlet to the aft bypass model. Second, surface static pressure taps were used to record pressures on the model (core engine) surface. In the vaned model, these model surface static pressure taps were arranged near the centers of the channels, while in the case of the clean model, the taps were arranged in streamwise rows such that the taps were located at similar azimuthal stations to that of the vaned model's channel exits.

2.5.1.1 Acquisition System

A NetScanner™ pressure transducer system was utilized to record all pressure data. Six Series 9846 pressure scanners containing sixteen silicon peizoresistive transducers each were installed in a Model 98RK-1 rack. The pressure sensors are temperature compensated. A microprocessor accounts for zero, span, linearity, and thermal effects, and is also used to perform zero calibrations. In addition to rezero capabilities, the microprocessors also allow for purge and leak check functionality. A NetScanner™ Model 9034 provided the atmospheric reference pressure which was recorded at the beginning of each run. Images of the 98RK-1 with 9864 scanners installed and the 9034 can be found in Fig. 2.18. A secondary digital display unit was used to visually monitor key measurements during a run including the tank farm pressure, viewing chamber pressure, total temperature, and stagnation chamber pressure.

All of the pressure scanners were recalibrated at the beginning of testing for their full pressure range. Nitrogen was used to supply positive pressure, while a vacuum pump was used to apply negative pressure during the calibration process. Thereafter, each scanner was rezeroed at the beginning of each run. The majority of the pressure scanners employed were used to collect the various static pressures on the outer nacelle wall and on the model surfaces. Most had a ±30 psid pressure range, but five ±15 psid scanners were employed as well. Several 0-100 psid scanners were used to collect the total pressures recorded in the stagnation chamber and with the total pressure probe. After rezero, the pressure scanners have an accuracy of ±0.05% Full Scale (FS). Table 2.2 summarizes the ranges of the pressure scanners and their respective accuracies. Data were typically collected at a scan rate of 3000 Hz.

Table 2.2 Series 9846 Pressure Scanner Ranges and Accuracies

Pressure Range	Static Accuracy	
±30 psi	±0.05 %FS	0.015 psi
±15 psi	±0.05 %FS	0.0075 psi
0-100 psi	±0.05 %FS	0.05 psi

The 98RK-1 rack provided electrical and pneumatic connections for each of the scanners, in addition to PC communication by Ethernet interface. The software associated with the NetScanner System, NUSS, was utilized to control the system from a personal computer. A LabVIEW program used to control wind tunnel operation and data acquisition called upon NUSS during experiments.

2.5.1.2 Inlet Plane Data

At a plane upstream of the model, radial total pressure surveys were conducted at multiple azimuthal stations. The aft bypass inlet plane, as it was referred to, is located 1.42 inches upstream of the forward tips of the aft vanes, which coincides with the start of the gearbox fairing. The aft bypass inlet plane is within the fully blocked region of the bypass geometry.

The five stations at which the radial profiles were conducted corresponded to the azimuthal centers of the five unique channels within the aft bypass region. Due to geometric restrictions, the azimuthal locations were spread out over both sides of the model in a manner such that every other channel corresponded to an azimuthal radial station. Azimuthal location is given by θ, which is measured from the top-center location. Positive θ is assigned to the side of the model known as the primary side, which was arbitrarily defined. As shown in Fig. 2.19 where the dashed radial lines indicate the traverse axes, radial profiles could be conducted at the azimuthal centers of channels 1, 2_s, 3, 4_s, and 5. Each channel is approximately 20° wide. Consequently, the stations were separated by approximately 40° (twice the increment from one channel to the next). Each azimuthal station had a corresponding outer wall static pressure tap which was also located at the inlet plane.

Using the inlet plane data, an annular profile of inlet conditions could be generated, as well as information regarding the boundary layers on both the inner and outer walls. Additionally, total pressure losses could be calculated by accounting for the difference between the measured core flow probe total pressure and the stagnation chamber pressure.

2.5.1.2.1 Total Pressure Probe

In order to minimize the flow disturbance and blockage generated by the total pressure probe, a probe with as small a diameter as possible was desired. After performing calculations regarding probe deflection, stress, and vibration, a 0.049 inch diameter (0.008 inch wall thickness) total pressure probe was purchased from United Sensor Corporation. The probe has a 90° miter joint so that it may be used very near the outer wall of the wind tunnel. Its overall length is 8 inches and it is fabricated from stainless steel. The probe does not have a reinforcement tube. The probe tip is 14 probe diameters long (0.686 inches) and its 30° chamfered tip will aid in accurate data collection in areas of the flow that may have slight angularity.

The probe was inserted through the probe wall plug, which fits in through holes inside the nacelle, and then through a Parker single ferrule tube to NPT male connector. The connector threaded into the probe wall plug and thereby sealed the wind tunnel. A Teflon ferrule within the connector reduced the connector's clamp diameter to that of the probe. The probe, probe plug, and connector can be seen in Fig. 2.20. More information regarding the probe wall plugs and NPT mounting chuck can be found in Sections 2.2.4 and 2.5.1.2.1.

2.5.1.2.2 Radial Traverse

A Zaber linear traverse was used to conduct the radial total pressure probe surveys. The motorized traverse direction and speed of travel were controlled in LabVIEW via a RS-232 serial cable. A potentiometer knob on the motor provided a manual override. The LabVIEW program was also able to monitor the current location of the traverse within its 150 mm (approximately 5.9 inches) traversing length via the internal position feedback mechanism. The device used in this study was a Zaber Model KT-LSR150B.

The functional extent of traversing length for this experiment was the difference between the inner and outer bypass surfaces and was equivalent to 0.54 inches. The probe was located as near the outer wall at the start of a run and then moved inwards during the course of a run. The stage was moved in increments of 0.5 mm

(approximately 0.020 inches) to the inner wall. A single radial traverse took approximately 75 seconds to complete.

The traverse could be mounted to the outside of the nacelle at five different locations (corresponding to the azimuthal inlet plane stations) with a mounting bracket. The probe is secured to the traverse with a clamp-type mechanism that was fastened to the traverse stage. The traverse, mounted and ready for operation, can be seen in Fig. 2.21. The reader is referenced to Appendix B for specific details regarding the traverse mount, clamp, and their assembly.

The probe was very delicate because of its small diameter and lack of a reinforcement tube, making it susceptible to buckling. Therefore, care was taken to always clamp the probe as near the tip as possible. This resulted with the functional traversing segment during tests be near the end of the traverse's limit and so a safety function was incorporated into the LabVIEW code to ensure that the traverse could not retract so far as to damage the probe.

2.5.1.3 Model Surface Static Pressure Taps

In order to keep the internal plumbing of the model surface static pressure taps simple, as few bends as possible were used. Since it was advantageous for the taps to exit the model end face in groups, the static taps were generally organized in streamwise rows on the model surface. The number of taps was limited by the space available in the pressure line reversal cap and by the number of available pressure transducers.

2.5.1.3.1 Clean Model

The clean model has a total of thirty-nine model surface static pressure taps. The taps are arranged in seven rows down the length of the model. Five rows are on one side of the model, known as the primary side. The remaining two rows are located on the opposite side, known as the complementary side, and they are positioned in exactly symmetric positions from those on the primary side of the model. In this manner, flow symmetry could be assessed within the facility.

The static pressure tap row locations are based upon the approximate locations of the vane exits (downstream end of the model). Since the channels created by the vanes

are oriented in a relatively straight, streamwise, direction for the aft 60% or more of the model, the tap rows of the clean model were centered about these locations. Fig. 2.22 displays the tap locations on the unwrapped clean model surface. Generally, the taps were spaced 1 inch apart in the streamwise direction, and the first tap of each row was located 0.370 inches from the beginning of the model.

Five rows of taps (three primary, two complementary) were located at azimuthal stations above the gearbox fairings, and so the taps extended the full length of the model, allowing for a total of six taps per channel. Two rows were located within the azimuthal range of the gearbox fairing and so they contained fewer taps – five and four, respectively. All taps were staggered (azimuthally) so that they were not located directly up- and downstream from one another.

2.5.1.3.2 Vaned Model

The vaned model has a total of forty-eight model surface static pressure taps. As with the clean model, the taps are arranged as near the center of the channels as possible. No two consecutive taps were located directly downstream of each other to minimize the chance of collected data effected by disturbed flow which had passed an upstream pressure tap. As shown in Fig. 2.23, an unwrapped schematic of the vaned model, most of the model surface static taps are located on one side of the model. Several taps had to be located on the opposite side of the model to allow for adequate spacing between the internal pressure lines within the model. Nine to ten model surface static pressure taps are located within each channel.

An additional four surface static pressure taps exist in one of the channel walls of the vaned model. These taps are in the aft end of the model, where the vanes are of sufficient thickness to allow for them. Located at mid height and facing the gearbox channel within the Ch $^{\#}5$ vane, these model wall surface static pressure taps were included to allow for further study of the flow within the most three-dimensional channel. Stars indicate the approximate location of the channel wall static taps in Fig. 2.23. An image of the channel wall surface static pressure taps is shown in Fig. 2.24.

2.5.2 Flow Visualization Techniques

2.5.2.1 Schlieren Photography

A Schlieren photography system was used to visualize the flow beyond the exit of the nacelle (in the viewing chamber) of both the clean and vaned models. Schlieren imaging allows for the visualization of density gradients within the flow arising from flow characteristics such as shock waves, expansion waves, or turbulent eddies. This is accomplished by making use of the change in the index of refraction within the density gradients. Due to the change in index of refraction, the light bends toward or away from a knife edge located at a focal point in front of the camera, thereby creating variations in intensity which can be recorded by a camera.

The Schlieren system was set up in the conventional, "z-type" manner as shown in Fig. 2.25. The light from a light emitting diode (LED) with iris was collimated through the test section by a 11.5" diameter parabolic mirror with a focal length of 64", redirected to a 2.5" square flat mirror by an identical parabolic mirror, past a knife edge at the focal point, and then into a camera lens. The razor blade was placed such that approximately half of the light was blocked. In order to visualize density gradients in the vertical and horizontal directions, horizontal and vertical knife edges, respectively, were used. Schlieren photography was carried out for each of the operating conditions of both models.

The LED light source was used in a pulsing mode with an exposure time of 20 μs. An oscilloscope measured the true exposure time, which was found to be 17.2 μs. A Nikon AF Nikkor 70-300mm 1:4-5.6G telephoto lens was mounted via a C-mount to the camera, a PCO.1600 charge-coupled device (CCD) model (acquired from Cooke Corporation). While running, a sequence of images, typically approximately 250 long, were obtained. Camera operation and control was conducted through the use of the accompanying software, CamWare.

For each set of runs, background and flat field images were also attained. The background images were taken with the light source off, while the flat field images were attained with the light on, but no flow. These images were used in image processing to remove any features in the still images originating from smudges and other imperfections

on the mirrors or in the glass of the windows. The program ImageJ was utilized for image processing. Processing was carried out by carrying out an established operation to remove the background and no-flow characteristics, which is accomplished in the following manner:

$$Image^{Post} = \frac{Image^{Pre} - Background_{ave}}{Flatfield_{ave} - Background_{ave}} \quad (2.1)$$

where the subscript "ave" refers to average and the superscripts "Pre" and "Post" refer to pre-processing and post-processing, respectively.

2.5.2.2 Surface Oil Flow Visualization

Model surface oil flow visualization was conducted to provide insight into the flow characteristics within the bypass model. In the most general sense, surface oil flow visualization (SOFV) is carried out by applying a mixture, typically oil based, containing a flow marker to the surface of interest. As the wind tunnel runs, shear stresses cause the mixture to move, thereby allowing visualization of the flow.

Methods for acquiring useful surface oil flow visualizations vary greatly and extensive experimentation is usually required to determine the method best suited for the particular application in mind. Mixtures typically contain oils (olive, motor, gear, oil treatments) to control viscosity so that the mixture does not run before the desired operating conditions are met, as well as before and after the run. Volatiles, such as kerosene, are often added to allow the mixture to dry during a run, while other additives, such as oleic acid or linseed oil, are used to thwart clumping of solid flow markers[36]. Powders, such as lampblack or chalk, and fluorescent dye are two of the commonly used flow markers. Application methods range from full coverage by spraying or paintbrush, speckling, stripes, and dotting. Each method has distinct characteristics and for the purposes of this application, two flow markers were used – one of which was found to be superior to the other.

The first method utilized a lampblack based mixture, while the second used fluorescent dye as the flow marker instead. Use of the fluorescent mixture appears to be much more advantageous than the lampblack based mixtures for several reasons. First, the fluorescent dye is a liquid, while the lampblack introduces particulate matter into the

mixture, thereby changing the flow characteristics of the mixture. Second, the dye's fluorescence can be taken advantage of in parts of the model where most of the mixture had been removed during the run simply because, by increasing the exposure time, photographs showing the flow streaklines can still be easily attained. The use of a lampblack mixture does not afford this flexibility.

2.5.2.2.1 Fluorescent SOFV

The fluorescent mixture consisted of STP oil treatment with several drops of fluorescent dye. Enough dye was added so as to allow for easily visualization under a black light. Since STP oil treatment is extremely viscous, SAE 10W-30 (motor oil) was added to the mixture for runs conducted at a lower Mach number to decrease the viscosity to allow the mixture to run. At maximum, a 40:60 ratio of motor oil to STP oil treatment was used.

In order to conduct SOFV, the facility was disassembled and the model removed. It was discovered that the SLA material (from which the models were constructed) tended to absorb oil from the mixtures. In order to combat this, black contact paper, which was acquired from a local hardware store, was applied to the model first, after carefully cutting appropriately shaped stencils for each of the model surfaces. Before cutting and applying the stencils, a 1/8" grid was drawn onto the contact paper with a pencil. The mixture was then applied to the model with a hypodermic syringe. The 26.5 gauge Leur lock needle's angled tip was carefully cut so as to straighten the tip. A small amount of pressure was applied to the syringe once and then very tiny dots were applied to the model on the grid points simply by contacting the needle tip to the model surface while holding the syringe perpendicular to the model. Constant application of pressure to the syringe was not needed; capillary action, combined with a single pressurization at the beginning, was sufficient to apply the mixture. The prepared clean model can be seen in Fig. 2.26 while Fig. 2.27 displays the model with applied mixture where a black light is used for visualization.

Once the mixture had been applied to all of the model surfaces of interest, the model was carefully positioned on the sting and mounted using the model alignment screws. The facility was then reassembled and the tunnel was then run once at the

desired operating condition. The facility was then disassembled and the model extracted, taking great care not to touch the model surface and smear the surface oil flow results. Photographs were taken under black lights using a tripod-mounted Nikon D3100 digital camera. Care was taken to fully document all SOFV results by taking images of the model as it was rotated.

In order to ensure that a) the mixture did not dry prior to running the tunnel and, b) the results did not smear, trail, or run post run, the process described above was carried out as quickly as possible. Typically, it took about an hour to apply the mixture, 1.5 - 2 hours to assemble the tunnel, 30 - 45 minutes to prepare and perform the actual run, and an additional 1.5 hours to disassemble the tunnel. It was found that the SOFV results were preserved, relatively unchanged, for about 12 hours. The fluorescence qualities were preserved much longer than that, but the mixtures tended to run, especially in the regions of the model where the mixture has pooled if allowed to sit for too long.

2.5.2.2.2 Lampblack SOFV

Surface oil flow visualization was carried out twice using a lampblack based mixture. The first time, the model was not extracted from the wind tunnel and a different mixture and method of application were used. This was the first trial with any kind of surface oil flow visualization and was completed largely to ascertain whether or not further investigation would be worthwhile.

For the first test, a solution consisting of motor oil, lampblack, and kerosene (due to its evaporative properties) was applied with a paintbrush in dots. The mixture was composed of 10 drops kerosene, 7 drops SAE 10W-30 motor oil, and enough lampblack to create a slightly pasty mixture. The choice of the paintbrush ultimately was driven by the fact that more than 50% of the model was largely inaccessible as it was upstream of the end of the nacelle. With a paintbrush, it was still possible to provide some coverage upstream of the nacelle's end plane. In order not to overload the brush, and thereby the model, the brush was merely wetted against the side of the bottle containing the mixture and great care was take not to ever dip the brush into the solution proper. Ideally, the mixture would have been applied in some sort of ordered arrangement, but this was extremely difficult to accomplish when blindly applying the mixture. Despite this, the

results of the clean model surface oil flow visualization provided some qualitative insight into the location and size of the recirculation region aft of the gearbox fairing on the clean model.

The second round of SOFV using a lampblack based mixture was carried out concurrently with the fluorescent runs. This lampblack mixture consisted of STP oil treatment and motor oil, in a similar manner to the fluorescent mixture. Lampblack, added in very small amounts, was carefully mixed in until the mixture was thoroughly dyed, but not to the point of clumping. Clear contact paper, cut from stencils, was applied to the model surfaces so that the SLA material could not absorb the liquidous content from the mixture. The mixture was applied in an identical manner to that of the fluorescent mixture – that is, using a hypodermic syringe in a structured 1/8" spaced grid. Fig. 2.28 shows an image of a fully prepared and gridded vaned model of which half of the model used the fluorescent mixture while the other half used the lampblack based mixture.

2.5.3 Data Acquisition with LabVIEW

A LabVIEW program was used to concurrently operate and control the wind tunnel and collect pressure data. The wind tunnel was controlled by regulating the position of the valves controlling the flow of air into the stagnation chamber. The Valtek FlowServe valve could be controlled by the LabVIEW program by varying the current sent to the valve. The second valve, a manual gate valve, was operated by the user. Two valves served as a safety and redundancy factor during testing.

During the course of a run, the valves controlling the amount of flow entering the stagnation chamber had to be continually adjusted. This was due to the decreasing tank farm pressure during the course of a run as more and more air entered and exhausted the wind tunnel. Although closed loop LabVIEW control is a possibility, the tuning process to achieve reliable and steady closed loop control was judged to be too sensitive for use in this study. The reason for this was largely due to the low stagnation chamber pressure required for this study, which required that the valves been in a "mostly closed" position. However, closed loop control of the LabVIEW controlled valve functions best when the

valve is at least 50% open and so a user-monitored open loop wind tunnel control was used instead.

When the clean model was installed in the tunnel, the manual gate valve was fully opened and the LabVIEW controlled valve was then used to regulate the stagnation chamber pressure (refer to Fig. 2.1 for a wind tunnel valve and plumbing diagram). With this setup, wind tunnel control was entirely conducted from the computer. When the vaned model was installed, it was found that this method of tunnel operation did not afford the amount of control that was required to maintain a consistent operation condition. Therefore, for vaned model tests, the LabVIEW controlled valve was set to 50% open and then the manual gate valve was slowly opened until the desired operating condition was achieved. During the course of a run, the user had to continually adjust the valve position to maintain a constant operating condition.

The LabVIEW program was also responsible for the collection of pressure data. While the wind tunnel was in operation, the pressure scanners continually recorded pressure data which were then processed and arranged in data matrices. Later data analysis removed any data that had been collected during tunnel start, ramp up, or during and after tunnel shut down.

The radial traverse system was also integrated into the LabVIEW program. Prior to running the automated traversing sequence, several parameters were first specified. The traversing start position, end position, and channel to be traversed (probe azimuthal location) were specified. The traverse sequence alternately moved the probe, paused to record pressure measurements, and then moved again. This process was repeated until the specified length had been covered.

The schlieren photography software, CamWare, was run independently from the LabVIEW program on the same computer.

2.5.4 Test Matrix

The prescribed inlet plane Mach number that this study intended to achieve was $M_{tunnel} = 0.700$, which was easily achieved with the clean model. When the vaned model was installed in the wind tunnel, however, it was found that the facility choked prior to

achieving the design point. The vaned model test maximum achievable tunnel Mach number was 0.538. While clean model data were only collected at a single operating condition, several operating conditions were used for the vaned model. In addition to five unchoked cases, two choked flow operating conditions were run for the vaned model. The choked cases were distinguished from each other by their respective subscripts which indicate the approximate P_0. Table 2.3 presents the test matrix employed in this study.

Table 2.3 Test Matrix

M_{tunnel}	Test Model	Inlet Plane Survey	Model Surface Static Taps	Schlieren		Surface Oil Flow	
				Horiz	Vert	Lampblack	Fluorescent
0.148	Vaned	x	x	x	x		x
0.294	Vaned	x	x	x	x		
0.385	Vaned	x	x	x	x		x
0.481	Vaned	x	x	x	x		
0.531	Vaned	x	x	x	x		
$0.538\|_{20.00}$	Vaned	x	x	x	x		
$0.538\|_{21.00}$	Vaned	x	x	x	x		x
0.704	Clean	x	x	x	x	x	

2.6 Facility Control and Operation

The primary metric to ensure constant wind tunnel operating conditions was the ratio of the pressure between a single static tap, $P_{st\ OP}$, at the inlet plane and the stagnation chamber pressure, $P_{chamber}$. The static tap used to measure $P_{st\ OP}$ was the Ch #1 outer wall tap, which was located near TC, and, since it was on the inlet plane, was model invariant. The tunnel operating condition pressure ratio, PR_{OP}, was defined as

$$PR_{OP} = \frac{P_{st\ OP}}{P_{chamber}} \tag{2.2}$$

and was monitored in real time during a run with the LabVIEW program.

However, since pressure losses exist between the stagnation chamber and the aft bypass inlet plane, PR_{OP} was not a good metric on which to base the true operating

condition. Although the total pressure probe provided the true local total pressure at the inlet plane, the probe's location varied between runs and, for some runs, wasn't even present. Therefore, it could not be used on a run-to-run basis to establish a reference true local total pressure for a given $P_{chamber}$. For this reason, a pressure recovery factor, *PRF*, was determined for each operating condition by comparing the core flow total pressure probe data at the Ch #1 azimuthal station to the stagnation chamber. In this manner, the true, loss-corrected total pressure at the inlet plane could be accurately determined for each operating condition based on the stagnation chamber pressure. The loss-corrected, operating condition representative total pressure, P_0, could be determined using the *PRF* regardless of the location of the probe.

$$PRF = \frac{P_{total}^{Ch\#1}}{P_{chamber}} \tag{2.3}$$

$$P_0 = PRF \cdot P_{chamber} \tag{2.4}$$

Typical losses within the facility were small so the correction provided by the *PRF* was small, leading to *PRF*s that were very nearly unity. P_0 was utilized over $P_{chamber}$ in subsequent data analyses since it was a more reliable measurement of the true total pressure.

The true facility operating condition was characterized by Mach number instead of pressure ratio in order to distinguish it from the un-corrected pressure ratio, PR_{OP}. M_{tunnel} was defined using the pressure ratio variant of the isentropic relation given by

$$M_{tunnel} = \sqrt{\frac{2}{\gamma - 1}\left[\left(\frac{P_{st\ OP}}{P_0}\right)^{\frac{1-\gamma}{\gamma}} - 1\right]} \tag{2.5}$$

In order to conduct a survey of the inlet plane, the wind tunnel needed to run at a relatively constant operating condition while the probe traversing sequence ran which took approximately 75 seconds to complete. The variation in operating condition during a run was assessed by calculating the maximum percent change in $P_{chamber}$, M_{tunnel}, and the tunnel operating Reynolds number, Re_{tunnel}, during the course of a traversing run. Re_{tunnel} is defined as

$$Re_{tunnel} = \frac{Md}{\mu}\sqrt{\frac{\gamma}{\mathcal{R}}}P_{st}\sqrt{\frac{1+\frac{\gamma-1}{2}M^2}{T_{chamber}}} \tag{2.6}$$

where μ is the viscosity and d is the characteristic length, in this case the difference between R_{outer} and R_{inner}, which is equivalent to 0.54 inches, was chosen. It was judged that a maximum allowable variation in M_{tunnel} and Re_{tunnel} of approximately 5% would constitute a 'steady' run.

Results show that for the two lowest values of M_{tunnel} variations exceeded the maximum allowable goal of 5%. This is likely due to the fact that the valves used to control stagnation chamber pressure provide the most control within the mid-range, that is, half way open. Variations for the other operating conditions proved to lie well within the desired allowable range.

The viscosity, μ, used in Eq. 2.6, was calculated using Sutherland's Law.[37,38] The model developed by Sutherland estimates μ based on the local temperature, T, reference conditions (signified by subscript ref), and an empirical constant, S. T can be defined via the isentropic relations given $T_{chamber}$ and the pressure ratio as shown in Eq. 2.7. The viscosity, μ, is given by the following series of equations

$$T = \frac{T_{chamber}}{\left(\frac{P_{chamber}}{p}\right)^{\frac{\gamma-1}{\gamma}}} \tag{2.7}$$

$$\mu = \frac{C_1 T^{3/2}}{T+S} \tag{2.8}$$

$$C_1 = \frac{\mu_{ref}}{T_{ref}^{3/2}}\left(T_{ref}+S\right) \tag{2.9}$$

where μ_{ref} = 1.716e-5 kg/(m s), T_{ref} = 273.15 K, and S = 110.4 K. Temperature must be given in Kelvin.

2.7 Flow Variables and Data Analysis Methods

The following section describes the calculations that were performed in the processing of the experimental data. The method for calculating uncertainties is described in Appendix D, along with calculations and sample values.

2.7.1 Inlet Plane

Several data processing adjustments were employed to better understand the inlet plane data that had been collected. Variations in operating conditions during the course of a run and between runs had to be removed to allow for comparison of data sets.

All inlet plane data was plotted against the normalized radial position, R^*. R^* is a function of the current probe position, R, and the inner and outer radii of the aft bypass region, respectively designated by R_{inner} and R_{outer}. R^* is expressed as

$$R^* = \frac{R - R_{inner}}{R_{outer} - R_{inner}} \tag{2.10}$$

By definition, R^* is zero at the inner wall and unity at the outer wall. The range of inlet plane data, however, is smaller. This is primarily due to the finite probe tip diameter, but was also attributed to user caution against damaging the probe by contact with the wall.

During the course of a run, it was found that the operating condition varied slightly as the high pressure air in the tanks was used up. To compensate, the valves were opened incrementally during the course of a run. As a result, the data were characterized by distinct 'z' or 'N' type shapes, depending on whether the data were plotted versus R^* or time, t. This effect was evident in all recorded pressure data including the total pressure probe and outer wall static taps at the inlet plane, which were designated by their respective subscripts of 'total' and 'st'. In order to remove the zigzag character from the total pressure data when presenting it, each instantaneous total pressure data point was normalized by the instantaneous stagnation chamber pressure to generate $P_{t,\,non\text{-}dim}$, defined as

$$P_{t,non-dim} = \frac{P_{total}}{P_{chamber}}\Big|_{instantaneous} \tag{2.11}$$

Inlet plane Mach number was calculated via the customary isentropic and so it was subsequently dependent on the static-to-total pressure ratio. Since both the static and total pressures had the same shape characteristics during a run, the pressure ratio was relatively constant. This led to a smooth Mach number profile. However, a second correction was required first.

It was discovered that the outer wall static pressure data were greatly influenced by the presence of the total pressure probe. The probe's influence was evident regardless of radial position and so it was critical that an accurate representation of the local outer wall static pressure be determined. Therefore, a two run system was employed. The probe was used in one run to attain the total pressure and a second run was used to attain a representative outer wall static pressure. The second run is designated by the subscript 'empty'.

In order to account for the difference in operating conditions between runs, a correction was applied to the empty run static pressure data. Based on the assumption of constant pressure ratio between runs, the static pressure data were adjusted based on the small difference in stagnation chamber pressures between runs. In this manner, the data from two runs were effectively reduced to one run. The adjusted empty run outer wall static pressure, $P^*_{st,empty}$, is described as

$$P^*_{st,empty} = P_{chamber,empty}\left(\frac{P_{st}}{P_{chamber}}\right) \tag{2.12}$$

Inlet plane Mach number, M_{inlet}, was calculated using the adjusted empty run outer wall static pressure and the probe total pressure via the customary pressure ratio based isentropic relations.

$$M_{inlet} = \sqrt{\frac{2}{\gamma - 1}\left[\left(\frac{P^*_{st,empty}}{P_{total}}\right)^{\frac{1-\gamma}{\gamma}} - 1\right]} \tag{2.13}$$

Inlet plane Mach number was the preferred metric for analysis of inlet plane data. However, velocity profiles were also calculated. In order to do so, inlet temperature, T, was calculated isentropically. The speed of sound, c, was then calculated and used to determine the velocity, U. This calculation process is described by Eq. 2.14 – 16.

$$T = \frac{T_{chamber}}{1 + \frac{\gamma - 1}{2} M^2} \tag{2.14}$$

$$c = \sqrt{\gamma \mathcal{R} T} \tag{2.15}$$

$$U = M_{inlet} c \tag{2.16}$$

The boundary layers on both the inner and outer walls were also of interest. Boundary-layer thickness, δ, was determined as the height at which the measured velocity, reached 99% of the freestream, or core, velocity. Since the total temperature for each traversing run was constant, the speed of sound was constant, allowing for the use of Mach number instead of velocity. The displacement thickness, δ^*, and momentum thickness, Θ, could also be written in terms of Mach number. The core Mach number, M_{core}, was taken as the average M_{inlet} with the range $0.35 \leq R^* \leq 0.65$. δ^* and Θ, therefore, took the form

$$\delta^* = \int_0^\infty 1 - \frac{M_{inlet}}{M_{core}} dr \tag{2.17}$$

$$\Theta = \int_0^\infty \frac{M_{inlet}}{M_{core}} \left(1 - \frac{M_{inlet}}{M_{core}}\right) dr \tag{2.18}$$

2.7.2 Model Surface Static Pressure

2.7.2.1 Clean Model

All clean model surface static pressure taps were normalized by P_0. P_0, defined in Section 2.6, is the approximate inlet plane total pressure within the core at the Ch $^{\#}1$ azimuthal location. Since the normalization was not carried out with the true local total pressure, clean model pressure data analysis could not be extended to the calculation of Mach number. Nevertheless, regions of low pressure likely correspond with higher Mach number. Since total pressure can only decrease with streamwise position, the normalized clean model surface static pressure data do at least provide a maximum possible boundary on the Mach number. Clean model pressure data were presented in contour plot format.

2.7.2.2 Vaned Model

Unlike the clean model, where all of the surface static pressure taps were within a single internal flow tube, the vaned model was composed of multiple internal flows as defined by the vanes. Instead of normalizing all of the static pressures by a single inlet plane total pressure, the vaned model data were normalized differently. The static pressure taps within each channel were normalized by that channel's inlet plane core total pressure, which was measured with the total pressure probe.

The data for each channel were presented independently. The normalized pressures for each channel were plotted, for each of the tested operating condition, versus model axial position, x. The local normal channel area, A, is plotted on the secondary axis as normalized by that particular channel's minimum (throat) area, A_{throat}. A composite image of the inner bypass fluorescent surface oil flow visualization results for each channel was typically presented with the pressure data. The surface oil flow visualization image also clearly designated the exact locations of the model's static pressure taps.

2.7.2.2.1 Isentropic Comparison

After assessing the experimental results of the channel pressure data, a question as a measure of how isentropic the experimental results were motivated an investigation into an isentropic case calculation. For the purposes of this computation, it was assumed that total pressure was conserved from the inlet plane to the location of the first model surface static pressure tap within each channel. This seemed reasonable because within that region the flow was fairly unimpeded and also did not exhibit much curvature. As before, it was further assumed that the wall static pressure was representative of conditions within the core flow of the channel.

Total and static pressure conditions at the first channel static tap were used to determine the Mach number via Eq. 2.19. Using the Mach number, the isentropic area ratio, $A/A^*|_{exp}$, at the first static pressure tap was determined using the Mach-area relation described in Eq. 2.20. Given the true local normal area at the first static pressure tap, the sonic ideal area, A^*, could be determined for each channel as shown in Eq. 2.21.

$$M = \sqrt{\frac{2}{\gamma - 1}\left[\left(\frac{P_{st}}{P_{total}}\right)^{\frac{1-\gamma}{\gamma}} - 1\right]} \tag{2.19}$$

$$\left(\frac{A}{A^*}|_{exp}\right)^2 = \frac{1}{M^2}\left[\frac{2}{\gamma+1}\left(1 + \frac{\gamma-1}{2}M^2\right)\right]^{\frac{\gamma+1}{\gamma-1}} \tag{2.20}$$

$$A^* = \frac{A_{first\ st\ tap}}{\left(A/A^*\right)|_{exp}} \tag{2.21}$$

With full knowledge of the true local normal area throughout each channel, the isentropic area ratio, $A/A^*|_{isen}$, could be calculated for all locations within each channel. Then, the process was carried out in reverse, and the Mach-area relation was used to determine Mach number, and thereafter, the isentropic ideal pressure ratios at all locations within the channels, $(P/P_{total})|_{isen}$.

The isentropic case calculation was further improved by applying one additional correction. This correction amounted to removing the approximate displacement thickness of each wall from the local normal area to define an effective, or flow usable, local normal channel area. The displacement thickness was estimated using the single parameter correlation method developed by Thwaites[39] in 1949. This final correction improved the agreement significantly, in some cases up to approximately 10% better. The Thwaites-corrected isentropic case calculation resulted in a known isentropic ideal pressure ratio, $(P/P_{total})|_{Thw\ isen}$, as a function of axial position.

The procedure employed to incorporate this displacement thickness area correction is herein fully described. The isentropic relations were utilized to calculate local T and ρ throughout each channel as shown in Eq. 2.22 and Eq. 2.23, respectively. T_{local} was then used to calculate local sound speed, and then, using M, the local flow velocity, u_{local}, in the form of Eq. 2.15 and Eq. 2.16. Viscosity, μ, was estimated from T_{local} using Sutherland's law, from which a local kinematic viscosity, v_{local}, was calculated by Eq. 2.24.

$$T_{local} = \frac{T_{chamber}}{\left(\frac{P_{total}}{P}\right)^{(\gamma-1)/\gamma}} \tag{2.22}$$

$$\rho_{local} = \frac{\rho_0}{\left(\frac{P_{total}}{P}\right)^{\frac{1}{\gamma}}} \tag{2.23}$$

$$\nu_{local} = \frac{\mu}{\rho_{local}} \tag{2.24}$$

Thwaites' method is based upon careful manipulation of the momentum-integral equation so that is uses a single correlation parameter known as λ, where λ is defined according to Eq. 2.25. Thereafter, Thwaites was able to predict the momentum thickness (Θ_{Thw}) according to Eq. 2.26, which was calculated numerically. *du/dx* was also calculated numerically and then used to determine λ. *H(λ)*, an empirical fit function, was then used to determine the displacement thickness, δ^*_{Thw}, as a function of axial position, according to Eq. 2.27. and Eq. 2.28.

$$\lambda = \frac{\Theta^2_{Thw}\left(du/dx\right)}{\nu_{local}} \tag{2.25}$$

$$\Theta^2_{Thw} = \frac{0.45\nu_{local}}{u^6}\left[\int_0^x u^5 dx\right] \tag{2.26}$$

$$H(\lambda) \approx 2.0 + 4.14z - 83.5z^2 + 854z^3 - 3337z^4 + 4576z^5 \quad \text{where } z = z(\lambda) = (0.25 - \lambda) \tag{2.27}$$

$$\delta^*_{Thw} = \Theta_{Thw} H(\lambda) \tag{2.28}$$

The area contained within the displacement thicknesses on all four walls was then subtracted from the local normal area. A new A^* was then calculated according to Eq. 2.21, for the new, Thwaites-adjusted, $A_{first\ st\ tap}$. The last step included using A^*_{Thw} to calculate A/A^*_{Thw}, and then in turn, $M_{Thw\ isen}$, and finally, $P/P_{total}|_{Thw\ isen}$.

In order to be able to determine how well the isentropic case calculations agreed with the experimentally recorded data, the percent difference between the two cases was calculated. The percent difference was calculated relative to the experimental data such that the new parameter is defined as

$$\left(\frac{\frac{P}{P_{total}}|_{Thw\ isen} - \frac{P}{P_{total}}|^{*}_{exp}}{\frac{P}{P_{total}}|^{*}_{exp}} \right) \cdot 100 \tag{2.29}$$

2.7.2.2.2 Mass Flow Rate

The mass flow rate, $\dot{m}$, within each channel was also calculated as a function of increasing operating condition. Conditions at the first static pressure tap within each channel were formulated in an identical manner to the isentropic case calculations. The inlet plane total pressure was assumed to be unchanged at the location of each channel's first static pressure tap, where the local normal area and static pressure were known. The mass flow rate (MFR) for each channel was determined using the compressible formulation (Eq. 2.30). The percent contribution to the facility total MFR was assessed for each channel as a function of operating condition.

$$\dot{m} = \frac{AP_{total}}{\sqrt{T_{local}}} \sqrt{\frac{\gamma}{\mathcal{R}}} M \left(1 + \frac{\gamma - 1}{2} M^2\right)^{-\frac{\gamma+1}{2(\gamma-1)}} \tag{2.30}$$

2.7.2.2.3 Total Pressure Losses Estimation

An estimation of the total pressure losses within each channel was carried out by making use of the previously estimated mass flow rates. This was accomplished by recognizing that the compressible mass flow rate formulation is a function of the local total pressure, Mach number, total temperature, and the local area. Mach number is itself a function of total and static pressures via the customary isentropic relation (Eq. 2.19). Therefore, for a fixed mass flow rate (that is, under the conservation of mass), total pressure may be iterated upon for each experimentally recorded static pressure. When examining the results of this calculation, the primary mode of evaluation is to check that the total pressure losses always increase. This would indicate that the total pressure never increases, which is a physical impossibility.

Figures

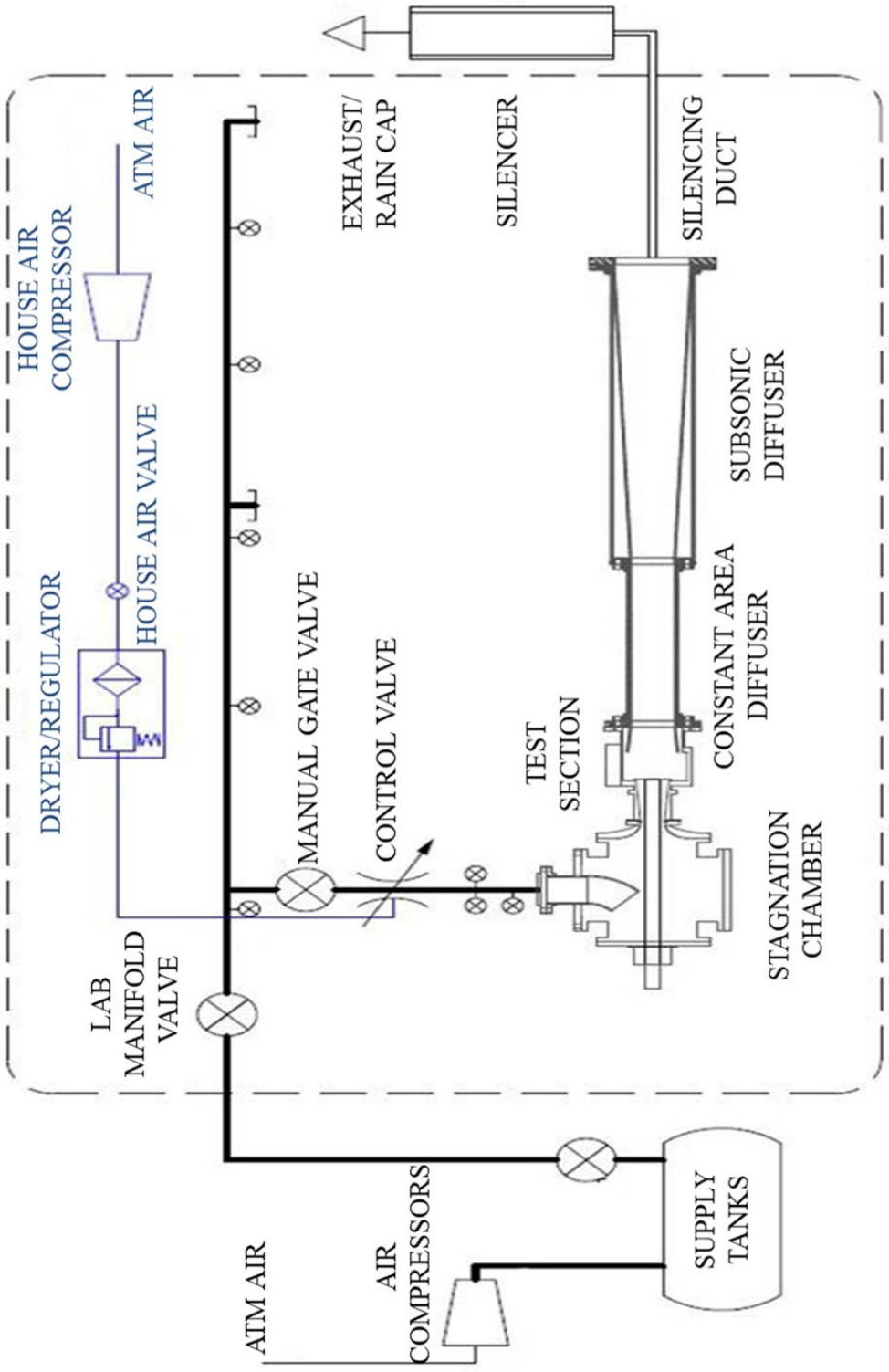

Fig. 2.1. Schematic of wind tunnel air supply system, control and safety features, and exhaust system. Image adapted from Sass.[40]

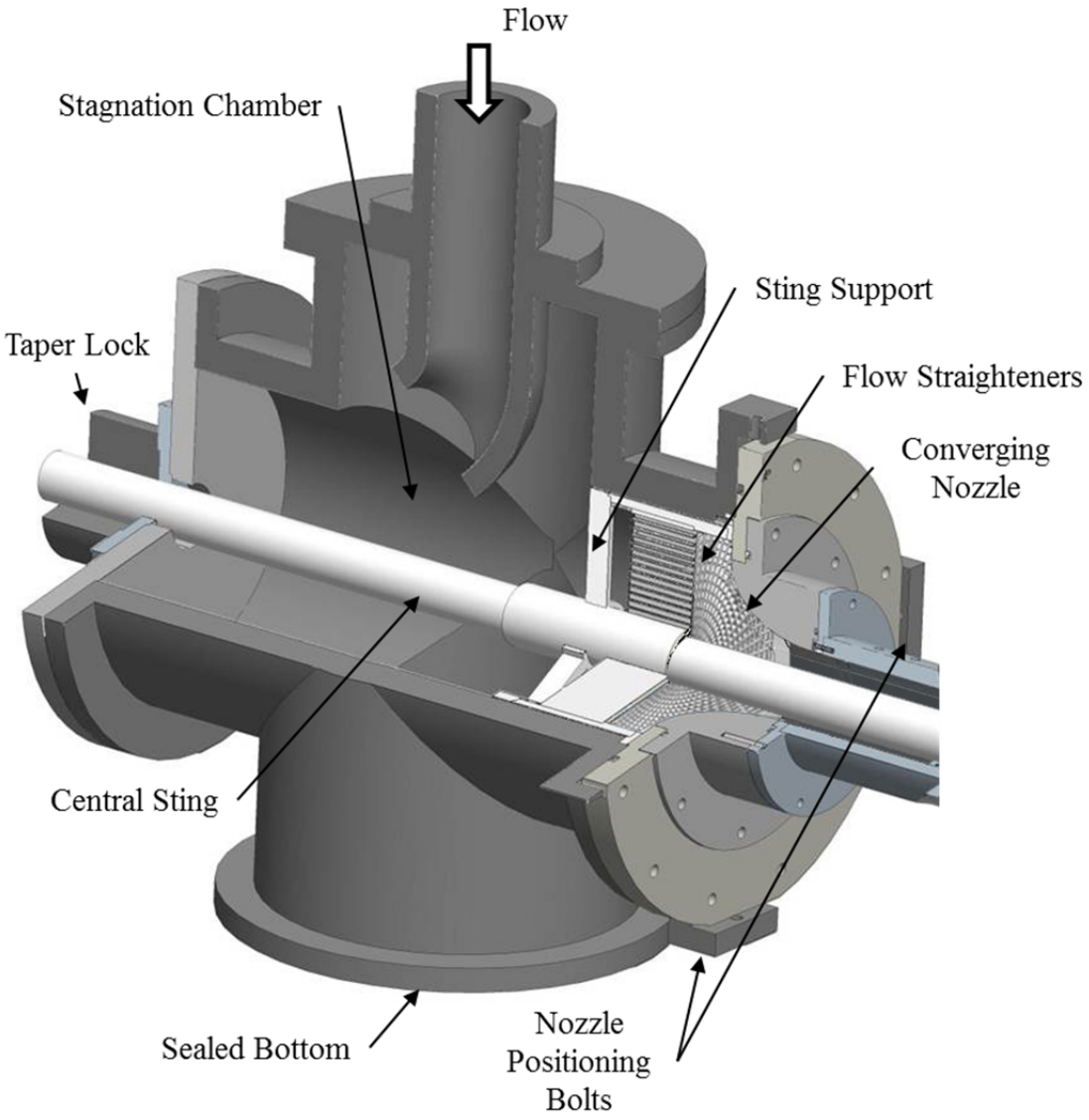

Fig. 2.2 Detailed view of the stagnation chamber construction, internal support structure, flow conditioning device, and nozzle positioning mechanism.

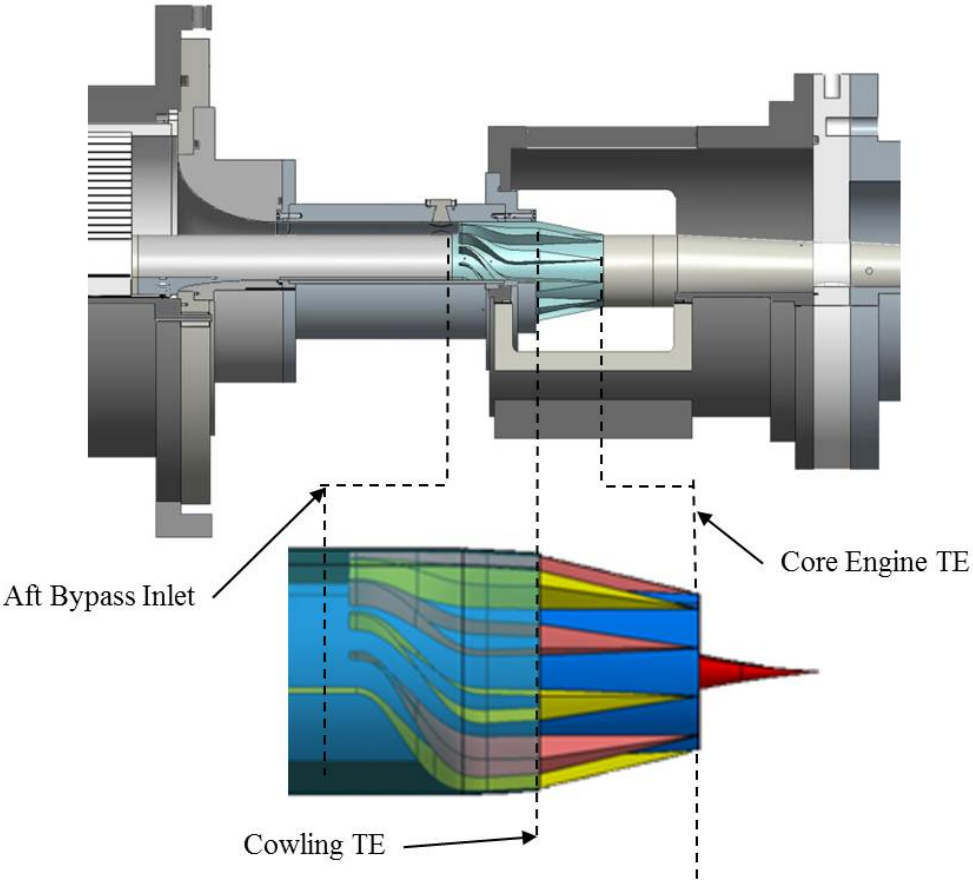

Fig. 2.3. Alignment of key aft bypass reference planes within test facility.

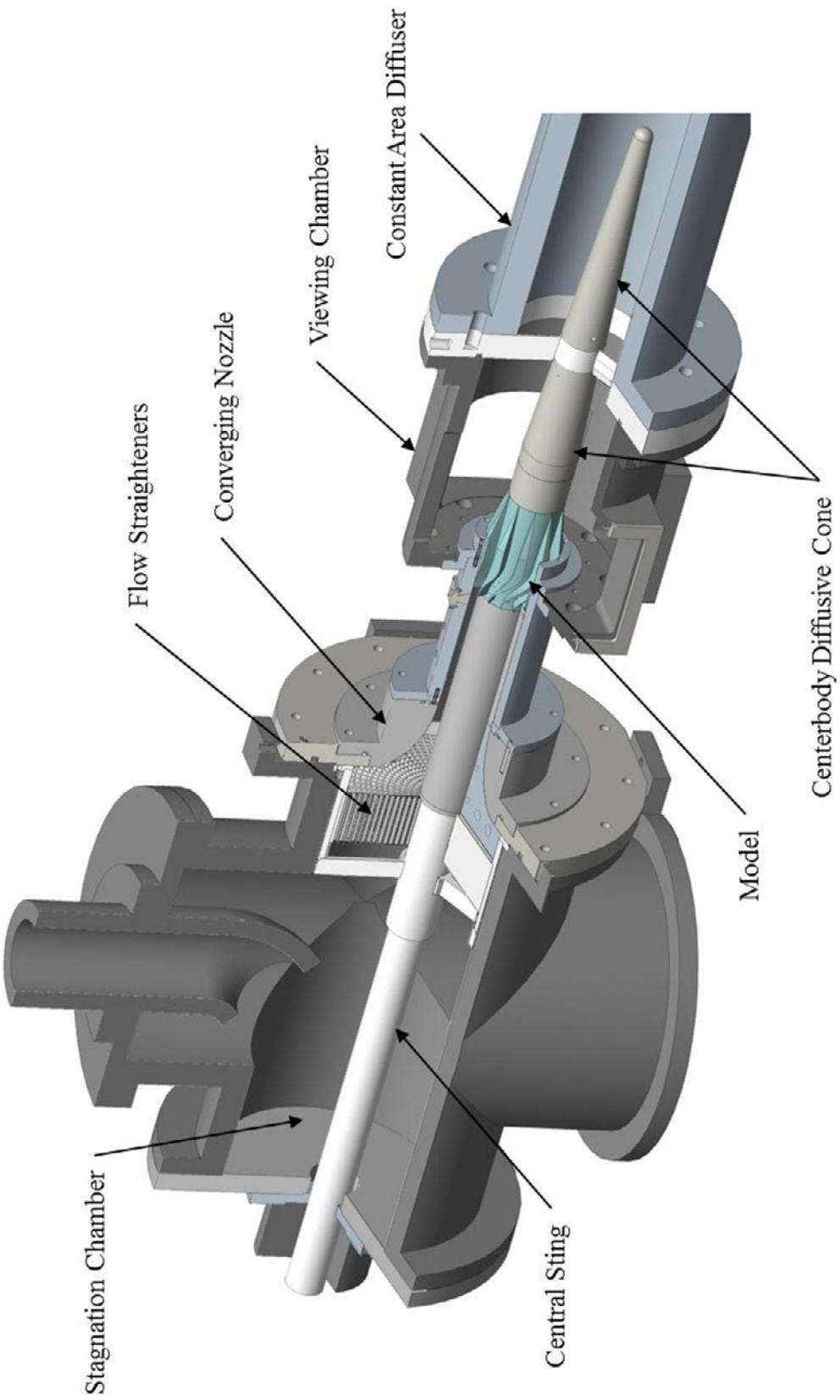

Fig. 2.4. Partial cross-section view of the aft bypass facility.

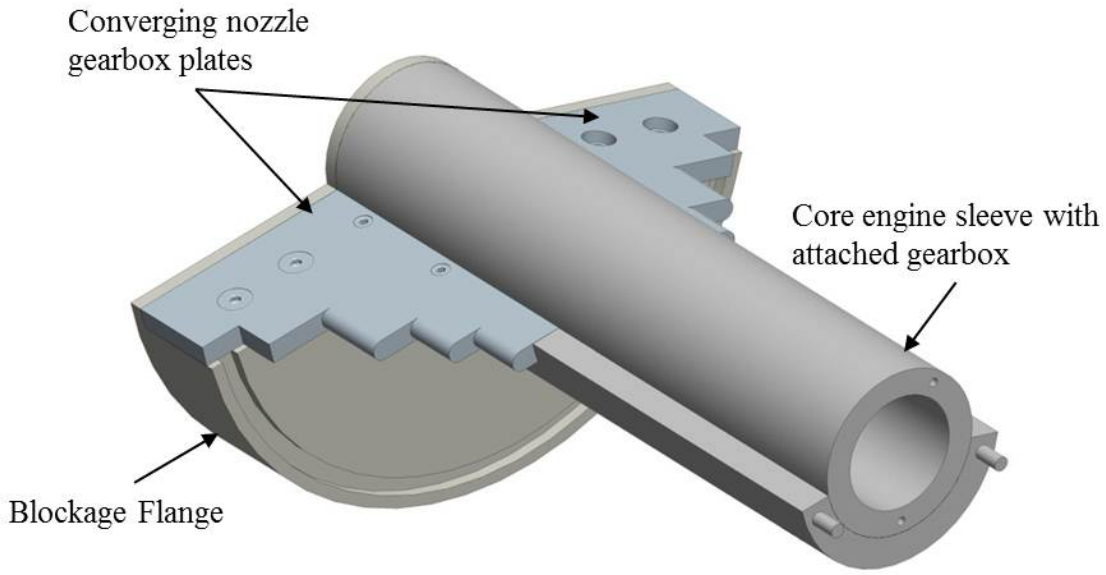

Fig. 2.5. The gearbox blockage assembly located within the converging nozzle.

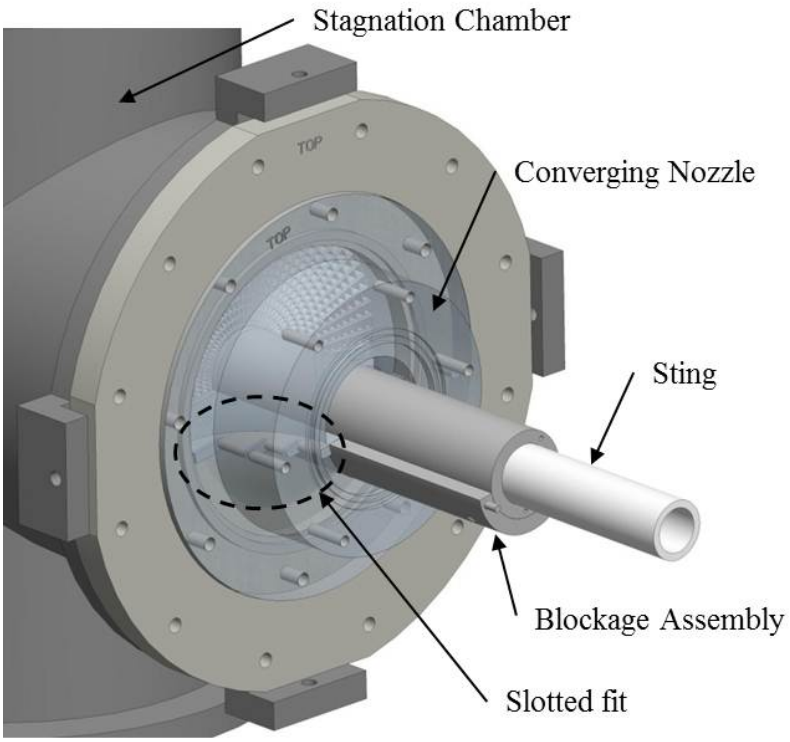

Fig. 2.6. Schematic showing how blockage assembly fits in slots of converging nozzle (shown transparently) to fully block the gearbox region.

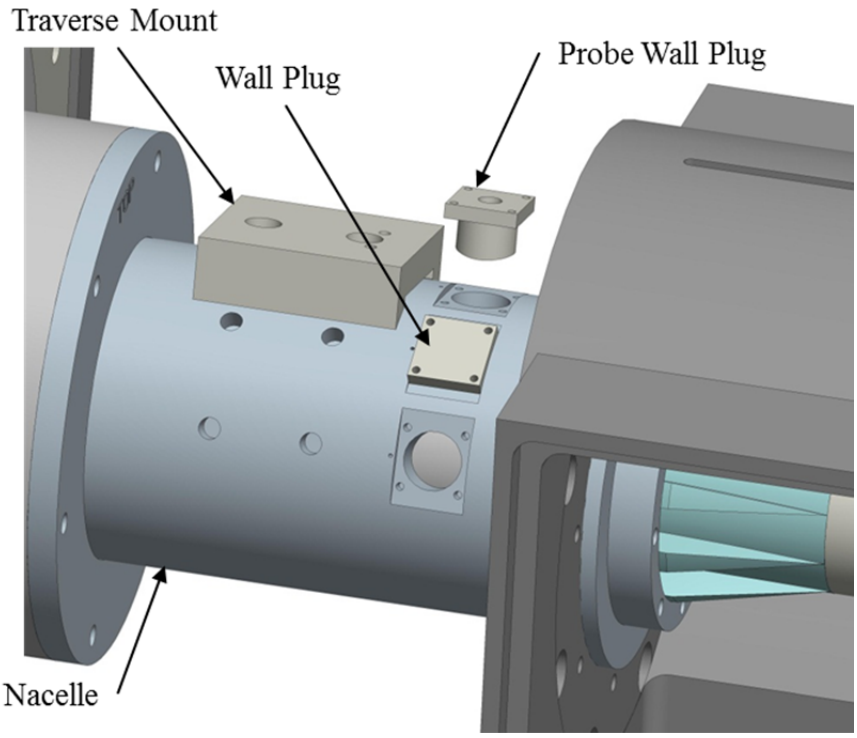

Fig. 2.7. Nacelle with traverse mounting block and wall plugs.

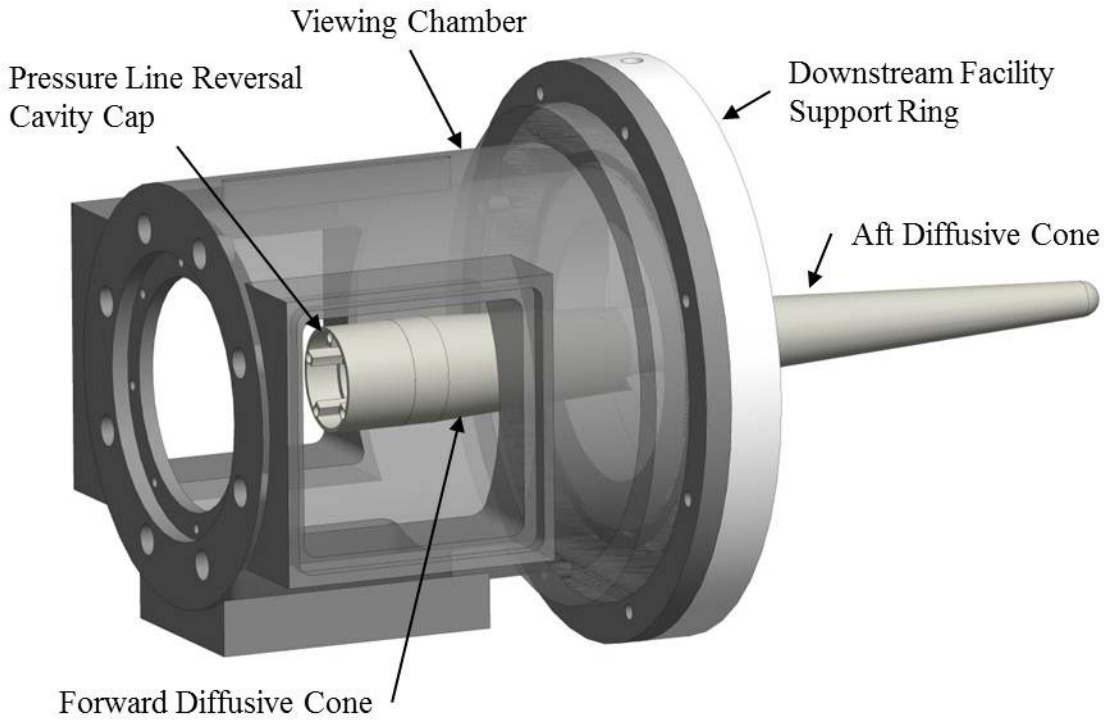

Fig. 2.8. Downstream centerbody components and structural support.

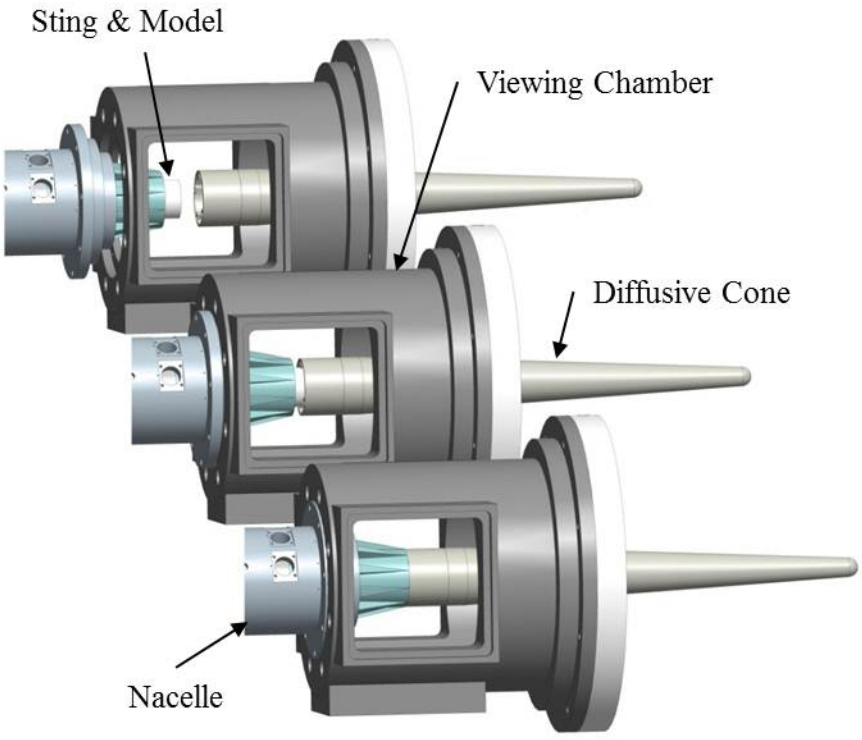

Fig. 2.9. Placement of downstream assembly over end of sting and nacelle.

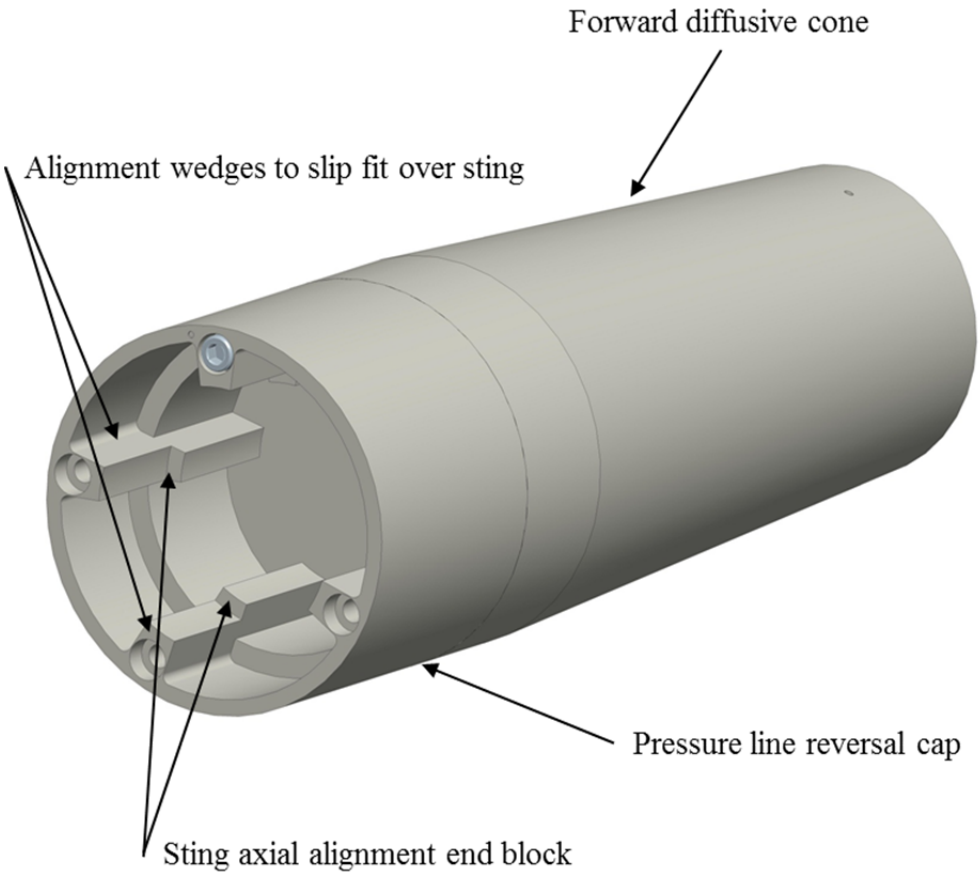

Fig. 2.10. The pressure line reversal cap provides a cavity in which the model surface static pressure lines can be turned around, covers the end of the sting, and aids in the alignment of aft centerbody components to the sting axis.

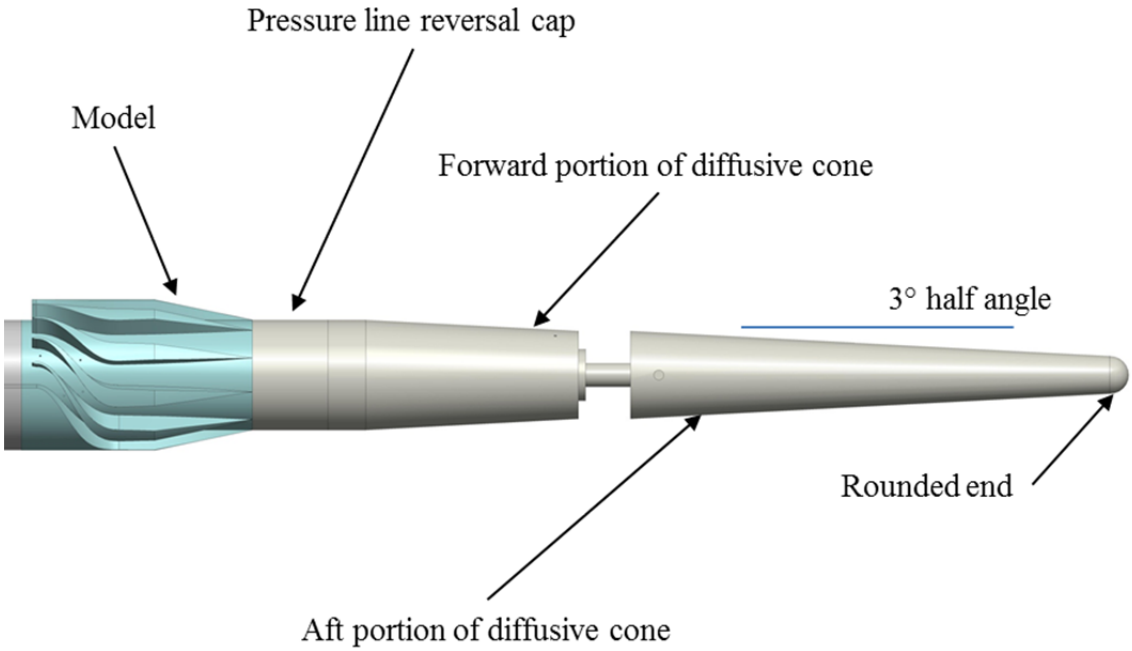

Fig. 2.11. Side view of the centerbody components located downstream of the model.

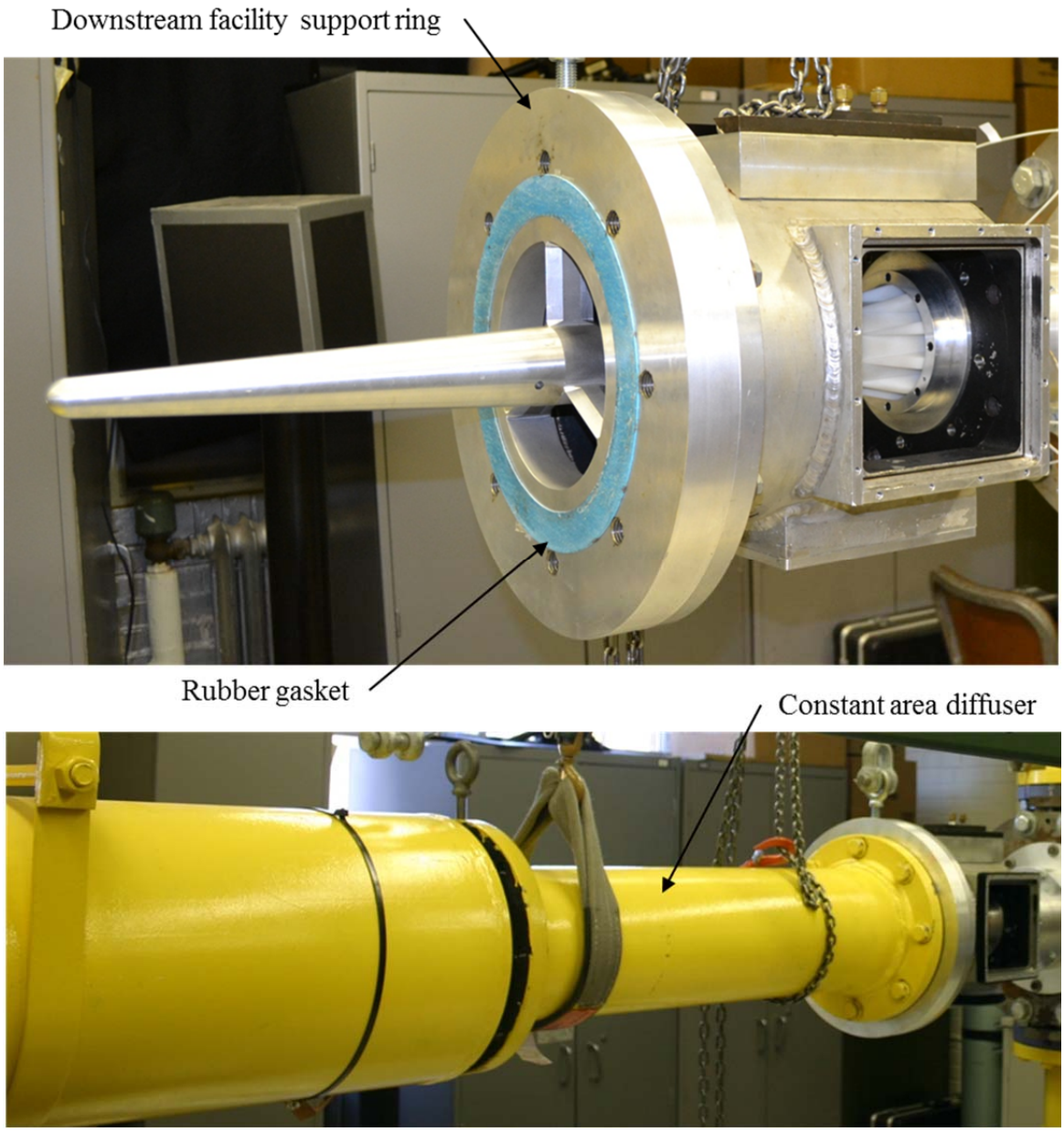

Fig. 2.12. Rubber gaskets are used to seal the interface between downstream diffusive components (instead of O-rings) which are mounted and aligned with eight oversized bolts.

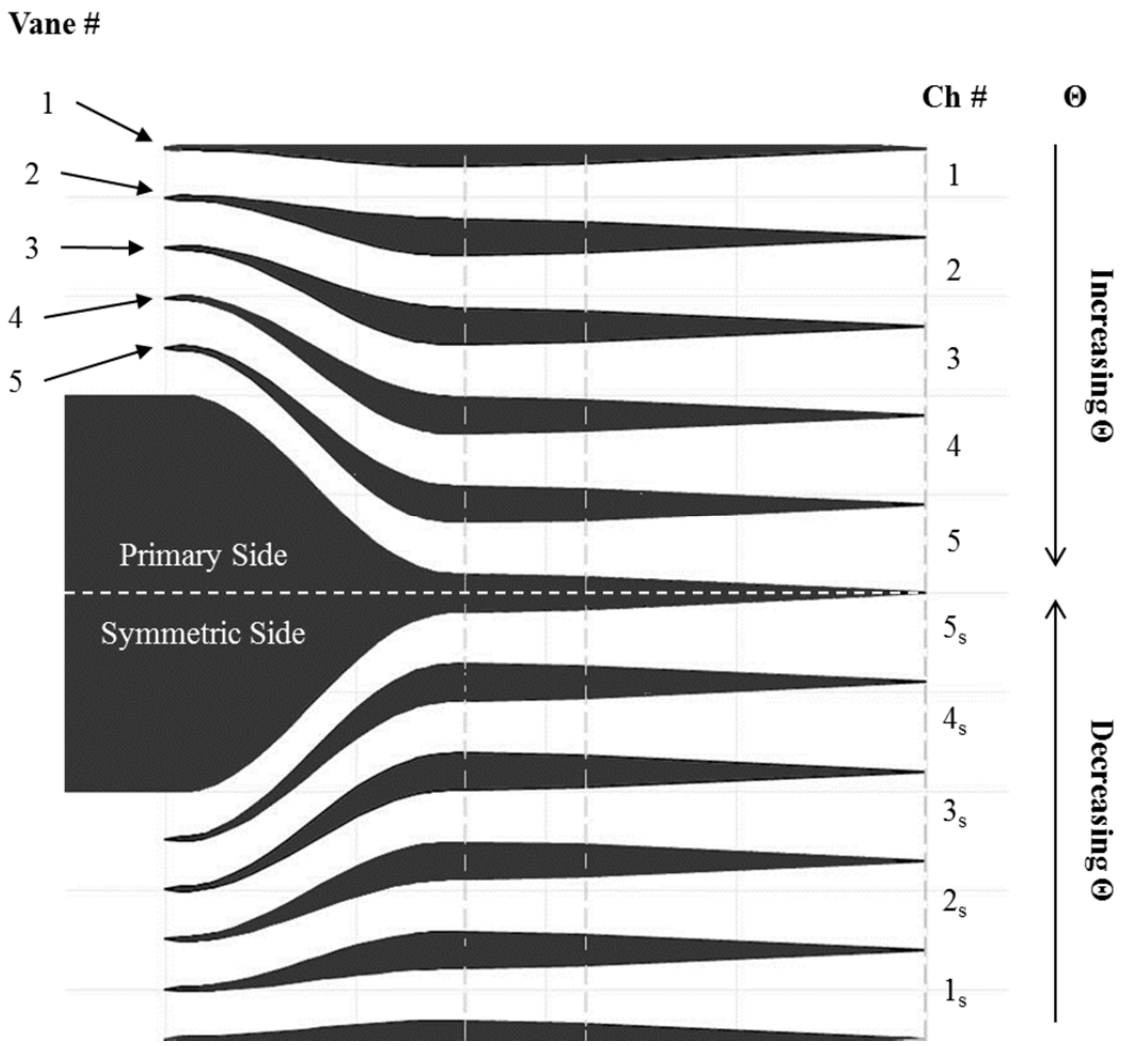

Fig. 2.13. Conventions used to define the aft bypass geometry including channel number, vane number, positive and negative azimuthal angle, θ, and the distinction between the primary and symmetric sides. Flow is from left to right. Adapted image; courtesy of GAC.

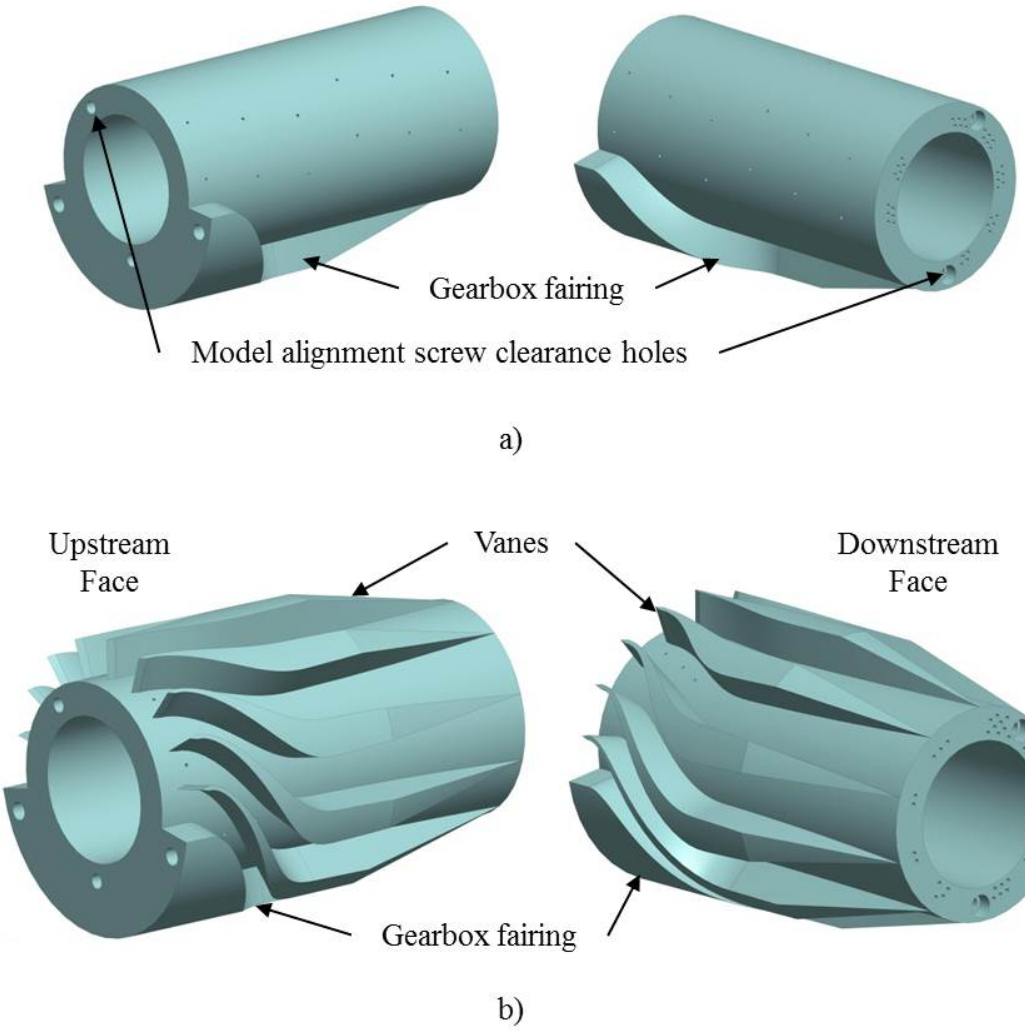

Fig. 2.14. The a) clean model and b) vaned model used in the aft bypass study.

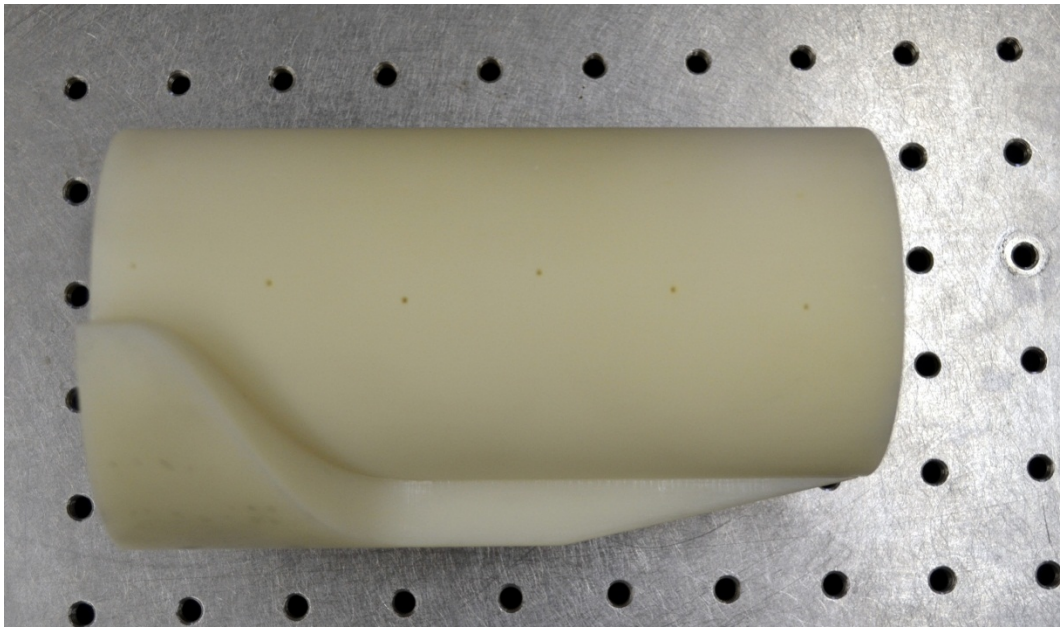

Fig. 2.15. The SLA clean model used in this study.

Fig. 2.16. The SLA vaned model used in this study.

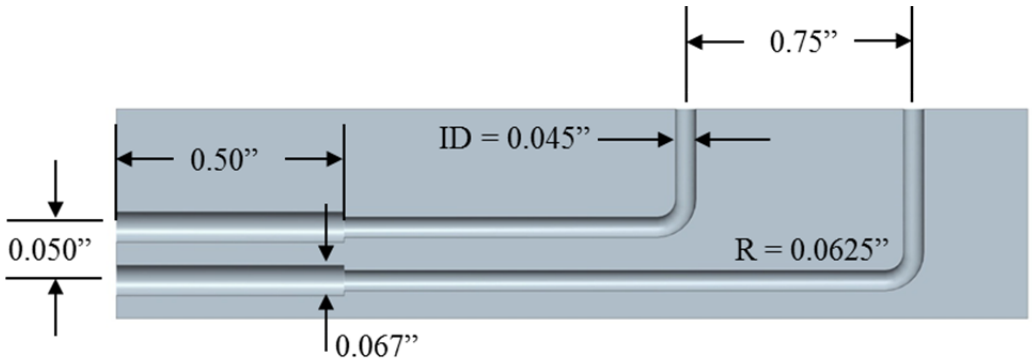

Fig. 2.17. A view of the internal pressure line plumbing with typical dimensions.

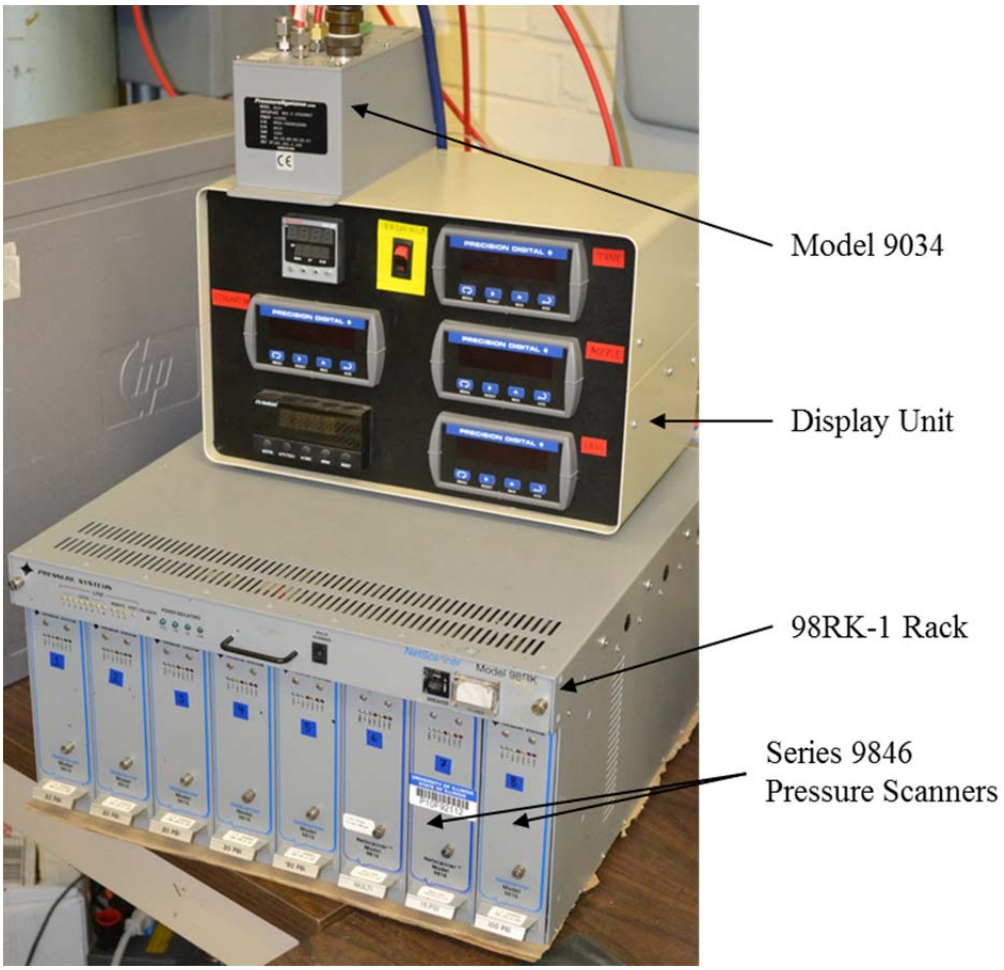

Fig. 2.18. The NetScanner data acquisition system and axillary digital display unit.

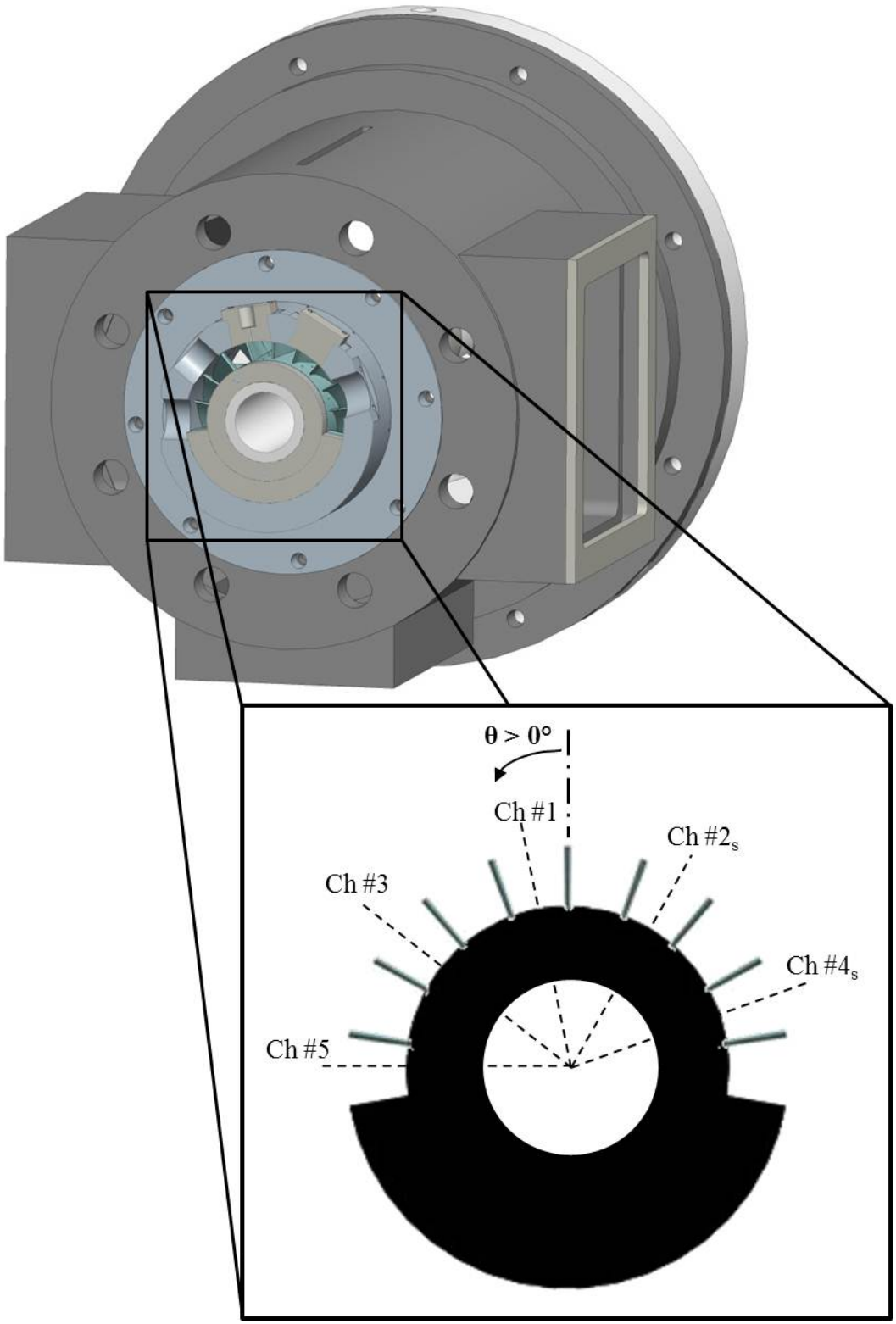

Fig. 2.19. Facility cross section illustrating the azimuthal radial probe traversing spacing and locations.

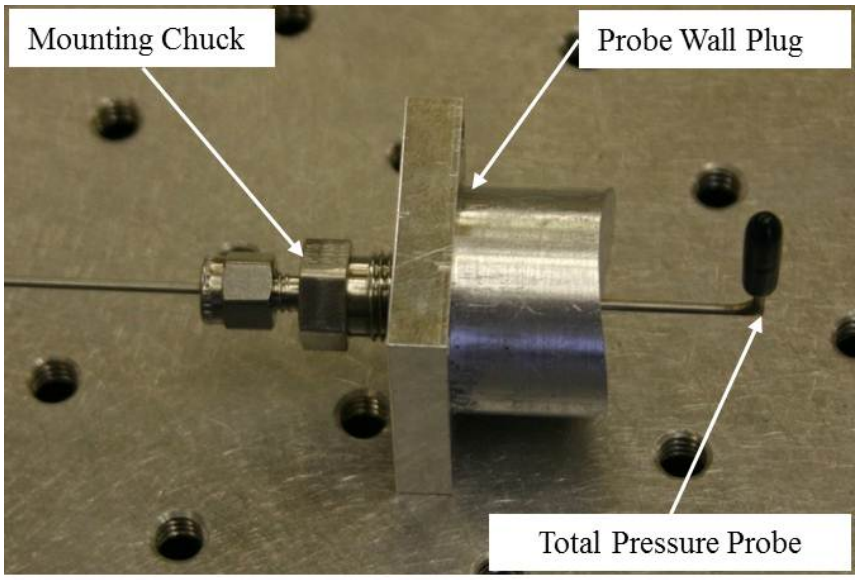

Fig. 2.20. The total pressure probe (with protective cover), the probe wall plug, and NPT mounting chuck.

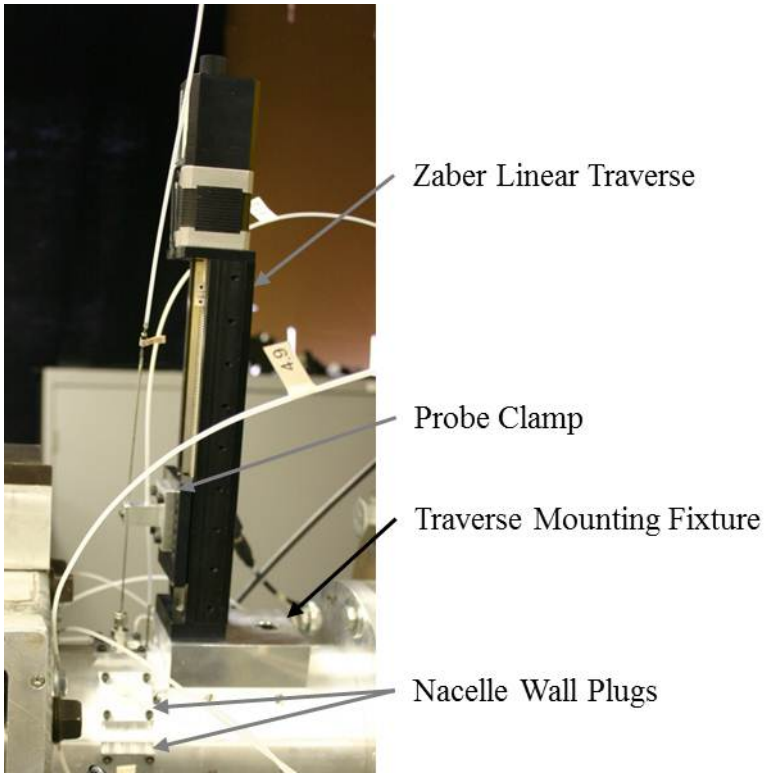

Fig. 2.21. Linear traverse setup and ready for operation.

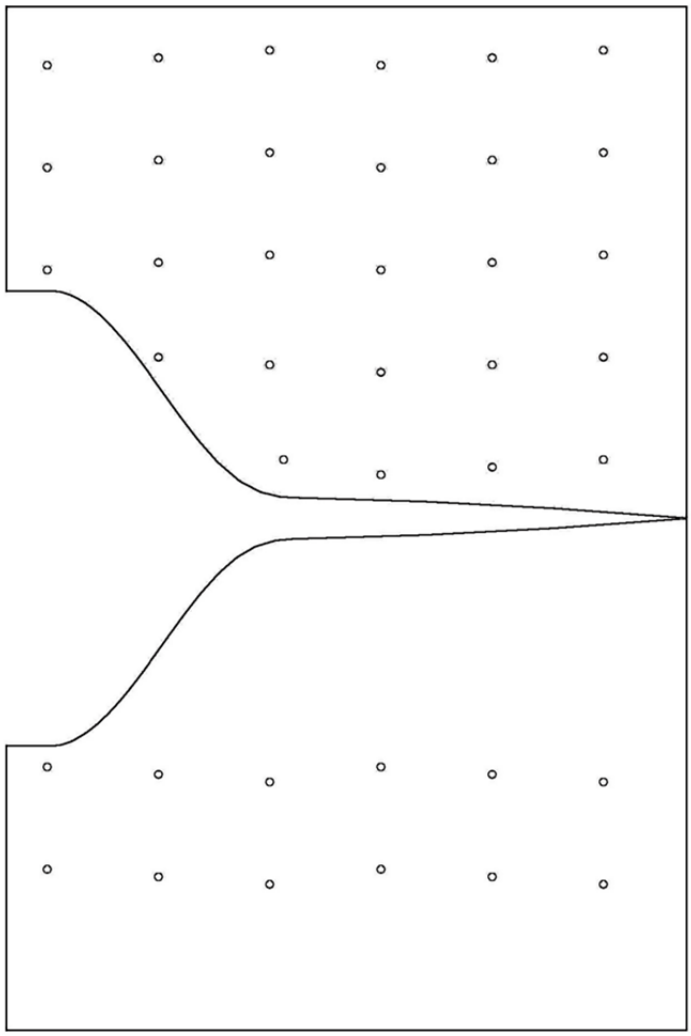

Fig. 2.22. Placement of model surface static pressure taps on the clean model.

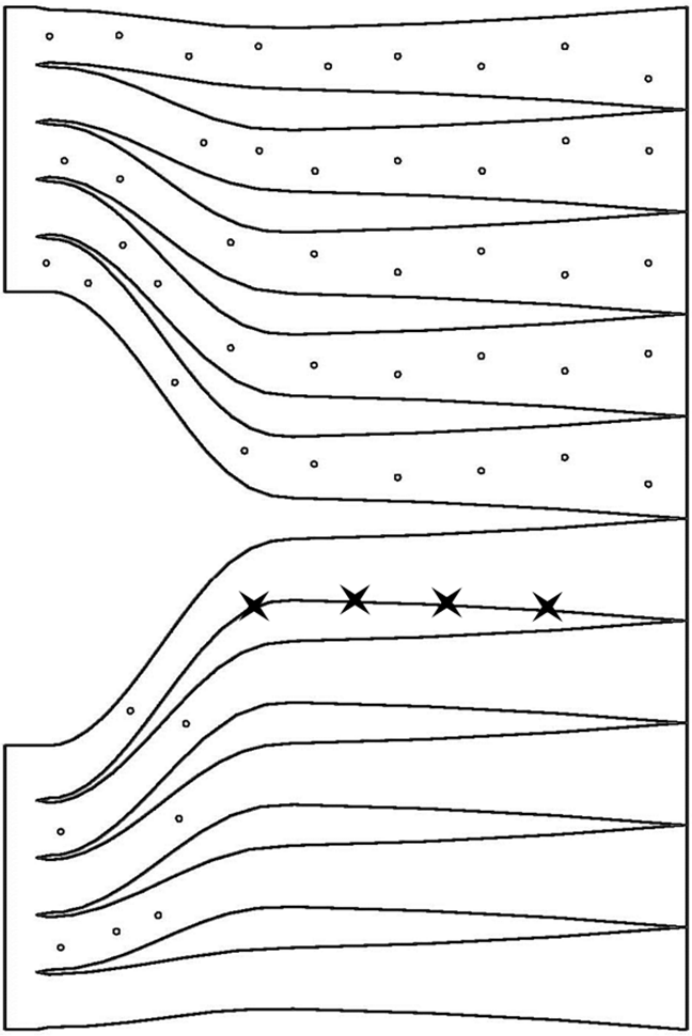

Fig. 2.23. Placement of model surface static pressure taps on the vaned model.

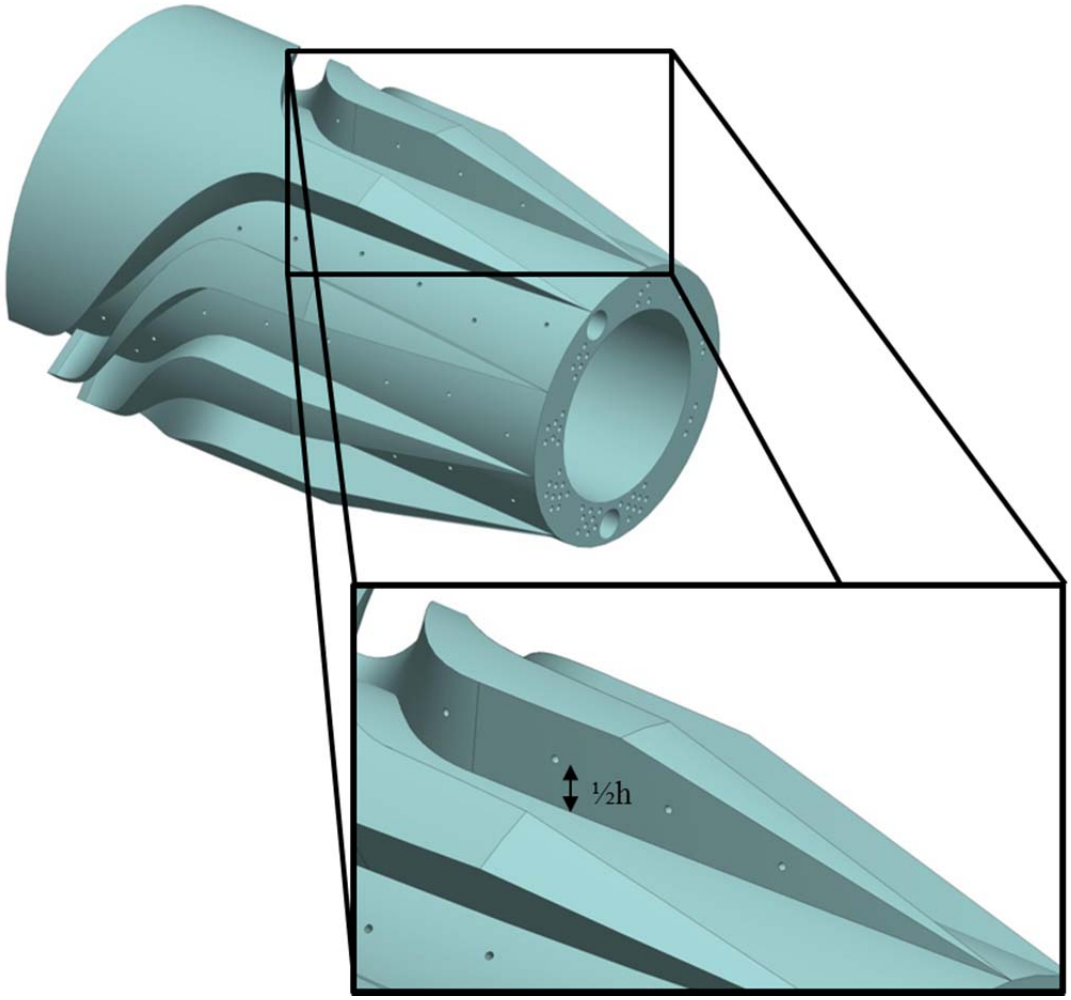

Fig. 2.24. Close up image of the channel wall static pressure taps located in Ch #5 (on Vane #5). The pressure taps were located at approximately one half the local vane height, and were evenly spaced along the straight portion of the channel exhaust.

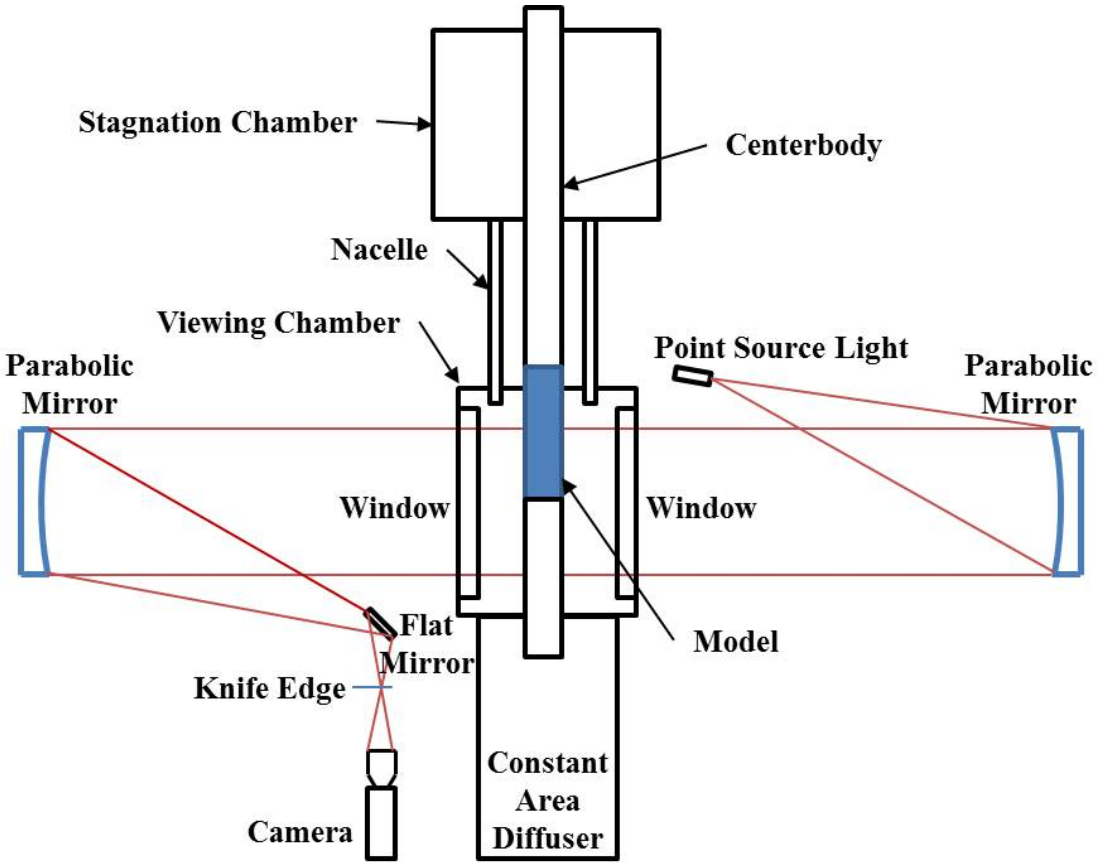

Fig. 2.25. Schematic of the "z-type" Schlieren photography setup.

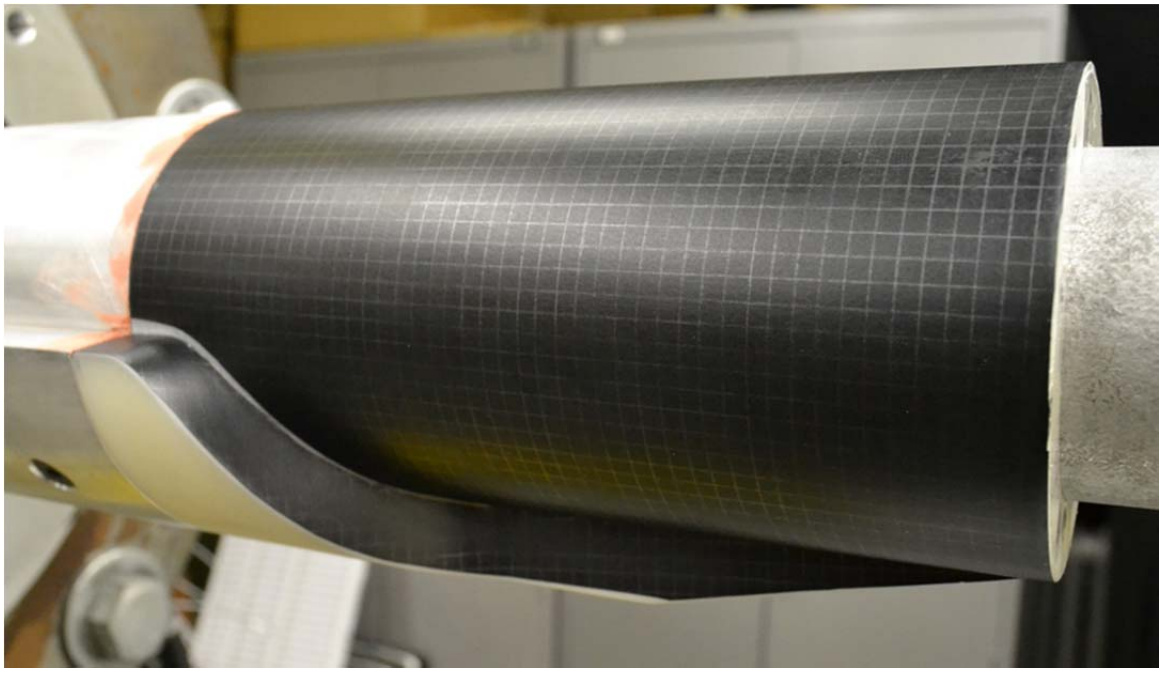

Fig. 2.26. Clean model prepared for surface oil flow visualization with gridded contact paper covering.

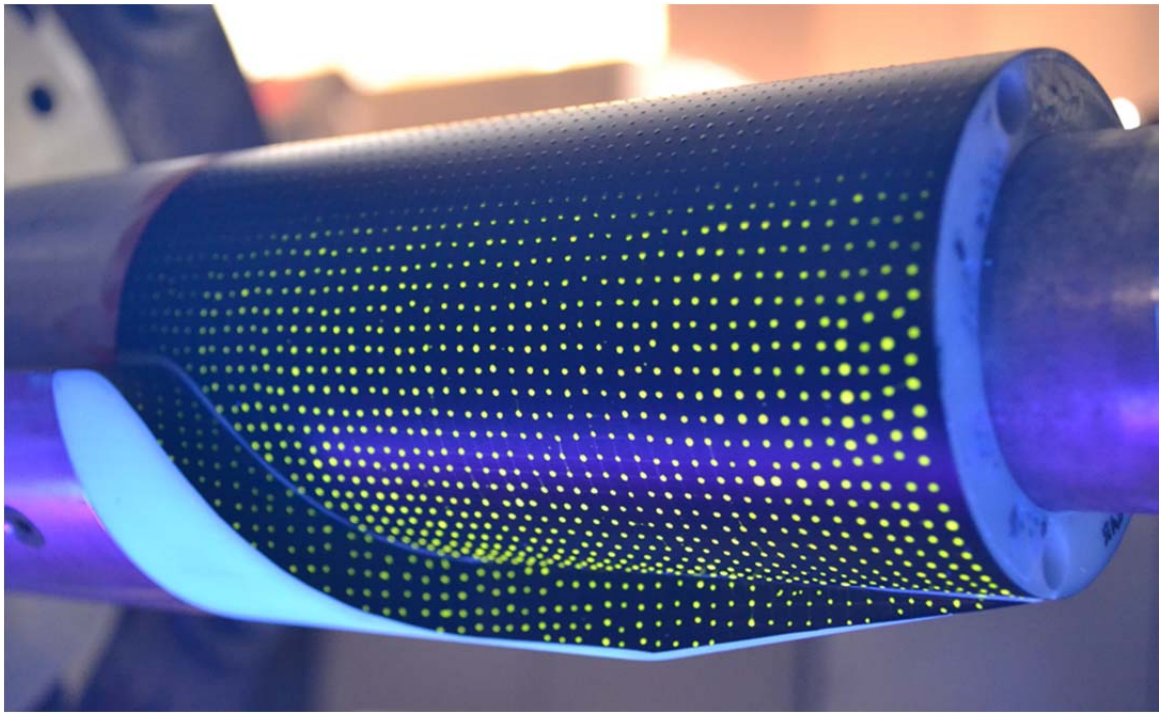

Fig. 2.27. Clean model with applied fluorescent surface oil flow mixtures in 1/8th inch grid spacing.

Fig. 2.28. Vaned model prepared for both fluorescent and lampblack based surface oil flow visualization.

Chapter 3

Results and Discussion

In this chapter, experimental data are presented and discussed. First, an analysis of the variations within run parameters is conducted. Then, the results from the inlet plane radial survey are presented. The variation of core flow conditions and wall boundary layers are discussed and trends highlighted for both the clean and vaned models. This is followed by the clean model surface static pressure data. Vaned model data and analyses are focused on the nature of the flow through each channel, a comparison of experimental data to an isentropic calculation, and also an estimate of total pressures losses incurred through each channel. The mass flow rates through each channel, and their relation to each other, are presented and discussed. Finally, surface oil flow visualization and Schlieren imagery from both models and multiple operating conditions are presented. These data combine to form an overall picture of the flow through the aft section of the high-flow nacelle bypass.

3.1 Run Variation Analysis

The maximum percentage variation in several key parameters during the course of a run were calculated in order to assess overall temporal consistency. $P_{chamber}$ was monitored to provide insight into the most basic metric of wind tunnel operating condition. Fluctuations in $P_{chamber}$ were due to the decreasing tank farm pressure (since the compressors could not fill the tanks as fast as they drained). This was combatted by slowly opening the valves during the course of a run.

M_{tunnel}, and Re_{tunnel} were monitored to assess the run-time flow state at the inlet to the aft bypass. The goal of a maximum allowable percent change in M_{tunnel} and Re_{tunnel} of 5% was maintained for nearly all of the tested operating conditions, as shown in Table 3.1. Table 3.1 presents the average percent change (%Δ) and standard deviation (σ) in

the aforementioned parameters across multiple runs for each operating condition. Six runs were carried out (five radial traverses and one 'empty tunnel' run) at each of the five probe locations to provide a total of 30 runs per operating condition. The maximum variation during a single run for each operating condition is shown in Table 3.2 to provide a sense of how broad variations were among the 30 runs.

Since the total mass flow used for the lower operating conditions was much smaller than that of the higher operating conditions, the tank farm pressure was much easier for the compressors to maintain. For this reason, the average variation in $P_{chamber}$ was much less than that for higher operating conditions (≈0.2% as compared to ≈2.7%).

However, the relative variation in M_{tunnel} and Re_{tunnel} was larger for these lower operating conditions. Average percent variation exceeded 5% for only the lowest operating condition, that of M_{tunnel} = 0.148. The variation generally decreased with increasing M_{tunnel}. This is especially true for the vaned model, for which the percent variation in M_{tunnel} ranged from approximately 6% for M_{tunnel} = 0.148 to approximately 0.4% for $M_{tunnel} = 0.538|_{21.00}$. The very small percent variation in M_{tunnel} for the two choked operating conditions can be attributed to the nature of choked flows. Choking enforces a fixed mass flow rate constraint, which can be shown to require a fixed Mach number, M_{tunnel}.

The tested clean model operating condition appears to have increased variation in M_{tunnel} and Re_{tunnel} as compared to the vaned model. This increase is attributed to the fact that the clean model operating condition was not a choked flow case and so M_{tunnel} was not expected to become constant. Accordingly, Re_{tunnel} also experienced some added variation. All three metrics, however, did not experience variations (average or maximum) that exceeded the 5% cutoff.

Table 3.1 Average Run-Time Percent Variation in Key Operating Parameters.

M_{tunnel}	Test Model	$P_{chamber}$			M_{tunnel}			Re_{tunnel}		
		Ave	%Δ	σ	Ave	%Δ	σ	Ave	%Δ	σ
0.148	Vaned	14.676	0.19	0.03	0.148	5.96	0.99	45743	6.32	1.00
0.294	Vaned	15.274	0.29	0.07	0.294	2.42	0.75	95452	2.18	0.98
0.385	Vaned	16.370	0.52	0.15	0.383	1.95	0.79	132646	1.70	0.85
0.481	Vaned	17.655	0.73	0.27	0.480	1.41	0.47	169296	1.85	0.73
0.526	Vaned	18.937	0.99	0.31	0.526	0.93	0.31	198404	1.74	0.60
$0.538\|_{20.00}$	Vaned	19.998	1.10	0.51	0.537	0.44	0.26	213710	1.49	0.66
$0.538\|_{21.00}$	Vaned	21.002	1.19	0.47	0.537	0.38	0.20	223582	1.60	0.64
0.704	Clean	19.405	0.64	0.18	0.701	1.14	0.69	244531	1.33	0.56

Table 3.2 Maximum Run-Time Percent Variation in Key Operating Parameters.

M_{tunnel}	Test Model	Maximum Percent Change		
		$P_{chamber}$	M_{tunnel}	Re_{tunnel}
0.148	Vaned	0.24	8.32	8.61
0.294	Vaned	0.58	5.29	5.69
0.385	Vaned	0.95	3.47	3.44
0.481	Vaned	1.28	2.20	3.05
0.531	Vaned	1.87	1.62	3.29
$0.538\|_{20.00}$	Vaned	2.70	1.46	3.16
$0.538\|_{21.00}$	Vaned	2.14	0.76	3.07
0.704	Clean	1.07	3.09	2.69

3.2 Inlet Plane

At least five total pressure probe radial traverses were conducted for each azimuthal station and operating condition. These runs were combined into a single representative run to be used in subsequent results. However, before a representative run could be generated with confidence, the individual runs had to be shown to be sufficiently similar and repeatable.

Fig. 3.1 a) shows five total pressure probe radial traverse runs conducted at the Ch $^{\#}1$ azimuthal station for M_{tunnel} = 0.531. Due to the run-time decrease in tank farm pressure and increased opening of the valves, the P_{total} profiles have the characteristic 'z' type profiles as described in Section 2.7.1. After non-dimensionalization to remove

changes in $P_{chamber}$, the radial profiles collapsed onto the curves defined by $P_{t,\ non\text{-}dim}$, as shown in Fig. 3.1 b), providing evidence for the repeatability between runs of the radial total pressure probe traverse. Within the core flow, the coefficient of variance (CV), that is, the percent standard deviation relative to the mean, was 0.03%, further showing the high degree of repeatability of the measurements.

M_{inlet} profiles were also very similar (Fig. 3.1 c); the data from all five runs collapses nicely within the outer and inner wall boundary layers as well as within the core flow. Within the core, the average Mach number between all runs was measured to be 0.531 (giving rise to the operating condition naming convention) with a CV of 0.09%. With the knowledge that the radial profiles were highly repeatable, the individual M_{inlet} profiles were simply averaged to generate the representative run as shown in Fig. 3.1 d).

It should be noted that azimuthal variations were experimentally measured within the range approximated by $10° \leq |\Theta| \leq 90°$ due to the positioning of the radial total pressure probe insertion locations. Therefore, the nature of the conditions within the range from 0° to 10° and from 90° to the gearbox fairing wall, located at 100°, could not be empirically measured. Instead, the conditions local to top-center and to the gearbox fairing wall are inferred upon based on the available data. No data extrapolations are made concerning the conditions within these ranges, however, the conditions are hypothesized qualitatively based on measured data available. It is important to remember that the true range of conditions within the inlet plane partial annulus is likely to continue with the local trends near the edges of the empirical range.

3.2.1 Clean Model

While conducting the clean model runs, a relatively high degree of control over $P_{chamber}$ was achieved because the LabVIEW program could be used to incrementally adjust the valve setting instead of manually opening the gate valve. Therefore, the 'z' characteristic is not very pronounced for the clean model operating condition (M_{tunnel} = 0.704), as evidenced by Fig. 3.2 a). The average core flow inlet plane P_{total} is 19.275 psia with a CV of 0.31% indicating that there is some azimuthal variation across the inlet

plane. This is corroborated by the $P_{t,\ non\text{-}dim}$ distribution shown in Fig. 3.2 b), where the Ch #3 and Ch #5 curves are slightly removed from the other three channels.

The inlet Mach number profiles are shown in Fig. 3.2 c), and Fig. 3.2 d) presents a more detailed view of the core flow measurements. Within the core, each profile is quite uniform. The detailed M_{inlet} profiles show that there appears to be some azimuthal variation, although it is not especially significant. Most notably, it appears as though there may be an increase in M_{inlet} for the two azimuthal stations nearest the gearbox fairing (Ch #4 and Ch #5), corresponding to $|\Theta| \approx 70°$ and 90°. The azimuthal variation in M_{inlet} does not otherwise seem to occur in any ordered manner.

As can be seen in Fig. 3.2 a) and c), the outer wall boundary layers (near $R^* = 1$) from all curves collapse together very nicely in terms of thickness and profile. This shows that there is little to no variation in boundary-layer profiles as a function of azimuthal location. Apart from some variation due to differing core flow M_{inlet} values leading to boundary layers with slightly steeper gradients, the inner wall boundary layers also exhibit little variation among each other. Comparison of the Ch #3 and Ch #4 inner wall M_{inlet} profiles in Fig. 3.2 d) illustrate these gradient discrepancies nicely. The Ch #5 inner wall boundary layer also appears to be slightly thicker than the others. This could be attributed to its proximity to the gearbox fairing wall and the wall effects local to it.

The inner wall boundary layer extends approximately out to $R^* = 0.10$. The outer wall boundary layer, meanwhile extends from $R^* = 1.0$ to approximately $R^* = 0.8$, so that it is approximately twice as thick as that of the inner wall. The reason for this is unclear as it is the inner wall that extends further upstream and would therefore be expected to produce a thicker boundary layer. It is possible that the converging nozzle contour would produce an adverse pressure gradient which would lead to a thickening outer wall boundary layer; however, these effects would likely be mitigated by the overall flow area compression which would be most strongly felt along the wall which undergoes the most curvature.

3.2.2 Vaned Model

For the lower vaned model operating conditions, the total facility mass flow rate was small enough to allow for very little run-time variation in tank farm pressure. This minimized the need to adjust the valve settings and generally resulted in P_{total} profiles that were very smooth and did not exhibit the 'z' type characteristic. As the overall mass flow rate increased, the compressors were unable to maintain sufficiently constant tank farm pressure, and, as a result, the valve had to be adjusted during the runs. Consequently, the 'z' radial-profile characteristic becomes more and more evident as the upper-most operating condition is approached. This trend can be visually observed by inspection of the P_{total} radial profiles for each tested operating condition. Numerical corroboration can be found in that the CV in core P_{total} measurements at each azimuthal position (channel inlet) increases with increasing M_{tunnel}, as shown in Table 3.3. The typical CV range from M_{tunnel} = 0.148 to $0.358|_{21.00}$ is from approximately 0.01% to 0.14%.

Table 3.3 Mean Core Flow P_{total} (psia) Conditions.

M_{tunnel}	Ch #1		Ch #2		Ch #3		Ch #4		Ch #5	
	Mean	**% CV**	**Mean**	**% CV**	**Mean**	**% CV**	**Mean**	**% CV**	**Mean**	**% CV**
0.148	14.652	0.005	14.673	0.006	14.669	0.008	14.673	0.007	14.662	0.009
0.294	15.258	0.014	15.259	0.030	15.257	0.009	15.258	0.036	15.234	0.010
0.385	16.315	0.020	16.301	0.041	16.391	0.044	16.298	0.074	16.356	0.038
0.481	17.589	0.057	17.609	0.065	17.574	0.065	17.617	0.041	17.626	0.085
0.531	18.862	0.070	18.909	0.140	18.825	0.181	18.951	0.089	18.769	0.128
$0.538|_{20.00}$	19.928	0.040	19.953	0.072	19.945	0.045	19.953	0.096	19.914	0.103
$0.538|_{21.00}$	20.953	0.112	20.942	0.094	20.947	0.137	20.933	0.097	20.944	0.126

For simplicity purposes, the core flow region was defined as that ranging from $0.3 \geq R^* \geq 0.7$ so that all boundary layers were sure to be excluded. Table 3.3 highlights the uniformity in P_{total} conditions between runs conducted at different azimuthal locations to generate the complete inlet plane data set for a given operating condition. The core flow P_{total} values were extremely uniform across all azimuthal stations for each operating condition. The maximum core flow P_{total} CV was measured for the M_{tunnel} = 0.531

operating condition and was still only 0.36%. As expected, P_{total} increases with increasing M_{tunnel}.

Fig. 3.3 through Fig. 3.16 present the vaned model inlet plane recorded data. As for the clean model inlet plane data, the P_{total}, $P_{t,\ non\text{-}dim}$, and M_{inlet} radial profiles are presented for each operating condition. These can be found in parts a) – c) of the odd numbered figures, respectively. The even numbered figures present M_{inlet} in a contour plot format instead of as radial profiles. The contour plot format was used to aid in visualization of the Mach number distribution within the fully blocked region. Superimposed on the contour plots are the inner and outer bypass walls and the gearbox fairing. In addition, the locations of the aft vane forward tips are clearly marked by the dashed lines. Since the flow is (or is nearly) symmetric, only one half of the annular region need be shown; the symmetry line is also designated in each M_{inlet} contour plot.

The radial profiles shown in part a) of odd numbered figures within Fig. 3.3 – Fig. 3.16 further confirm that there is very little radial variation in P_{total}. Although a small amount of azimuthal variation is visible, the previously described results indicate that this variation is actually very minor. In any case, the normalized total pressure, $P_{t,\ non\text{-}dim}$, radial distributions, shown in part b), show no azimuthal variation as each curve collapses very nicely within the core flow.

Unlike probe total pressure, the core flow Mach number, M_{inlet}, is not uniformly distributed within the inlet plane (even numbered figures within Fig. 3.3 – Fig. 3.16). Except for the lowest operating condition (M_{tunnel} = 0.148, Fig. 3.4), radial profiles indicate that M_{inlet} decreases in a steady manner as the gearbox fairing is approached such that the maximum is found at the inlet to the topmost channels (Ch $^{\#}$1, measured 10.1° from top-center). The minimum is found at the inlet to the channel directly adjacent to the gearbox fairing (Ch $^{\#}$5, measured 90° from top-center). This distinct azimuthal variation in M_{inlet} can be very easily visualized by inspection of the annular contour plots.

It is important to note that the Ch $^{\#}$5 azimuthal location is 10° removed from the gearbox fairing and, subsequently, no quantitative statements can be said about M_{inlet} any nearer to the fairing. However, one would expect that M_{inlet} would continue to decrease with decreasing distance to the fairing due to wall effects. Similarly, one would also expect that M_{inlet} would increase as $|\Theta| = 0°$ is approached.

Table 3.4 provides a summary of core flow M_{inlet} conditions and CVs at each azimuthal station for all operating conditions. The percent decrease in M_{inlet} from the Ch $^{\#}1$ to Ch $^{\#}5$ location increases with M_{tunnel} from approximately 5.5% to a maximum of approximately 9.3% (disregarding the single operating condition which did not exhibit the azimuthal variation trend, $M_{tunnel} = 0.148$, and, for which the measured variation was very small). For each azimuthal station, the CV decreased with increasing M_{tunnel}. This trend fits with the idea that Mach number approaches a constant value as choked conditions are attained.

Table 3.4 Vaned Model Mean Core Flow M_{inlet} Conditions.

M_{tunnel}	Ch $^{\#}1$		Ch $^{\#}2$		Ch $^{\#}3$		Ch $^{\#}4$		Ch $^{\#}5$	
	Mean	**% CV**	**Mean**	**% CV**	**Mean**	**% CV**	**Mean**	**% CV**	**Mean**	**% CV**
0.148	0.145	0.272	0.145	0.420	0.147	0.332	0.141	0.432	0.144	0.512
0.294	0.294	0.105	0.290	0.127	0.286	0.102	0.279	0.110	0.278	0.151
0.385	0.380	0.075	0.378	0.081	0.374	0.077	0.365	0.076	0.359	0.076
0.481	0.480	0.049	0.474	0.052	0.459	0.061	0.446	0.043	0.443	0.079
0.531	0.531	0.045	0.516	0.066	0.500	0.062	0.489	0.066	0.481	0.085
$0.538|_{20.00}$	0.538	0.069	0.530	0.054	0.509	0.057	0.498	0.044	0.488	0.080
$0.538|_{21.00}$	0.538	0.057	0.529	0.044	0.512	0.059	0.498	0.064	0.491	0.090

The relationship between M_{inlet} and $|\Theta|$ could be interpreted to indicate that the channels with less curvature have a tendency to pass more relative mass than the channels nearer to the gearbox fairing since M_{inlet} is greater near top-center. When coupled with the knowledge that the percent variation in M_{inlet} within the annulus increases with M_{tunnel}, one might propose that, with increasing M_{tunnel}, the upper channels swallow a greater component of the facility mass flow as the lower channels, due to their larger pressure losses that often accompany highly three-dimensional geometry, fail to pass their fair share of the total.

Outer wall boundary layers were assessed by investigation of the radial profiles shown in Fig. 3.3 – Fig. 3.16 (odd numbers). Identifying trends between multiple figures is often difficult, and so for this reason the boundary-layer thickness, displacement thickness, and momentum thicknesses were plotted independently. Boundary-layer

thickness, δ, is plotted as a function of both channel number (azimuthal position) and operating condition (M_{tunnel}) in Fig. 3.17. Displacement thickness, δ^*, and momentum thickness, Θ, are similarly shown in Fig. 3.18 and Fig. 3.19.

Little dependency on azimuthal position can be found in outer wall δ, as it is fairly uniform for all $|\Theta|$. Neither is there a clear trend relating δ to M_{tunnel} (operating condition). However, near the gearbox (Ch $^{\#}5$), δ can be seen to clearly decrease with M_{tunnel}. This trend can be seen in Fig. 3.17 a) upon inspection of the order of the data series at the Ch $^{\#}5$ location, or, more clearly, within Fig. 3.17 b). The outer wall boundary layer consistently extends inward to $R^* = 0.82 - 0.84$, such that the thickness is approximately 0.059 – 0.067 inches. The only clear exception to this range is the Ch $^{\#}5$ boundary layer for low M_{tunnel}, as already described.

As with boundary-layer thickness, δ^* and Θ show little dependency on channel number until they approach the gearbox, at which point they both increase in thickness. This increase lessens with increased M_{tunnel}, as shown in Fig. 3.18 b) and Fig. 3.19 b). The $P_{t,\ non\text{-}dim}$ radial profiles shown in part b of Fig. 3.3 – Fig. 3.16 (odd figures) further indicate that the outer wall boundary layers exhibit little azimuthal dependency by the collapsing onto a single radial profile. In addition to the consistently similar measurements for δ^* and Θ (when far from the fairing), the collapsing $P_{t,\ non\text{-}dim}$ profiles indicate very uniform outer wall boundary layers that exhibit very similar thicknesses and gradients.

The inner wall boundary layers were assessed in an identical manner to those of the outer wall. Boundary-layer thickness, displacement thickness, and momentum thicknesses for the inner wall boundary layer are presented as functions of channel number and M_{tunnel} in Fig. 3.20, Fig. 3.21, and Fig. 3.22, respectively. Radial profiles can be found in Fig. 3.3 – Fig. 3.16 (odd figures).

It appears as though there is a weak correlation between azimuthal location and inner wall boundary-layer thickness such that δ increases as the fairing is approached (Fig. 3.20 a). However, no correlation was found relating δ to M_{tunnel}. Except for the lowest operating condition, boundary-layer thickness was relatively constant for most azimuthal stations, as shown in Fig. 3.20 b). In general, inner wall boundary layers are considerably thicker than those of the outer wall. The Ch $^{\#}5$ inner wall boundary layer,

which is usually the thickest, typically extends inwards to $R^* = 0.26$, or about 0.115 inches thick. This is equivalent to a 70-90% increase. A thicker inner wall boundary layer would be expected as that boundary layer starts growth directly downstream of the flow conditioners and therefore has more (approximately six inches longer) over which it can grow. The outer wall, meanwhile, must undergo the curvature of the converging nozzle.

Near the fairing, the inner wall boundary-layer velocity gradient increases, as can be seen in the P_{total} and $P_{t,\ non\text{-}dim}$ radial profiles. This results in the Ch #5 boundary layers containing a much larger deficit than the other azimuthal stations. This tendency is clear when δ^* and Θ are plotted as a function of M_{tunnel} (Fig. 3.21 and Fig. 3.22 b), where the Ch #5 curve is well above those of the other channels. As with δ, the displacement and momentum thicknesses also appear to have a weak correlation with channel number. For both quantities, the thickness tends to increase as the fairing is approached, providing further evidence to the increasing mass and momentum deficits near the fairing.

3.3 Model Surface Static Pressures

Model surface static pressure tap data were evaluated differently for the clean and vaned models. Clean model data were normalized by the approximate inlet plane total pressure, P_0, and were presented in a contour plot format. Vaned model data, meanwhile, were analyzed and presented on an individual channel basis. The static pressures within each channel were normalized by the probe measured, core flow total pressure, within the inlet to that channel.

3.3.1 Clean Model

A representative contour plot of the pressure ratio from the clean model operating condition is shown in Fig. 3.23. Recall that by isentropic flow relations a low static to total pressure ratio results in a higher Mach number (and hence speed), so in the contour plot, the high speed regions appear as red while low speed regions (higher pressure ratio) appear in shades of blue. The open boxes in the figure represent the locations of each

model surface static tap. The TE of the outer bypass cowling is also designated in the figure. Except for several pressure taps to check for flow symmetry, the majority of the taps were located on one side of the model, so a large region of the model's surface contains no data.

Near the start of the gearbox fairing, that is, at the fairing shoulder, the pressure ratio is quite low, indicating a higher Mach number. This observation fits with the inlet plane data recorded for the clean model, wherein the Ch $^{\#}4$ and $^{\#}5$ radial profiles had a slightly higher M_{inlet} than that measured in the other channels. The tendency for the pressure ratio to increase with downstream location can be seen in Fig. 3.24 where the recorded static pressure time trace of a streamwise row of pressure taps is shown (refer to Fig. 2.22 for the placement of pressure taps). Pressure taps are numbered by streamwise position. For this particular row of pressure taps, the second tap is located very near the shoulder of the aft fairing. This likely accounts for that measurement's misplacement in the figure. The general increasing pressure with streamwise position trend is confirmed in the contour plot of all the model surface static taps. In general, the contour plot displays a fair amount of symmetry, although there are some measurements that deviate from this trend beyond x_{cowl}.

In general, the pressure ratios increase with downstream location for all of the model surface static pressure taps. This seems to indicate that the flow Mach number is decreasing, but one must be careful with this assertion since the normalization is carried out by the stagnation chamber pressure which is not necessarily representative of the local total pressure at all locations on the model, particularly in any parts of the model that may be experiencing flow separation.

The experimental static pressures in Fig. 3.24 are plotted as a function of time in order to show that the wind tunnel and data acquisition system were operating at a steady condition, leading to time independent data collection.

3.3.2 Vaned Model

3.3.2.1 Channel Analyses

The normalized experimental pressure ratio for each channel was plotted, for each tested operating condition, versus model axial position. The origin is located at the start of the model. The vane tips, therefore, are located at x = 0.280, while the cowling end plane is located at x = 3.525 inches. The local normal channel area is plotted on the secondary axis as normalized by that particular channel's minimum (throat) area. For comparison, a composite image of the surface oil flow visualization from the choked operating condition, $M_{tunnel} = 0.538|_{21.00}$ is displayed above the graph. Fig. 3.25 through Fig. 3.29 display the above described experimental channel pressure data for each of the five channels in order from the "Ch #1" case, 10.1° removed from azimuthal top-center (Fig. 3.25) to the "Ch #5" case, 90° removed from top-center, the channel directly adjacent to the gearbox fairing (Fig. 3.29).

Note that the shape of the pressure ratio curves found in the data are representative of the curves typically found through a converging diverging nozzle. As the area decreases within the converging section, the channel pressure ratios tend to decrease. Beyond the throat, the pressure ratio sometimes continues to decrease, which would indicate supersonic conditions. However, all of the pressure ratios ultimately increase again, indicating a subsonic expanding flow. This similarity is better evidenced when the pressure ratio data is related to the area ratio (as normalized by A_{throat}), which is also plotted in Fig. 3.25 through Fig. 3.29. Generally, the minimum recorded pressure ratio occurs very near to $A/A_{throat} = 1$.

At any given station within each channel, the pressure ratio decreases with increasing M_{tunnel}. This is true for all stations within the channels, causing the data curves to never cross. The dependence of pressure ratio on M_{tunnel} is fully expected and is consistent with the isentropic relations.

Another expected result is that for all stations beyond the cowling end plane (x = 3.525 inches), x_{cowl}, the pressure ratio remains constant. Further, for a given operating condition, the average value of all stations for $x > x_{cowl}$ is also constant among all channels. For instance, for the $M_{tunnel} = 0.526$ case, the mean pressure ratio for all model

surface static pressure taps beyond x_{cowl} is 0.745 with a coefficient of variance (CV) of 0.13%. Among all operating conditions, the largest CV is 0.14%, showing great consistency in the data. These results confirm that of the all channels encounter the same far-field conditions upon exiting the cowling, bringing them to uniform static pressure.

As described above, for a given operating condition, each channel exhausts at identical experimental pressure ratios. In all cases, the exhaust pressure ratio is well above the sonic limit. Subsonic exhaust conditions do not match the original experimental goals since a major purpose of the aft bypass is to reaccelerate the bypass flow to supersonic freestream conditions. Clearly, the experimental exhaust conditions did not match the stated goals, despite the fact that the wind tunnel was operating at choked conditions. Ultimately, it was determined that the wind tunnel total-to-static pressure ratio was not high enough and so the tunnel had been unable to swallow the shock. Since the wind tunnel had not 'started' its supersonic operation, all of the tested operating conditions were in actuality, off-design conditions and did not successfully match the experimentally desired conditions. Improving the attainable pressure ratio through the wind tunnel would have required a great deal of facility redesign, and so experimental data were instead taken at multiple off-design conditions. The off-design experimental data were still deemed to be highly useful to gain understanding the nature of the flow through the aft bypass during other portions of the flight envelope.

Returning to the channel pressure ratio data curves, if it is assumed, that, at most, the sonic condition is met in any channel, then there are several possible explanations for why the minimum pressure ratios are found downstream of the channel throat instead of coinciding exactly with the minimum area ratio. First, the axial locations of the pressure taps were randomly assigned and so the minimum recorded experimental pressure ratio, may actually be located between taps and is therefore unrecorded. Second, all static pressure tap readings were normalized by the approximate total pressure at the inlet plane, and so losses in total pressure within the channels were not accounted for. The fact that total pressure losses are not taken into account may also explain why the experimental pressure ratios can be below the sonic condition (P/P_0 = 0.528). Losses would decrease P_0, thereby increasing P/P_0.

If we allow for the possibility of supersonic conditions, a third explanation manifests itself. In that case, beyond the throat, the pressure ratio would drop below sonic conditions and a shock in the diverging section of would lead to a pressure jump back to subsonic conditions. Since any pressure jump across a shockwave would be a localized effect, capturing it would be extremely difficult given the limited number of pressure taps within each channel. As a result, it is difficult to determine whether or not shockwaves exist within any of the channels based purely on the experimental pressure ratios. No obvious evidence of shocks was found in the surface oil flow visualizations.

However, an argument for the existence of shock structures can be made. The minimum pressure ratio measured in any channel is approximately $P/P_0 = 0.400$. In almost all cases, the pressure ratio at the next static pressure tap is greater than that of the sonic condition ($P/P_0 = 0.528$) indicating that the flow must then be fully subsonic. In order for the Mach number to fall to, at maximum, sonic conditions, then a 24.2% reduction in total pressure would be required. To achieve less than sonic conditions, the total pressure losses would have to be even greater. Such a large decrease in total pressure over such a short span seems to be an unlikely occurrence.

The pressure jump across a normal shock where the in-flow has a Mach number of 1.22 (corresponding to $P/P_0 = 0.400$), is minimal as the total pressure ratio is only 0.991. However, since the flow near the throat is clearly highly three-dimensional, and most likely separated (see Section 3.4.1.2 regarding surface oil flow visualization), it is difficult to predict the effective channel area, true shock strength, or its orientation. In addition, in these kinds of flows, the assumption that the wall static pressure (experimentally recorded) is an accurate representation of the channel core static pressure may be incorrect.

Regardless of the true strength, a shock would absolutely aid in achieving the required pressure losses. Therefore, it can be hypothesized that supersonic conditions are achieved beyond the channel throat and that some shock structures are located before the next static pressure tap whose measured pressure ratio is 0.528 or greater. The proposed shock location coincides with the recirculation region seen in the inner bypass surface oil flow visualization shown in Fig. 3.25 through Fig. 3.29.

The channel pressure ratio data seems to indicate that the channels choke successively, beginning with the channels nearest the gearbox. As can be seen in Fig. 3.25 through Fig. 3.29, more and more operating conditions share the same first static tap pressure ratio as channel number increases. For instance, the first static tap pressure ratio in Ch #1 and Ch #2 is shared between the two highest operating conditions $M_{tunnel} = 0.538|_{20.00}$ and $0.538|_{21.00}$ while the Ch #3 first static tap pressure ratio also includes $M_{tunnel} = 0.531$. Since multiple operating conditions share the first static tap pressure ratio, it seems as though a minimum pressure ratio limit has been reached.

The successive channel choking theory fits well with the proposal previously set forth relating the vaned model inlet plane M_{inlet} distribution to mass flow rate described in Section 3.2.2. As can been seen in the inner surface oil flow visualization presented in the channel pressure ratio figures, the flow within the channels nearer to the gearbox exhibit many more features commonly attributed with separated flows. Increased amounts of separation, and hence pressure losses, would also contribute to the channel's inability to swallow more mass, and thereby provide further evidence for the successive choking theory.

3.3.2.2 Isentropic Case Comparisons

In an effort to determine how ideal the experimental results were isentropic calculations were performed in each channel. The calculation procedure used in the isentropic/ideal case is described in detail in Section 2.7.2.2.1. There are several key assumptions involved in the calculation. The first is that there are no total pressure losses from the inlet plane, where the total pressure probe is located, to the first static pressure tap within each channel. Second, it is assumed that the model surface static pressure was representative of the local core flow static pressure. The loss in area due to the displacement thickness on each wall was also estimated and used to improve upon the ideal case calculation.

The area used in the calculations is the local normal area. The coordinates of the four channel corners are used to define a channel centerline. By defining the normal direction as being everywhere tangent to the centerline, the curvature of each channel is accounted for. The local normal area is computed as the area bounded by the intersection

of the normal plane and the channel corner coordinates. Corrections for the inner and outer wall curvature are also included in this calculation.

It is believed that the experimental to isentropic comparison should be considered a qualitative comparison at best. It is known that there is a good deal of flow separation within the channels from the surface oil flow visualization. It cannot be expected that the isentropic relations used in quasi-one dimensional converging diverging nozzle flows would be fully applicable in highly three-dimensional, separated internal flows found in this study.

Agreement is measured by the percent difference between the isentropic and experimental cases as shown in Fig. 3.30 through Fig. 3.34 for each of the five channels. Some of the figures do not include data for some of the larger values of M_{tunnel}. This is because at high M_{tunnel}, A^* is sometimes less than A_{throat}, causing the area ratio to fall below unity and thereby disallowing the use of the Mach-area relation (which is only defined for $A/A^* \geq 1$). Therefore, only the operating conditions for which $A/A^* \geq 1$ is true throughout the entire channel are displayed in the figures.

For the channel with the least amount of curvature (Ch #1, Fig. 3.30), the level of agreement is quite good until the two choked operating conditions are reached, at which point the percent difference routinely exceeds 10%. As channel number increases, the percent difference for a specific operating condition tends to increase. The largest percent difference is typically found within the region of the channels containing the most curvature and most aggressive local area changes (near the throat). This is, no doubt, in large part due to the fact that the experimental data are normalized by the channel inlet total pressure instead of the local total pressure, thereby neglecting total pressure losses. Total pressures losses are known to increase with increased channel three-dimensionality (approaching the gearbox) and with velocity squared (increased M_{tunnel}) and hence are likely to be significant within this experiment, especially near the channel throats. This would account for the large discrepancy between the experimental and isentropic cases.

The percent difference between experimental and isentropic cases for Ch #3 (Fig. 3.32) and Ch #5 (Fig. 3.34) contain a unique feature. For these two cases, the percent difference is sometimes actually negative, seemingly indicating that the experimental

pressure ratio was greater than the isentropic pressure ratio. The reasoning for this occurrence is not clear as it does not make physical sense for the experimental conditions to exceed the isentropic/ideal case. However, the negative percent difference is usually found near the channel throats, which is near the location where the experimental flow is likely to act in a most non-isentropic manner since the flow there is undergoing a great deal of compression, direction change, and pressure losses, and, in all likelihood, separation.

3.3.2.3 Channel Total Pressure Losses Estimation

An estimation of the total pressure losses within each channel was conducted. Since the compressible mass flow rate formulation is a function of only pressure, temperature, and local area, total pressure may be iterated upon for each experimentally recorded static pressure given a mass flow rate. This procedure is more clearly outlined in Section 2.7.2.2.3.

When examining the results of total pressure losses estimation within each channel, the primary mode of evaluation was simply to check that the total pressure never increased, as this is physically impossible. For the channels that underwent the least amount of curvature, the total pressure losses estimate followed this trend, as shown in Fig. 3.35, where the estimated total pressures at each static tap within the top-most channel (Ch $^{\#}$1) are presented. The estimated total pressures for the remaining four channels are shown in Fig. 3.36 through Fig. 3.39. The first data point in each series is located at x = -1.14 inches and represents the recorded total pressure within the core flow at the inlet plane (where x = 0 is located at the start of the model). The decrease in total pressure between the inlet plane and first static tap is negligible, as one would expect for a uniform flow undergoing few disturbances. Also, as expected, the decrease in total pressure through the channel increased with increased operating condition.

For the channels which experienced a great deal of curvature, and thereby resulted in highly complex, three-dimensional, separated, and, ultimately highly non-isentropic flows, the requirement that estimated total pressure always decrease did not hold, especially near the channel throats, as can be seen in Fig. 3.37 through Fig. 3.39. However, the estimated local total pressure did decrease from channel inlet to exit as

summarized in Table 3.5, where the estimated channel entry total pressure and the percent reduction at channel exit are displayed. Although the accuracy of the calculations within the channel may be questionable, the more general requirement that total pressure losses increase from in-flow to out-flow is satisfied.

Table 3.5 Summary of Estimated Total Pressure Losses within Each Channel.

M_{tunnel}	Channel #6		Channel #4		Channel #8		Channel #2		Channel #10	
	Entry [psia]	%Δ at Exit	Entry [psia]	%Δ at Exit	Entry [psia]	%Δ at Exit	Entry [psia]	%Δ at Exit	Entry [psia]	%Δ at Exit
0.148	14.656	0.35	14.654	0.51	14.652	0.39	14.657	1.12	14.659	1.00
0.294	15.233	1.48	15.228	2.19	15.222	1.74	15.238	4.72	15.244	4.24
0.385	16.278	2.67	16.273	4.11	16.267	3.68	16.299	8.23	16.307	7.74
0.481	17.555	4.78	17.548	7.28	17.543	7.29	17.580	13.64	17.596	13.32
0.526	18.749	6.76	18.752	10.19	18.779	11.12	18.819	18.31	18.840	18.04
$0.538|_{20.00}$	19.885	9.16	19.868	12.44	19.881	14.07	19.916	21.31	19.932	21.01
$0.538|_{21.00}$	20.878	11.52	20.862	15.01	20.877	16.74	20.912	24.29	20.928	23.98

3.3.2.4 Channel Mass Flow Rate

The mass flow rate (MFR) within each channel was calculated at the first channel static pressure tap based on experimental data from its compressible formulation, as described in Section 2.7.2.2.2. Based on the channel experimental measurements, it appears as though the channels successively choke as the facility mass flow rate is increased. The channel adjacent to the gearbox chokes first (Ch #5), followed by the next one up (Ch #4), and so on until finally the top-most channel (Ch #1) chokes, leading to facility choke. With this theory in mind, data regarding the relative mass flow rates between channels were of interest so as to ascertain whether or not mass flow dumping between channels occurred.

Fig. 3.40 displays each channel's percent contribution to total mass flow rate for each of the seven tested operating conditions. The two channels nearest the gearbox fairing (Ch #4 and #5) each contribute equally to the total mass flow rate and this contribution only decreases minimally with increasing M_{tunnel}. The contribution that these channels provide to the total is also significantly smaller than that provided by the other

three channels. This may be attributed to the smaller throat local normal area found in these channels, thereby accounting for their decreased mass flow capabilities.

A clear trade-off does occur between the middle channel (Ch #3) and the two top-most channels (Ch #1 and #2). As M_{tunnel} increases, the percent total mass flow passing through Ch #3 decreases, while that in Ch #1 and #2 tends to increase, showing clear dumping of mass flow from Ch #3 into Ch #1 and #2. The increases between Ch #1 and #2 are nearly identical, indicating that Ch #3 does not appear to preferentially dump into one or the other channel. Also of interest, it was observed that for the M_{tunnel} = 0.148 - 0.385 cases, Ch #3's contribution to the total was less than that of Ch #1, but greater than that of Ch #2. It is interesting that there should be this type of mass flow contribution distribution where the distribution does not act monotonically, but exhibits changes of slope as well as large discontinuities (the jump from Ch #5 and #4 to Ch #3, for instance).

The contribution distribution calculated in this study was compared to that calculated by Kim, Kumano, Liou, Povinelli, and Conners.[30] Comparison of operating conditions was hindered because the CFD simulation's boundary conditions were freestream values since their study encompassed the supersonic inlet as well as the bypass duct. Nevertheless, the level of agreement is quite good, as shown in Fig. 3.41. This agreement appears to provide added confidence in the results of this study. One area of possible contention, however, regards the contributions of the two channels nearest the gearbox fairing. The results of this study indicate that these two channels contribute equally to total MFR, whereas the CFD simulation predicts that Ch #5 contributes less than Ch #4.

Also of interest, it was observed that for the $M_{tunnel} \leq 0.385$, the contribution to total mass flow rate did not increase with channel number in a monotonic manner. The contribution of Ch #3 fell between that of the top two channels (Ch #1 and Ch #2). Further, large discontinuities of channel contributions existed even at very low M_{tunnel}, such as the jump from Ch #5 and Ch #4 to Ch #3.

3.4 Flow Visualization

The following section presents the results of the flow visualization techniques – surface oil flow visualization and schlieren photography, used in this study. Since schlieren photography is a purely optical method, it could be conducted at any time. The surface oil flow visualization, however, was not conducted until all the desired pressure data were collected to avoid the possibility that oil in the pressure taps would affect pressure measurements.

3.4.1 Surface Oil Flow Visualization

Two types of surface oil flow visualization – one with a lampblack pigment based mixture and the other with a fluorescent dye base, were conducted on the model surface. It was found that the fluorescent mixture was preferable to the lampblack based mixture. Even so, the lampblack-based visualization also provided very interesting and useful data. Surface oil flow visualization was conducted on both the clean and vaned models.

3.4.1.1 Clean Model

Fluorescent surface oil flow visualization was conducted for the clean model at M_{tunnel} = 0.704. The recirculation region's exact flow characteristics can be best described by several parameters. They include the location of the center of circulation, the point of flow separation from the aft fairing, the location of the shear layer dividing the outer flow and the recirculation region, and, lastly, the location of a stagnation point on the fairing wall dividing streamwise and reversed flows.

The result of the fluorescent based surface oil flow visualization can be seen in Fig. 3.42. Fluorescent results were extremely detailed due to their structured and very fine grid spacing. However, some of the fluorescent mixture located within the separated regions did not flow much. A less viscous solution would have likely yielded better results within this region. Although the lampblack dots weren't as uniformly spaced or sized, the results of the mixture, yielded more detail within the recirculation region. The result of the lampblack based clean model surface oil flow visualization is shown in Fig. 3.43, presented in an unwrapped form.

The fluorescent and lampblack based clean model surface oil flow visualizations both yielded extremely symmetric results. The two cases also appear to be very similar to each other in terms of recirculation region location, point of flow separation, and with regards to the azimuthal extent of the separation region.

A large recirculation region is evident aft of the gearbox whose position and size can be quite accurately estimated from the images. As shown in Fig. 3.43, the recirculation is very pronounced; some of the reversed flow streaks extended significantly upstream. Unfortunately, fluorescent results did not yield nearly as much detail within this region. In both cases, the point of separation was located at the shoulder of the fairing. With flow separation occurring so soon, it appears that the flow does not tend to follow the fairing contour for any length of time. The aft fairing, without the aid guide vanes, therefore, seems to provide little guidance to the flow in terms of pressure recovery or flow separation.

The clean model surface oil flow visualization also provided some insight into the location of the shear layer that separates the attached and separated flows. Originating at the point of flow separation near the beginning of the aft fairing, the shear layer extends downstream along the model surface at a slight downward angel. Its location can be best characterized by the line which separates the flow that moves in a purely streamwise direction and that which also contains a significant downward (towards increasing $|\Theta|$) component. This can be best seen in the fluorescent visualization (Fig. 3.42) where dashed lines indicate the approximate region of the shear layer.

This fairing wall stagnation point can only be seen in the fluorescent mixture results. It is located just downstream of the nacelle end plane, bringing up the possibility that the location of the stagnation point is somehow driven or influenced by the nacelle's termination.

Jian[27,28] conducted a computational study of the clean model wind tunnel geometry with imposed experimental conditions. The model surface shear stress plots that were generated as a part of that study compared well qualitatively with the experimental results. The two cases shared similar flow separation points and location of recirculation regions. The reader is referenced to Jian's works for more detailed

information regarding the computational study and the comparison to experimental results.

3.4.1.2 Vaned Model

Vaned model surface oil flow visualization was conducted at three operating conditions. They were M_{tunnel} = 0.148, 0.385, and $0.538|_{21.00}$. A large amount of vaned model surface oil flow visualization is presented in conjunction with the channel pressure data in Section 3.3.2.1, where the results of the inner bypass surface are shown at $M_{tunnel} = 0.538|_{21.00}$.

The results of the vaned model surface oil flow visualization revealed extremely complicated flow structures within the channels. Multiple large recirculation regions can be found on the channel walls. In some cases, these regions can even be found on both walls of a single channel. The large degree of flow distortion and inferred three-dimensionality point to a flow containing multiple regions of flow separation wherein total pressure losses are likely to be very high.

It was found that the flow structures found in all three tested operating conditions were very similar to each other and displayed an expected increase in structure size and prevalence. For instance, wall recirculation regions seemed to grow in size as M_{tunnel} increased. The choked operating conditions did not yield any additional flow structures. No definitive evidence of shock structures were discovered in the surface oil flow visualization of any of the tested operating conditions.

Within the channel undergoing the least amount of curvature (Ch $^{\#}1$) the oil flow streaklines show that the flow is fairly straight and uniform along both walls. Within Ch $^{\#}2$, the wall curvature increases, and recirculation regions begin to appear on the channel walls. The recirculation regions are located at or just downstream of the location of maximum curvature along each channel wall. The remaining three channels all contain wall recirculation regions.

In order to provide a description of the vaned model surface oil flow visualization observations, the channel walls were broken into several zones. The first zone starts at the vane tips and extends downstream until just before the channel bends back towards the streamwise direction. The next zone is local to that bend of the channel; it ends at the

point where the channel has turned back in the streamwise direction. The third zone is from the end of the corner to x_{cowl}. The last zone covers the remainder of the model. The placement of the zones can be visualized in Fig. 3.44.

Additionally, a convention was established with regards to naming the channel walls. The "bypass inner surface," that is, the surface representing the outer shell of the core engine (and is therefore the inner wall of the bypass), is the floor of the channel. Therefore, the surface oil flow visualization results presented with the channel pressure data is composed of bypass inner surface images. The "lower wall" is channel side wall that is further way from top-center, and, therefore closer to the aft fairing. The "upper wall", meanwhile, is the channel side wall that is nearer to top-center, and further from the aft fairing.

Within the first zone, the bypass inner surface streaklines indicate a tendency for the flow to trend towards the lower wall as can be seen in Fig. 3.45. The side wall streaklines (not visible in the figure) display little to no radial component anywhere from the vane tips to the corner of the channel wall (that is, anywhere within zone $^{\#}1$).

Originating within the corner of the lower wall, bypass inner surface streaklines tend to emanate towards the opposite side of the channel (towards the upper wall) as pointed out in Fig. 3.45. As channel curvature increases (from Ch $^{\#}1$ to Ch $^{\#}5$), the trend of bypass inner surface flows to move towards the upper wall increases such that flow angularity exceeds 60° with respect to the streamwise direction within the corner of Ch $^{\#}5$ while it is nearly perfectly streamwise in Ch $^{\#}1$. On the side walls, recirculation regions form near the point where the bypass inner surface flow shifts from the lower wall to the upper wall. These recirculation regions may or may not be associated with similar regions on the bypass inner surface, which would be a very strong indication of highly three dimensional flow, as can be seen in Fig. 3.46 and Fig. 3.47.

The bypass inner surface streaklines are largely oriented in the streamwise direction through the remainder of the aft bypass. The side wall streaklines, however, begin to show increased activity. Within the third zone, between the recirculation region and the cowling end plane, there is often a region of flow reversal coupled with inner and outer radial components driving the flow towards the center of the side wall, as can be seen in Fig. 3.46 and Fig. 3.47. These types of flow features are only characteristic of the

upper wall; these coupled radial and reversed flow components are not seen on the lower walls.

When creating the photo record of the surface oil flow visualization, many images were taken of the model as it was rotated. By using this method, nearly all surface oil flow features are recorded. Appendix E provides a series of images taken in this format for each of the three tested operating conditions.

3.4.2 Schlieren Photography

Schlieren photography was utilized to provide insight into the flow beyond the cowling end plane. By conducting imagery with both a vertical and horizontal knife edges, horizontal and vertical aberrations in flow density were visualized. An instantaneous image of each of the conducted runs can be found in Fig. 3.48. As would be expected, the images corresponding to low M_{tunnel} do not display a great amount of flow features. This is due to the fact that the density gradients are small for these subsonic flows. However, the prevalence and size of the aberrations does grow with M_{tunnel}.

For both models (and all operating conditions), the vertical knife edge images tend to show more variation than those corresponding to the horizontal knife edge. This indicates that, since the gradients visualized are normal to the direction of the knife edge, the horizontal density gradients are much more varied than those in the vertical direction. Since the flow momentum is in the streamwise (horizontal) direction, this is not an unexpected observation.

A series of instantaneous images was averaged to create a single representative time-average image for each operating condition (Fig. 3.49). Approximately 25-30 instantaneous images were used for each operating condition to create the average images which were used to identify steady flow features within the exhaust flow. Horizontal knife edge images show a clearly strengthening shear layer at the exhaust near top-center. The strongest shear layer can be found in the clean model case, for which M_{tunnel} is the greatest. Vertical knife edge images reveal a strengthening pattern of vertical bands which are emitted downstream. Very little can be seen near BC (bottom-center) for any

operating condition or model, especially for the horizontal knife edge. However, some faint band-like structures similar to those found near top-center can be seen when the knife edges is placed in a vertical orientation.

The schlieren imagery confirms that the exhaust flow is not supersonic by the lack of visible shock or expansion wave structures in either instantaneous or time-averaged images. This observation confirms that the current wind tunnel and vaned model geometry iteration were unable to achieve the desired operating conditions.

The significant difference in flow distribution between the clean and vaned models can be extracted from the schlieren imagery. Very few density gradients are observed, in either the horizontal or vertical directions, near bottom-center of the clean model. The fastest vaned operating condition, $M_{tunnel} = 0.538|_{21.00}$, however, displays a much larger amount of aberrations near bottom-center. This is true despite the fact that the clean model M_{tunnel} is much larger (0.704 as compared to 0.538). Clearly, the vaned model geometry does a much better job of distributing the flow around the annulus at the aft bypass exhaust than the clean model does.

Figures

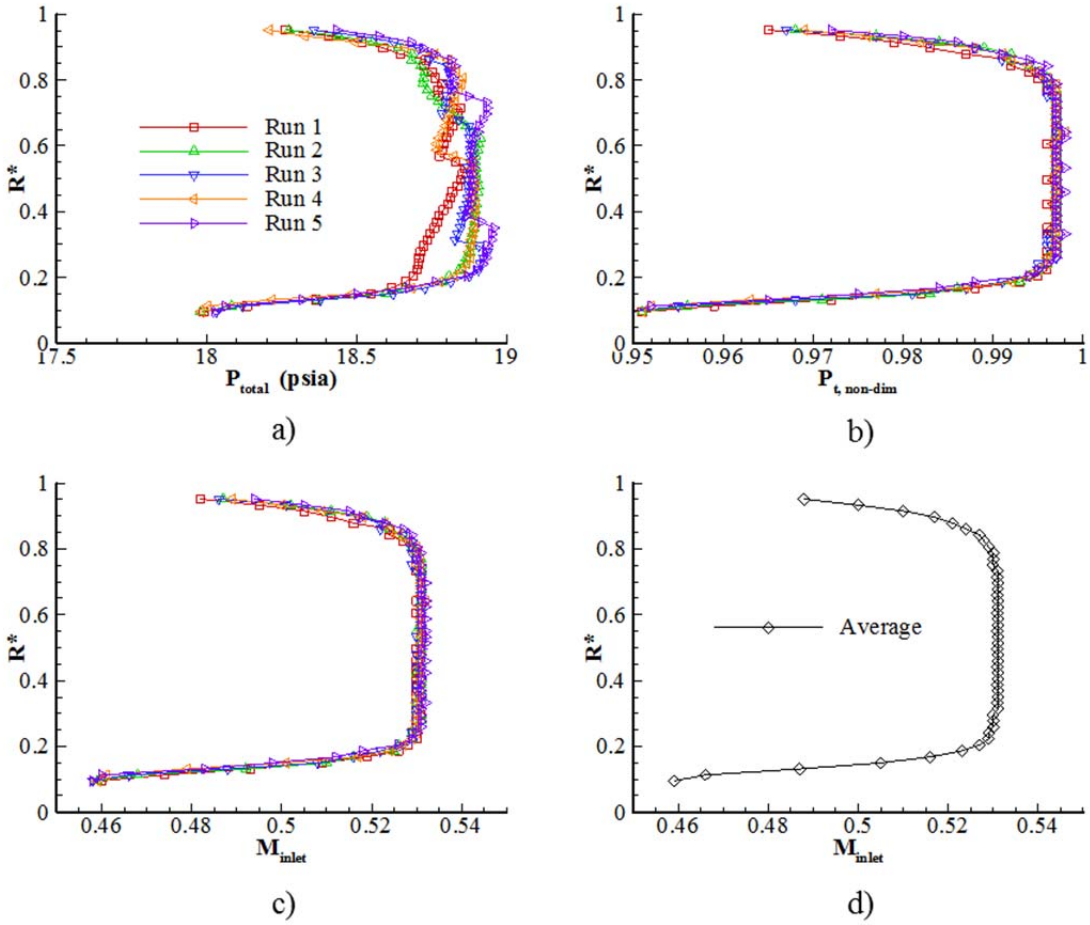

Fig. 3.1. Inlet plane radial profiles at the Ch #1 location, M_{tunnel} = 0.531, for five independent runs. Profiles are a) probe total pressure, P_{total}, b) normalized probe total pressure, $P_{t,non\text{-}dim}$, c) inlet plane Mach number, M_{inlet}, and d) five-run average M_{inlet}.

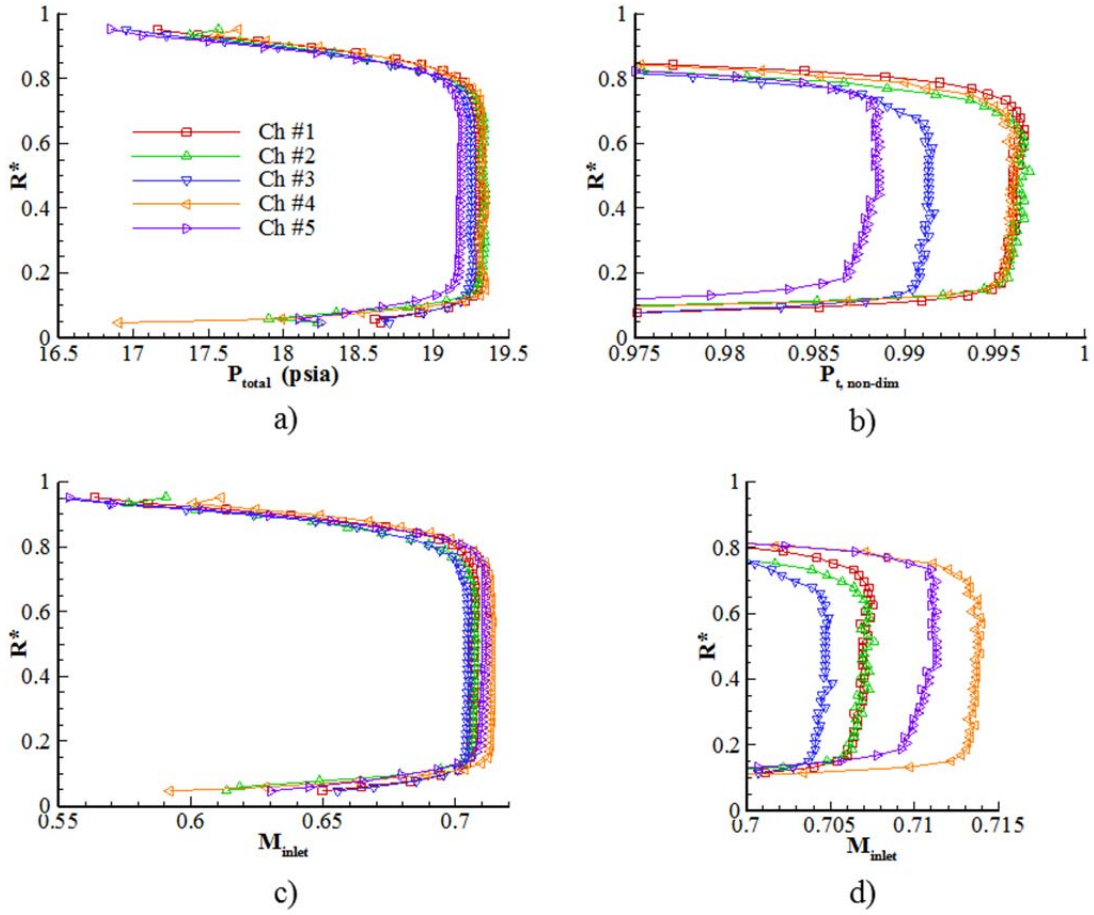

Fig. 3.2. Clean model (M_{tunnel} = 0.704) inlet plane radial profiles of a) probe total pressure, b) non-dimensionalized probe total pressure, c) inlet Mach number with d) zoomed-in view.

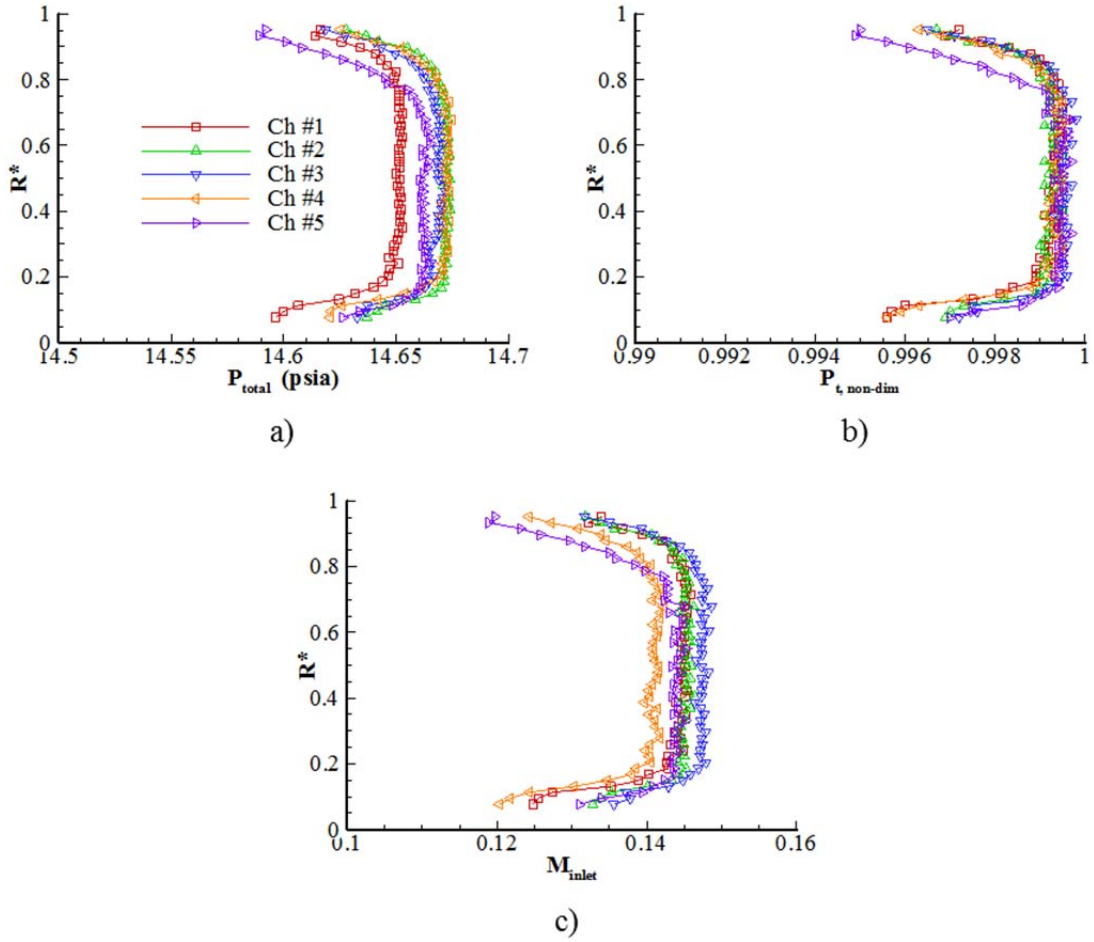

Fig. 3.3. Vaned model (M_{tunnel} = 0.148) inlet plane radial profiles of a) probe total pressure, b) non-dimensionalized probe total pressure, c) inlet Mach number.

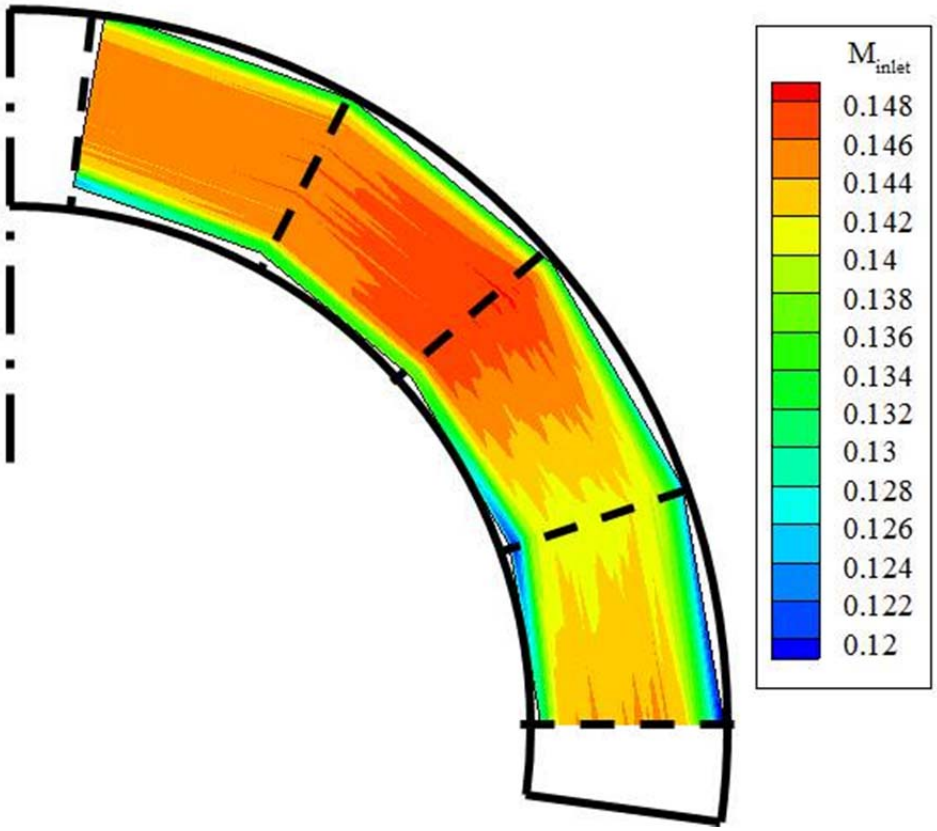

Fig. 3.4. Vaned model (M_{tunnel} = 0.148) inlet plane M_{inlet} contour plot.

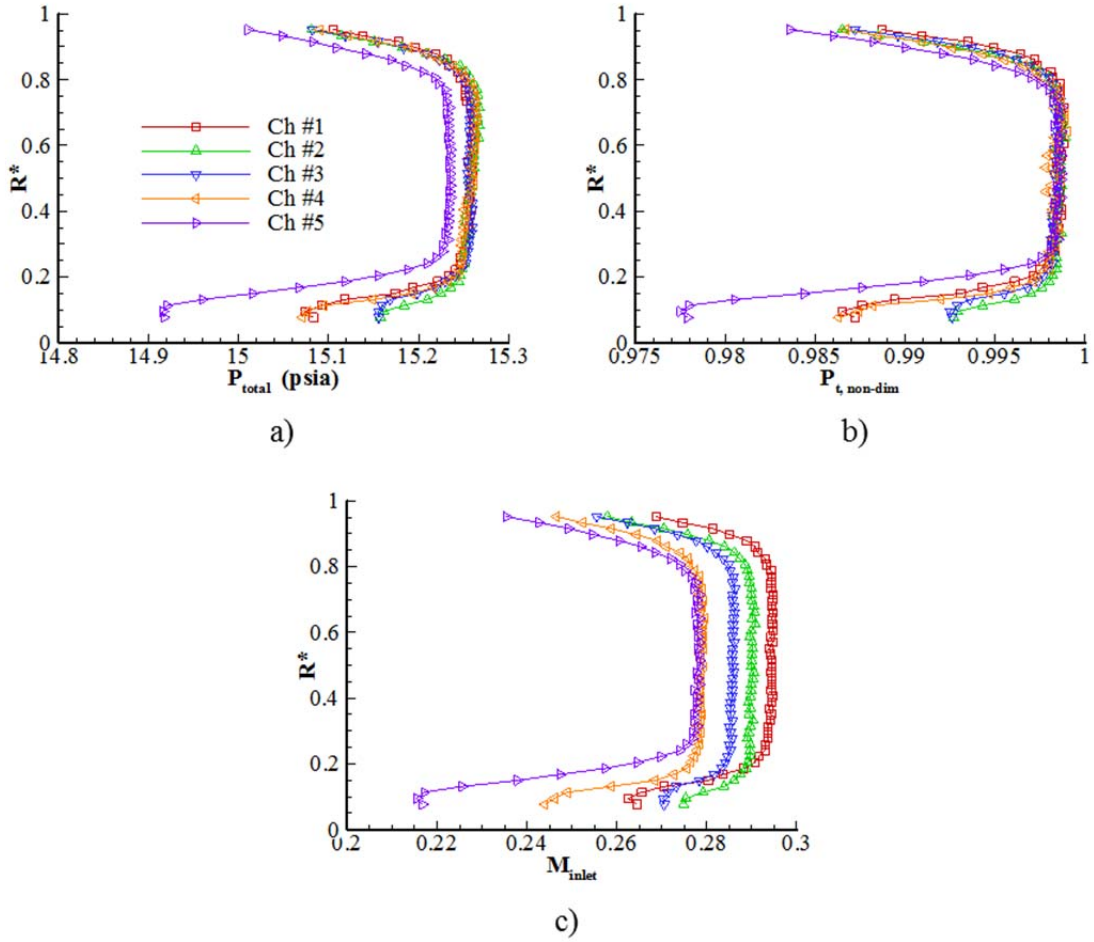

Fig. 3.5. Vaned model (M_{tunnel} = 0.294) inlet plane radial profiles of a) probe total pressure, b) non-dimensionalized probe total pressure, c) inlet Mach number.

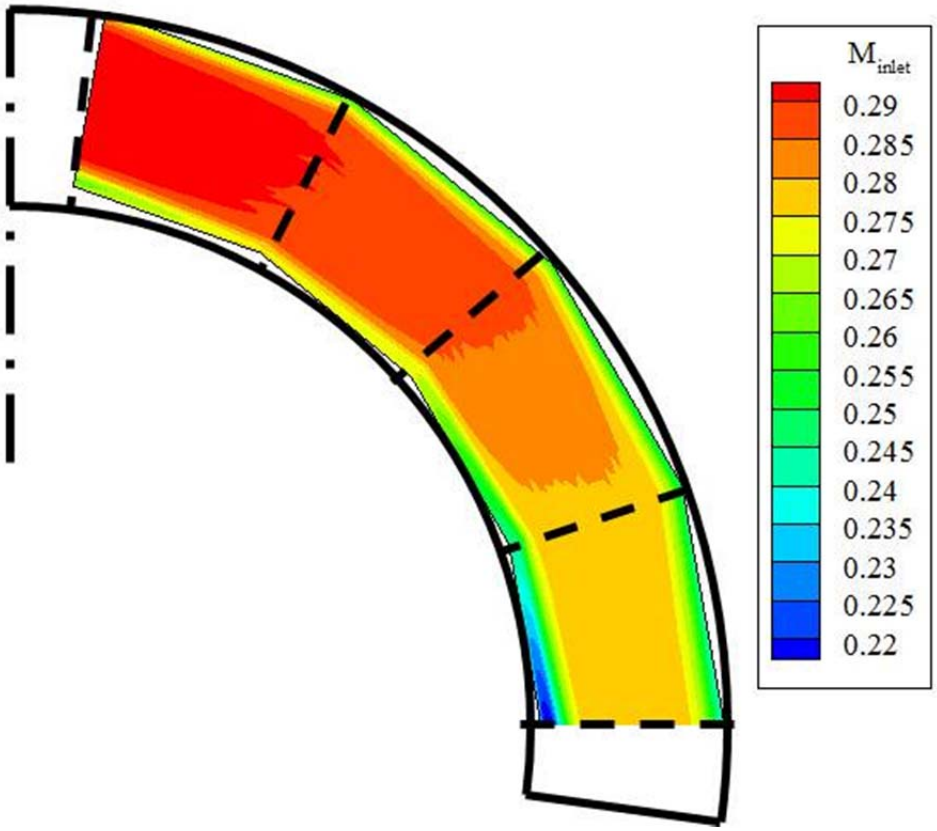

Fig. 3.6. Vaned model (M_{tunnel} = 0.294) inlet plane M_{inlet} contour plot.

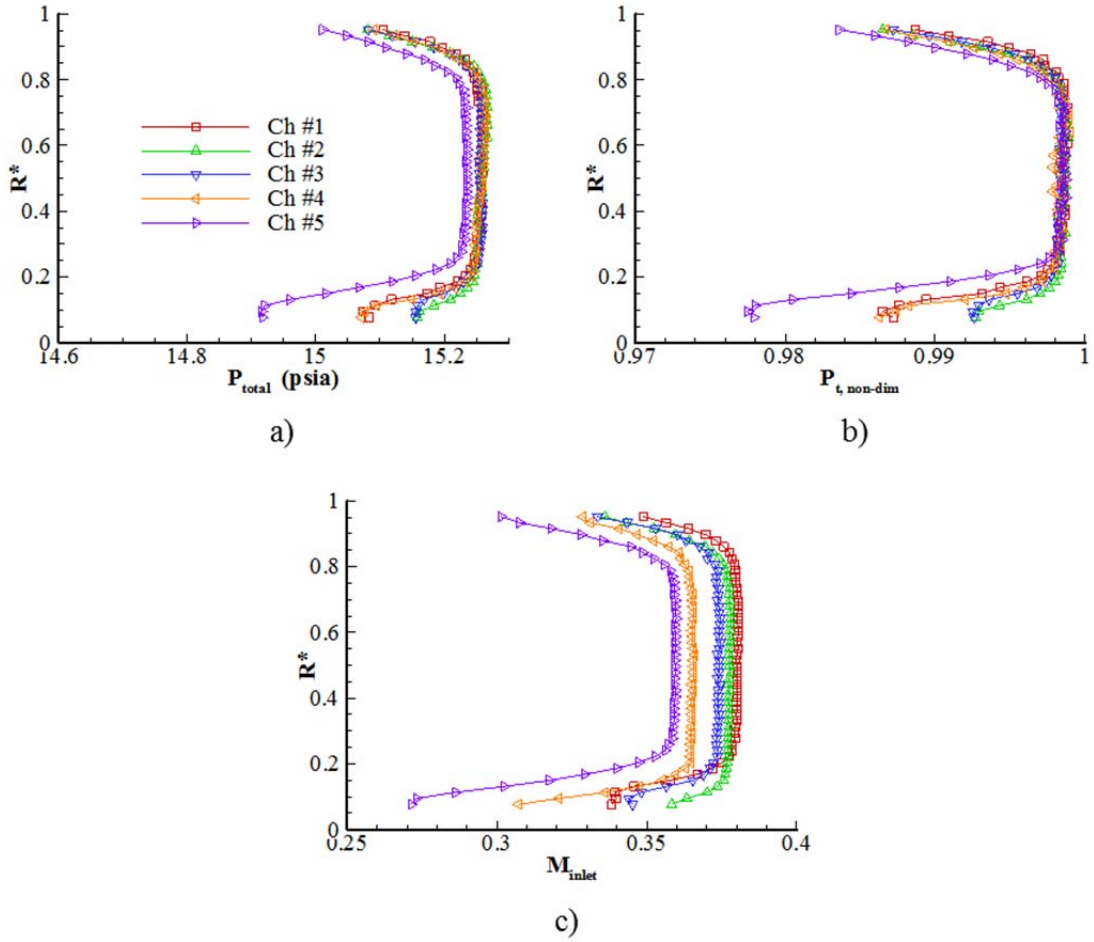

Fig. 3.7. Vaned model (M_{tunnel} = 0.385) inlet plane radial profiles of a) probe total pressure, b) non-dimensionalized probe total pressure, c) inlet Mach number.

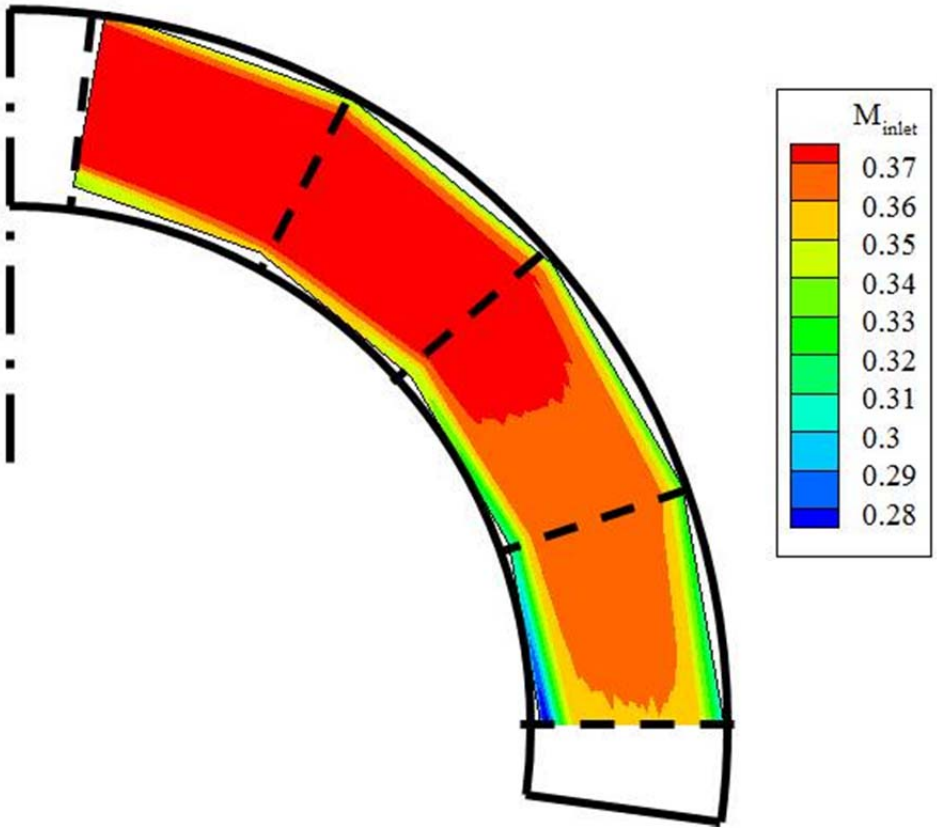

Fig. 3.8. Vaned model (M_{tunnel} = 0.385) inlet plane M_{inlet} contour plot.

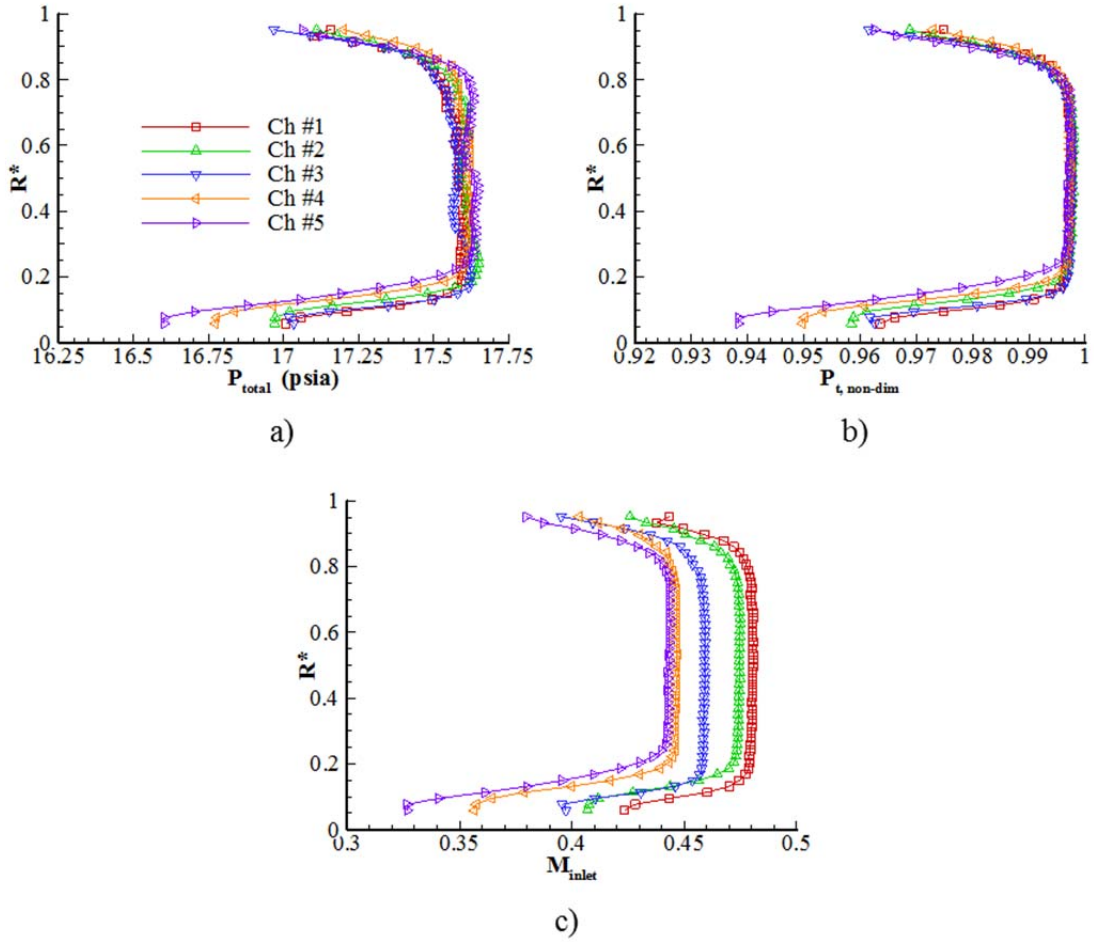

Fig. 3.9. Vaned model (M_{tunnel} = 0.481) inlet plane radial profiles of a) probe total pressure, b) non-dimensionalized probe total pressure, c) inlet Mach number.

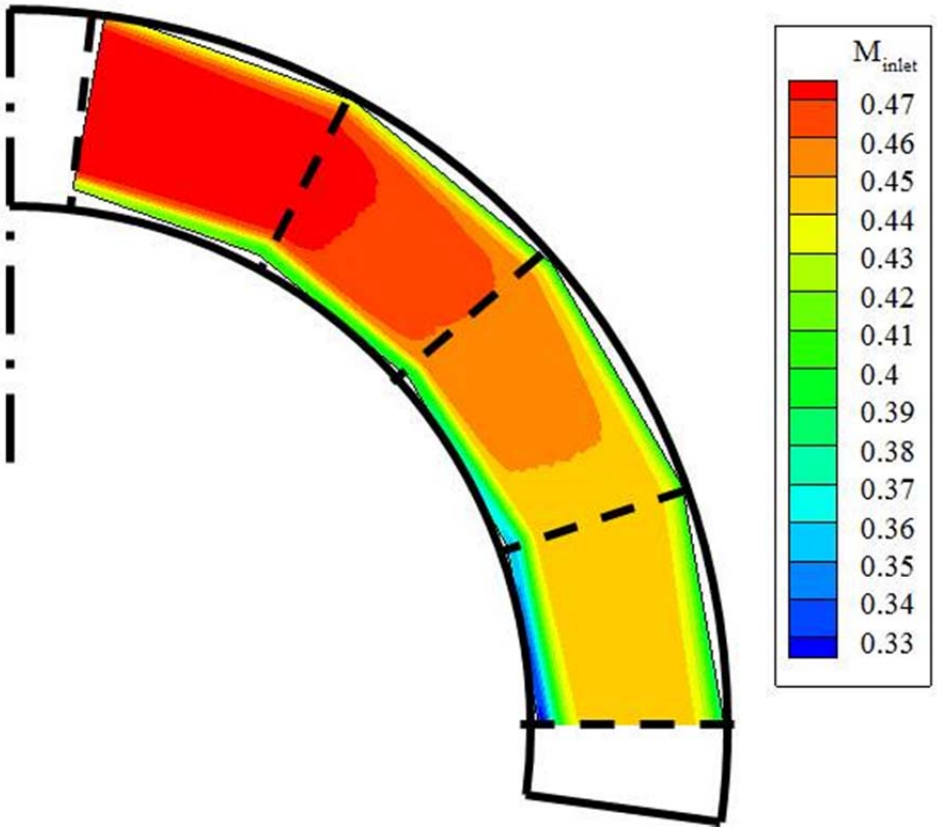

Fig. 3.10. Vaned model (M_{tunnel} = 0.481) inlet plane M_{inlet} contour plot.

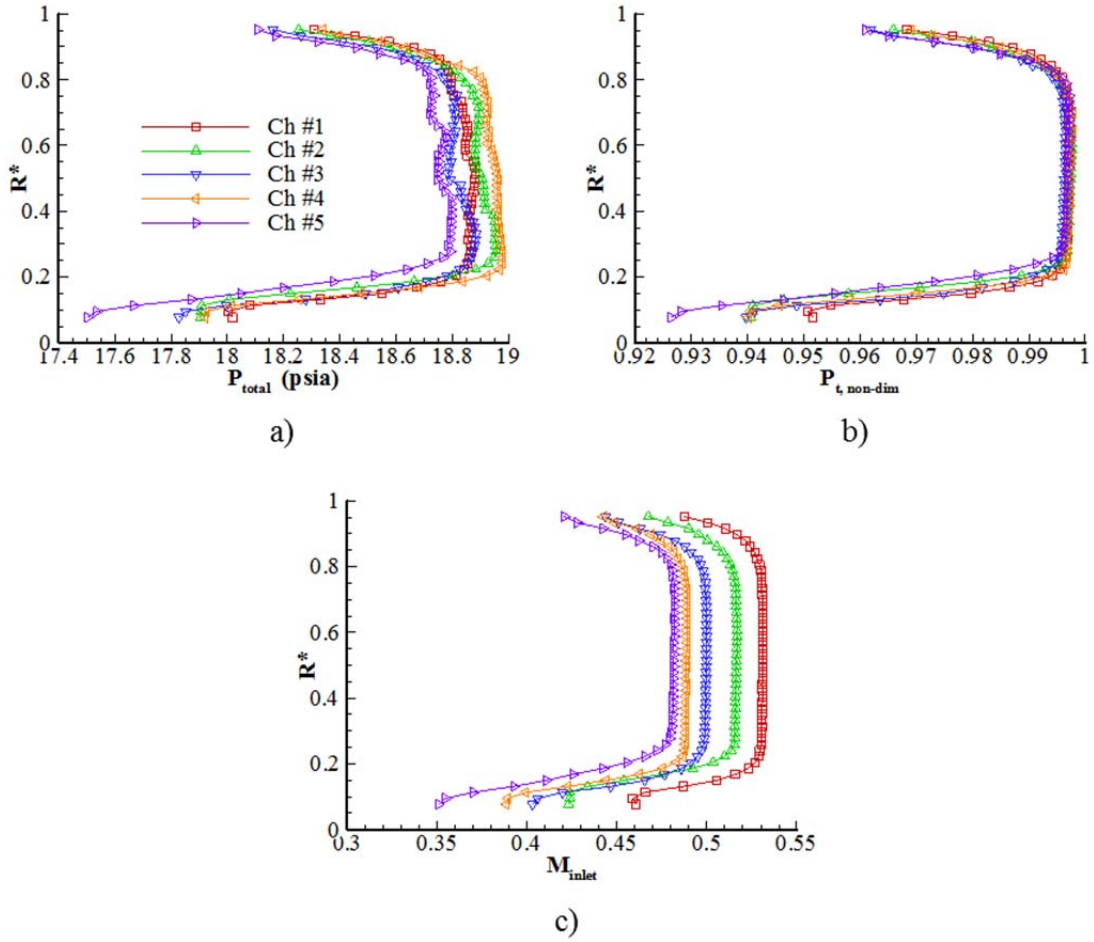

Fig. 3.11. Vaned model (M_{tunnel} = 0.531) inlet plane radial profiles of a) probe total pressure, b) non-dimensionalized probe total pressure, c) inlet Mach number.

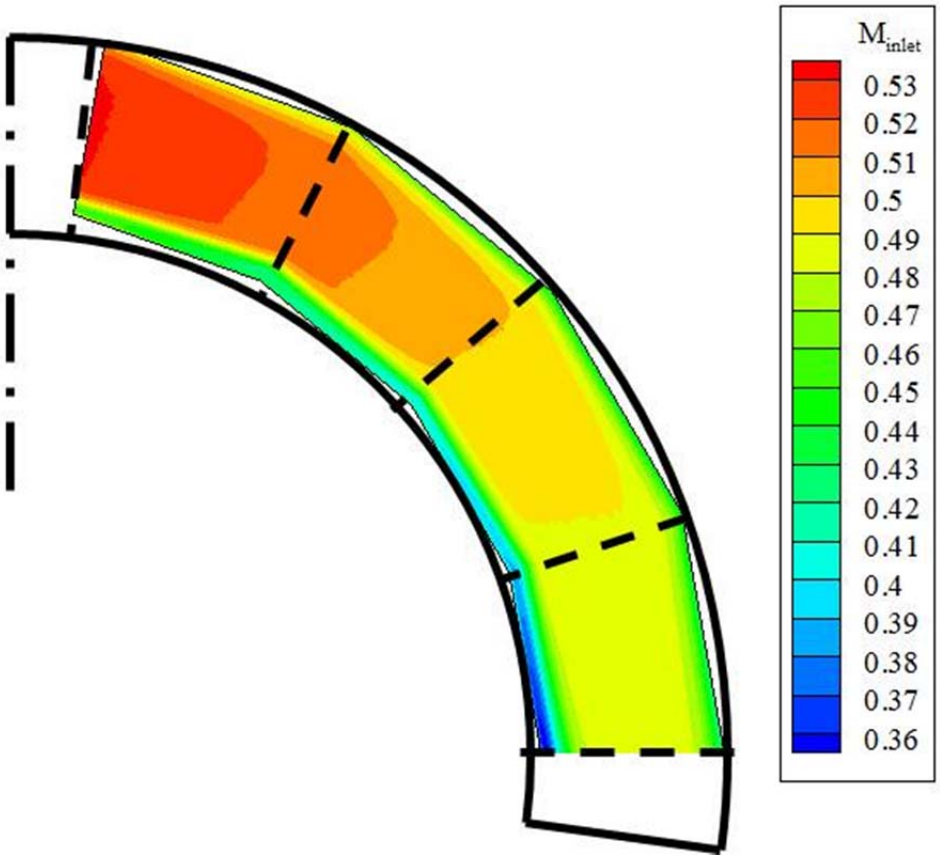

Fig. 3.12. Vaned model (M_{tunnel} = 0.531) inlet plane M_{inlet} contour plot.

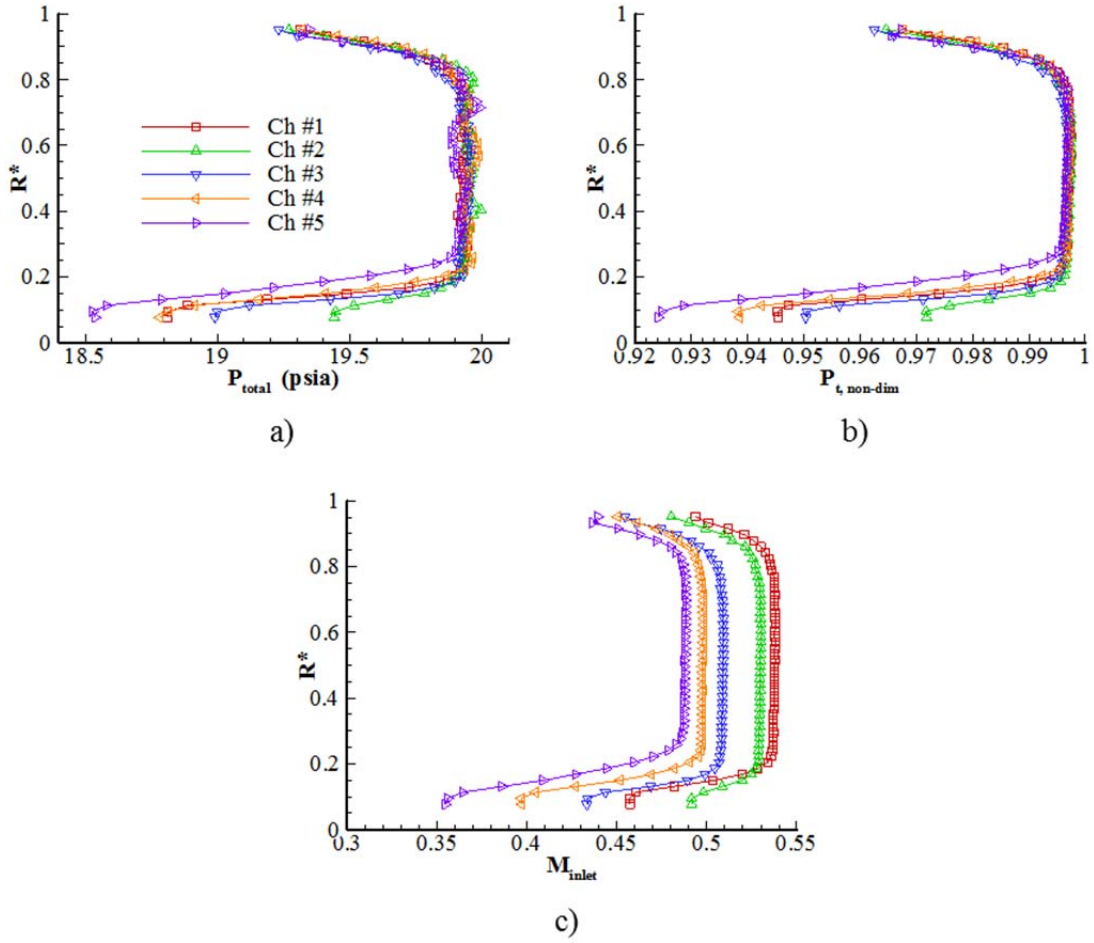

Fig. 3.13. Vaned model (M_{tunnel} = 0.538|$_{20.00}$) inlet plane radial profiles of a) probe total pressure, b) non-dimensionalized probe total pressure, c) inlet Mach number.

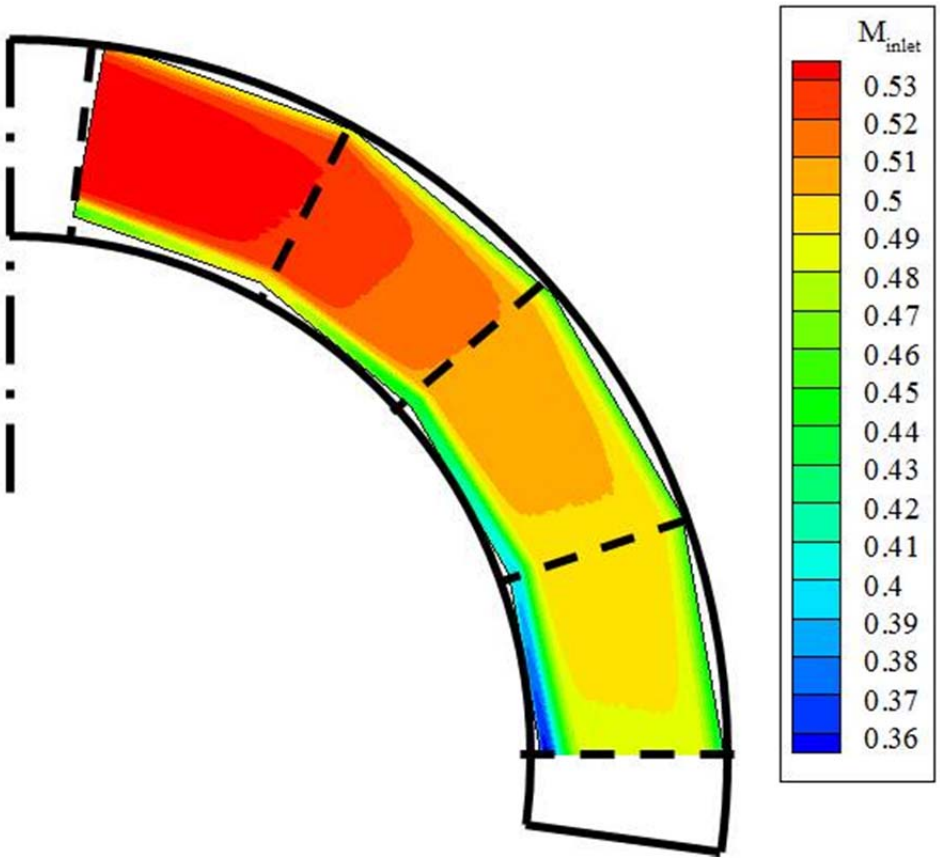

Fig. 3.14. Vaned model ($M_{tunnel} = 0.538|_{20.00}$) inlet plane M_{inlet} contour plot.

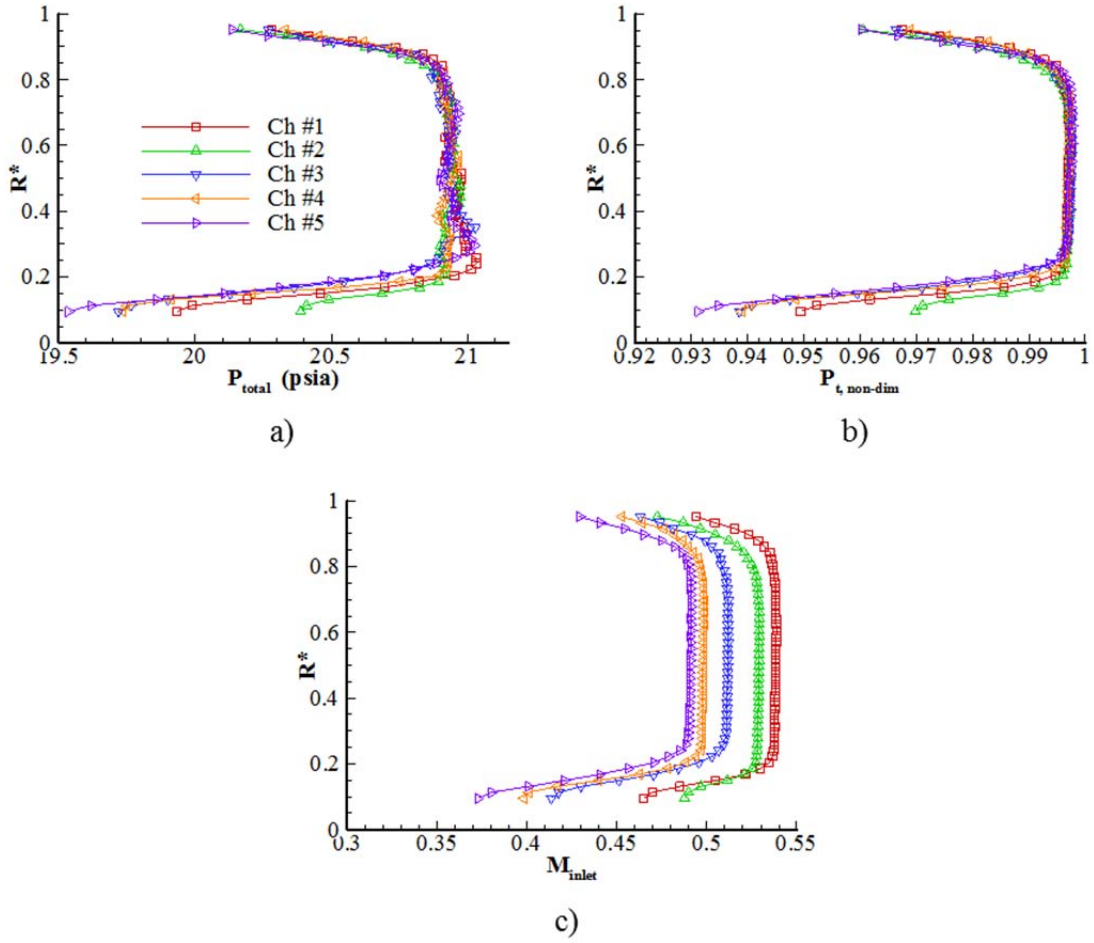

Fig. 3.15. Vaned model (M_{tunnel} = 0.0.538|$_{21.00}$) inlet plane radial profiles of a) probe total pressure, b) non-dimensionalized probe total pressure, c) inlet Mach number.

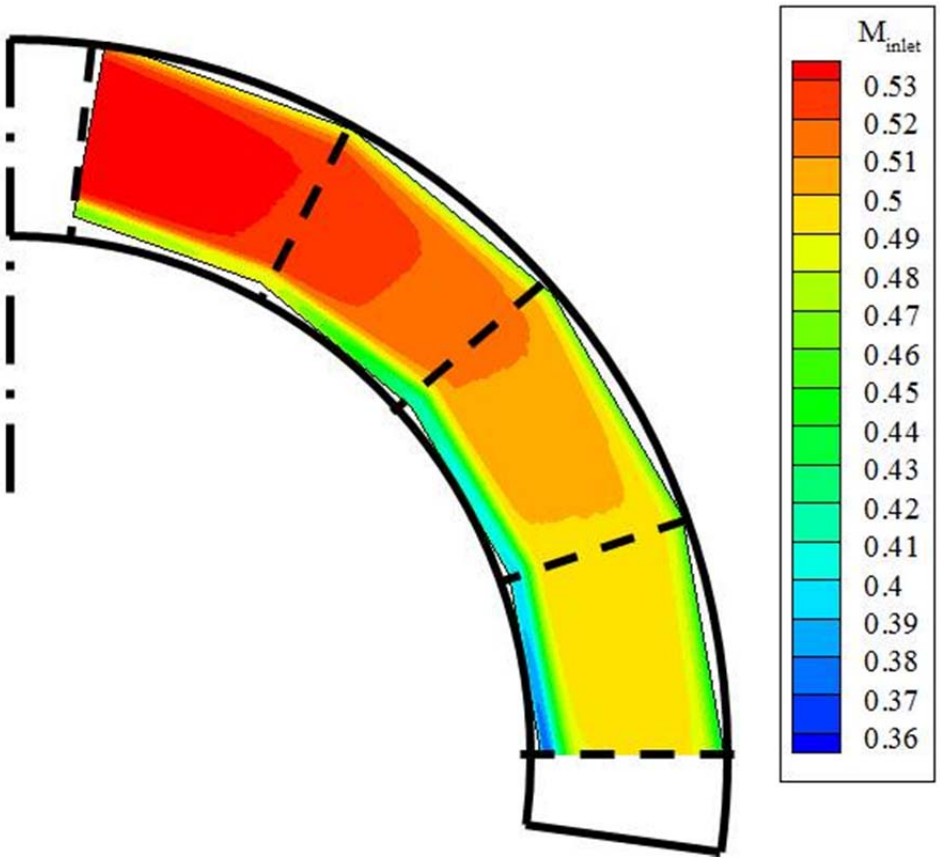

Fig. 3.16. Vaned model ($M_{tunnel} = 0.538|_{21.00}$) inlet plane M_{inlet} contour plot.

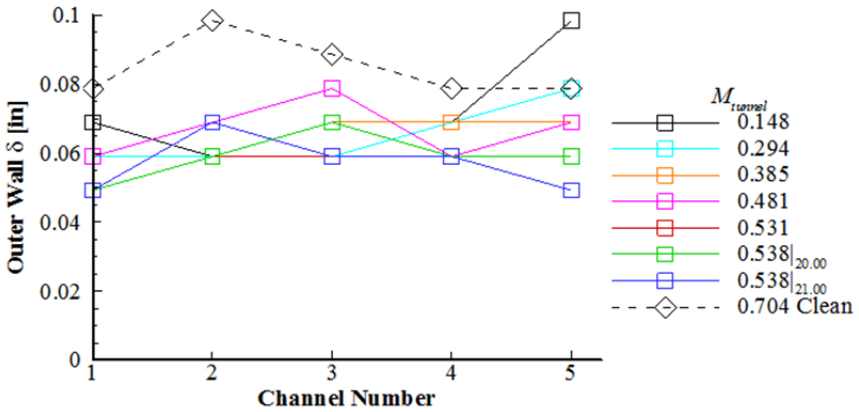

a)

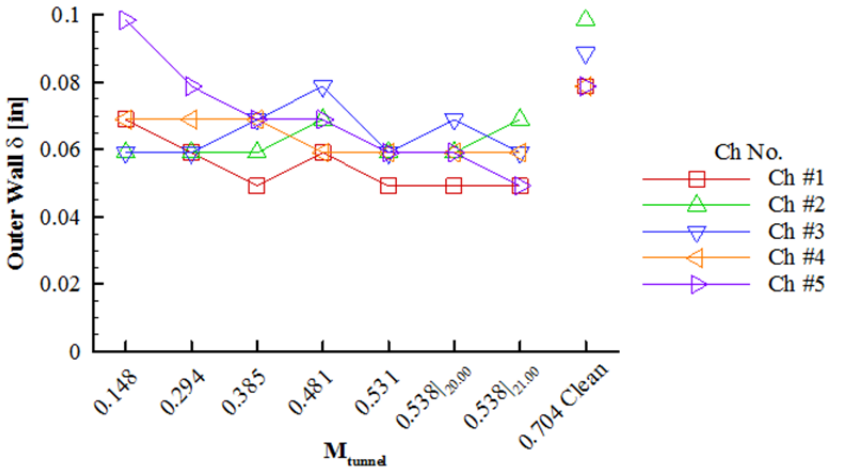

b)

Fig. 3.17. Outer wall boundary-layer thickness at the inlet plane as a function of a) channel number, and b) M_{tunnel}.

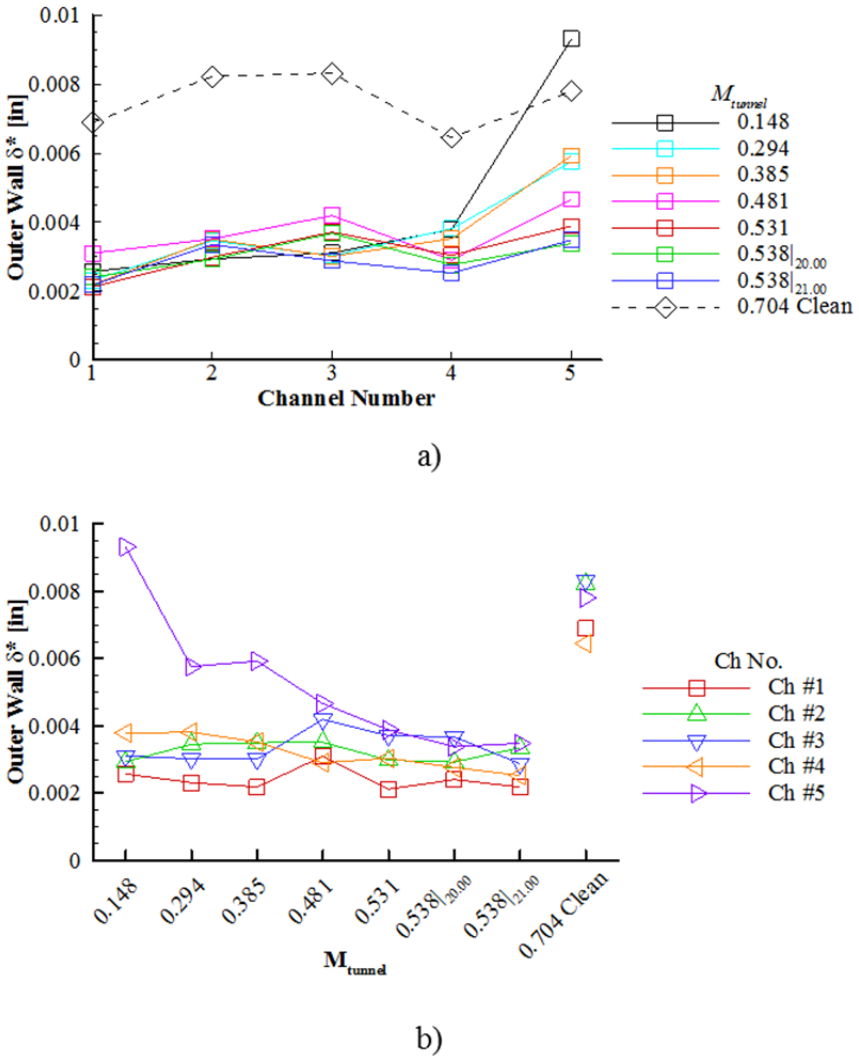

Fig. 3.18. Outer wall displacement thickness at the inlet plane as a function of a) channel number, and b) M_{tunnel}.

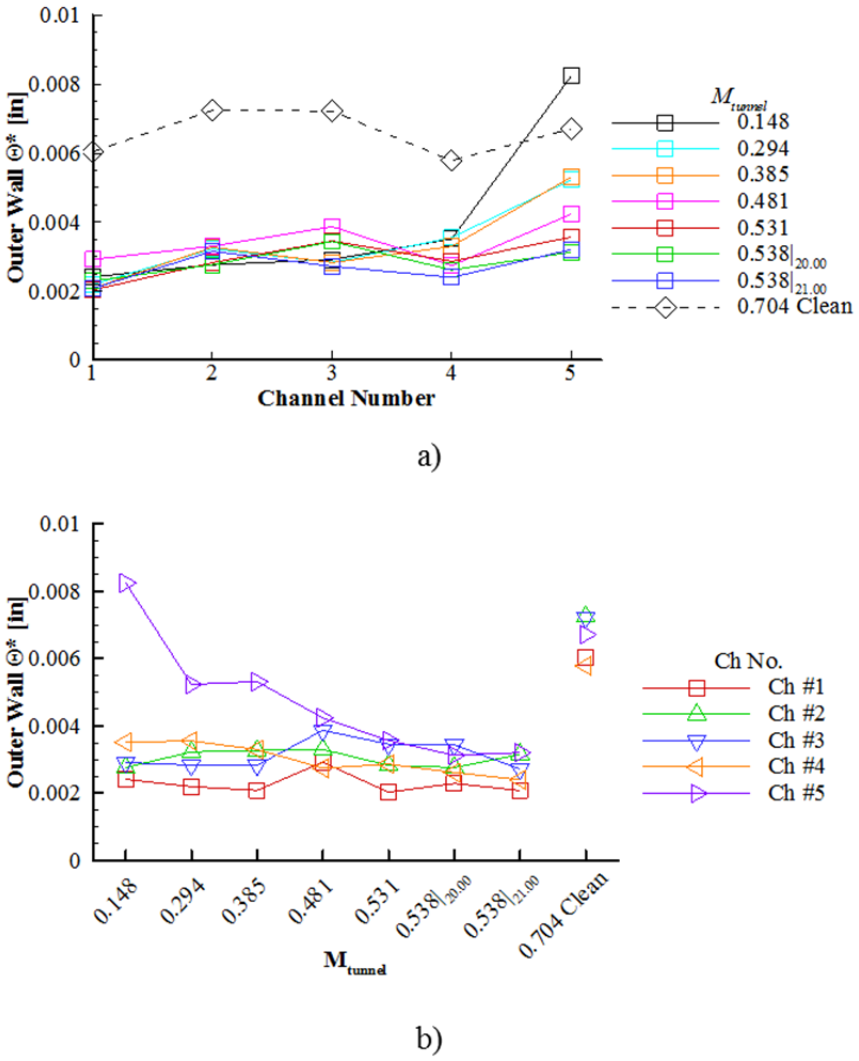

Fig. 3.19. Outer wall momentum thickness at the inlet plane as a function of a) channel number, and b) M_{tunnel}.

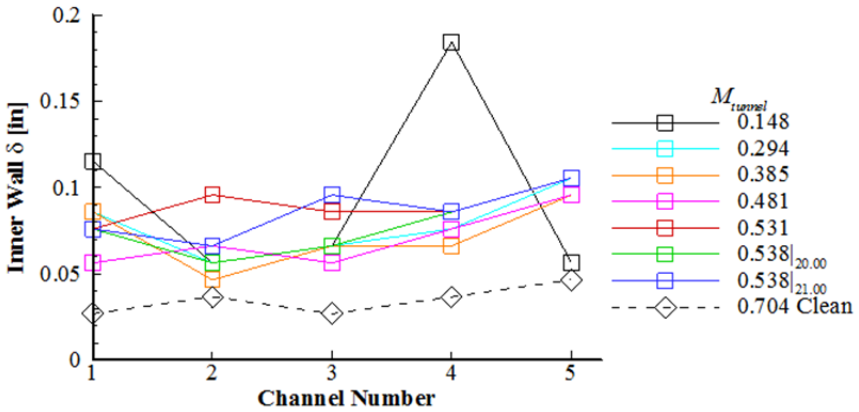

a)

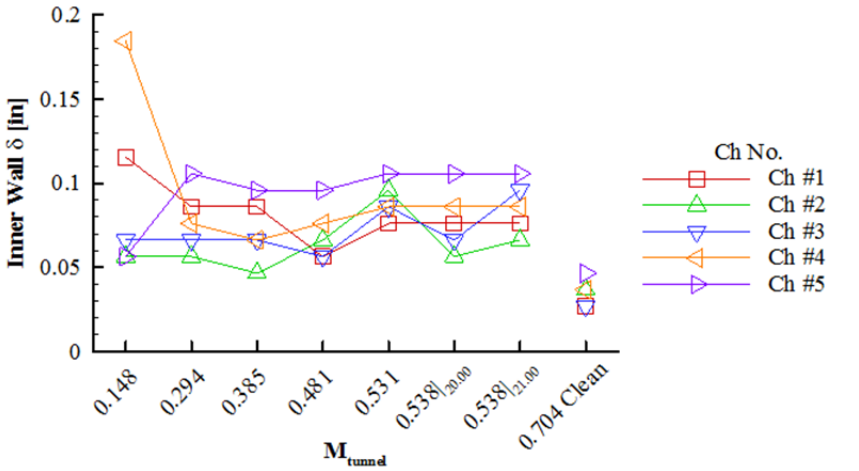

b)

Fig. 3.20. Inner wall boundary-layer thickness at the inlet plane as a function of a) channel number, and b) M_{tunnel}.

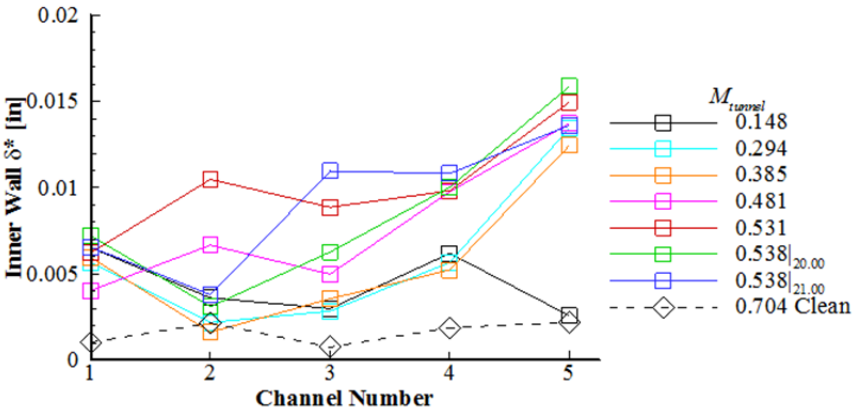

a)

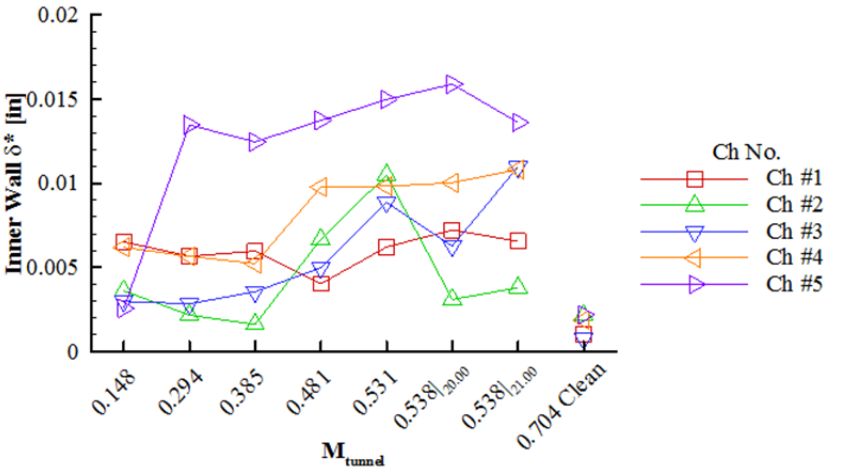

b)

Fig. 3.21. Inner wall displacement thickness at the inlet plane as a function of a) channel number, and b) M_{tunnel}.

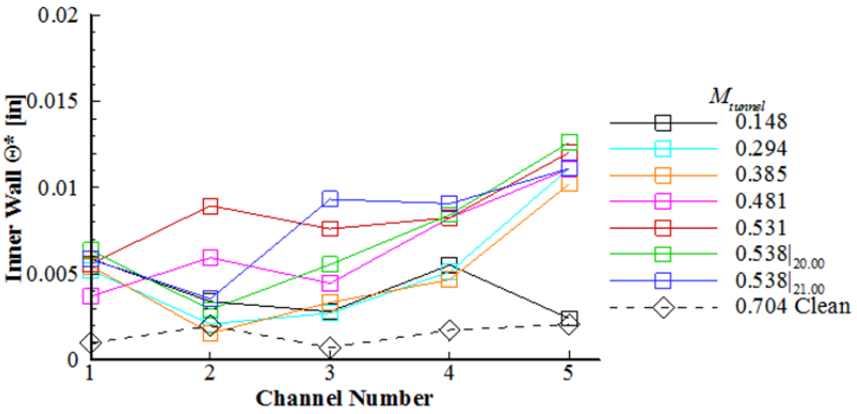

a)

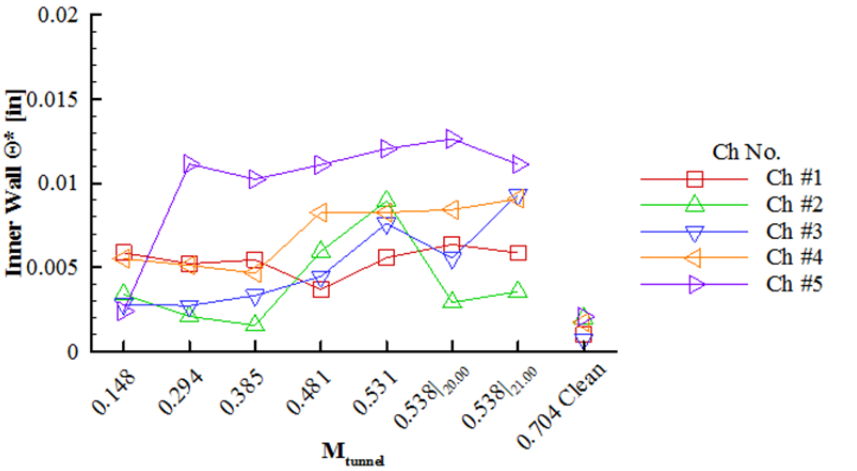

b)

Fig. 3.22. Inner wall momentum thickness at the inlet plane as a function of a) channel number, and b) M_{tunnel}.

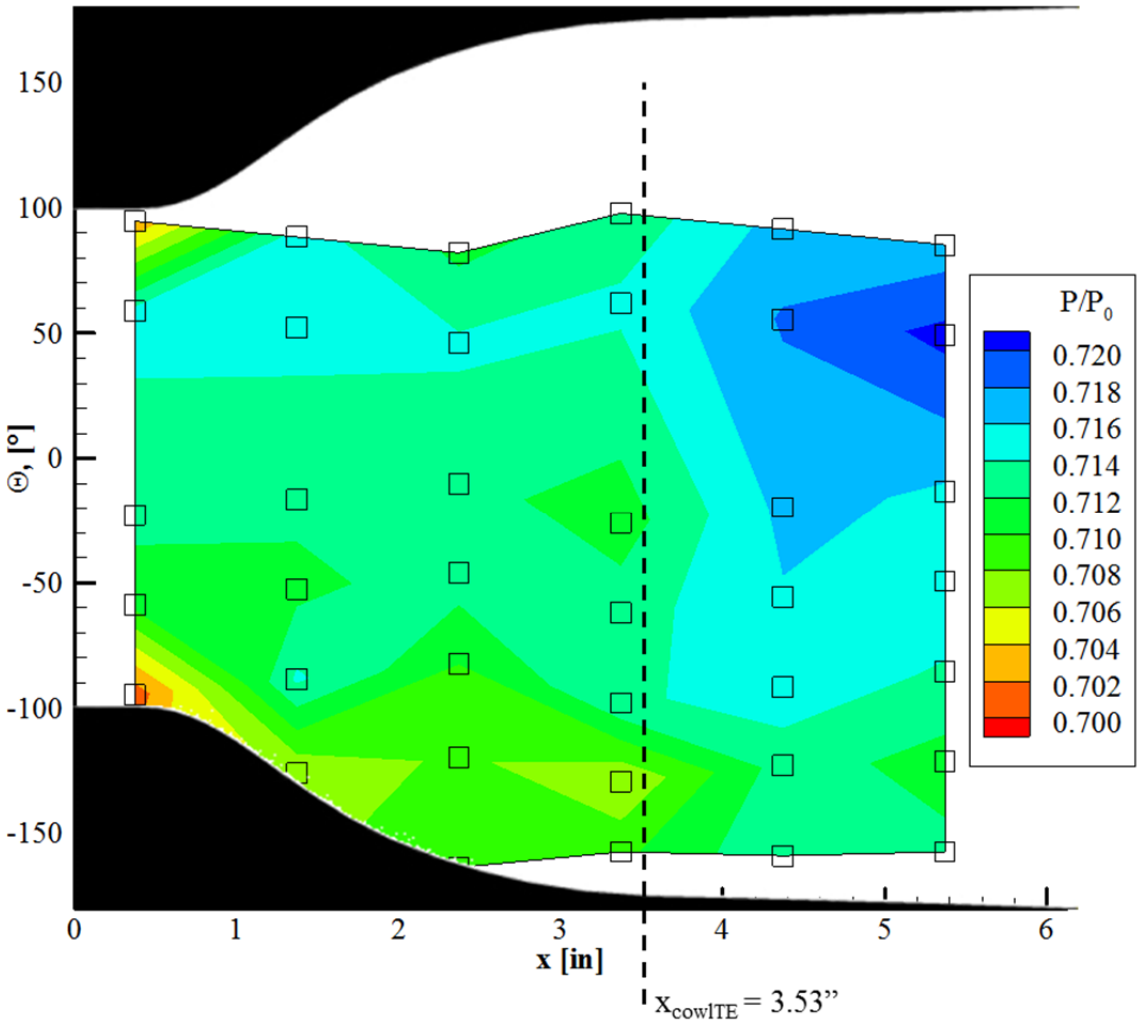

Fig. 3.23. A representative contour plot of the clean model surface static pressure data at M_{tunnel} = 0.704 (normalized by inlet plane total pressure, P_0). Open squares designate model surface static pressure taps.

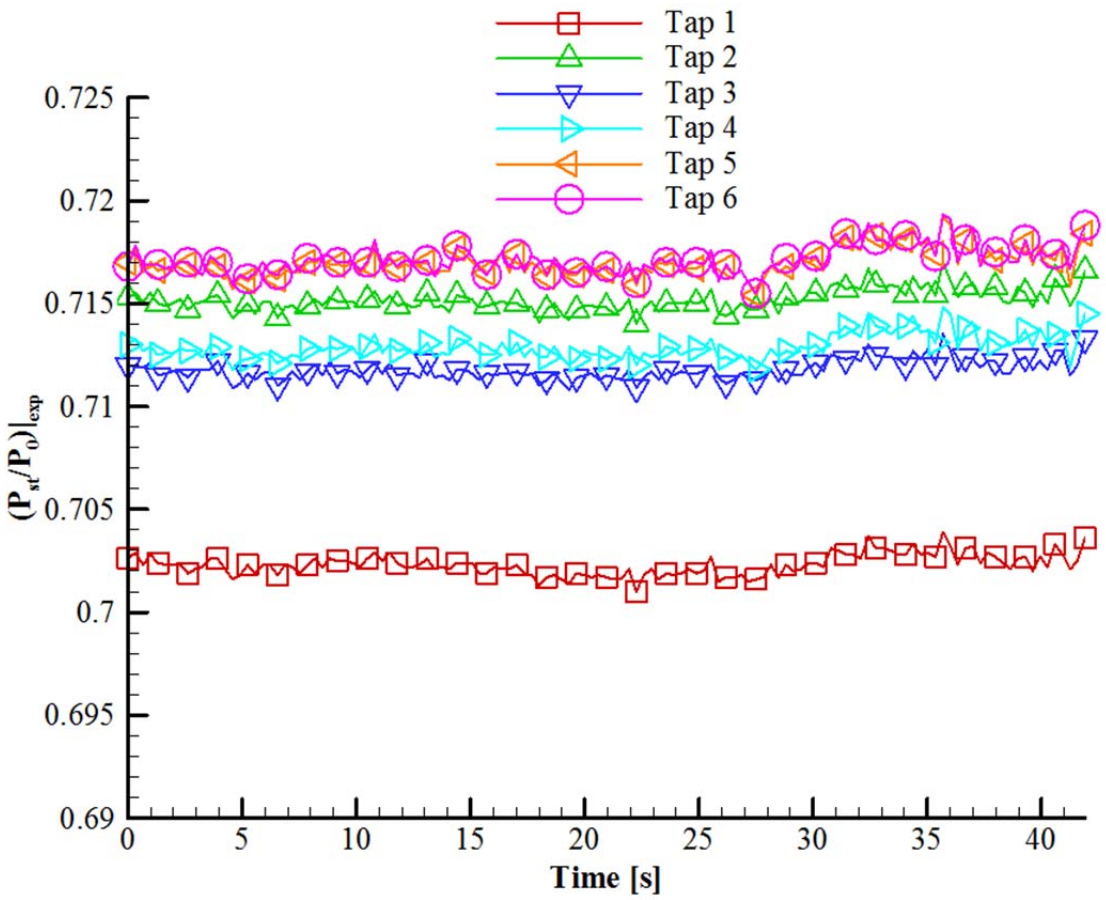

Fig. 3.24. Time traces of $(P_{st}/P_0)|_{exp}$ measured along one row of taps on the clean model. Presented data are average values for five independent, identical runs. Taps are numbered according to streamwise position.

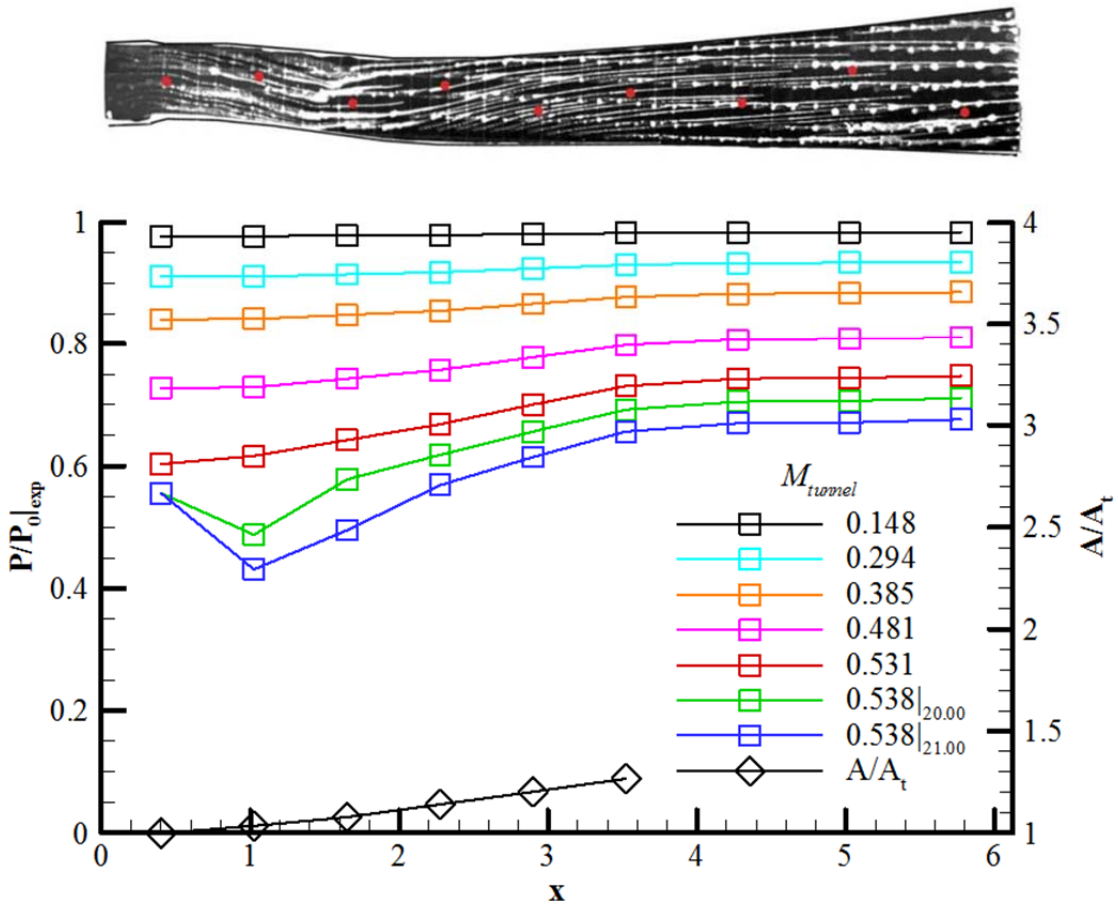

Fig. 3.25. Normalized experimental pressure ratio within Ch #1, 10.1° from top-center as a function of axial position, for all tested operating conditions.

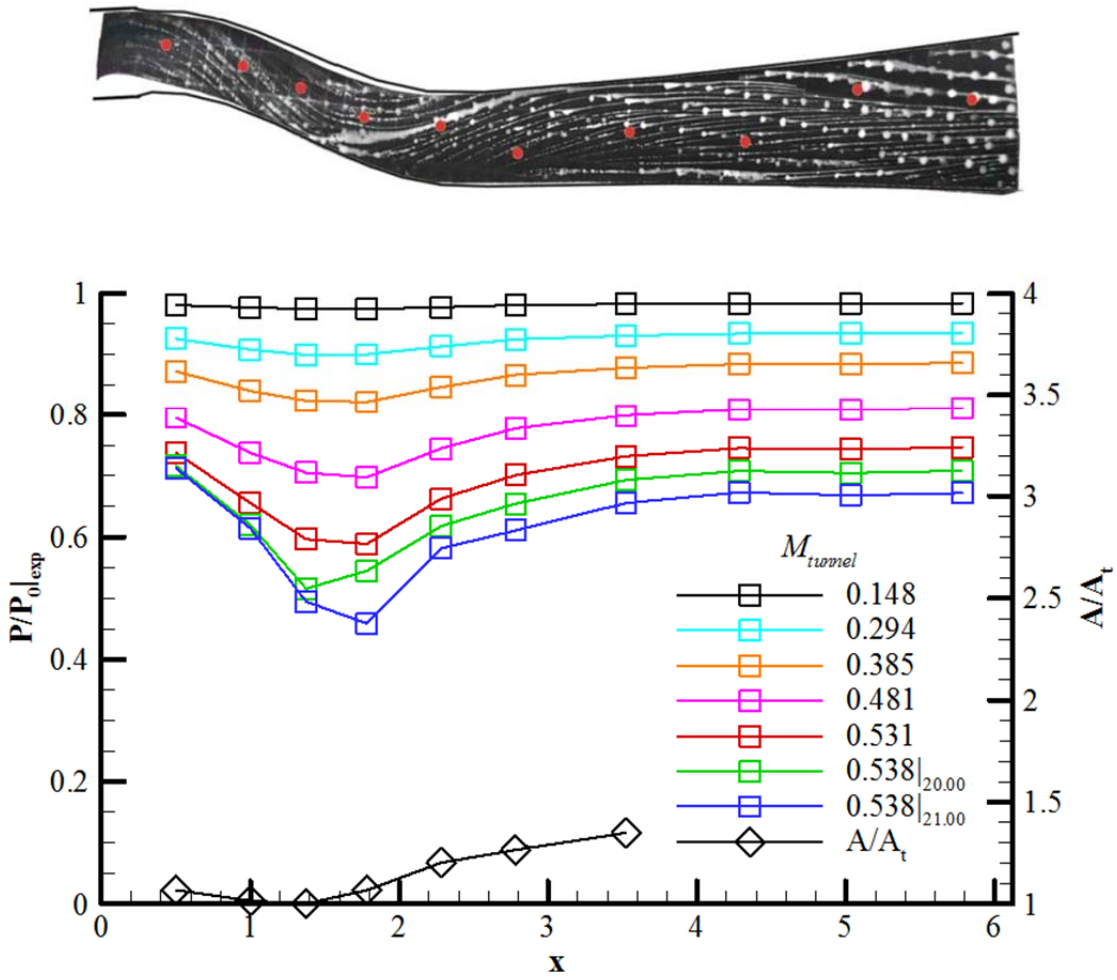

Fig. 3.26. Normalized experimental pressure ratio within Ch #2, 30.3° from top-center as a function of axial position, for all tested operating conditions.

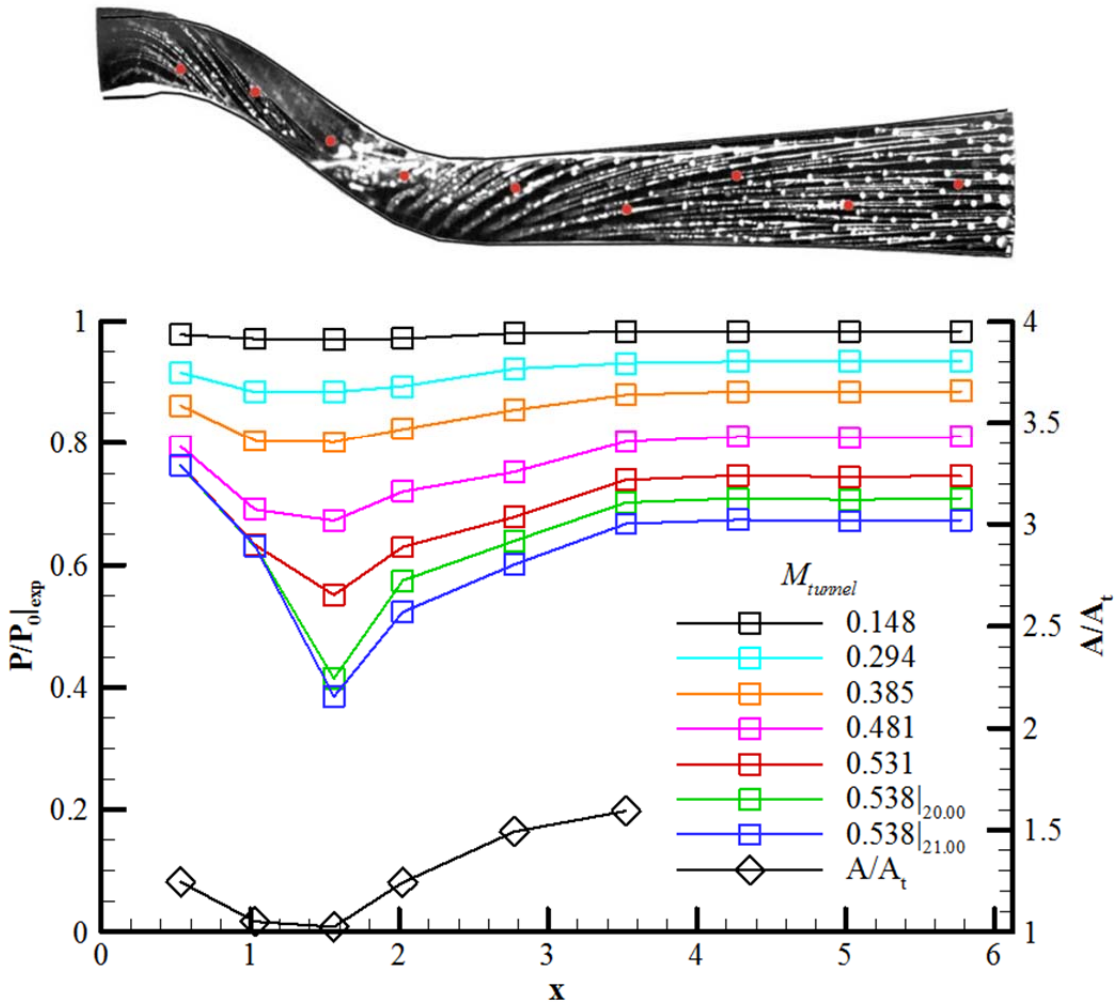

Fig. 3.27. Normalized experimental pressure ratio within Ch #3, 50.4° from top-center as a function of axial position, for all tested operating conditions.

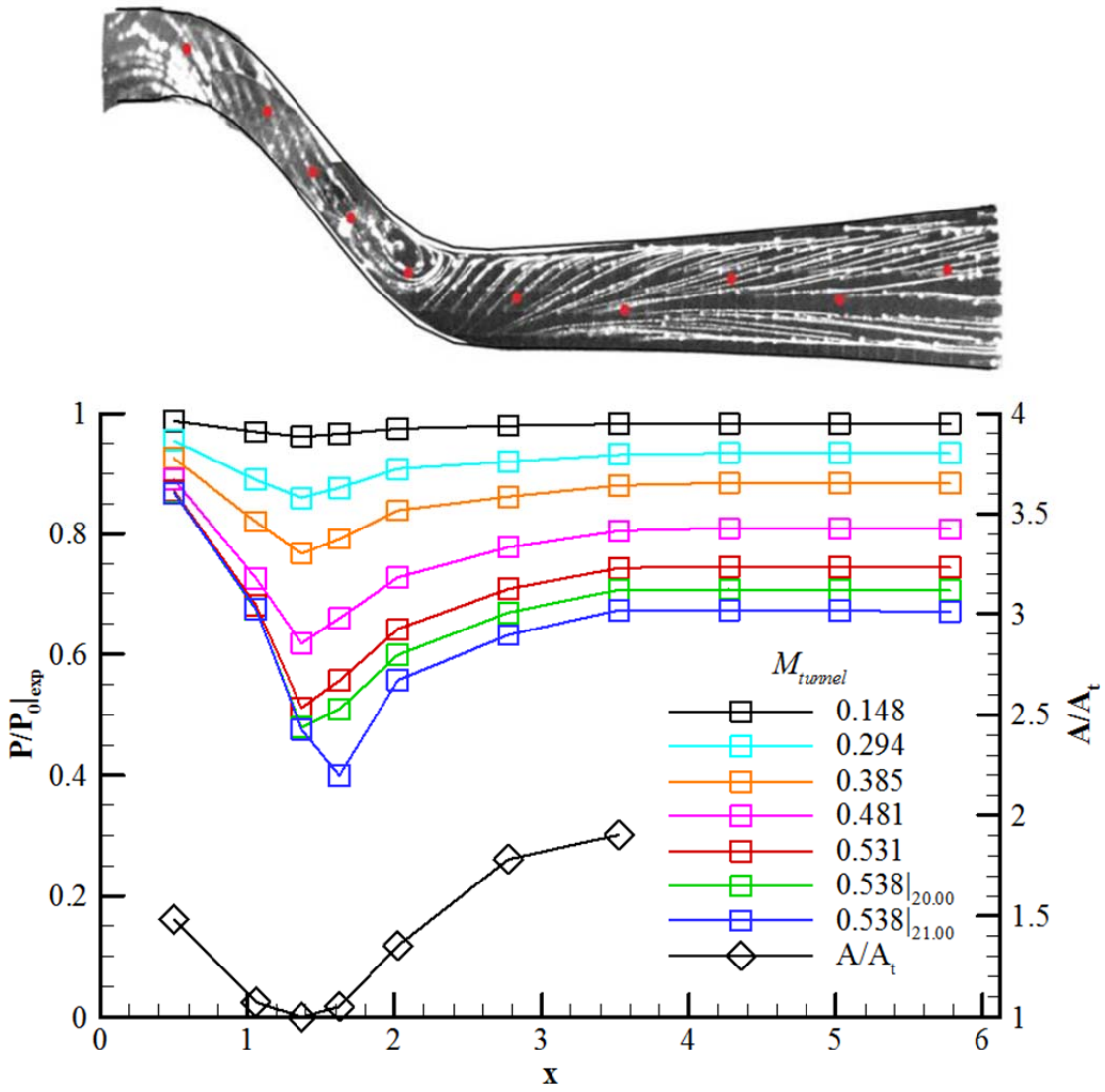

Fig. 3.28. Normalized experimental pressure ratio within Ch #4, 70.6° from top-center as a function of axial position, for all tested operating conditions.

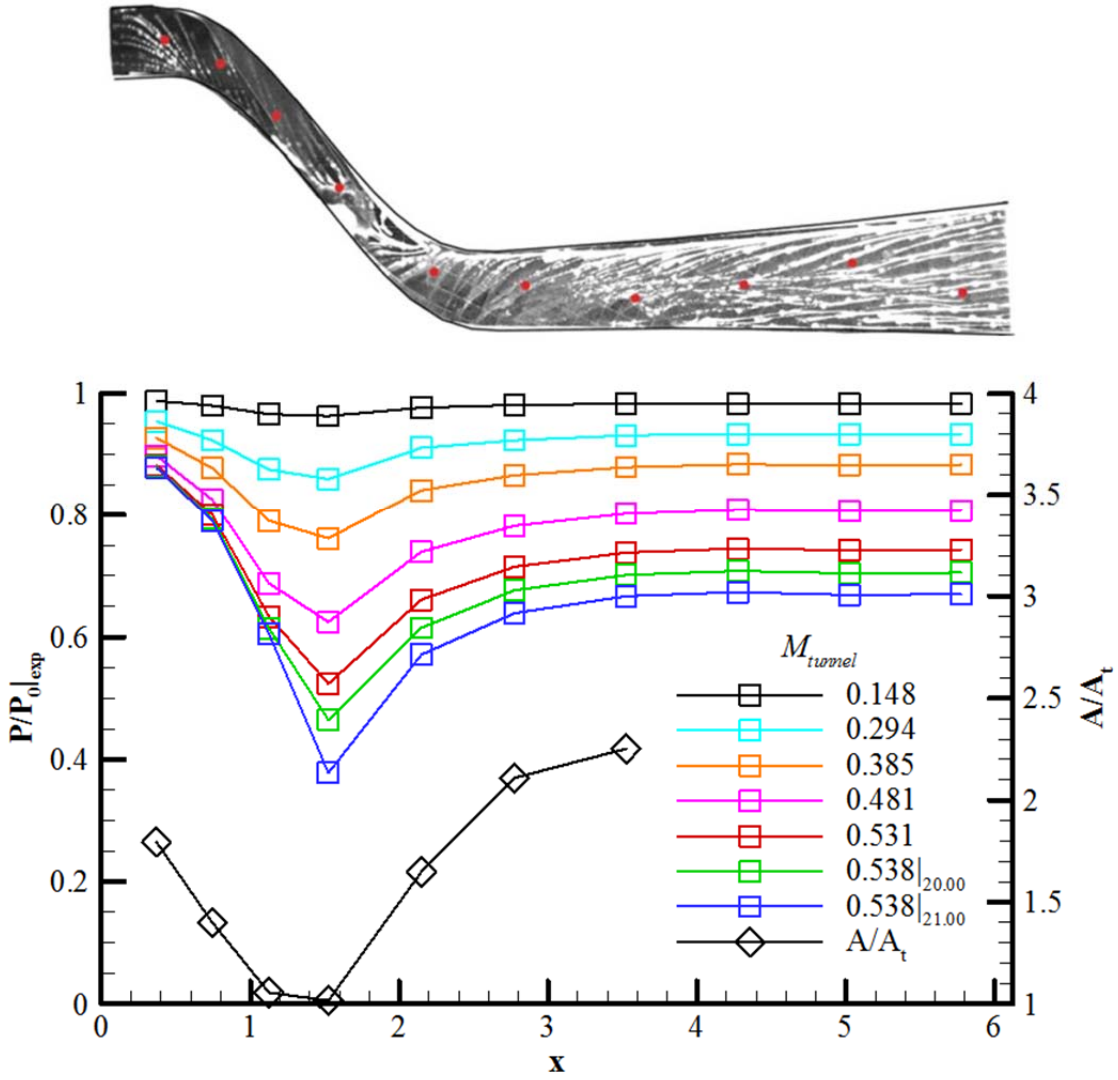

Fig. 3.29. Normalized experimental pressure ratio within Ch #5, 90° from top-center as a function of axial position, for all tested operating conditions.

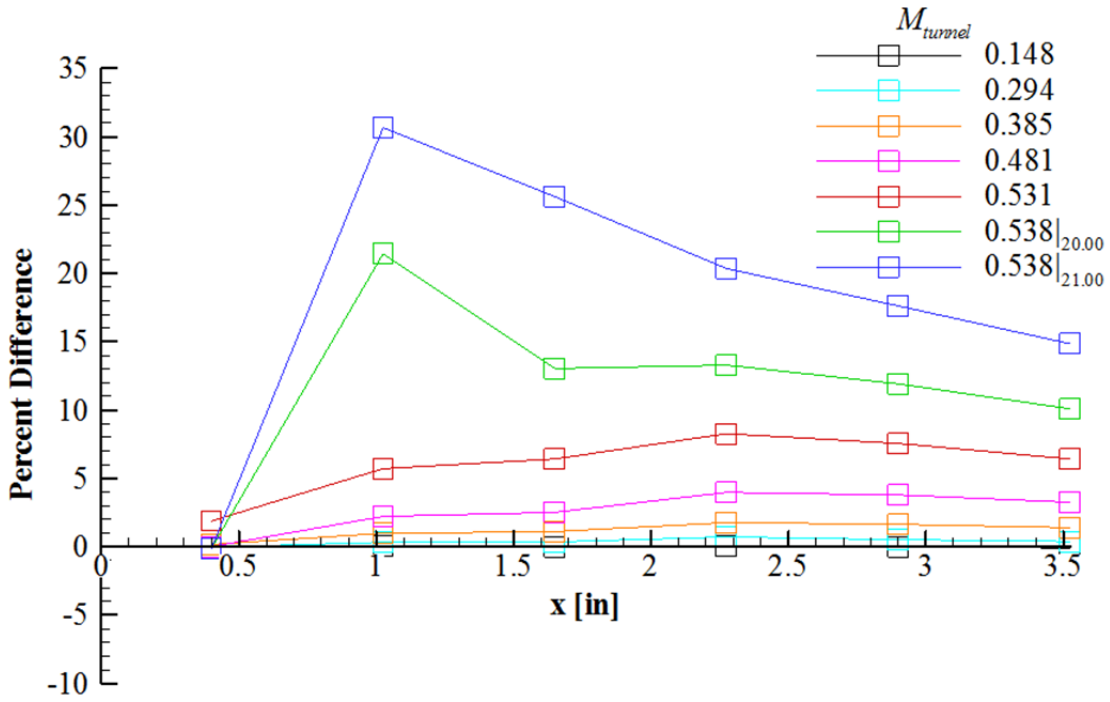

Fig. 3.30. Percent difference between experimental and isentropic pressure ratios within Ch #1, 10.1° from top-center.

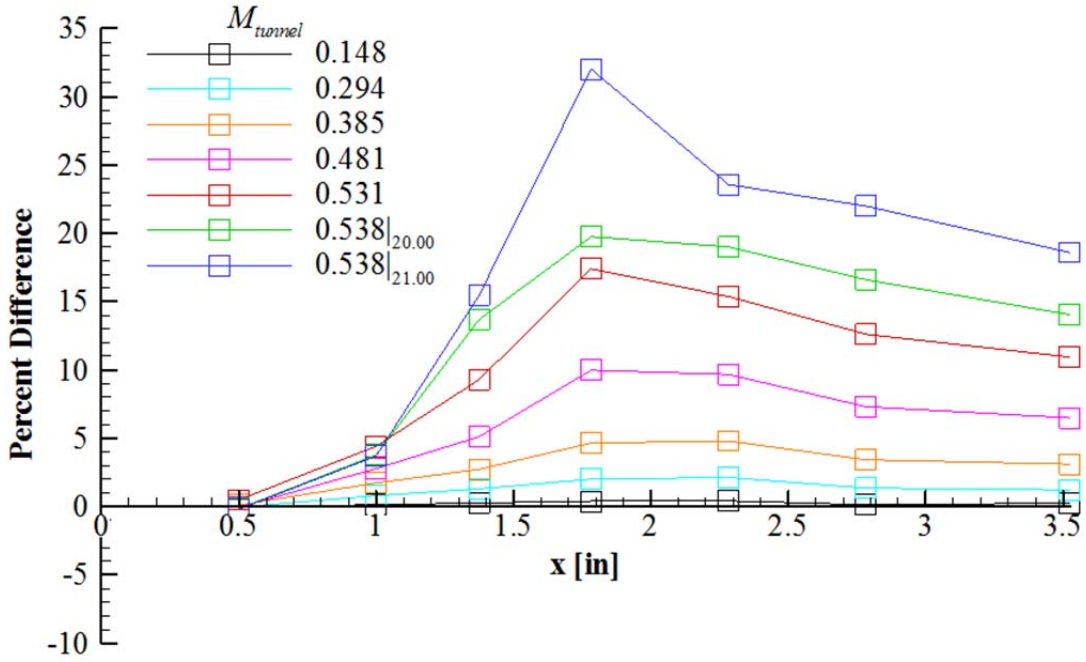

Fig. 3.31. Percent difference between experimental and isentropic pressure ratios within Ch #2, 30.3° from top-center.

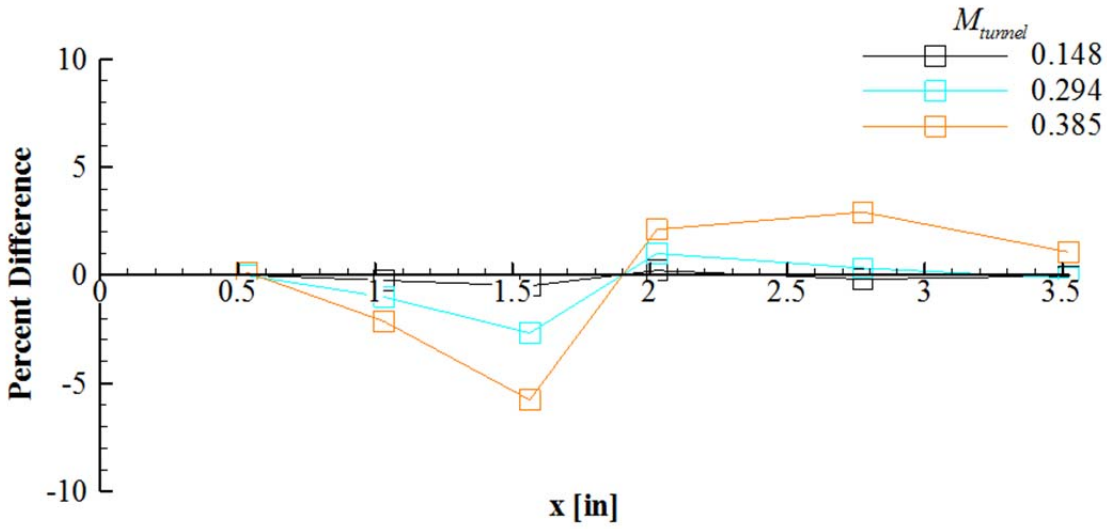

Fig. 3.32. Percent difference between experimental and isentropic pressure ratios within Ch #3, 50.4° from top-center.

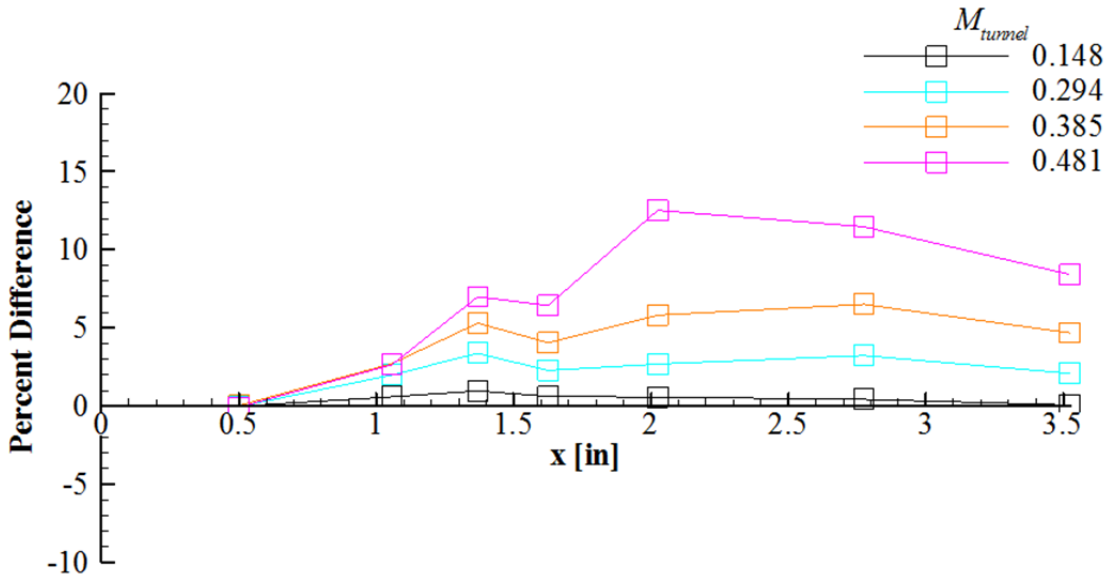

Fig. 3.33. Percent difference between experimental and isentropic pressure ratios within Ch #4, 70.6° from top-center.

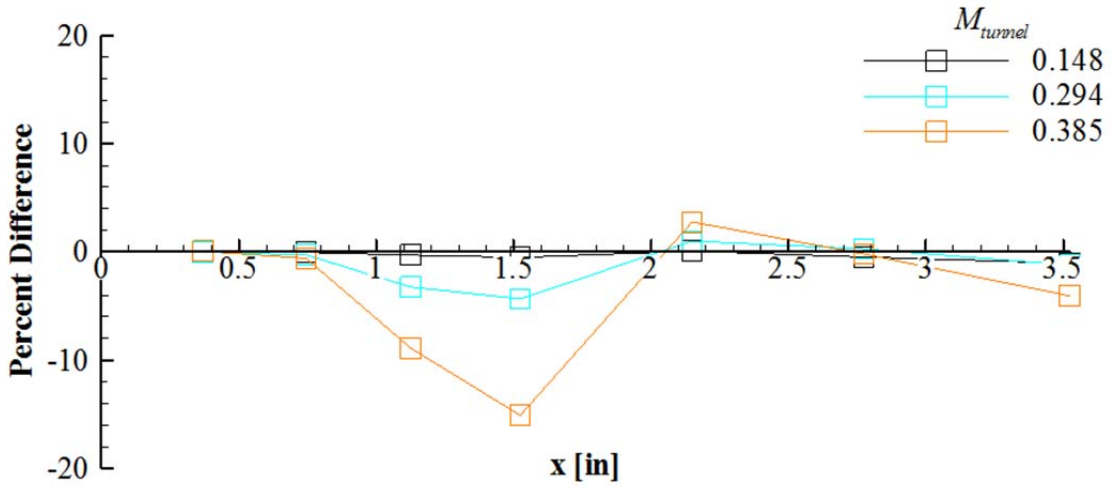

Fig. 3.34. Percent difference between experimental and isentropic pressure ratios within Ch #5, 90° from top-center.

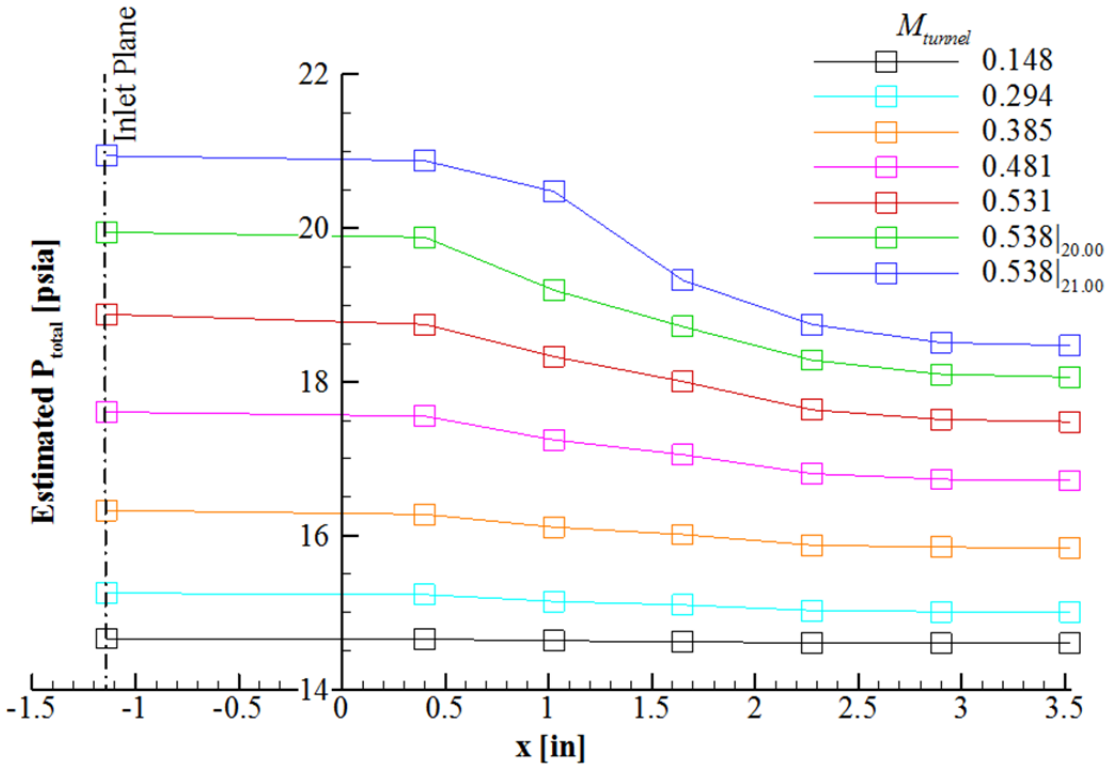

Fig. 3.35. The estimated total pressure (psia) at each static pressure tap within Ch #1 for all tested operating conditions.

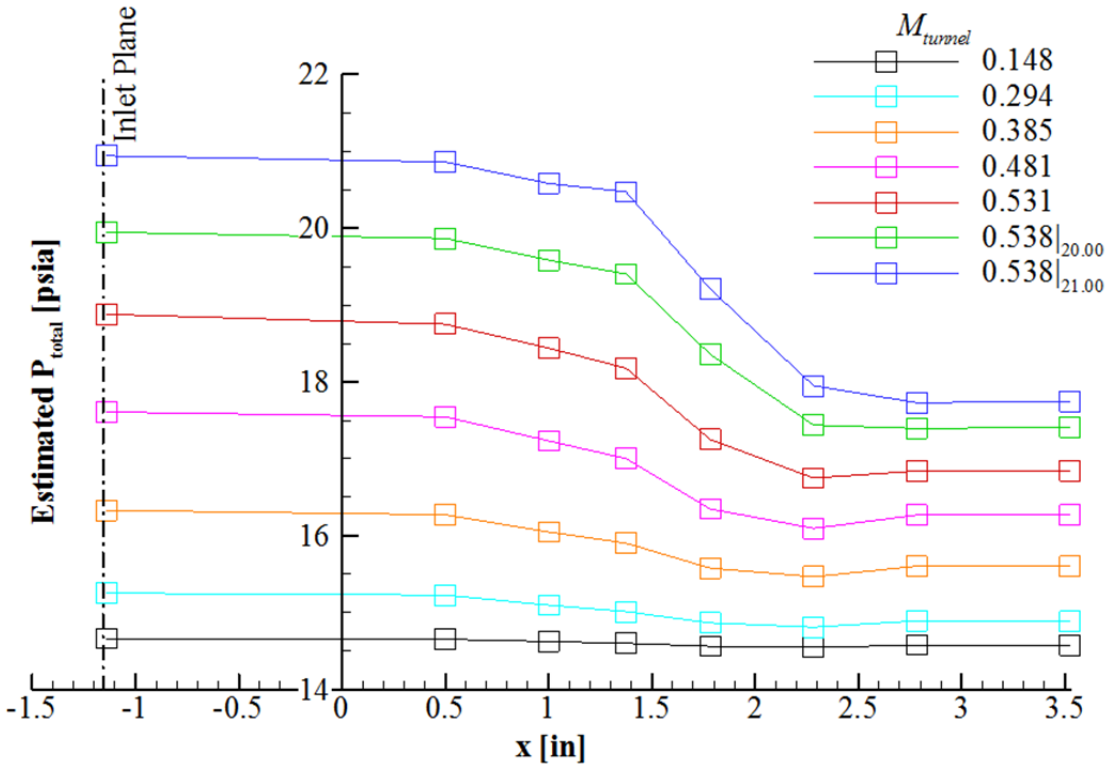

Fig. 3.36. The estimated total pressure (psia) at each static pressure tap within Ch #2 for all tested operating conditions.

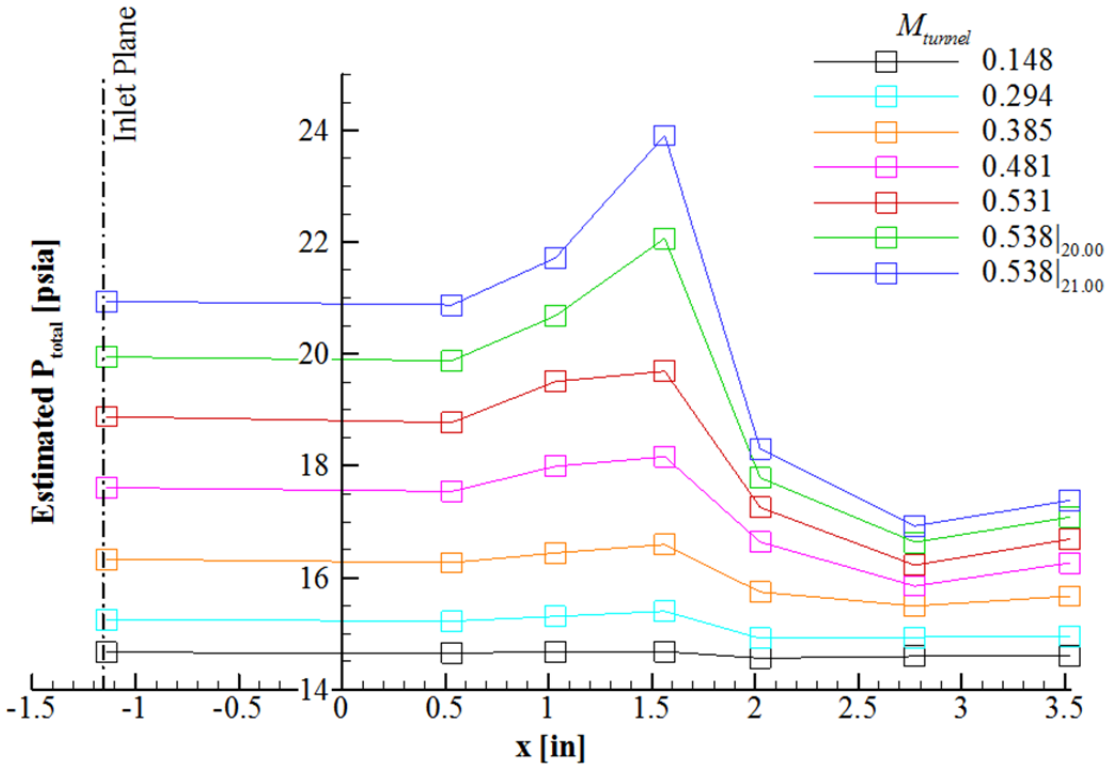

Fig. 3.37. The estimated total pressure (psia) at each static pressure tap within Ch #3 for all tested operating conditions.

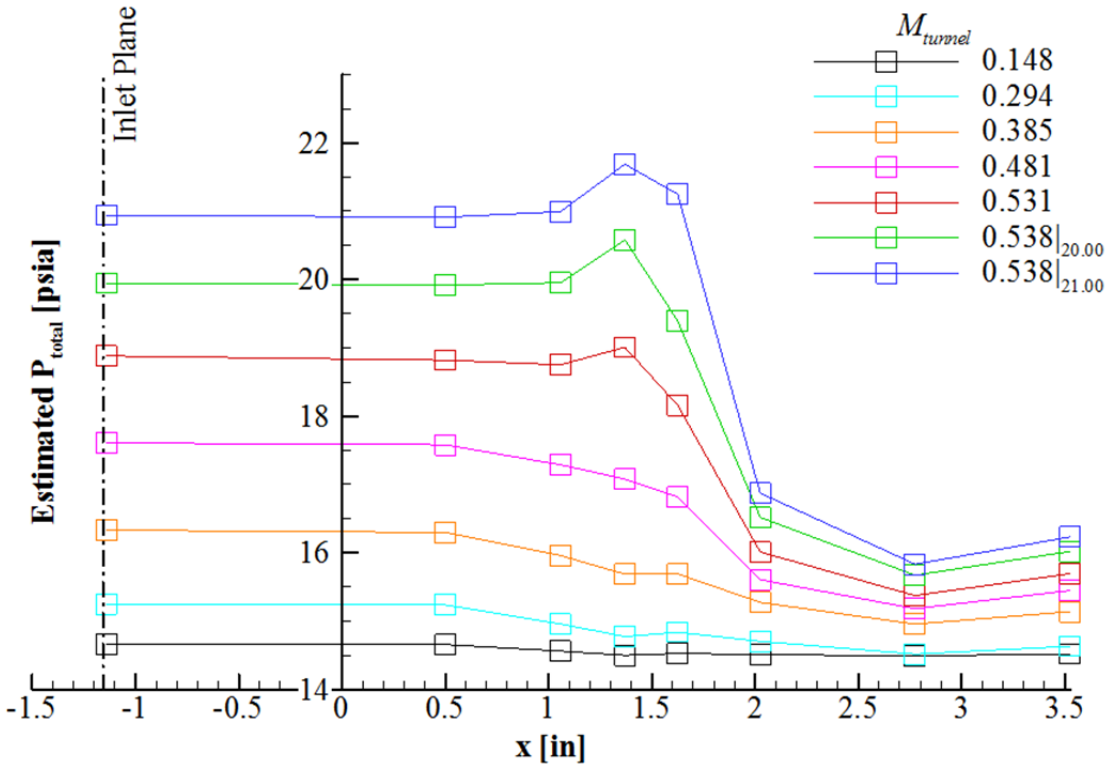

Fig. 3.38. The estimated total pressure (psia) at each static pressure tap within Ch #4 for all tested operating conditions.

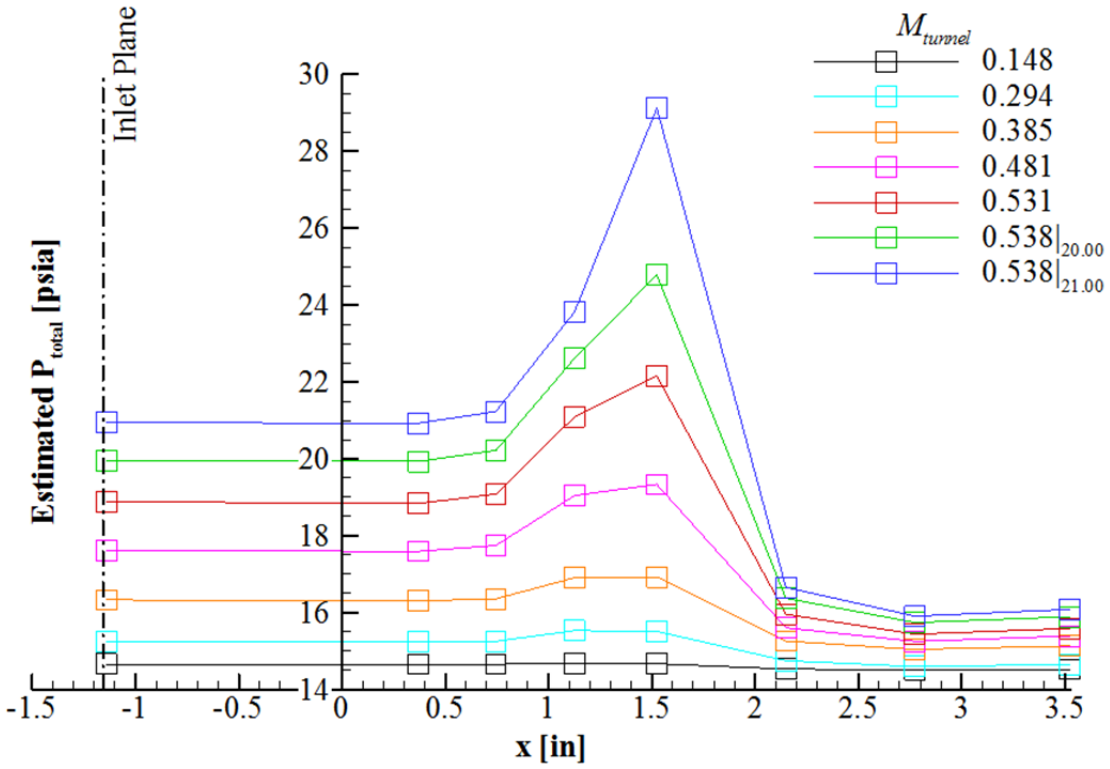

Fig. 3.39. The estimated total pressure (psia) at each static pressure tap within Ch #5 for all tested operating conditions.

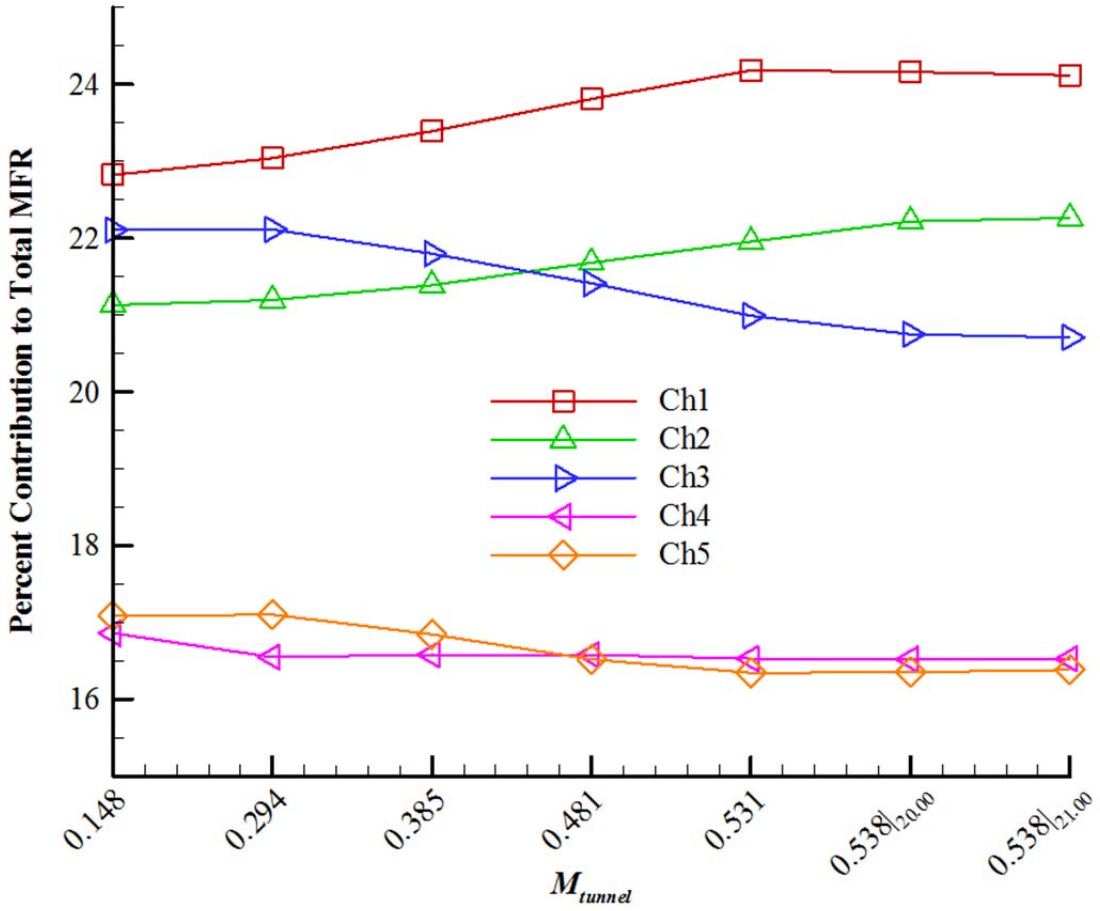

Fig. 3.40. Channel-wise percent contribution to total mass flow rate for various prescribed experimental operating conditions.

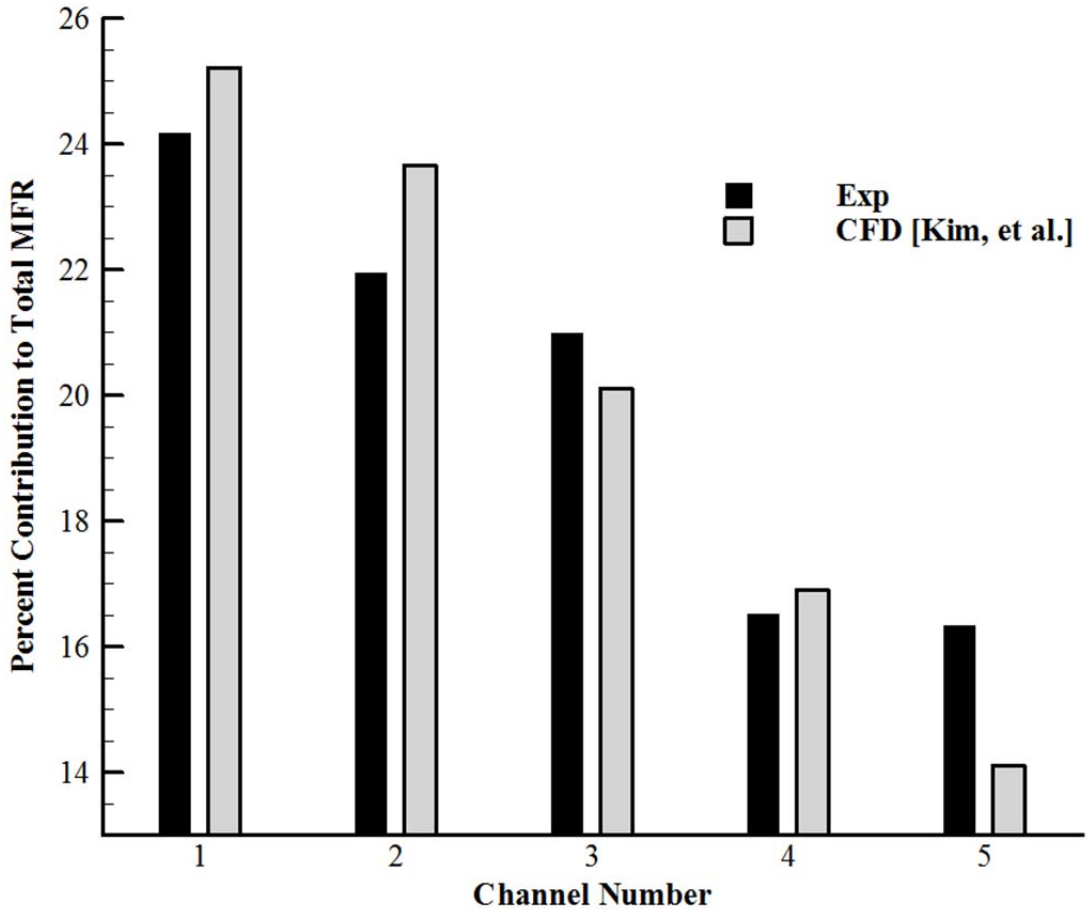

Fig. 3.41. Comparison on the percent contribution to total mass flow rate on a per channel basis between experimental (M_{tunnel} = 0.531) and CFD study[30] (freestream Mach number of 1.7) results. Comparison between study operating conditions is difficult because the two studies utilize different boundary conditions from which to reference.

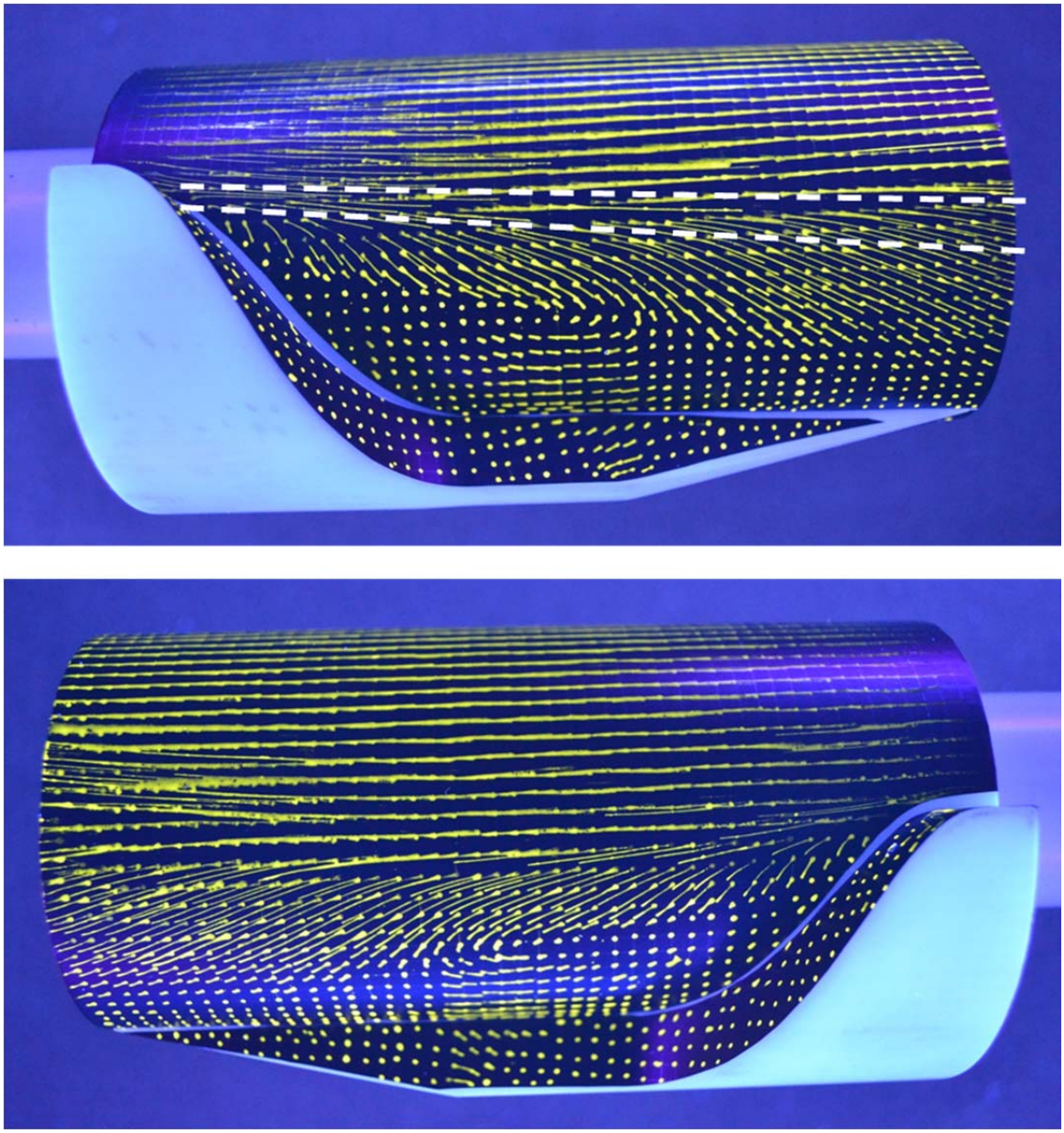

Fig. 3.42. Clean model fluorescent surface oil flow visualization at M_{tunnel} = 0.704. Views from opposite sides of the model show great symmetry. The dashed lines indicate the approximate upper and lower boundaries of the separation shear layer.

Fig. 3.43. Clean model lampblack surface oil flow visualization at M_{tunnel} = 0.704. Model surface is unwrapped, showing clear model symmetry.

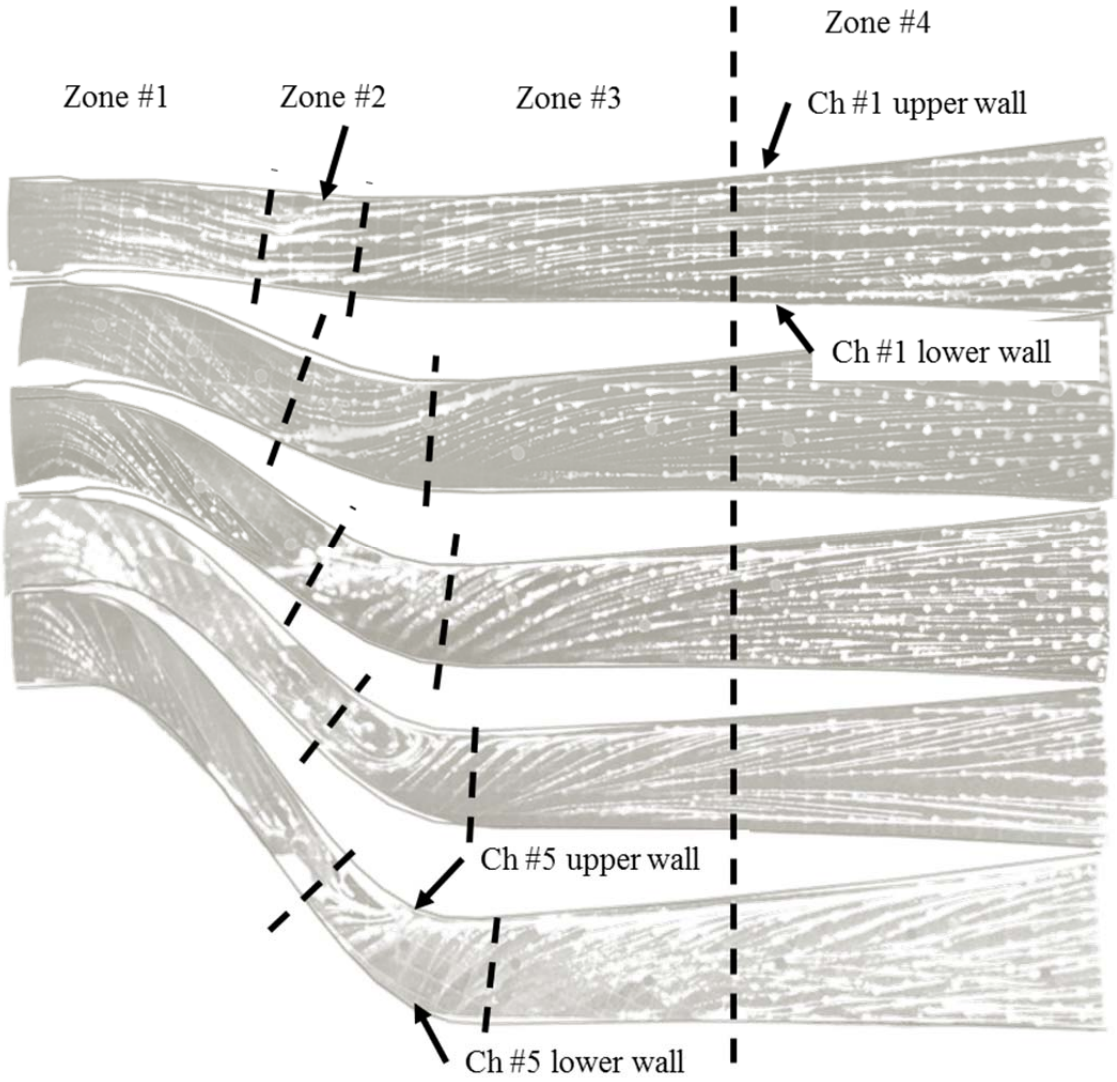

Fig. 3.44. The four zones employed in the description of the vaned model surface oil flow visualization and wall naming convention.

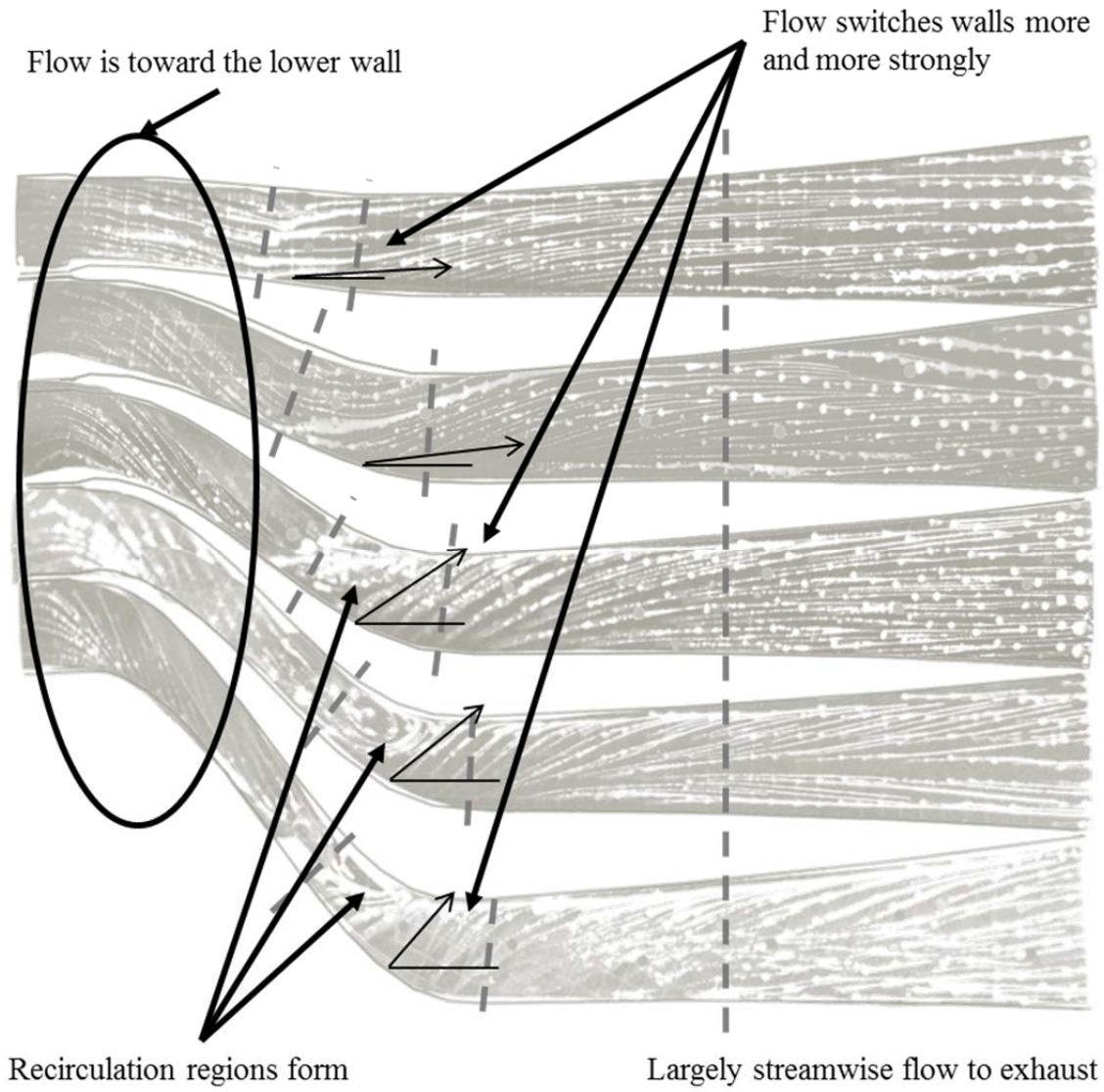

Fig. 3.45. Inner bypass surface oil flow visualization trends. Imagery is from $M_{tunnel} = 0.538|_{21.00}$ case.

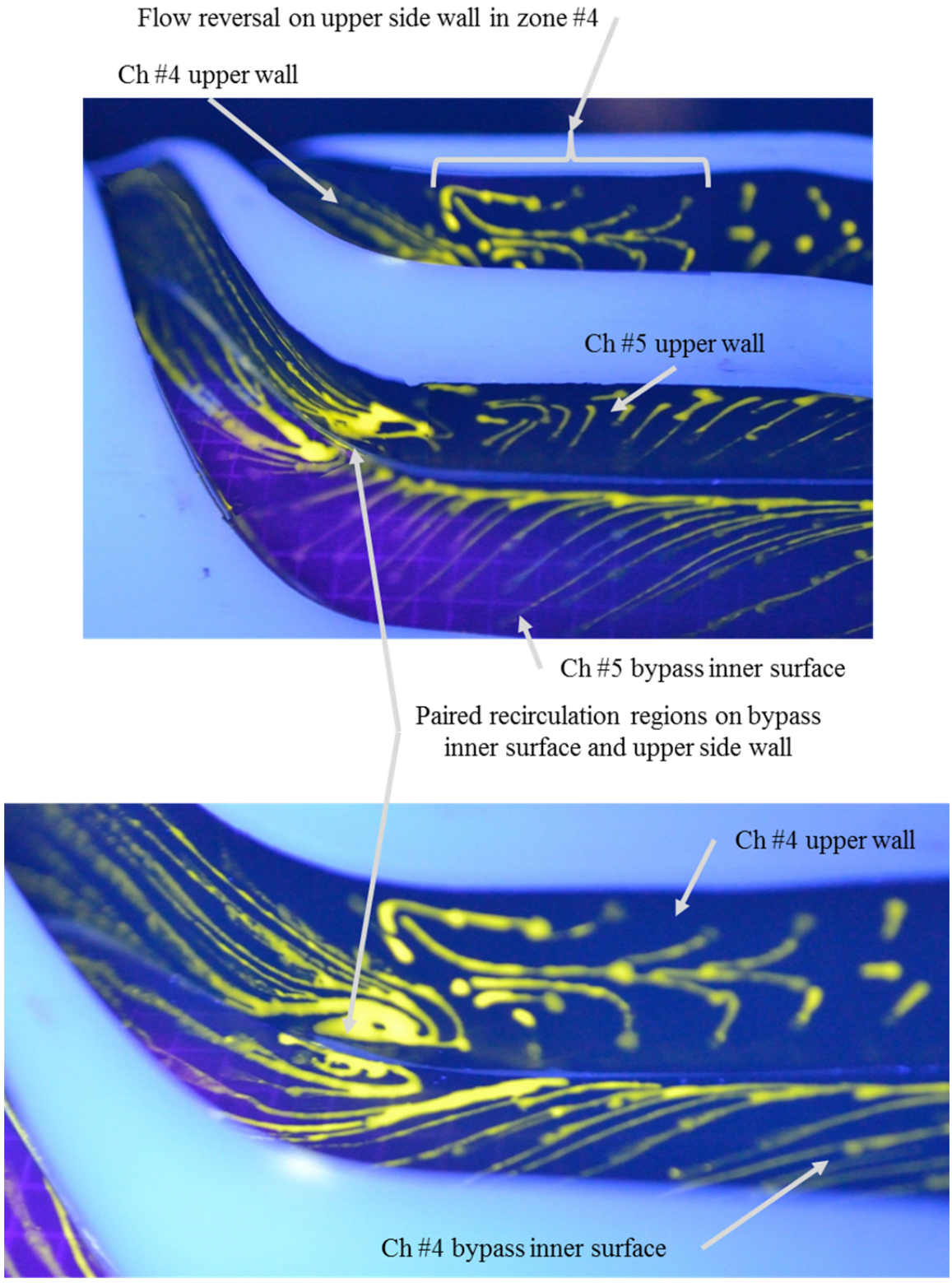

Fig. 3.46. Vaned model channel wall characteristics for $M_{tunnel} = 0.538|_{21.00}$.

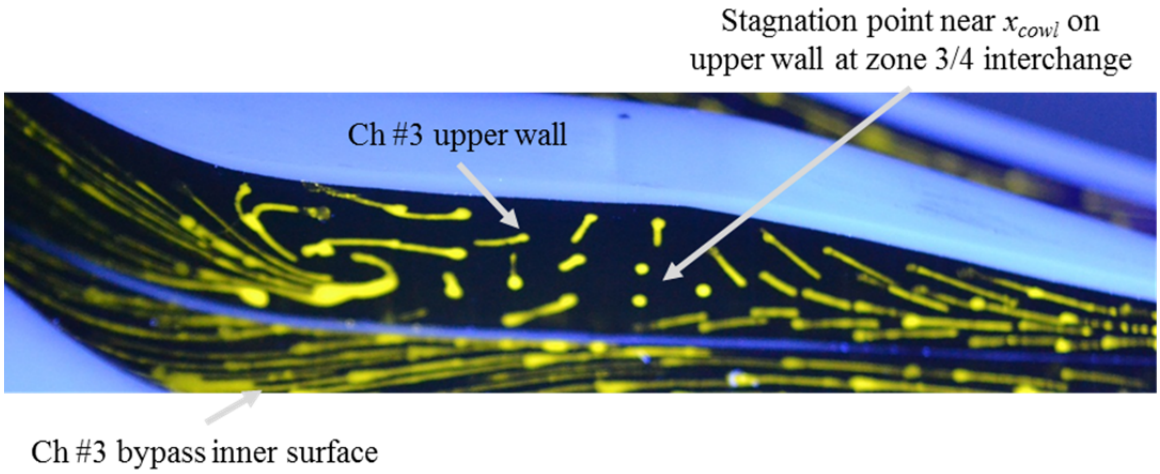

Fig. 3.47. Vaned model channel wall characteristics for $M_{tunnel} = 0.294$.

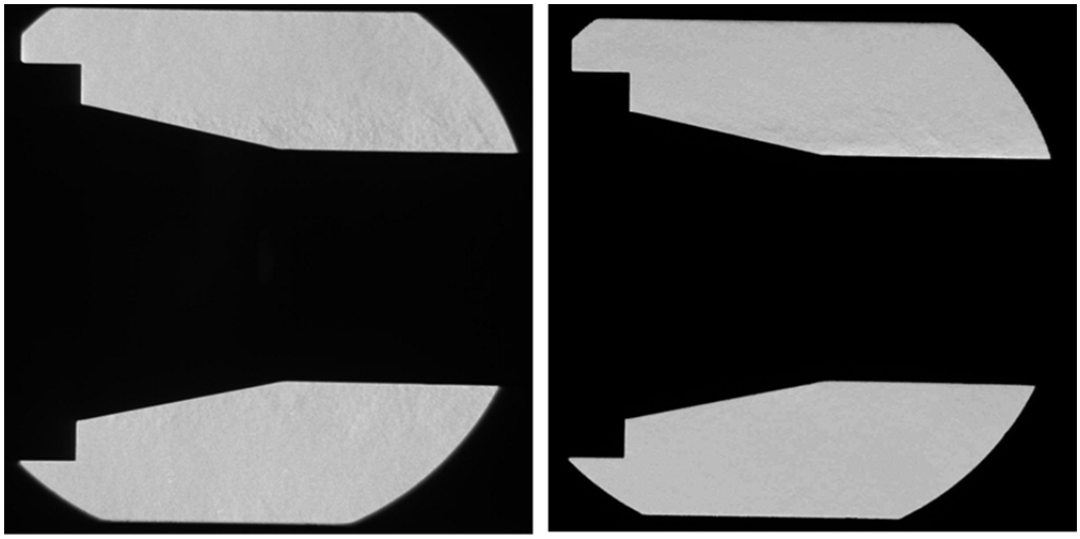

a)

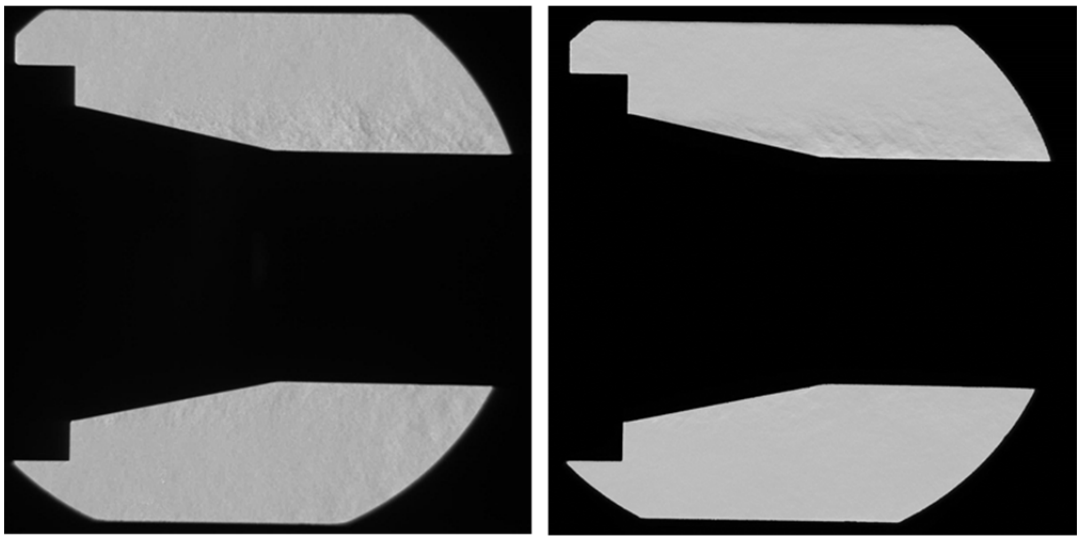

b)

Fig. 3.48. Instantaneous schlieren imagery with vertical (left column) and horizontal (right column) knife edges for a) $M_{tunnel} = 0.148$, b) $M_{tunnel} = 0.294$, c) $M_{tunnel} = 0.385$, d) $M_{tunnel} = 0.481$, e) $M_{tunnel} = 0.531$, f) $M_{tunnel} = 0.538|_{20.00}$, g) $M_{tunnel} = 0.538|_{21.00}$, and h) the clean model at $M_{tunnel} = 0.704$.

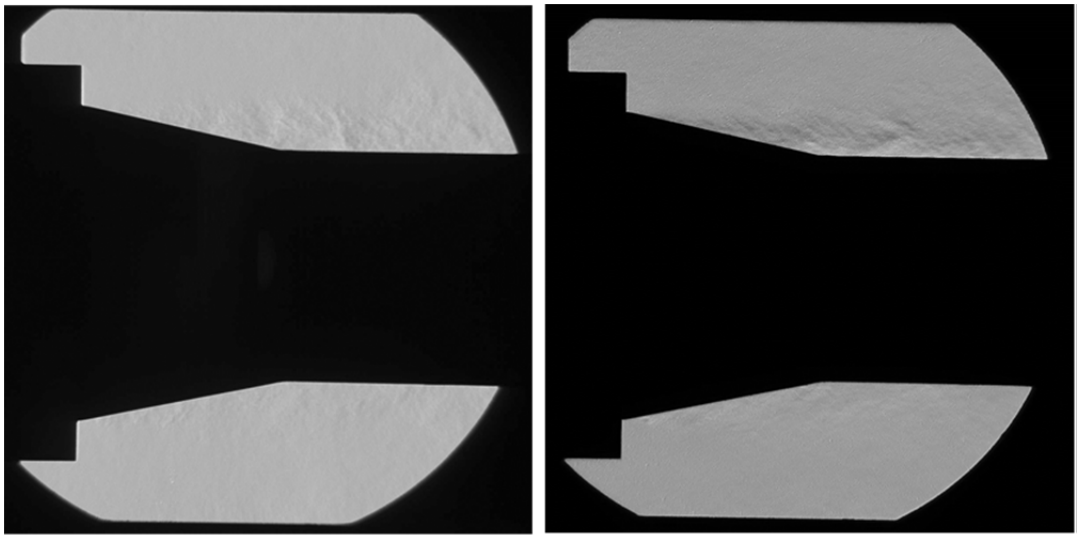

c)

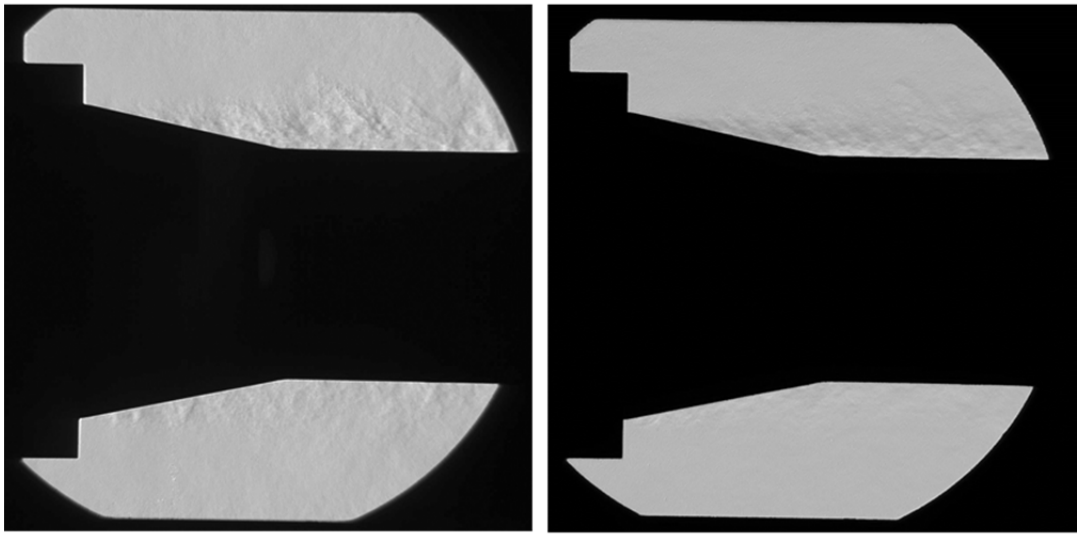

d)

Fig. 3.48 (cont.).

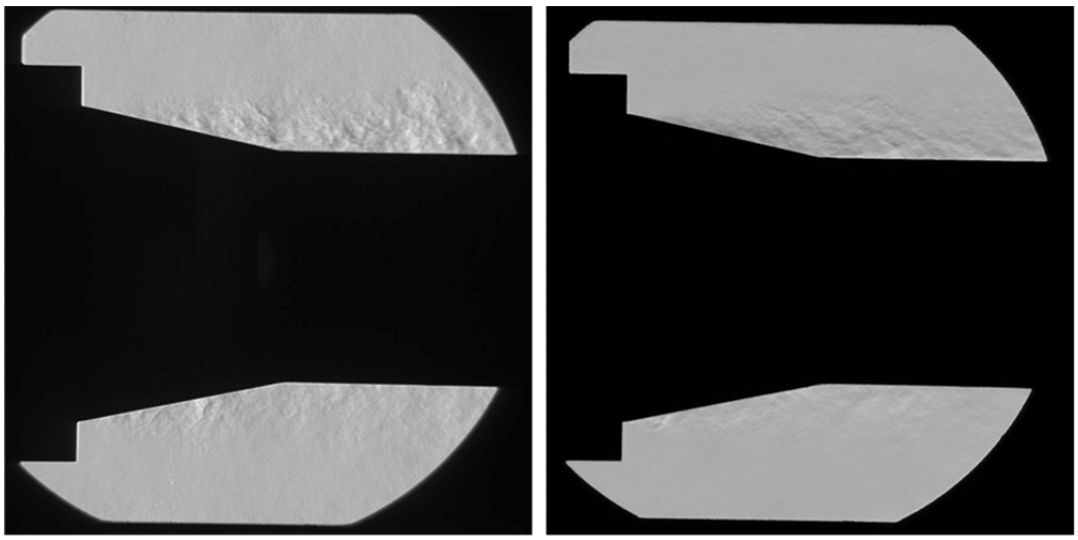

e)

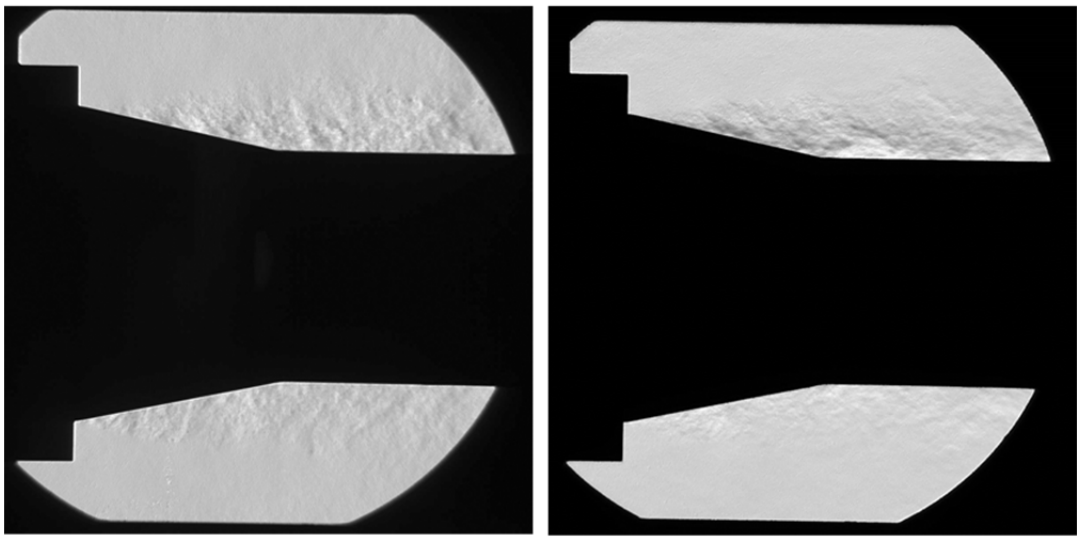

f)

Fig. 3.48 (cont.).

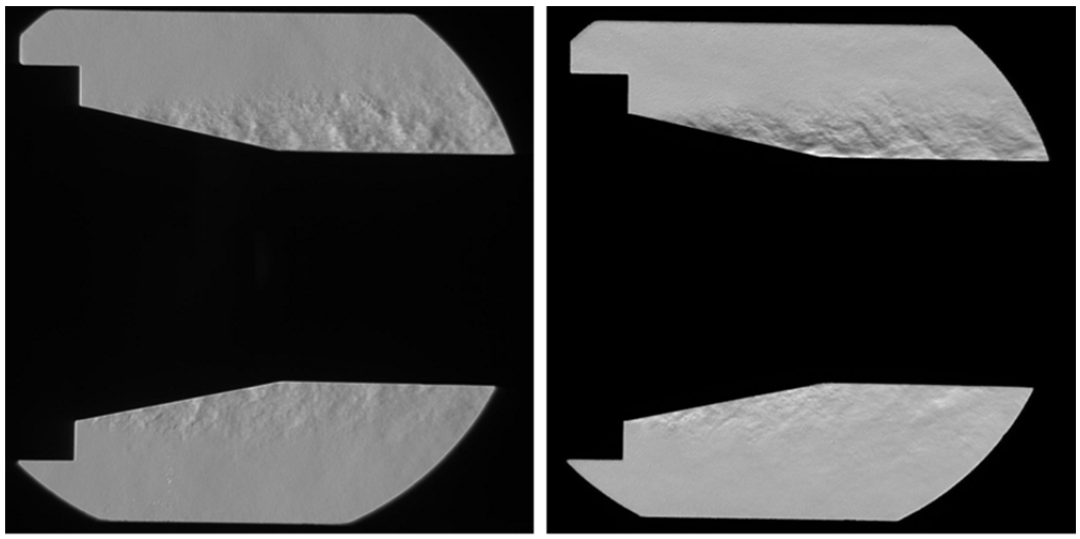

g)

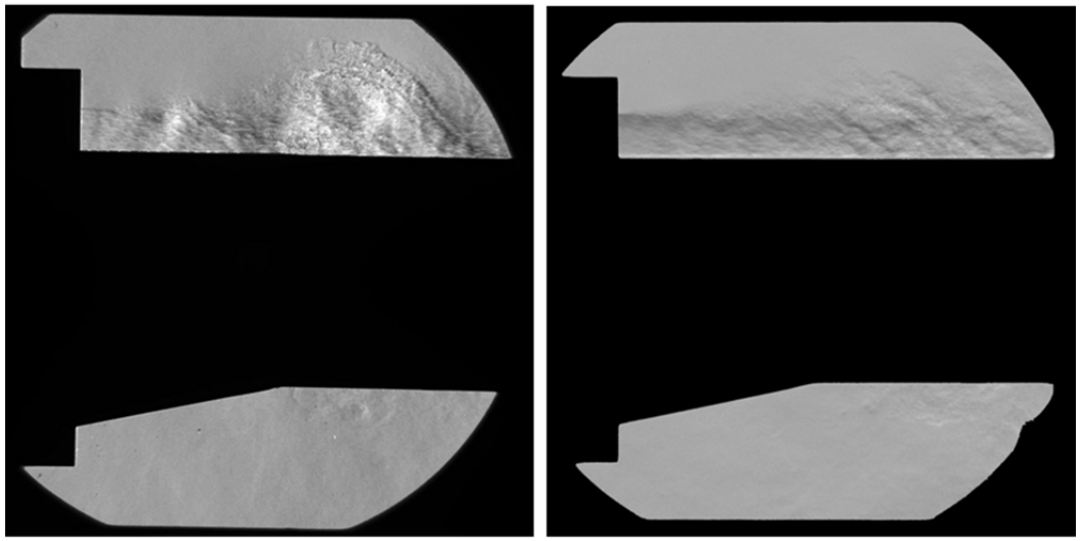

h)

Fig. 3.48 (cont.).

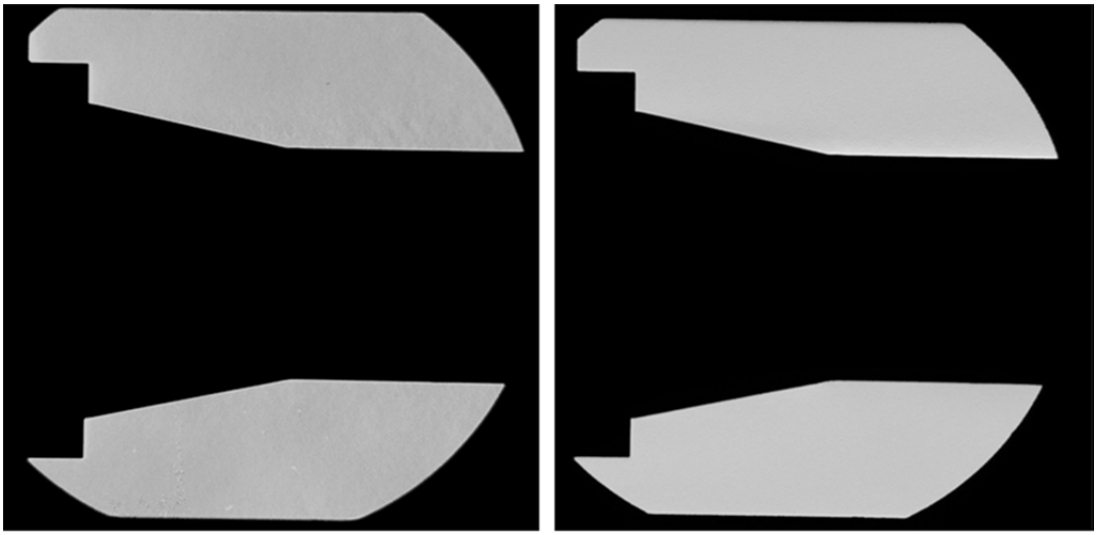

a)

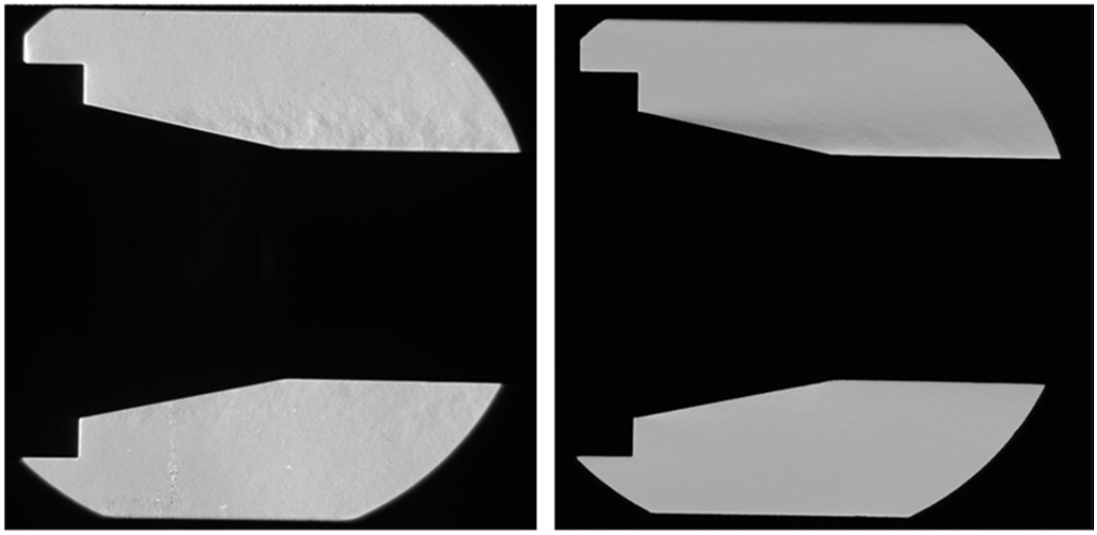

b)

Fig. 3.49. Average schlieren imagery with vertical (left column) and horizontal (right column) knife edges for a) $M_{tunnel} = 0.148$, b) $M_{tunnel} = 0.294$, c) $M_{tunnel} = 0.385$, d) $M_{tunnel} = 0.481$, e) $M_{tunnel} = 0.531$, f) $M_{tunnel} = 0.538|_{20.00}$, g) $M_{tunnel} = 0.538|_{21.00}$, and h) the clean model at $M_{tunnel} = 0.704$.

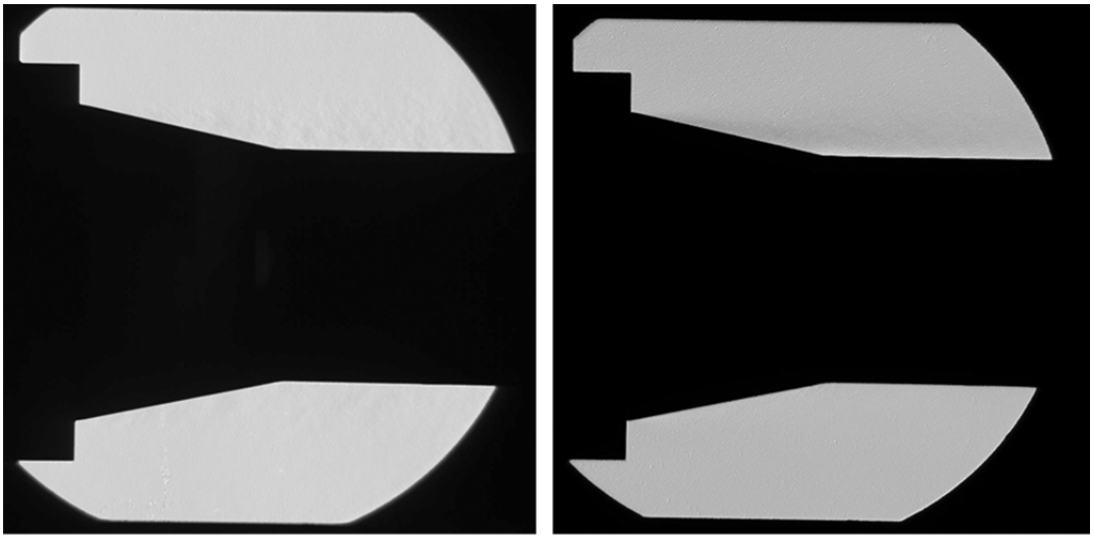

c)

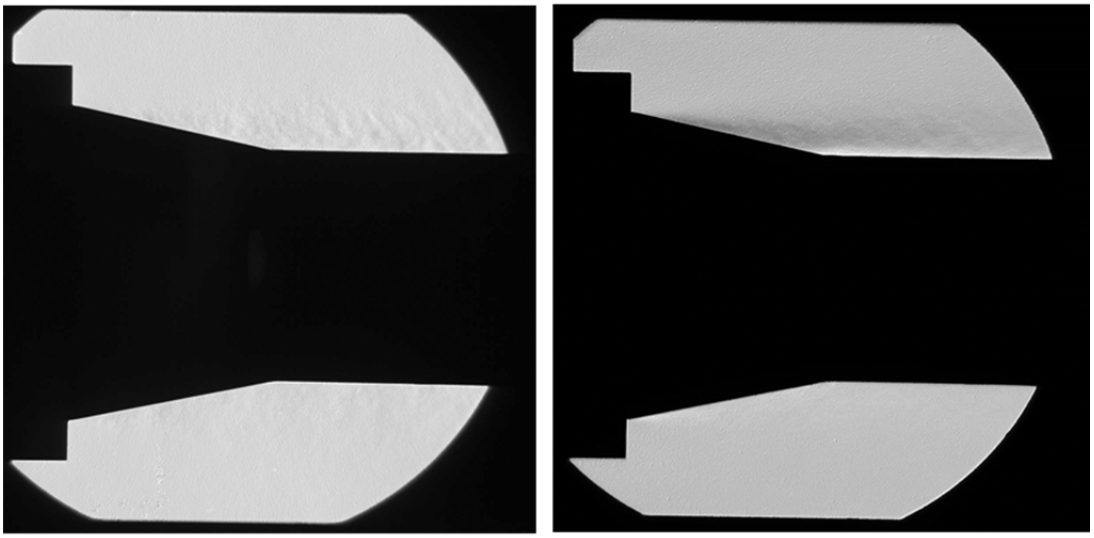

d)

Fig. 3.49 (cont.).

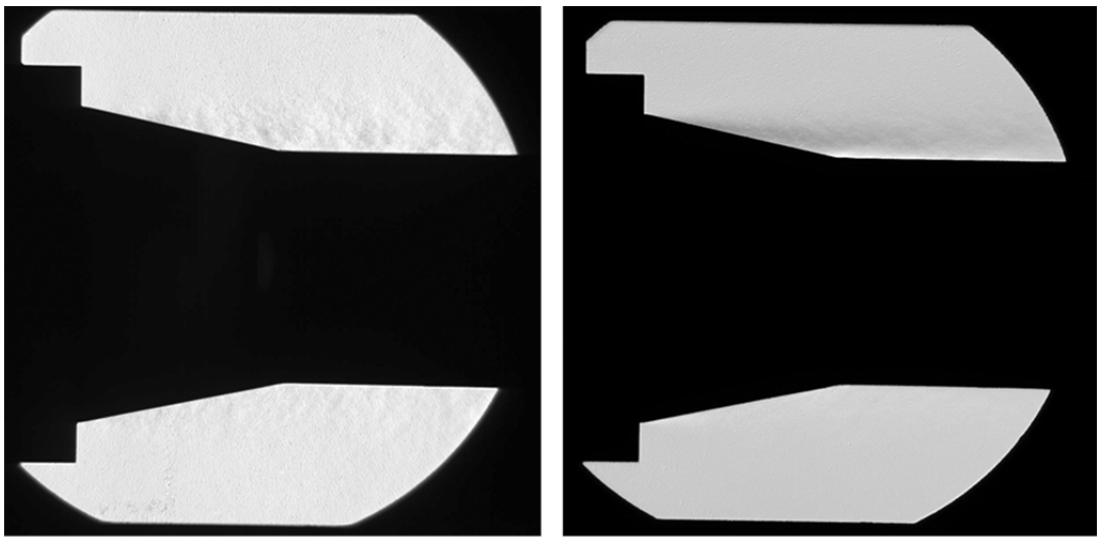

e)

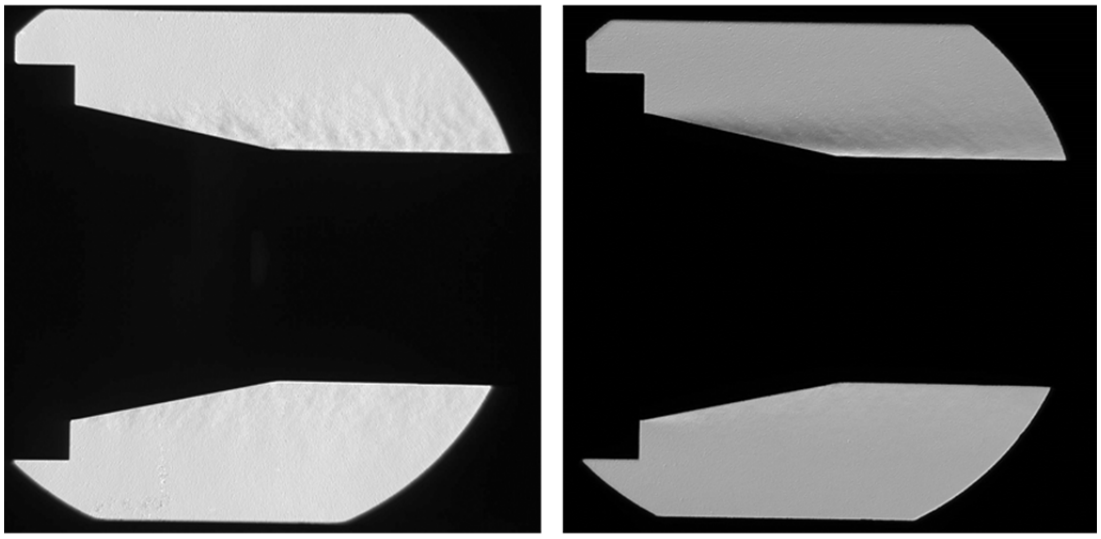

f)

Fig. 3.49 (cont.).

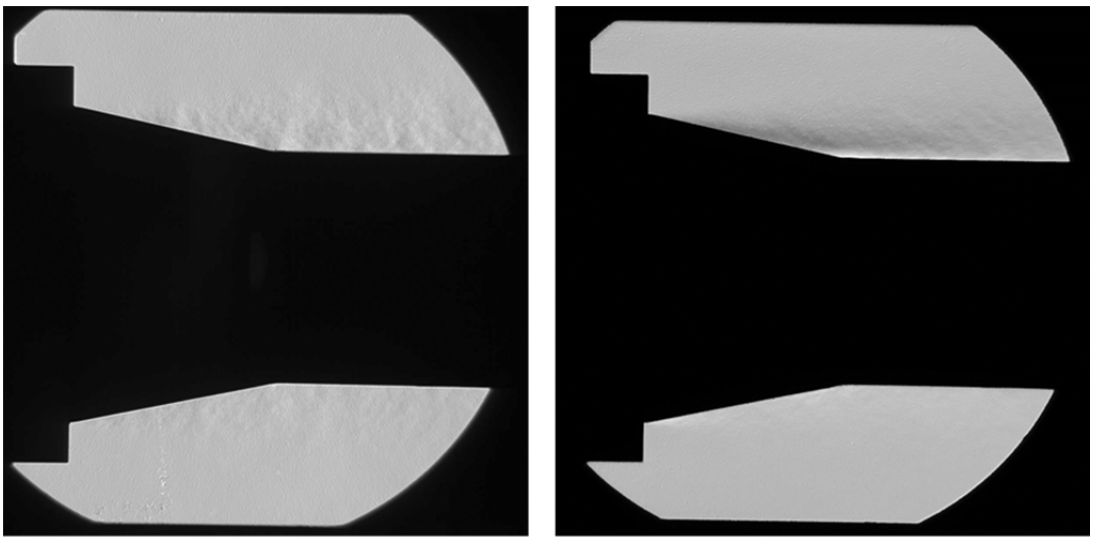

g)

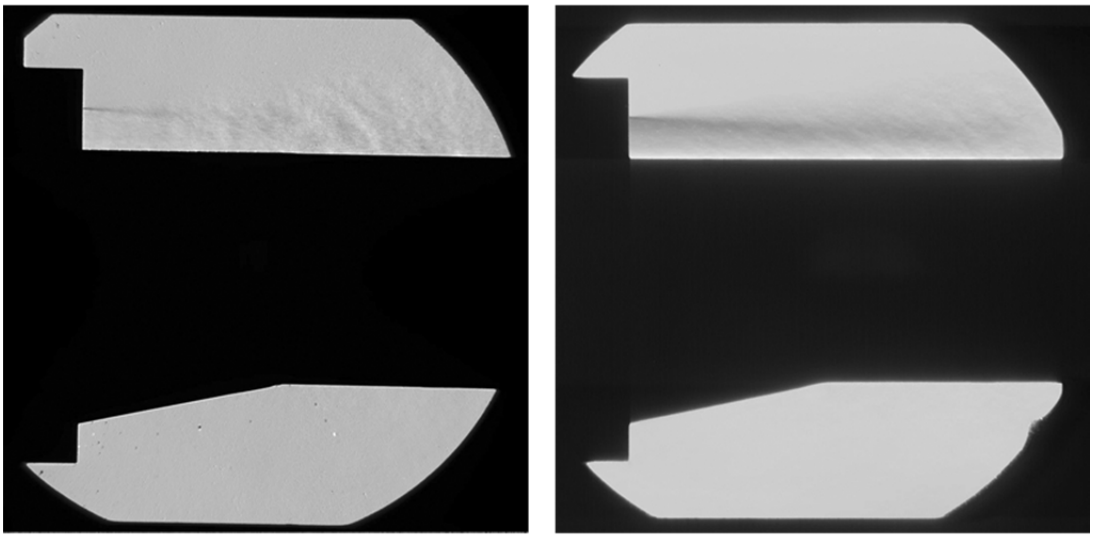

h)

Fig. 3.49 (cont.).

Chapter 4

Summary, Conclusions, and Recommendations

4.1 Summary

The focus of this work was to gain an understanding of the nature of a highly three-dimensional internal flow representing an engine bypass. The geometry, known as the aft bypass, was designed to achieve several purposes. First, the flow, which enters the aft bypass with a semi-annular cross-section, must be redistributed to a uniform, nearly-fully annular, cross-section at the exit. Second, the subsonic flow entering the aft bypass must be accelerated as it passes through the bypass in order to achieve fully supersonic conditions upon exiting. In order to complete these tasks, a series of thick guide vanes, which also serve structural purposes, are utilized. The primary approach to gaining an understanding of this complex flow was to conduct a small scale (approximately 6%) wind tunnel investigation.

This work was motivated by the need to minimize propulsion system contribution to sonic boom. The development of a novel supersonic engine concept, utilizing several recent technological advancements, by Gulfstream Aerospace Corporation has given rise to a secondary engine bypass. The high-flow nacelle bypass, as it is called, has a highly complex internal geometry created by forward and aft close out fairings around the core turbofan's external gearbox, a set of thin forward guide vanes, and a set of thick, strut-like, aft guide vanes. Experimental research of the flow through both the forward and aft vanes of the bypass has been conducted; the work relating to the flow through the aft vanes is the subject of this paper.

An existing axisymmetric supersonic wind tunnel with a central sting was modified for use with this study. The fully blocked region, that is the area where the gearbox fairing is at its largest extent, was extended upstream into the stagnation chamber so as to only simulate the flow through the aft portion of the bypass. Two models, which slide on the central sting, were used. One model, known as the clean model, consisted

only of the aft close out fairing, while a second model also included the thick vanes. Due to insufficient pressure ratio through the wind tunnel, design operating conditions were not achieved for the vaned model due to premature flow choking. Radial surveys were conducted at five azimuthal locations within a defined, aft bypass, inlet plane. Static pressure taps on the model surface provided quantitative data within the channels. Channel experimental data were compared to the isentropic ideal case, and channel mass flow rate analyses and estimations of total pressure losses were also conducted. Surface oil flow visualization within the bypass and Schlieren photography at the exhaust were used to provide qualitative insight into the flow.

4.2 Conclusions

As a result of the experiments conducted of the aft bypass models over a range of operating conditions, several key conclusions were drawn concerning the flow through the aft bypass and the effectiveness of the fairing and aft vanes.

1. Clean model M_{inlet} values show only a very weak dependence on azimuthal location, whereas a strong dependence was found for the vaned model. The addition of the aft bypass vanes caused the flow through the channels nearest the gearbox (those with greatest amount of curvature) to have a lower M_{inlet}, which increased monotonically as the azimuthal location approached top-center.
2. Boundary layers on both walls at the inlet plane were quite uniform and displayed consistent profiles. Clean model outer wall boundary layers are thicker than those of the vaned model. The opposite is true of the inner wall boundary layers. Near the gearbox fairing (Ch $^{\#}5$), the boundary layers are thicker and usually contain larger mass and momentum deficits, as evidenced by the measurements in δ, δ^*, and Θ.
3. The clean model (aft fairing alone) is generally ineffective. Surface oil flow visualizations indicate that there is a very large recirculation region behind the aft fairing which separates almost immediately. Schlieren imagery shows that the flow is not evenly distributed circumferentially at the exit to exhaust in a uniform

manner, which is an explicit objective of the aft bypass. Clean model pressure data doesn't provide much insight into flow characteristics since static pressure typically does not change much when transitioning from attached to separated (or recirculating) flows.

4. Vaned model exhaust flow is fully subsonic, indicating that the channels are not accelerating the flow to supersonic conditions. Vaned model tests reached a choke point and so vaned data are representative of off-design conditions as the facility, as operated, did not achieve design conditions. The inability to reach design conditions was attributed to insufficient pressure ratio across the wind tunnel, thereby limiting the attainable conditions. Therefore, vaned model data was collected only at off-design operating conditions; the maximum M_{tunnel} achieved was 0.538, which was the facility choke Mach number (maximum $P_{chamber}$ was 21.00 psia).
5. Curves generated from pressure data acquired within the aft bypass channels is functionally similar to those within a converging-diverging nozzle. Static to total pressure ratios decrease within the converging section as the flow is accelerated. If the sonic condition is not reached at the throat, the pressure ratio increases again as the flow is decelerated subsonically. If the sonic condition is met at the throat, then the flow accelerates until a shock within the channel causes the pressure ratio to increase, where after the flow expands subsonically.
6. The theory for the existence of shocks within the diverging sections of the channels is based on the knowledge that a) the exhaust is definitively subsonic, and, b) the pressure ratios downstream of the throat are well beyond the sonic limit. Therefore, a shock is the only mechanism by which the flow can return to subsonic conditions at the exhaust.
7. The vaned model does appear to successfully distribute the partial annulus, high speed incoming flow into a uniformly distributed, fully annular, exhaust. The achievement of this stated goal of the aft bypass can be seen by verifying that the recorded pressure data at and beyond the exhaust for each operating condition is the same for all channels (that is, for all azimuthal locations).

8. The channels appear to choke in a successive manner, so that the channels undergoing the most curvature (Ch #5 and Ch #4), choke first, followed by Ch #3, and then, lastly by the channels which experience the least curvature (Ch #2 and Ch #1). Evidence for the successive channel choking theory can be found in the channel pressure data, by noting how more and more operating conditions share the same first static pressure tap pressure ratio as the channel curvature increases.
9. The conditions at a single location within each channel were specified and used to compute the isentropic conditions throughout the remainder of the channel. The percent difference from the experimental conditions were computed at each static pressure tap location within each channel and for all tested operating conditions. The isentropic-to-experimental comparison provided fair results (within approximately 5%) for the lower operating conditions, but the level of agreement diverged with increasing M_{tunnel}. The largest percent difference was always found to occur shortly past the channel throat.
10. Based on the conditions assumed at the start of the isentropic comparison, the mass flow rate could be computed. Using the experimentally recorded static pressures, and, under the assumption of continuity to maintain the same mass flow rate, the total pressure at each pressure tap could be estimated. As expected, the total pressure was estimated to decrease from entry to exit within each channel. However, total pressure was sometimes estimated to increase, especially near and just downstream of the channel throats. An increase of total pressure is impossible without the addition of mass, and so, the total pressure estimation method appears to breakdown in these locations.
11. Fluorescent surface oil flow visualizations within the channels have shown that numerous recirculation regions on all channel walls, especially near the channel throat. These indicate that the flow within the channels is highly three dimensional and is therefore unlikely to act in an isentropic manner.
12. Since the flow near and just downstream of the channel throats appears to be highly three-dimensional, and, therefore highly non-isentropic, the isentropic-to-experimental comparison and estimation of total pressure losses within these

regions are not reliably estimated. This provides an explanation for why these calculations seemed to fail within these regions.

13. Calculated values for percent contribution towards total mass flow through each channel are fairly consistent with those obtained in at least one computational study.[30] Mass flow rate tends to decrease with increasing channel curvature. When plotted as a function of M_{tunnel}, it was found that the percent mass flow passed through Ch #4 and Ch #5 seemed constant. However, it was found that the percent mass flow through Ch #3 decreased with M_{tunnel}, and a corresponding increase was found in Ch #1 and Ch #2. This transfer of mass flow rate responsibility between channels fits with the successive channel choking theory described previously.

4.3 Recommendations

There are several directions in which this project could continue. Recommendations for future work can be best organized in a manner that is driven by the amount of facility redesign that would be required to accomplish the task. Therefore, recommendations are divided into tasks that could be accomplished quickly and easily with minimal redesign, tasks that are geared towards continued testing of the same (or very similar) aft bypass configurations through moderate facility redesign, and, last, a series of tasks which would require a large degree of redesign. The moderate redesign tasks are intended to allow for on-design testing; tasks involving a large degree of redesign are related to potential future research projects that will better reflect the high-flow nacelle bypass concept. Recommendations in each category are presented below:

Tasks Requiring Minimal Redesign:

1. Conduct clean model runs at (at least) one vaned model operating condition to compare inlet plane data for same M_{tunnel}.
2. Increase the axial separation distance between the inlet plane outer wall static pressure taps and the probe tip to remove the negative effects generated by the presence of the probe. This would allow for the elimination of the "two-run"

system currently employed. This could be accomplished by moving the outer wall static pressure taps or by simply shortening the total pressure probe tip length.

3. Increase model integrity to allow for greater stagnation chamber pressures. This would aid in achieving design operating conditions without putting the model at risk.

Tasks Requiring Moderate Redesign:

1. Replacement of the viewing chamber with one with a smaller inner diameter. This would allow for decreased back pressure by avoiding the exhaust-to-farfield effect. However, this would come at the cost of decreased exhaust realism
2. Add capability to conduct exhaust radial total pressure profiles to accurately assess pressure losses through each channel and, if local static pressure is also recorded, flow Mach number.
3. Incorporate a second throat into the model/test region exhaust/exit to swallow the shock. This would allow for further decrease in facility back pressure so that M_{tunnel} can be increased to achieve design conditions.

Tasks Requiring a Large Amount of Redesign:

1. Testing of next generation aft bypass vane configurations which may have altered vane profiles, placements, and numbers of vanes.
2. Inclusion of the core engine exhaust flow by blowing through the central sting. In addition to more accurately reflecting the true operating conditions, inclusion of the core exhaust would also act to decrease facility back pressure and thereby allow for increased facility M_{tunnel}.
3. Conduct single facility full bypass experiments. A single facility experiment would allow for correct modeling of forward-to-aft vane influences that are convected downstream and projected upstream. A single facility, full bypass geometry, test could be conducted in the supersonic wind tunnel by removing the gearbox blockage assembly and then replacing it with the forward gearbox fairing and fully blocked section positioned at an appropriate axial position.

References

[1] Anderson, J.D., *Modern Compressible Flow With Historical Perspective*, 3rd ed., McGraw-Hill, New York, NY, 2003, pp. 9-11.

[2] Wilcox, D.C., *Basic Fluid Mechanics*, 3rd ed., Birmingham Press Inc., San Diego, CA, 2007, pp. 353-354.

[3] Federal Aviation Administration Regulations: Title 14, Volume 2, Chapter 1, Section 91.817

[4] Eames, J.D., "Concorde Operations," *Society of Automotive Engineers (SAE)*, 912161, 1991.

[5] Sparrow, V., and Coulouvrat, F., "Status of Sonic Boom Knowledge," *International Civil Aviation Organization (ICAO)*, Paper CAEP/7-IP/18, 2007.

[6] Seebass, A.R., and George, A.R., "Design and Operation of Aircraft to Minimize Their Sonic Boom," *Journal of Aircraft*, Vol. 11, No. 9, September 1974, pp. 509-517.

[7] Plotkin, K.J., Page, J.A., Graham, D.H., Pawlowski, J.W., Schein, D.B., Coen, P.G., McGurdy, D.A., Haering Jr, E.A., Murray, J.E., Ehernberger, L.J., Maglieri, D.J., Bobbitt, P.J., Pillon, A., Salamone, J., "Ground Measurements of a Shaped Sonic Boom," AIAA 2004-2923, *10th AIAA/CEAS Aeroacoustics Conference*, May 2004.

[8] Mack, R.J., "A Supersonic Business-Jet Concept Designed for Low Sonic Boom," NASA TM-2003-212435, October 2003.

[9] Conners, T.R., Howe, D.C., Whurr, J.R., and Smith, C.F., "Conceptual Design, Integration, and Development Plan for an Efficient Low Sonic Boom Propulsion System Employing Advanced Supersonic Engine Cycles," Final Report – Public Distribution, NASA Contract NNC04CA29C, amended August 27, 2007.

[10] Conners, T.R., Howe, D.C., and Whurr, J.R., "Impact of Engine Cycle Selection on Propulsion System Integration and Vehicle Performance for a Quiet Supersonic Aircraft," AIAA Paper 2005-1016, 2005.

[11] Conners, T.R., Gulfstream Aerospace Corporation, Savannah, GA, U.S. Patent Application for "Low Shock Strength Propulsion System," Application No. 12/257,982; Filed 24 Oct. 2008.

[12] Howe, D.C., Simmons III, F., and Freund, D., "Development of the Gulfstream Quiet Spike for Sonic Boom Minimization," AIAA 2008-0124, 2008.

[13] Cowart, R., and Grindle, T., "An Overview of the Gulfstream / NASA Quiet Spike Flight Test Program," AIAA 2008-0123, 2008.

[14] Simmons III, F.. Freund, D., Spivey, N.D., and Schuster, L., "Quiet Spike™: The Design and Validiation of an Extendable Nose Boom Prototype," AIAA Paper 2007-1774, 2007.

[15] Wilson, J.R., "Quiet Spike: Softening the Sonic Boom," *Aerospace America*, Oct. 2007, pp. 38-42.

[16] Conners, T.R., Merret, J.M., and Howe, D.C., "Wind Tunnel Testing of an Axisymmetric Isentropic Relaxed External Compression Inlet at Mach 1.97 Design Speed," AIAA 2007-5066, 2007.

[17] Howe, D.C, "Improved Sonic Boom Minimization with Extendable Nose Spike," AIAA Paper 2005-1014, 2005.

[18] Conners, T.R., Howe, D.C., and Henne, P.A., Gulfstream Aerospace Corporation, Savannah, GA, U.S. Patent Application for "Isentropic Compression Inlet for Supersonic Aircraft," Application No. 11/639,339; Filed 15 Dec. 2006.

[19] Conners, T.R., and Howe, D.C., "Supersonic Inlet Shaping for Dramatic Reductions in Drag and Sonic Boom Strength," AIAA 2006-0030, January 2006.

[20] Conners, T.R., and Wayman, T.R., "The Feasibility of High-Flow Nacelle Bypass for Low Sonic-Boom Propulsion System Design," AIAA Paper 2011-3797, June 2011.

[21] Yeong, Y. H., Chiles, I. M., Bragg, M. B., Elliott, G. S., Loth, E., and Conners, T. R., "Wind Tunnel Testing of a Nacelle Bypass Concept for a Quiet Supersonic Aircraft," *39th AIAA Fluid Dynamics Conference*, AIAA Paper 2009-4207, San Antonio, TX, June 2009.

[22] Yeong, Y. H., "Wind Tunnel Testing of a Nacelle Bypass Concept for a Quiet Supersonic Aircraft," M.S. Thesis, Department of Aerospace Engineering, University of Illinois at Urbana-Champaign, Urbana, IL, 2009.

[23] Chiles, I. M., Loth, E., Yeong, Y. H., Bragg, M. B., and Elliott, G. S., "Computations of Engine Bypass in a Wind Tunnel Configuration," *39th AIAA Fluid Dynamics Conference*, AIAA Paper 2009-4208, San Antonio, TX, June 2009.

[24] Chiles, I. M., "Simulations of a Bypass Flow Between an Engine and a Nacelle," M.S. Thesis, Department of Aerospace Engineering, University of Illinois at Urbana-Champaign, Urbana, IL, 2009.

[25] Herrera, A. A., Bragg, M. B., and Elliott, G. S., "Experimental Study of Forward Guide Vanes in a High-Flow Engine Bypass Nacelle for Supersonic Flight," *50th AIAA Aerospace Sciences Meeting*, Nashville, TN, Jan. 2012 (submitted for publication)

[26] Herrera, A. A., "An Experimental Study of the Forward Guide Vanes of an Engine Bypass Nacelle for Low-Boom Supersonic Flight," M.S. Thesis, Department of Aerospace Engineering, University of Illinois at Urbana-Champaign, Urbana, IL, 2011.

[27] Jain, N., and Bodony, D. J., "Computation Assessment of Flow Through a High-Flow Nacelle Bypass," *50th AIAA Aerospace Sciences Meeting*, Nashville, TN, Jan. 2012 (submitted for publication)

[28] Jain, N., "Computational Assessment of Flow through a High-Flow Nacelle Bypass for Low Supersonic Boom," M.S. Thesis, Department of Aerospace Engineering, University of Illinois at Urbana-Champaign, Urbana, IL, 2011.

[29] Kim, H. J., Kumano, T., Liou, M.-S., Povinelli, L. A., and Conners, T. R., "Flow Simulation of Supersonic Inlet with Bypass Annular Duct," *Journal of Propulsion and Power*, Vol. 27, No. 1, January-February 2011.

[30] Kim, H. J., Kumano, T., Liou, M.-S., and Povinelli, L. A., "Optimal Shape Design of Supersonic Bypass Inlet,", *AIAA/ISSMO Multidisciplinary Analysis Optimization Conference*, AIAA Paper 2010-9171, Fort Worth, TX, Sept. 2010.

[31] Henne, P. A., "A Gulfstream Perspective on the DARPA QSP Program and Future Civil Supersonic Initiatives," FAA Civil Supersonic Aircraft Workshop, Arlington, VA, Nov. 2003.

[32] Sauter, J. M., "Design of an Axisymmetric Supersonic Wind Tunnel and Experimental Study of Supersonic, Power-off Base Flow Phenomena," M.S. Thesis, Department of Mechanical Engineering, University of Illinois at Urbana-Champaign, Urbana, IL 1989.

[33] Chang, W., "Design and Development of a Rectangular Supersonic Wind Tunnel Facility for the Study of Shock/Boundary Layer Interactions," M.S. Thesis, Department of Aerospace Engineering, University of Illinois at Urbana-Champaign, Urbana, IL 2011.

[34] Kim, H. J., Kumano, T., Liou, M.-S., Povinelli, L. A., and Conners, T. R., "Flow Simulation of Supersonic Inlet with Bypass Annular Duct," *Journal of Propulsion and Power*, Vol. 27, No. 1, January-February 2011.

[35] Dinsmore and Associates, Inc., "DSM Somos: ProtoGen 18420," http://www.dinsmoreinc.com/wp-content/uploads/2009/03/protogen-18420-material-sheet.pdf. [retrieved July 19, 2011].

[36] Lu, F.K., "Surface Oil Flow Visualization Still Useful After All These Years," *The European Physical Journal - Special Topics*, Vol. 182, No. 1, pp. 51-63.

[37] Wilcox, D.C., *Basic Fluid Mechanics*, 3rd ed., Birmingham Press Inc., San Diego, CA, 2007, pp. 31.

[38] White, F.M., *Viscous Fluid Flow*, 3rd ed., McGraw-Hill, New York, NY, 2006, pp. 27-28.

[39] White, F.M., *Viscous Fluid Flow*, 3rd ed., McGraw-Hill, New York, NY, 2006, pp. 265-269.

[40] Sass, J., "Mach 2.5 Axisymmetric Super Sonic Wind Tunnel Operations Manual," University of Illinois at Urbana-Champaign, Aeronautical Laboratory A, Internal document, 2010.

[41] Coleman, H.W., and Steele, W.G., *Experimentation and Uncertainty Analysis for Engineers*, John Wiley & Sons Inc., 1989.

[42] Chapra, S.C., and Canale, R.P., *Numerical Methods for Engineers*, 5th ed., McGraw-Hill, New York, NY, 2006., pp.590-593.

[43] Chapra, S.C., and Canale, R.P., *Numerical Methods for Engineers*, 5th ed., McGraw-Hill, New York, NY, 2006., pp.89-90.

Appendix A

Aft Bypass Facility Assembly

The step by step assembly process for the aft bypass facility is as described below:

1. *Run a long chord through the sting. Insert sting from upstream end if taper lock is already on the sting. Otherwise, insert from downstream end. Pull chord through leave it hanging so that it can be used as a pull chord later.*
2. *Position sting such that the downstream faces of the sting sleeve and the flow conditioners are coincident. (Fig. A.1) Tighten taper lock to fix the sting in place.*
3. *Assemble the gearbox blockage assembly. Use glazing putty to fill screw counterbores and screw caps. Sand to smooth. (Fig. A.2)*
4. *Slide the gearbox assembly over the sting and up against the flow straighteners within the stagnation chamber. (Fig. A.3)*
5. *Put on converging nozzle alignment flange and tighten bolts. (Fig. A.4)*
6. *Put on converging nozzle. Insert gearbox blockage plates in nozzle slots first, and then align entire assembly to screws to ensure symmetry about vertical plane. (Fig. A.5)*
7. *Put on assembled nacelle component and tighten screws. Ensure that the converging nozzle and nacelle seem centered about the sting. There should be no gap between nacelle inner wall and gearbox blockage assembly at bottom-center. It not aligned, loosen (but not remove) converging nozzle alignment flange and use the four outside screws to align it properly. Then re-tighten. (Fig. A.6)*
8. *Slide model (clean or vaned) on sting.*

9. *Feed pressure lines through central sting using pull chord. Plumb ends of pressure lines to the bent stainless steel tubing.*

10. *Insert stainless steel tubing into the model surface static pressure tap exits on the end face of the model. Epoxy in place. Allow to dry. Using a razor blade, trim epoxy from areas where it will interfere with pressure line reversal cavity cap. (Fig. A.7)*

11. *Slide model back into the nacelle and align it. Tighten model screws to fix in place. (Fig. A.8)*

12. *Fasten the downstream facility support ring to the viewing chamber.*

13. *Assemble the centerbody diffusive cone with pressure line reversal cavity cap on to the downstream facility support ring. Rotate such that pressure line reversal cavity cap is orientated correctly. Tighten set screw in diffusive cone. (Fig. A.9)*

14. *Loop a chain hoist through the viewing chamber windows. Use cardboard or rags to protect window frame edges from chain. Attach second hoist to downstream facility support ring eyehook. Raise viewing chamber and diffusive cone assembly to height.*

15. *Slide viewing chamber upstream to nacelle and model. Slide pressure line reversal cavity cap over end of sting and around stainless steel tubing while simultaneously inserting nacelle through viewing chamber. Tighten screws, taking great care to do so evenly and always monitoring the pressure line cavity reversal cap's fit against the model. (Fig. A.10 and Fig. A.11)*

16. *Apply glazing putty to model and pressure line reversal cavity cap. Allow to dry and then sand smooth. (Fig. A.12)*

17. *Using a chain winch on either end, raise the diverging diffuser upwards as high as possible. Must be very careful during this procedure to raise evenly and not to damage the turn buckles and trolleys. (Fig. A.13)*

18. *Place constant area diffuser on table downstream of the tip of the diffusive cone. Use chain winch to pick up the upstream end. Use crane to pick up downstream end and then raise. (Fig. A.14)*

19. *Tap a gasket on either end face of the constant area diffuser.*
20. *Very carefully, insert diffusive cone in upstream end of constant area diffuser while turning the crane to angle the constant area diffuser in place. Be wary of the upstream end of the suspended diverging diffuser.*
21. *Insert several viewing chamber to constant area diffuser bolts for alignment purposes.*
22. *Lower the diverging diffuser very carefully with the two chain winches. Be sure to keep it level and to see that it doesn't rest on the constant area diffuser or the exhaust ducting while lowering. Stop before the load transfers to the turn buckles. (Fig. A.15)*
23. *Insert several bolts on both ends of the diverging diffuser to start alignment process. Allow load to transfer to the turn buckles so that gravity will aid in alignment process.*
24. *Insert and evenly tighten all remaining bolts.*
25. *Insert open gate and key. Ensure the middle bay wind tunnel has closed gate and key installed. Then add remaining screws to exhaust ducting. (Fig. A.16)*
26. *Ensure all bolts and screws are securely fastened.*
27. *Put on viewing chamber windows and nacelle wall plugs.*

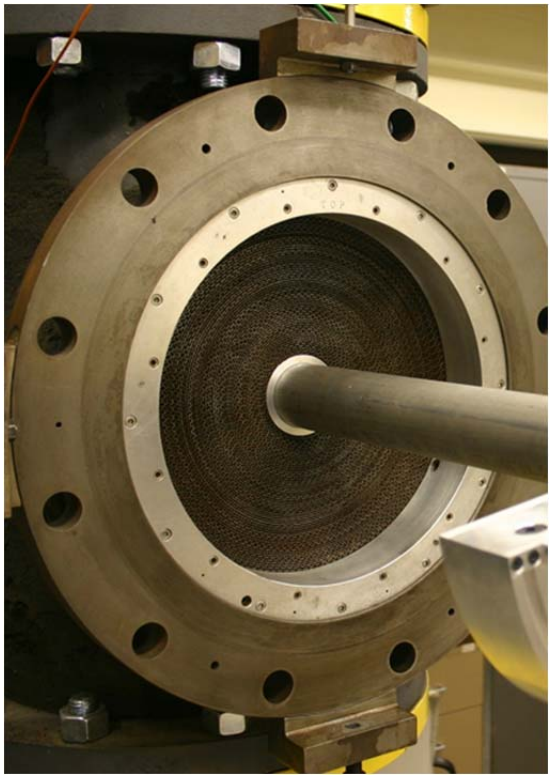

Fig. A.1. Insertion of sting through stagnation chamber.

Fig. A.2. Gearbox blockage assembly.

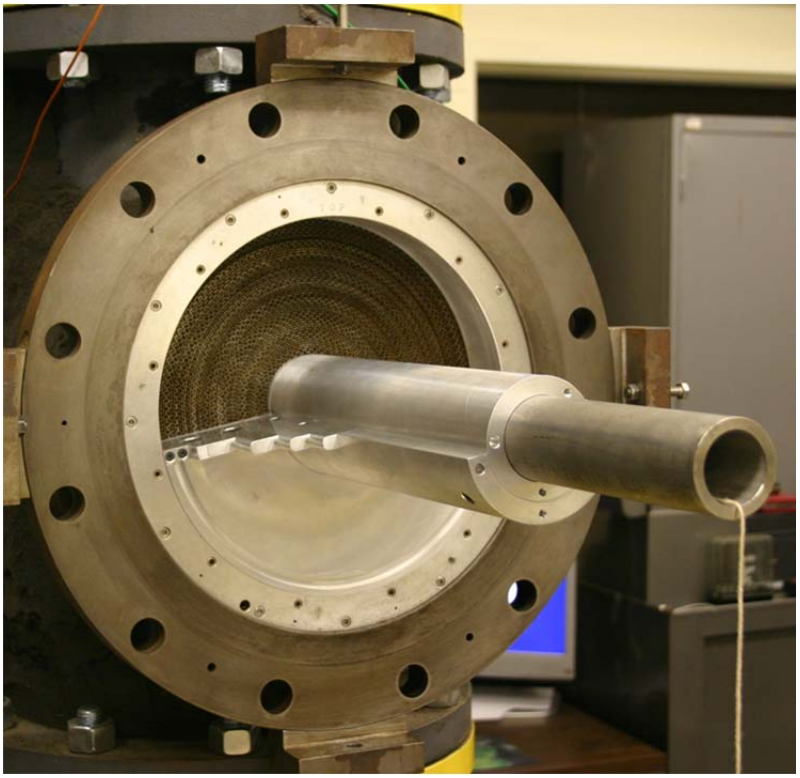

Fig. A.3. Positioning of gearbox blockage assembly.

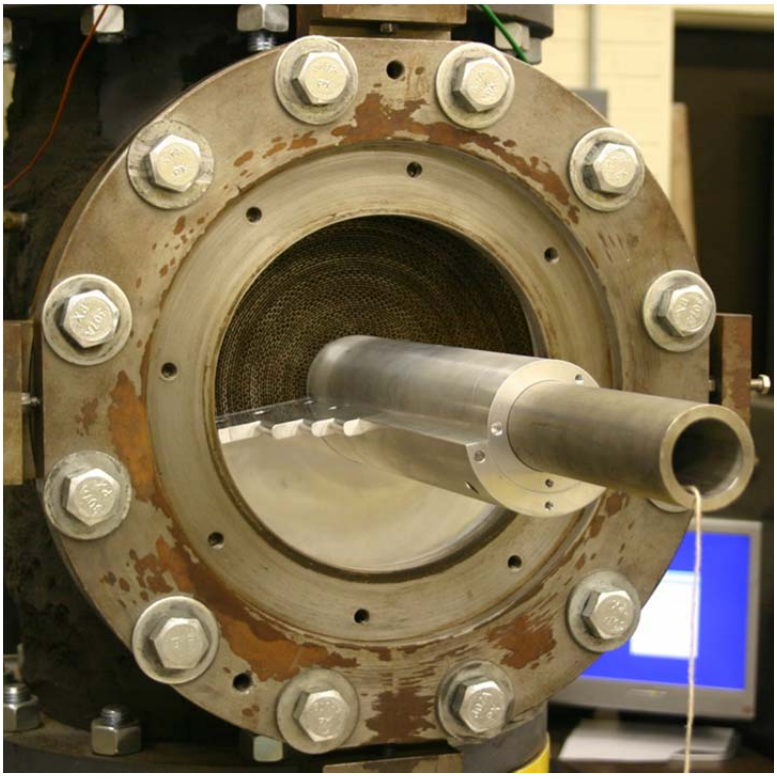

Fig. A.4. Addition of converging nozzle alignment flange.

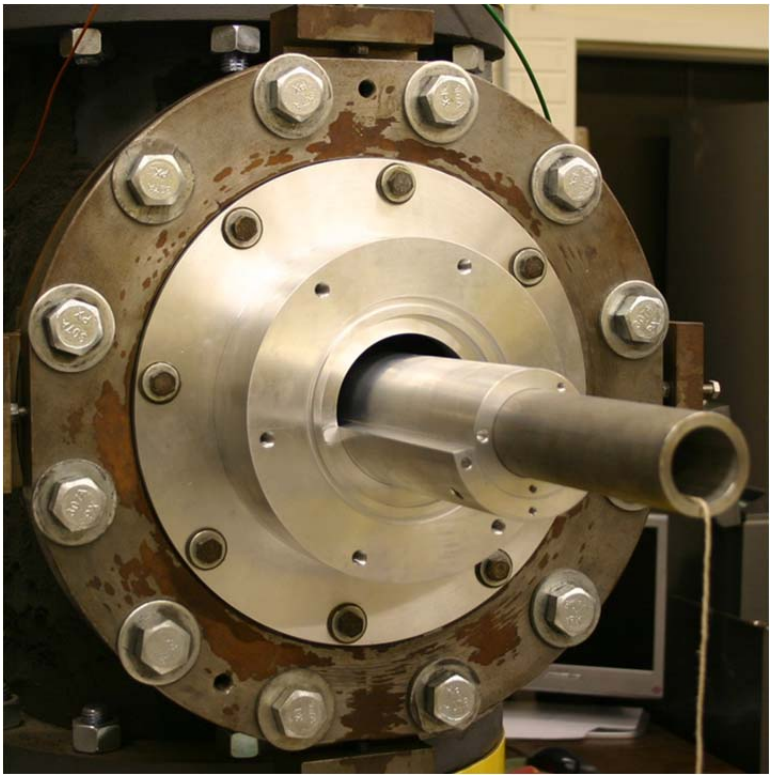

Fig. A.5. Placement and alignment of converging nozzle.

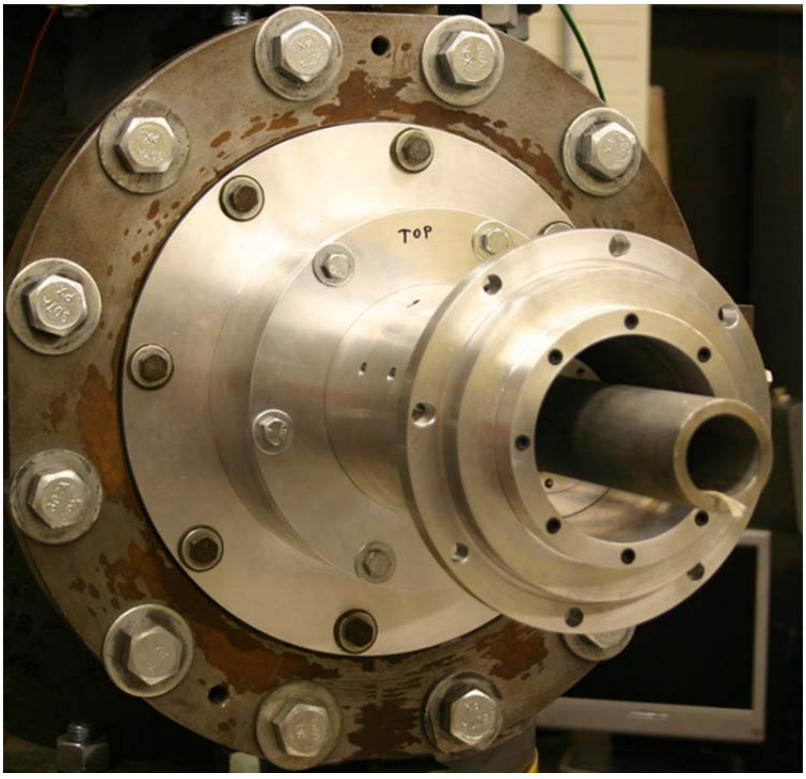

Fig. A.6. Placement of nacelle component.

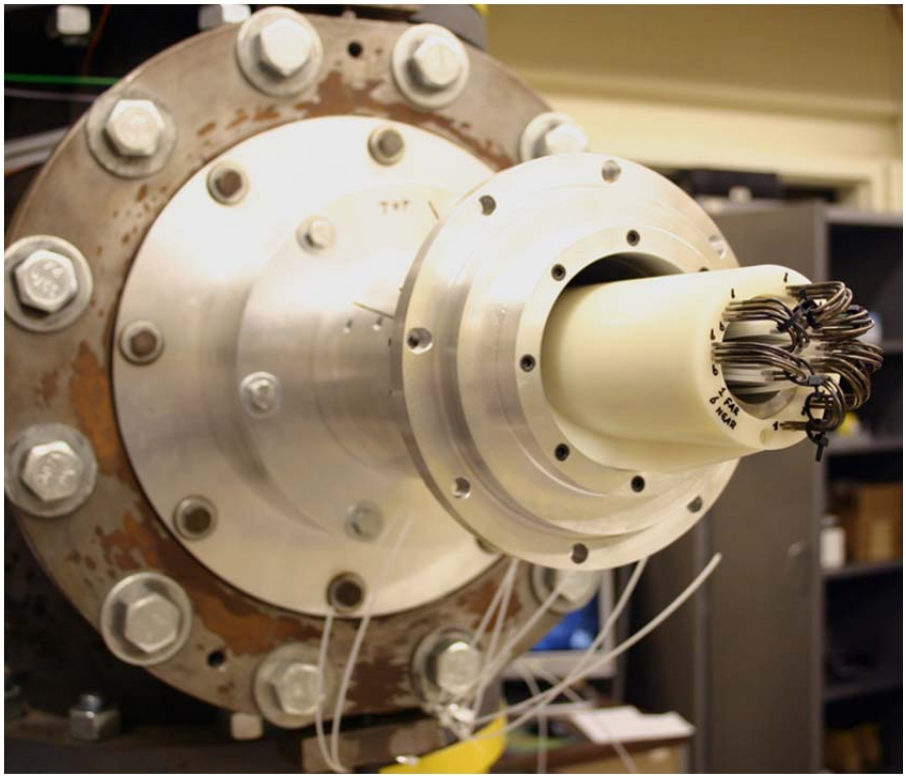

Fig. A.7. Plumbing of pressure line reversal stainless steel tubing.

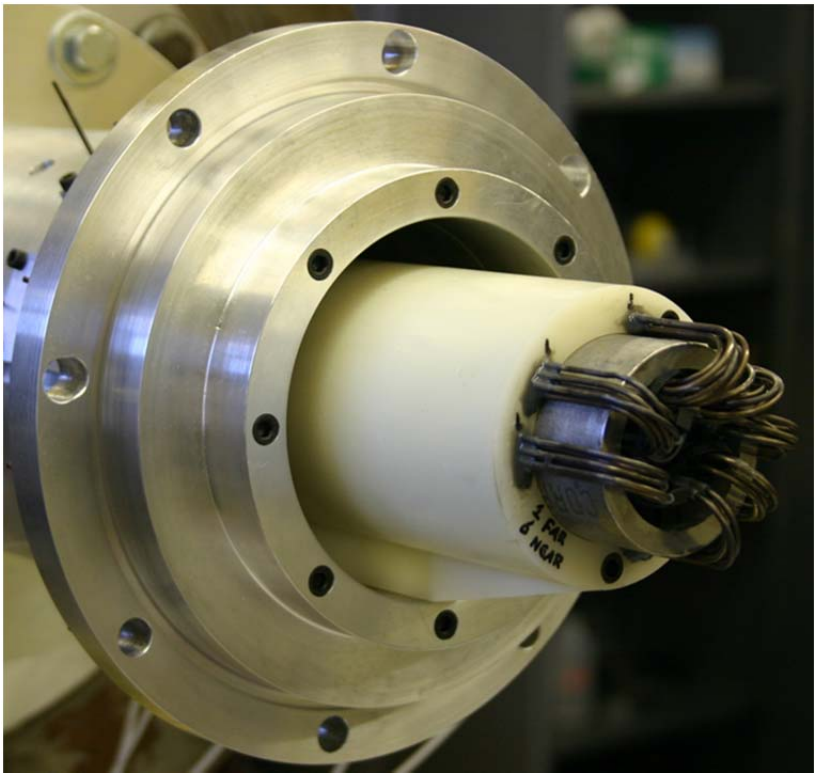

Fig. A.8. Pressure lines epoxied, trimmed, and model fixed in place.

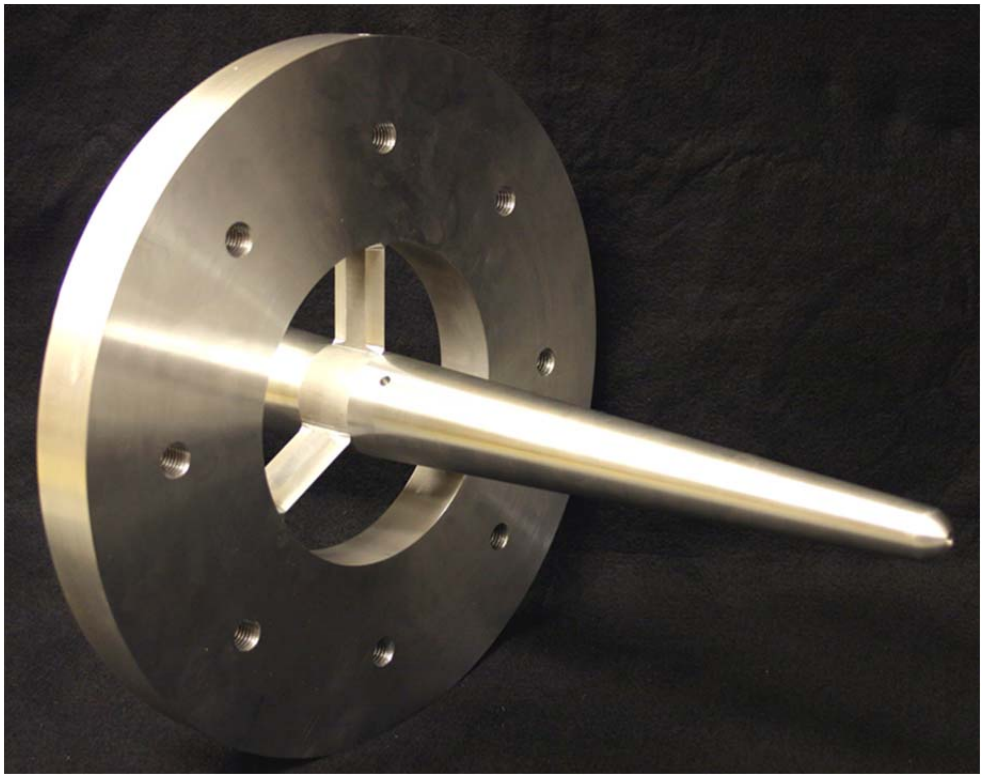

Fig. A.9. Assembly of downstream centerbody diffusive cone (aft end).

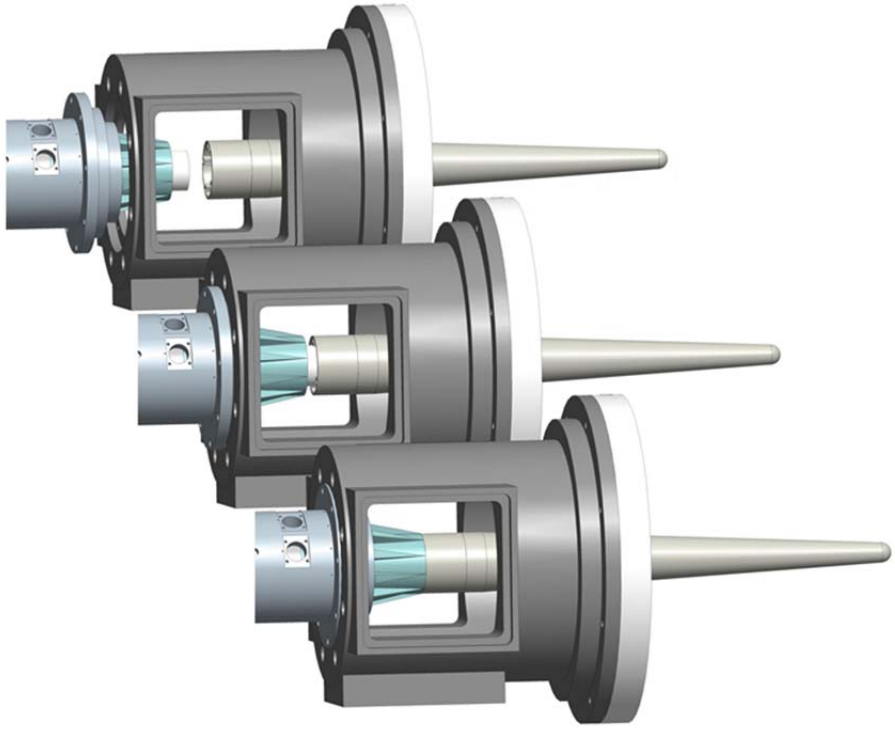

Fig. A.10. Careful positioning and alignment of the pressure line reversal cavity cap over the end of the sting and viewing chamber over the nacelle.

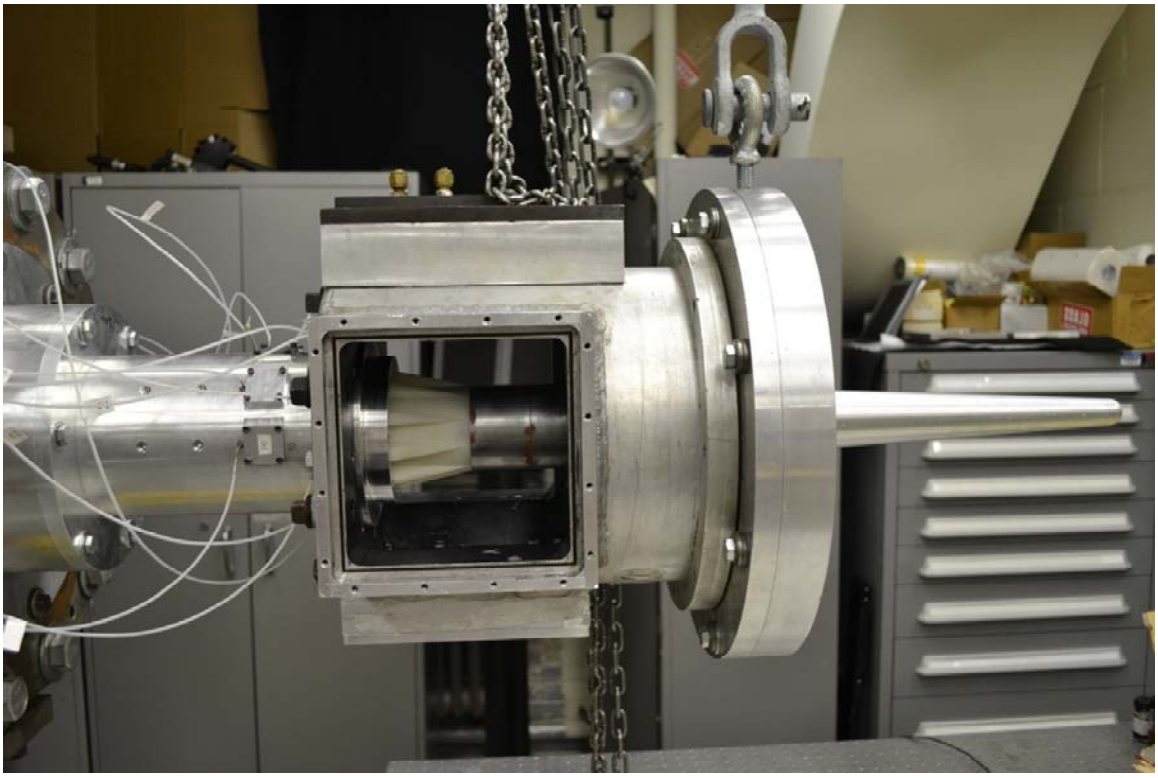

Fig. A.11. Positioning of viewing chamber and downstream centerbody components.

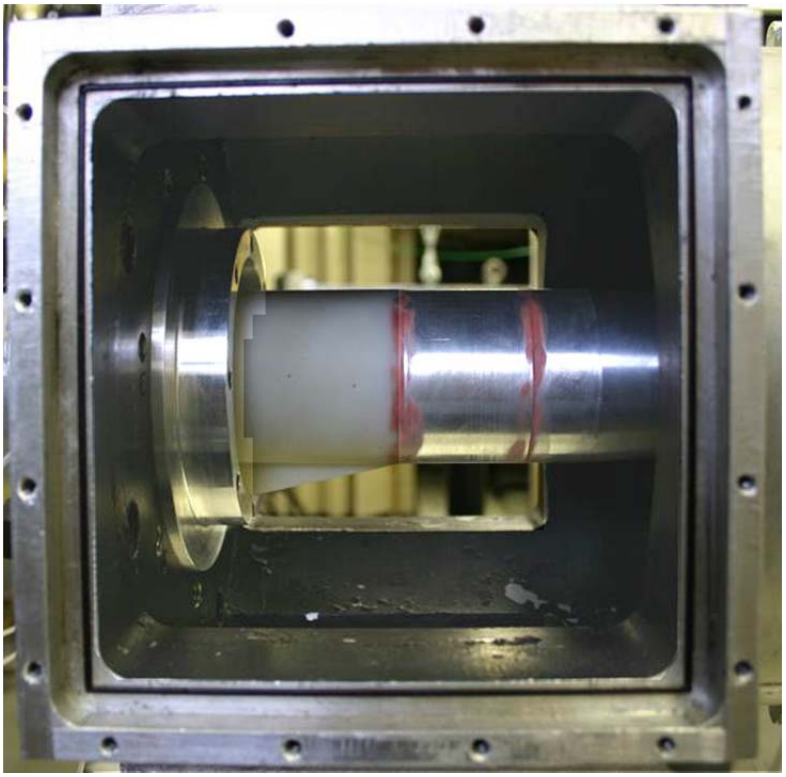

Fig. A.12. After having glazed and sanded to smoothen part interfaces.

Fig. A.13. Raising the diverging diffuser.

Fig. A.14. Positioning the constant area diffuser.

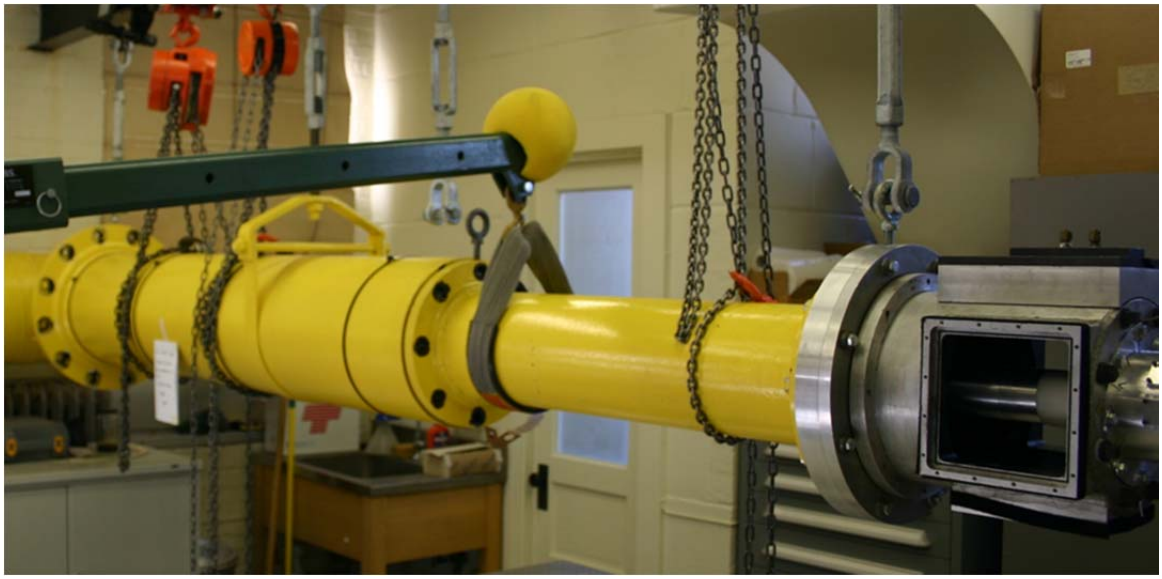

Fig. A.15. Placement of constant area diffuser and lowering of diverging diffuser.

Fig. A.16. Insertion of the open exhaust gate.

Appendix B

Miscellaneous Facility Component Drawings

The following appendix contains engineering drawings of all aft bypass specific wind tunnel components. Drawings are arranged in the order by which they are installed in the facility upon assembly. For those components which make up a subassembly, an additional drawing is used to show their relative placement. Within the bill of materials of the subassembly drawings, fasteners are named by their McMaster-Carr part numbers. Thread type and size, length, and other specifications can be found in the notes relating to those features in the component drawings.

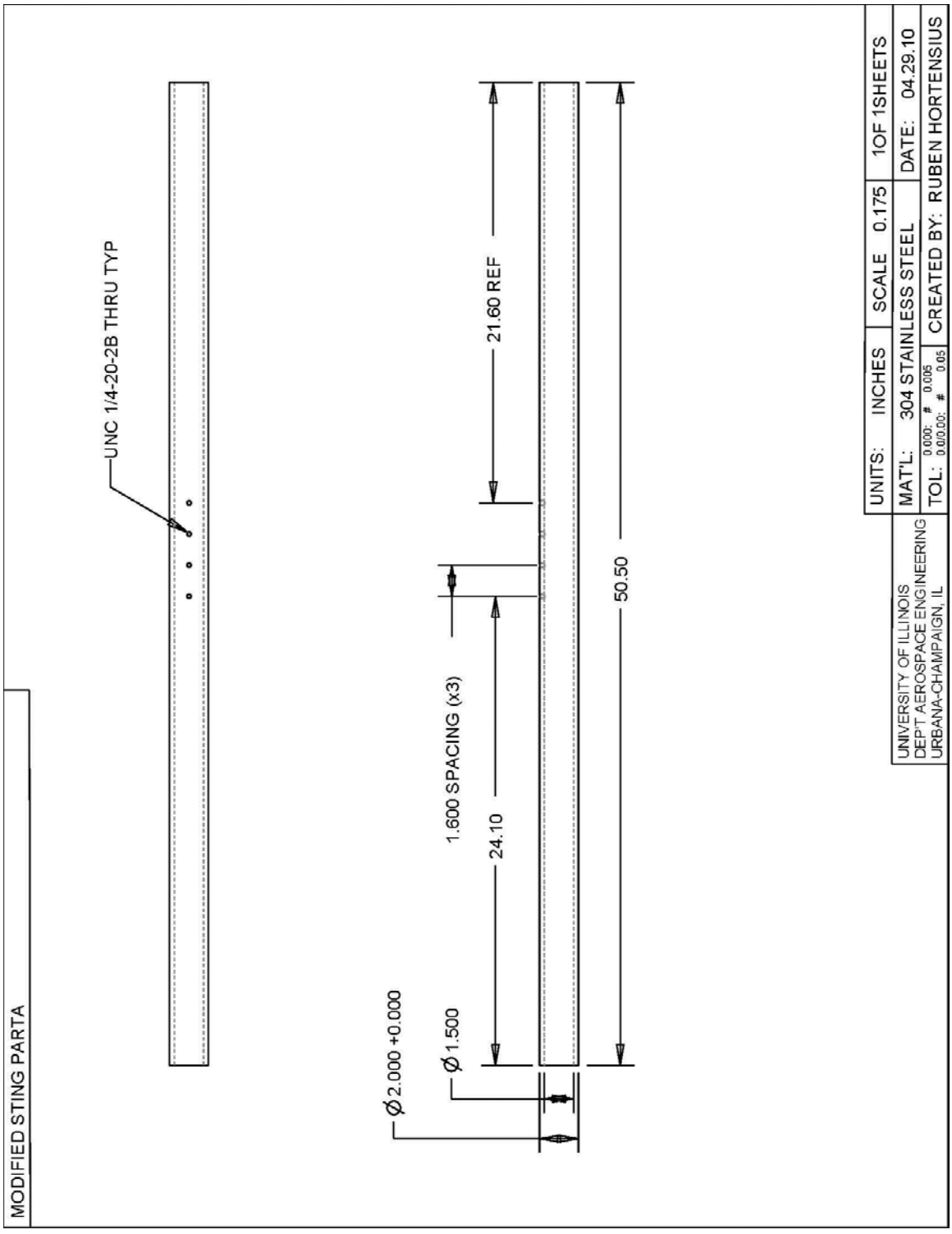

Fig. B.1. Sting Part A Engineering Drawing.

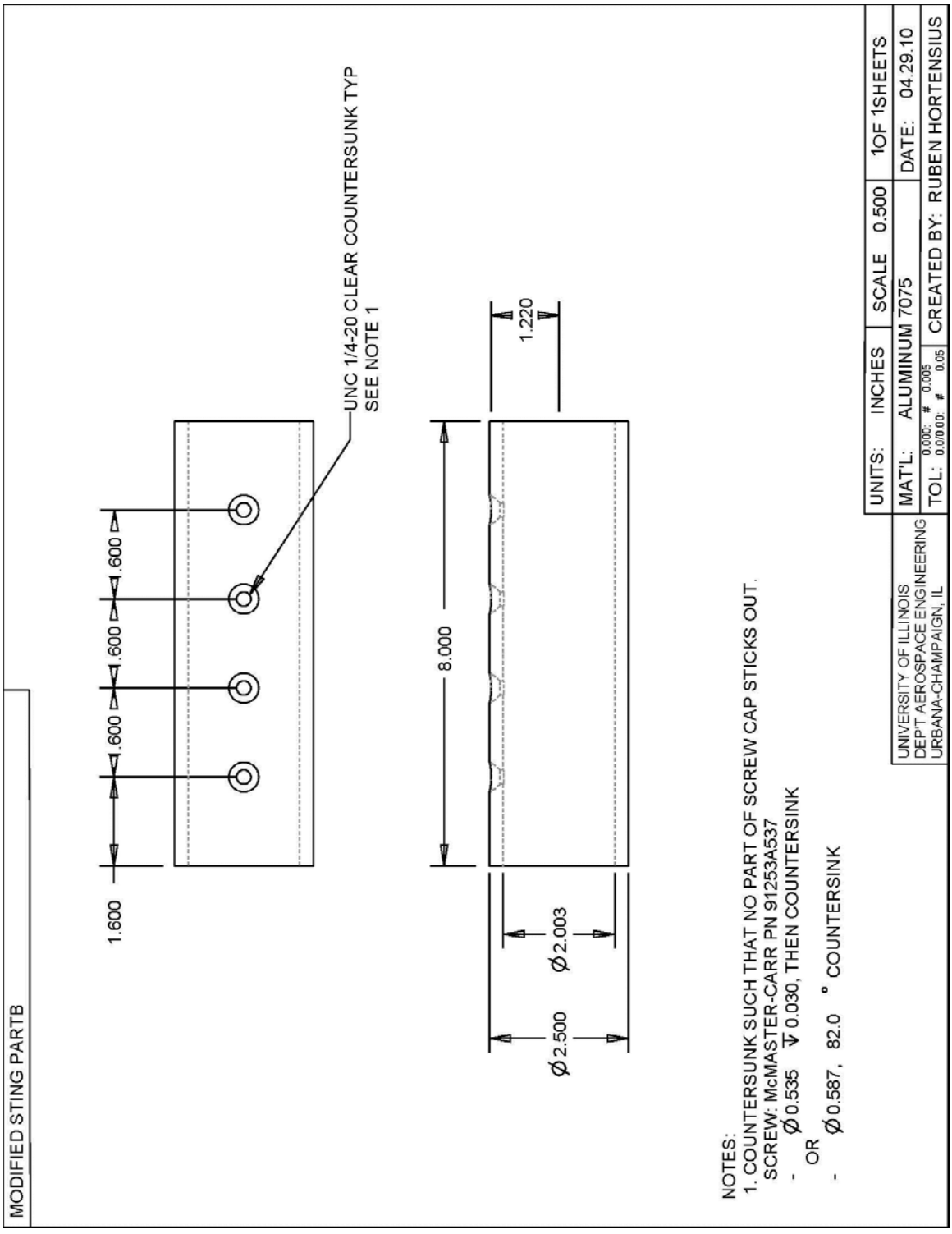

Fig. B.2. Sting Part B Engineering Drawing.

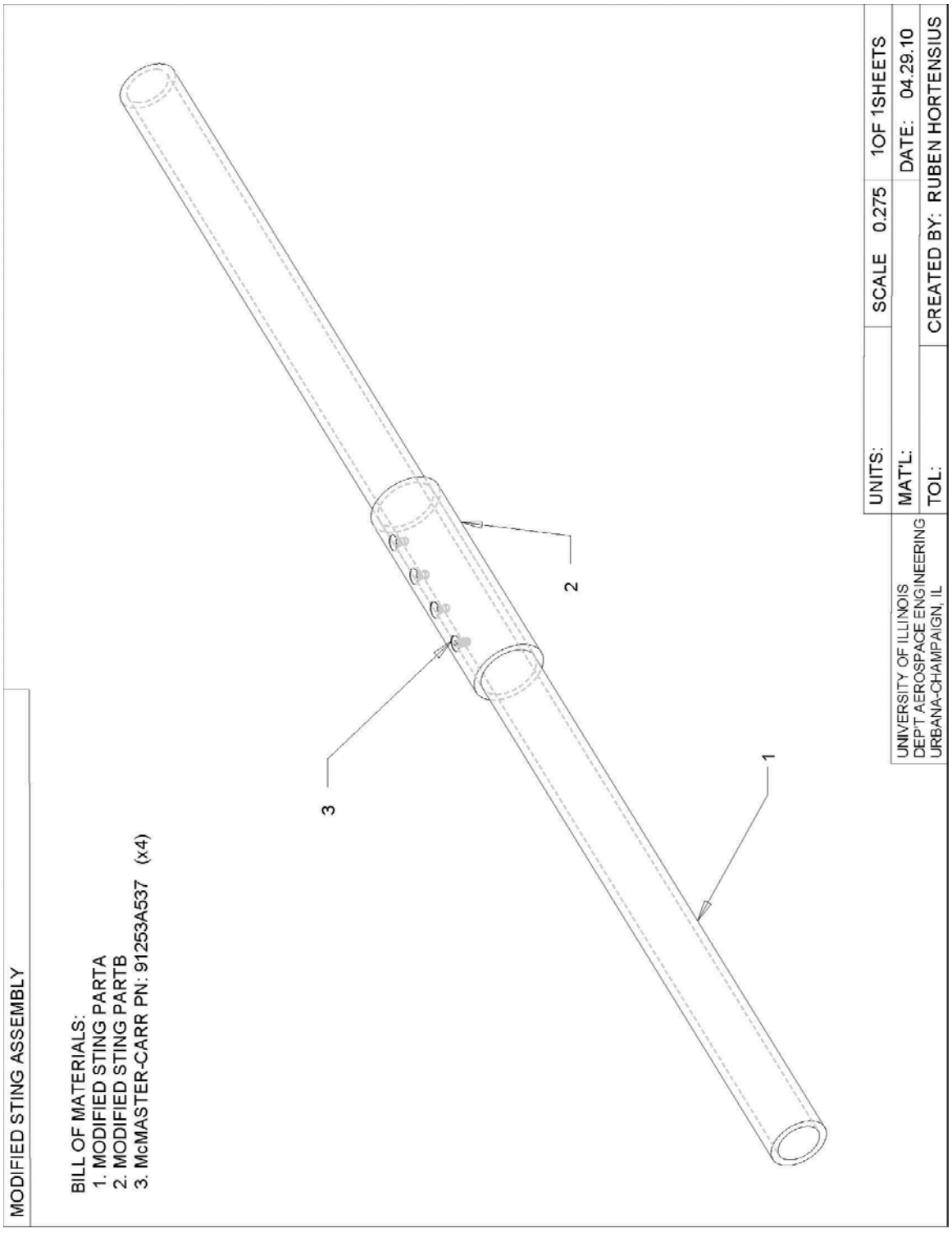

Fig. B.3. Sting Subassembly Drawing.

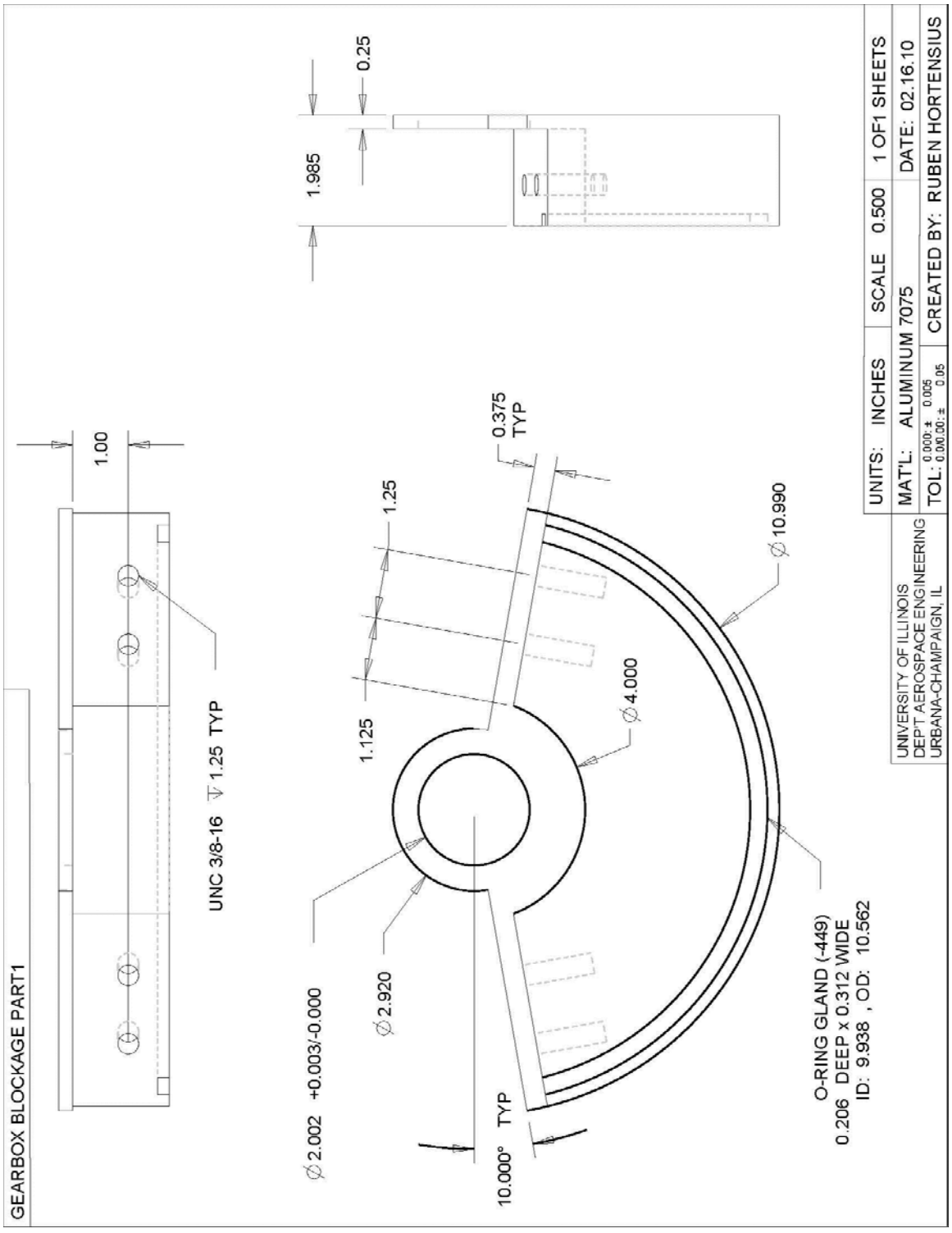

Fig. B.4. Gearbox Blockage Partial Flange Engineering Drawing.

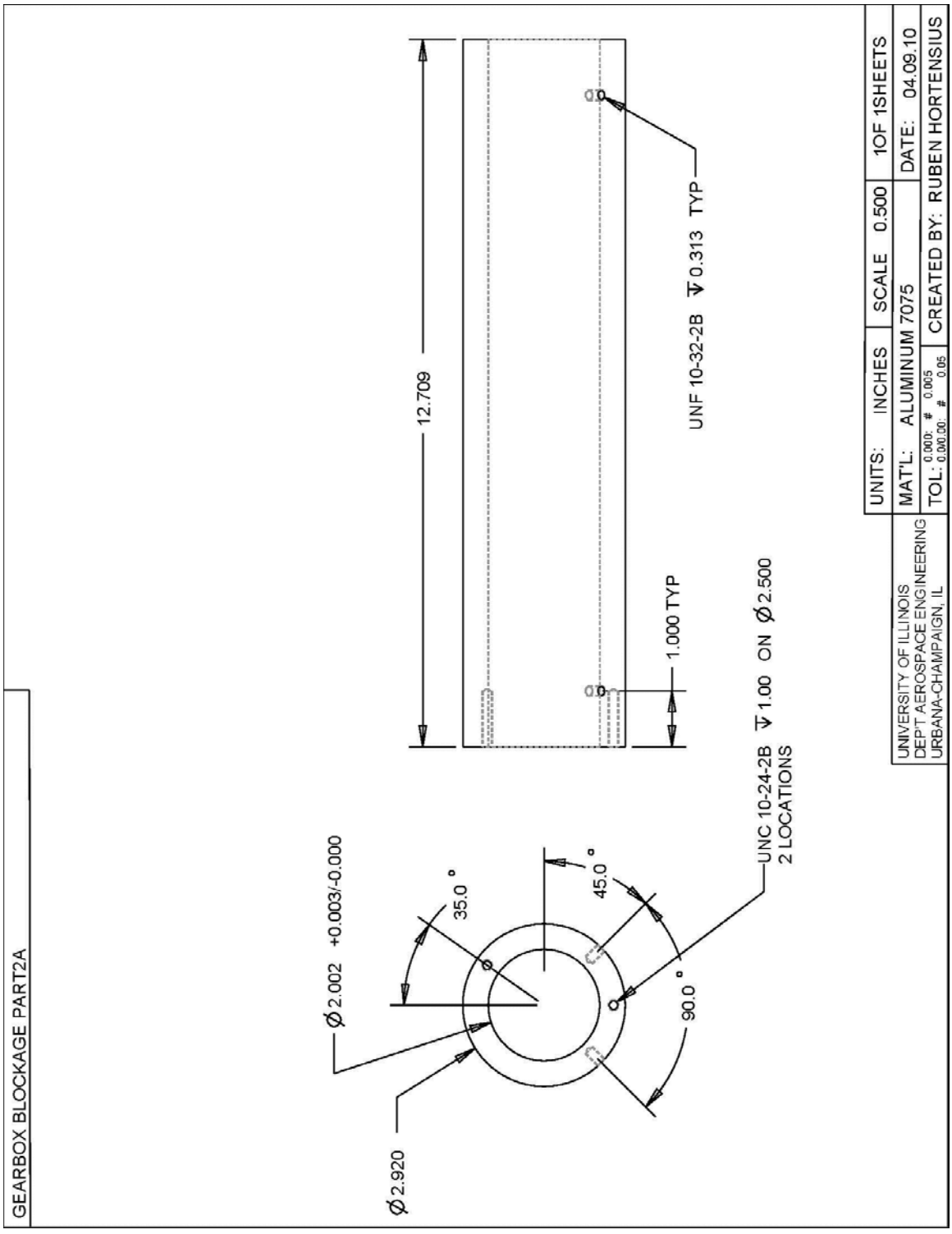

Fig. B.5. Gearbox Blockage Centerbody Part A.

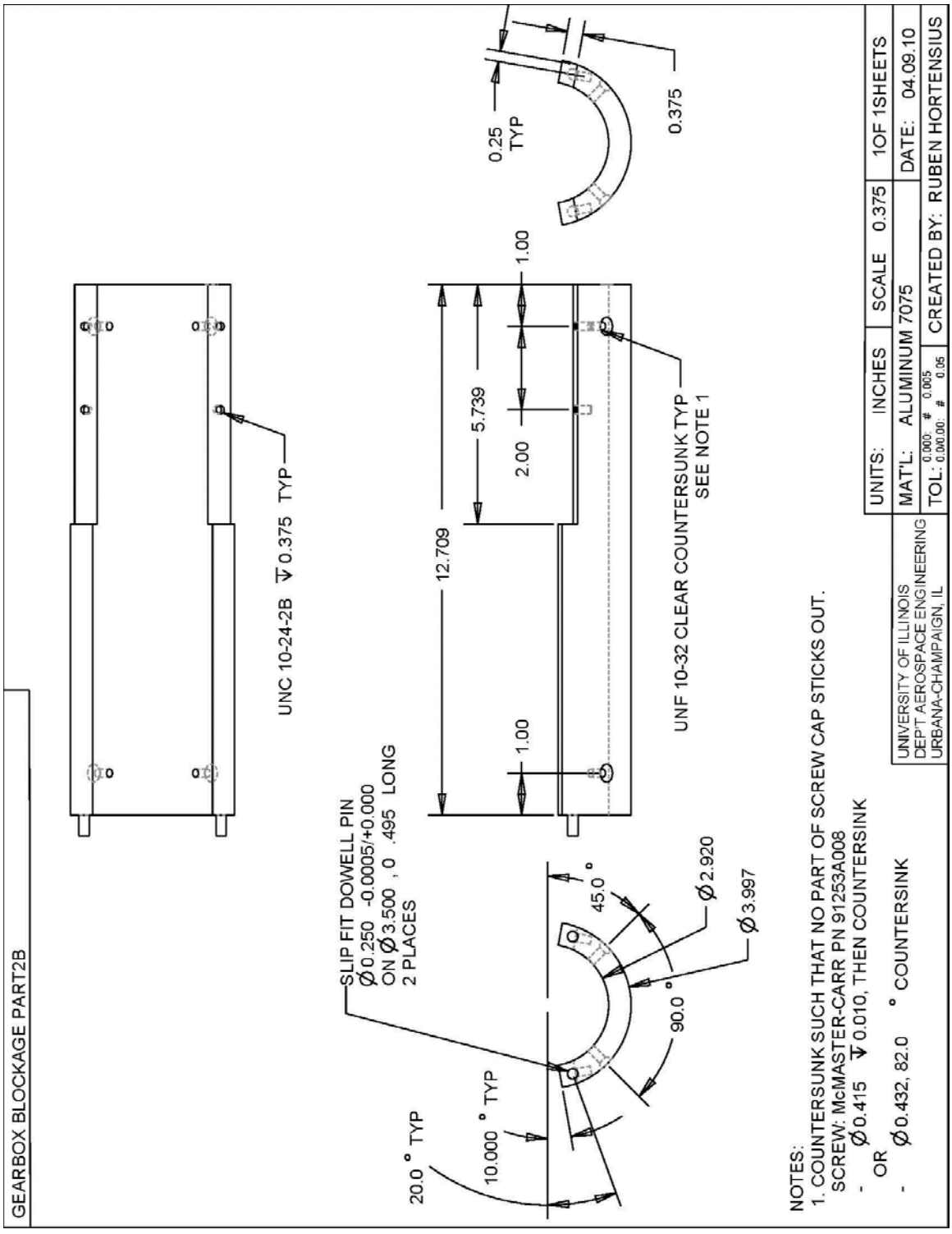

Fig. B.6. Gearbox Blockage Centerbody Part B.

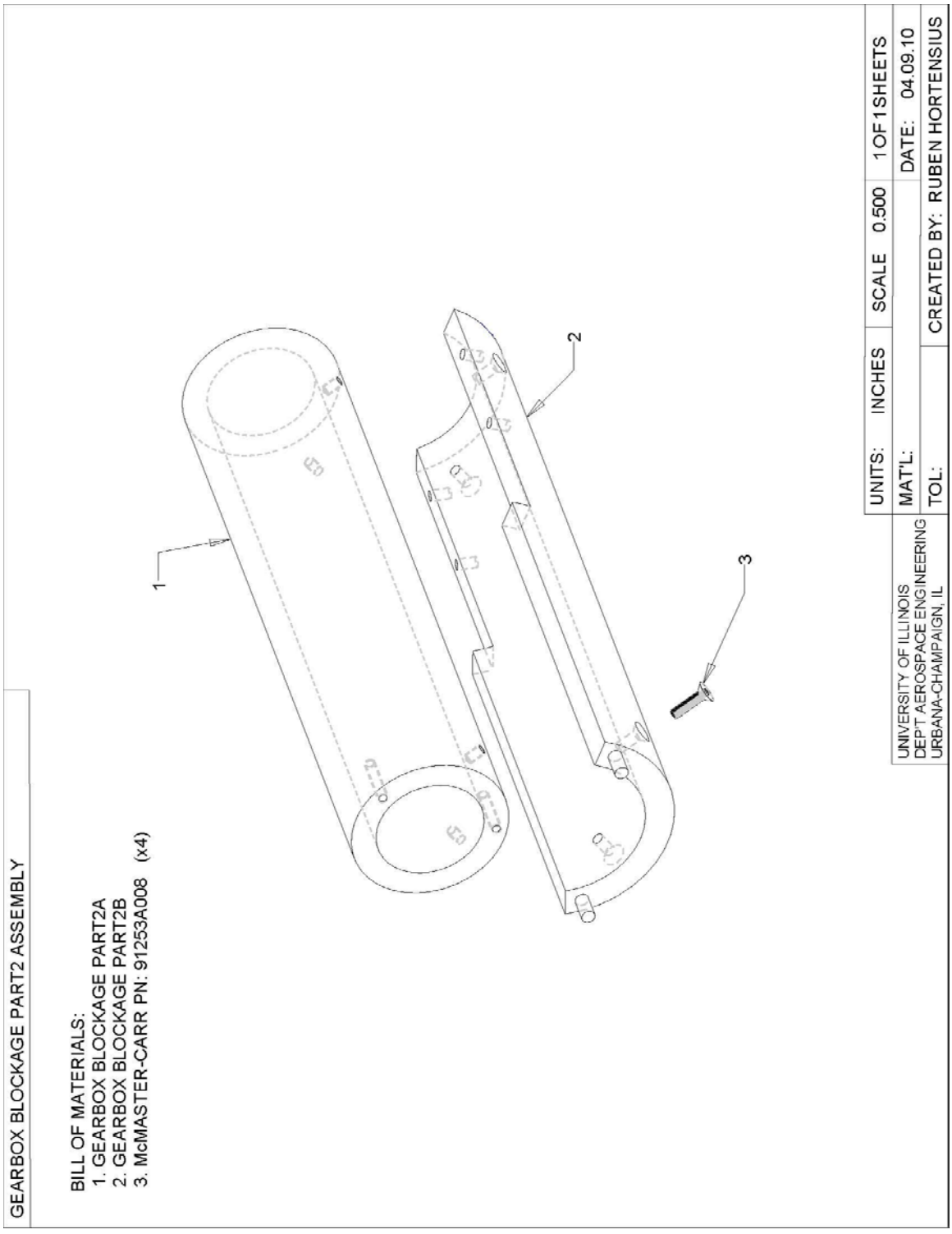

Fig. B.7. Gearbox Blockage Centerbody Subassembly Drawing.

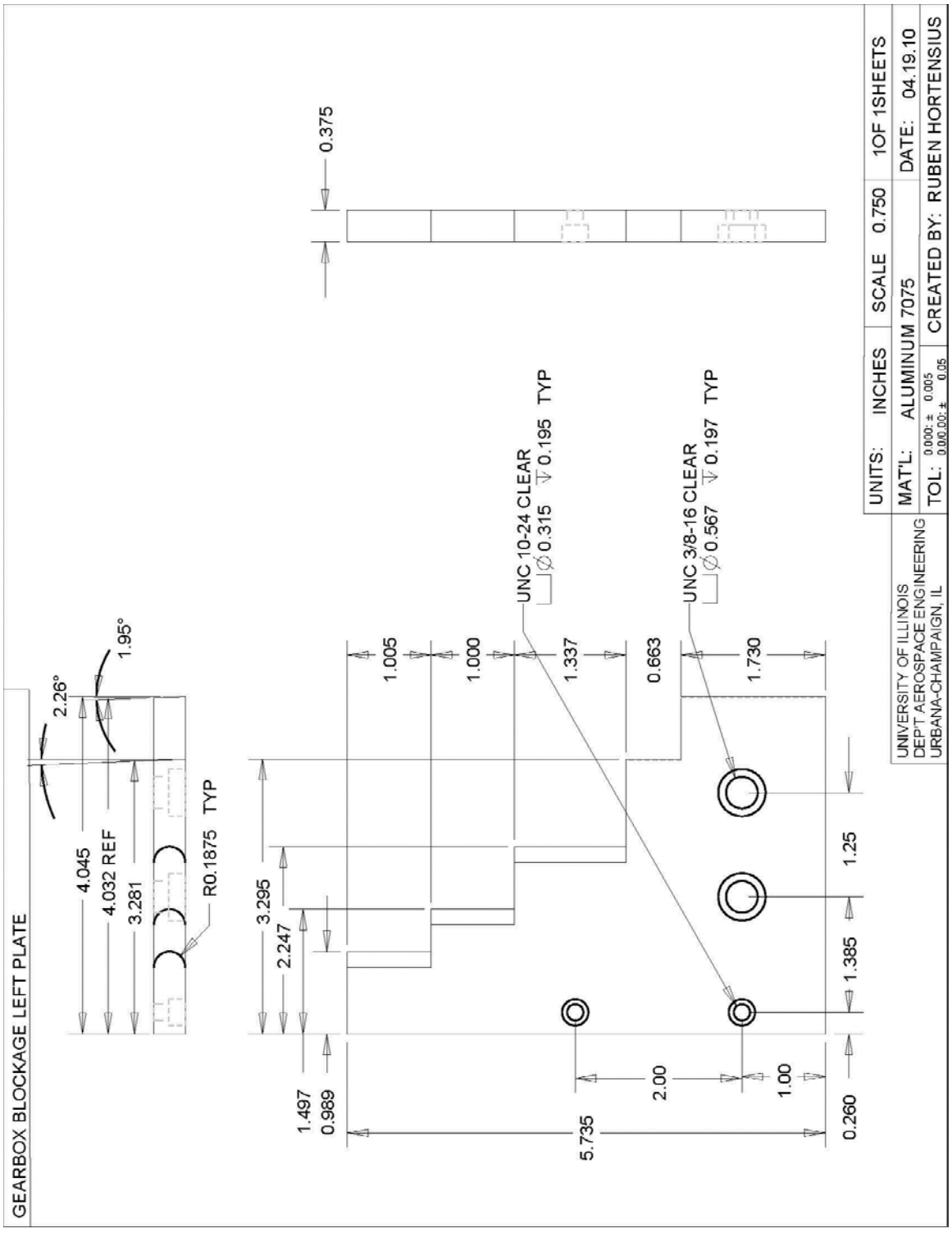

Fig. B.8. Gearbox Blockage Left Plate Engineering Drawing.

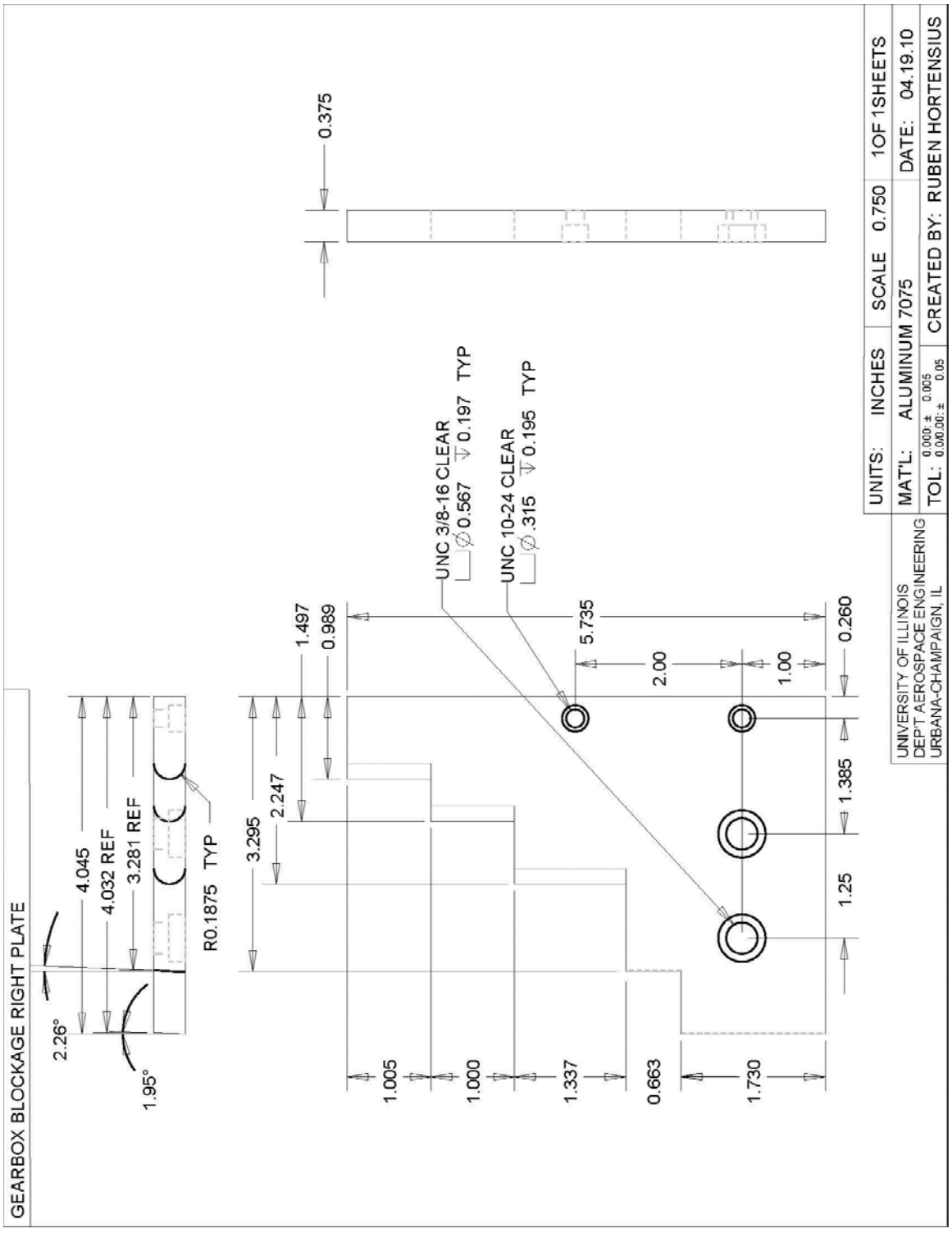

Fig. B.9. Gearbox Blockage Right Plate Engineering Drawing.

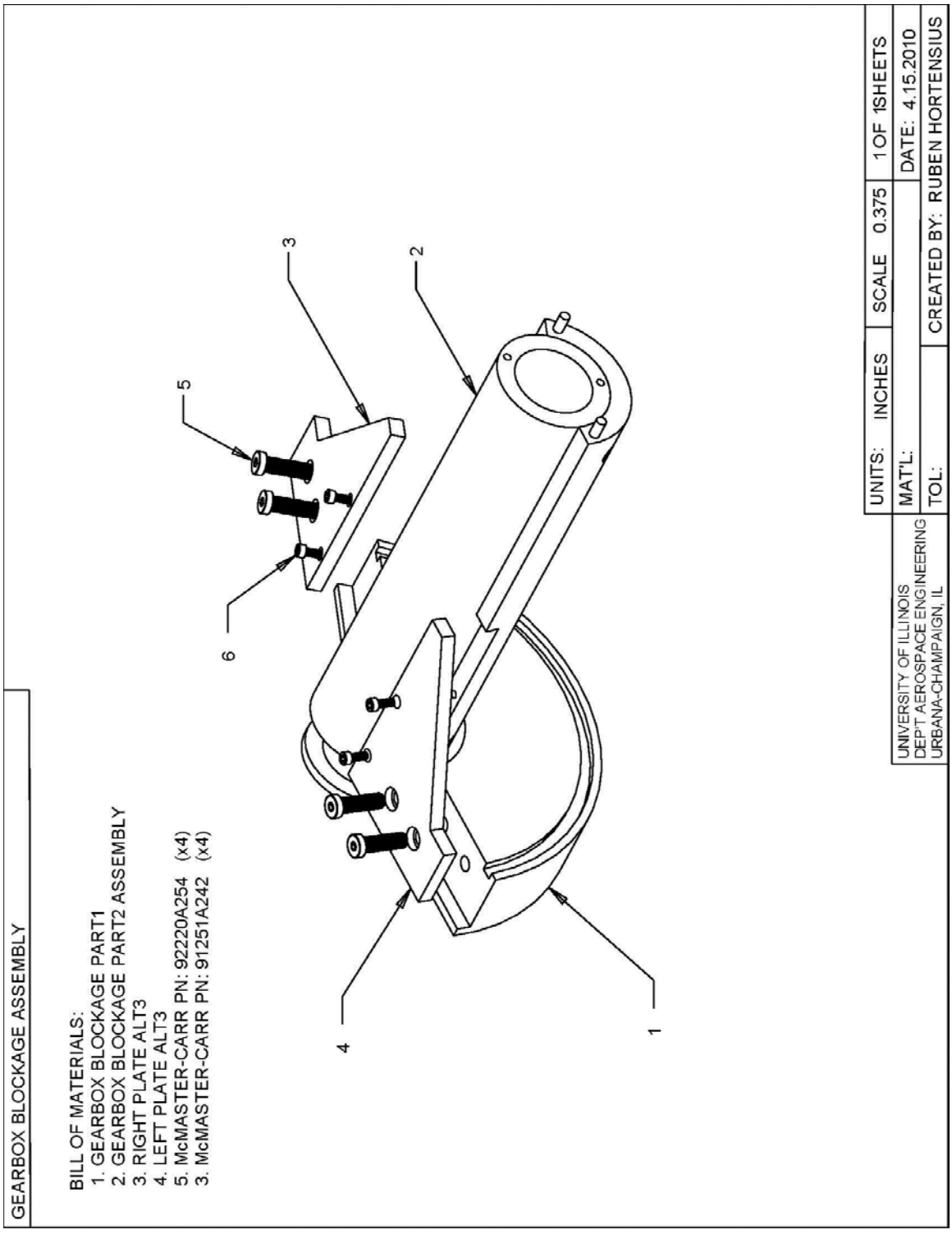

Fig. B.10. Gearbox Blockage Subassembly Drawing.

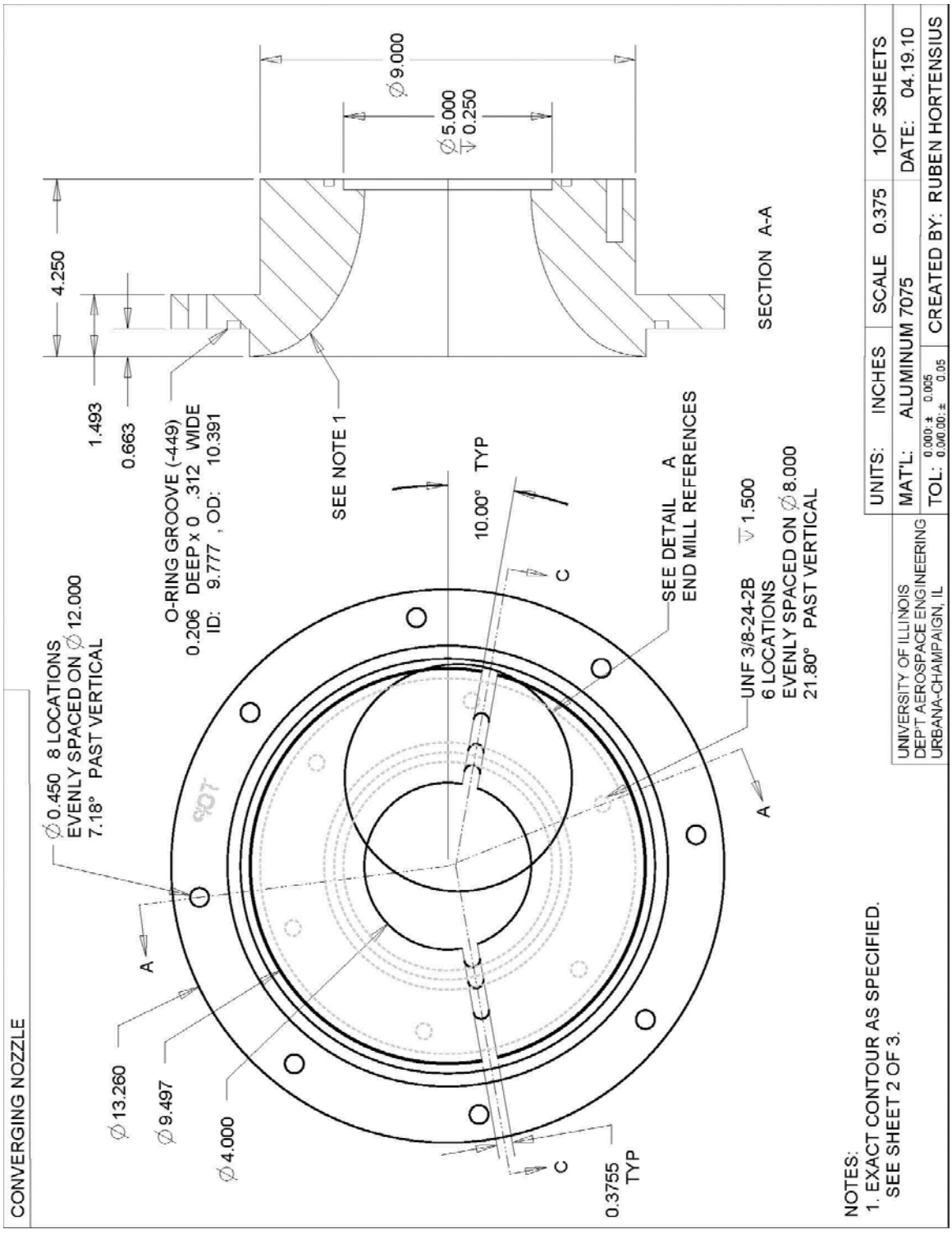

Fig. B.11. Converging Nozzle Engineering Drawing.

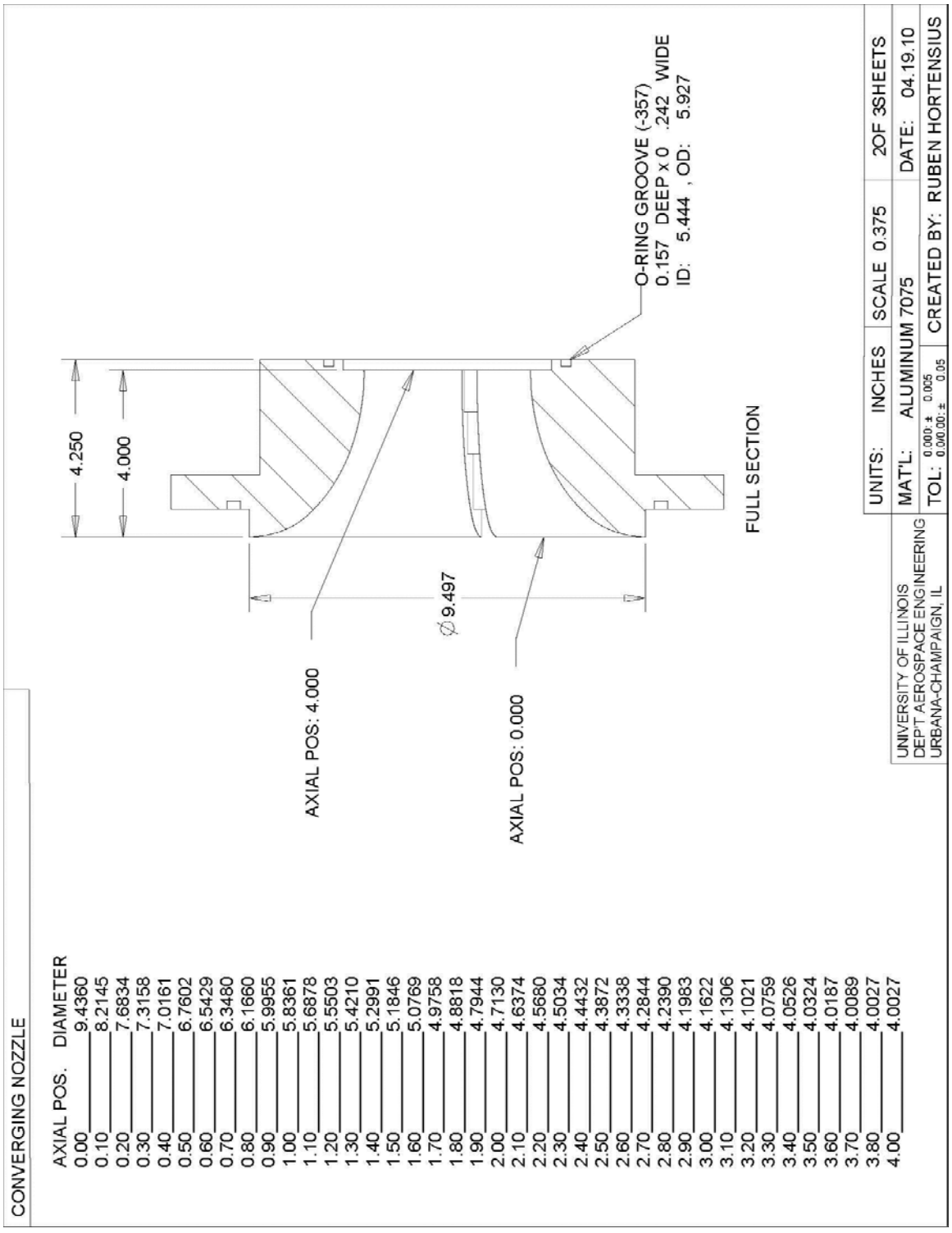

Fig. B.11 (cont.). Converging Nozzle Engineering Drawing.

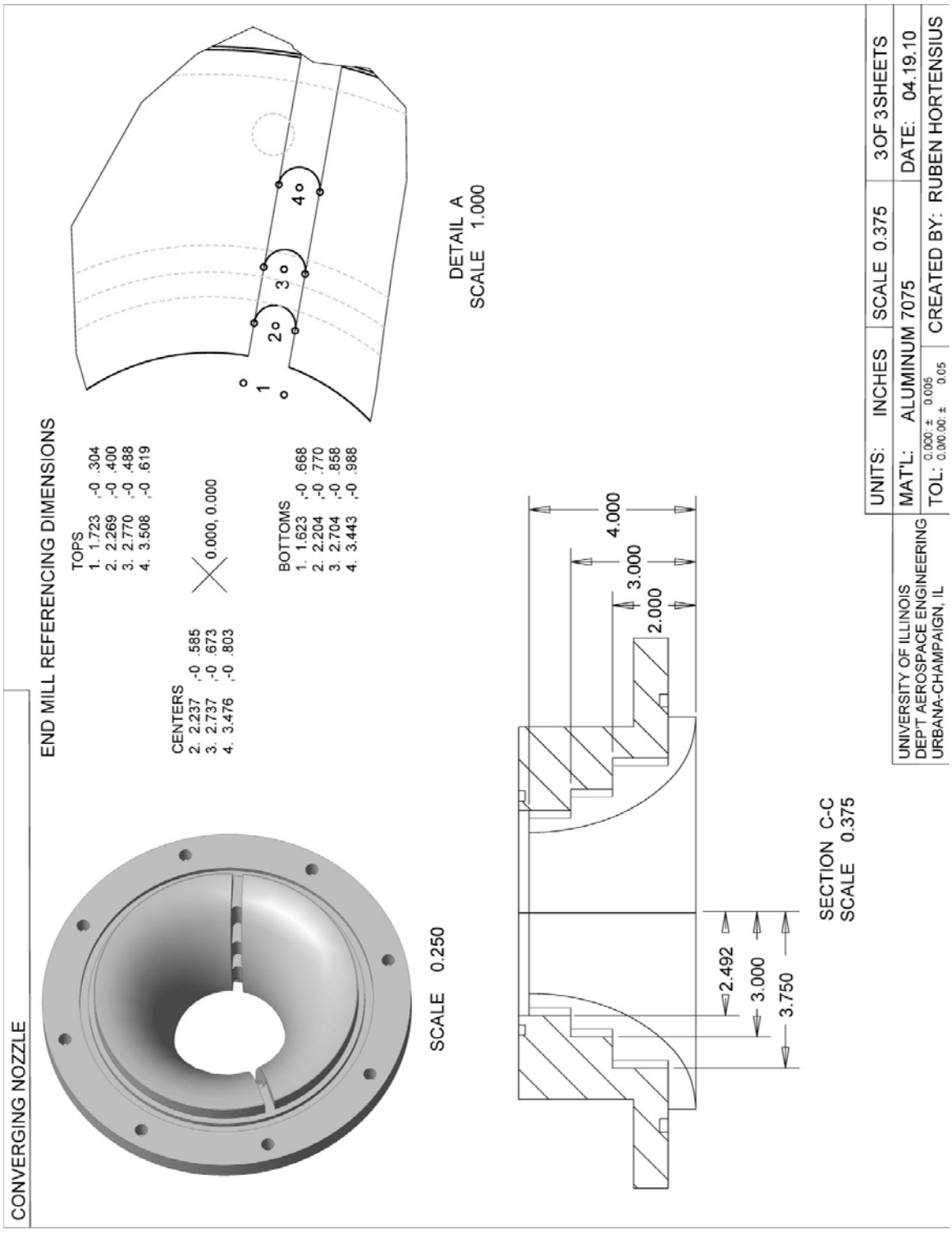

Fig. B.11 (cont.). Converging Nozzle Engineering Drawing.

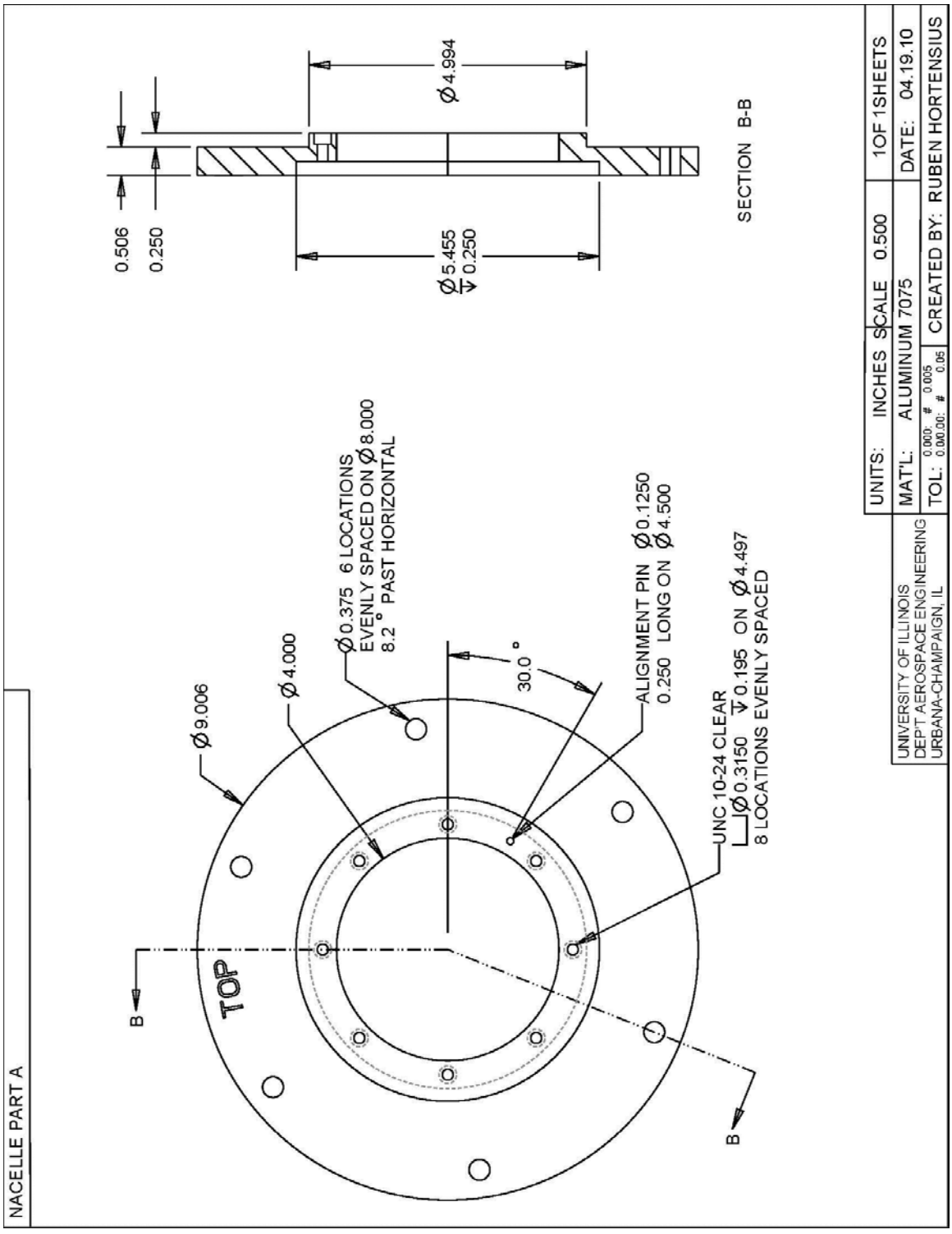

Fig. B.12. Nacelle Part A Engineering Drawing.

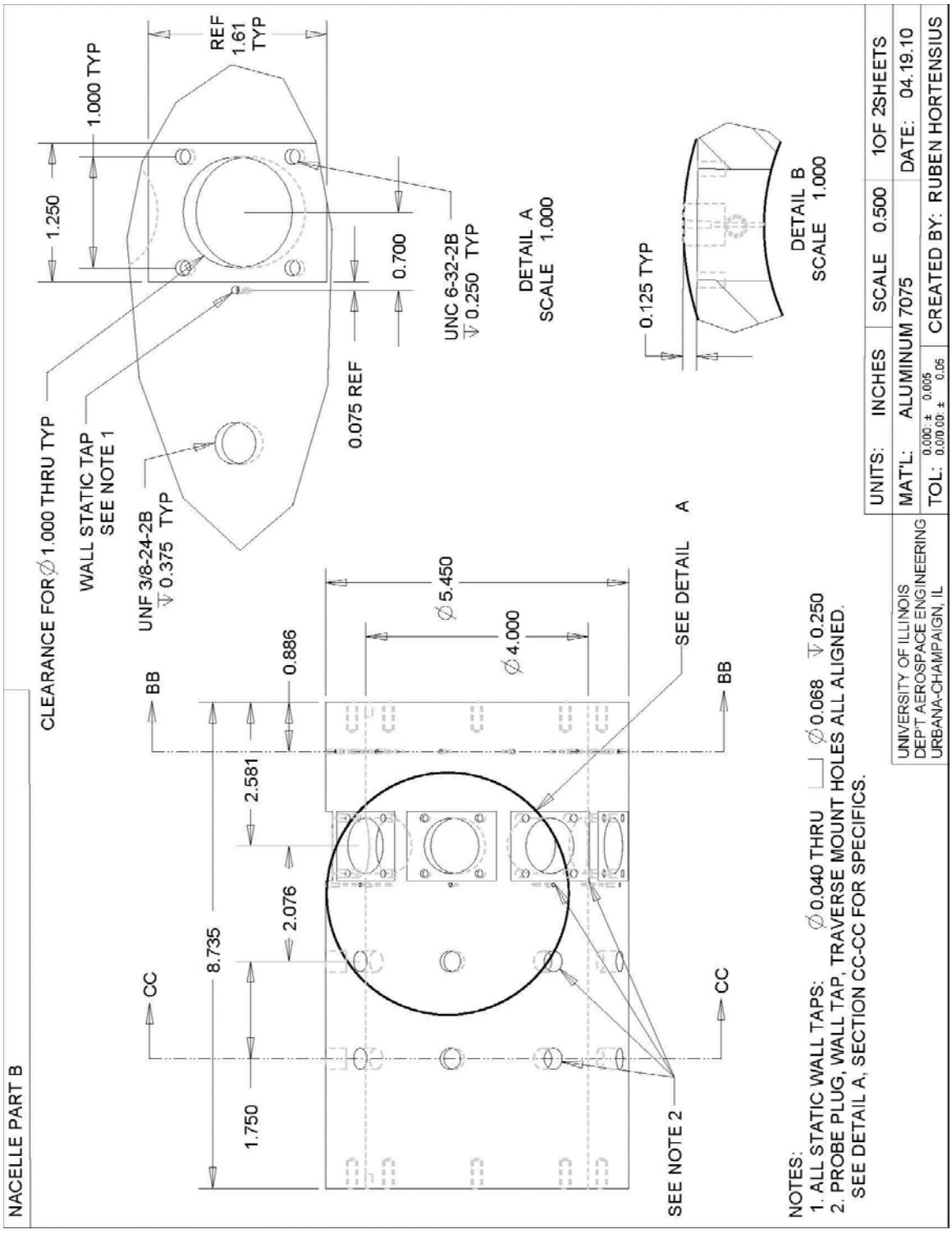

Fig. B.13. Nacelle Part B Engineering Drawing.

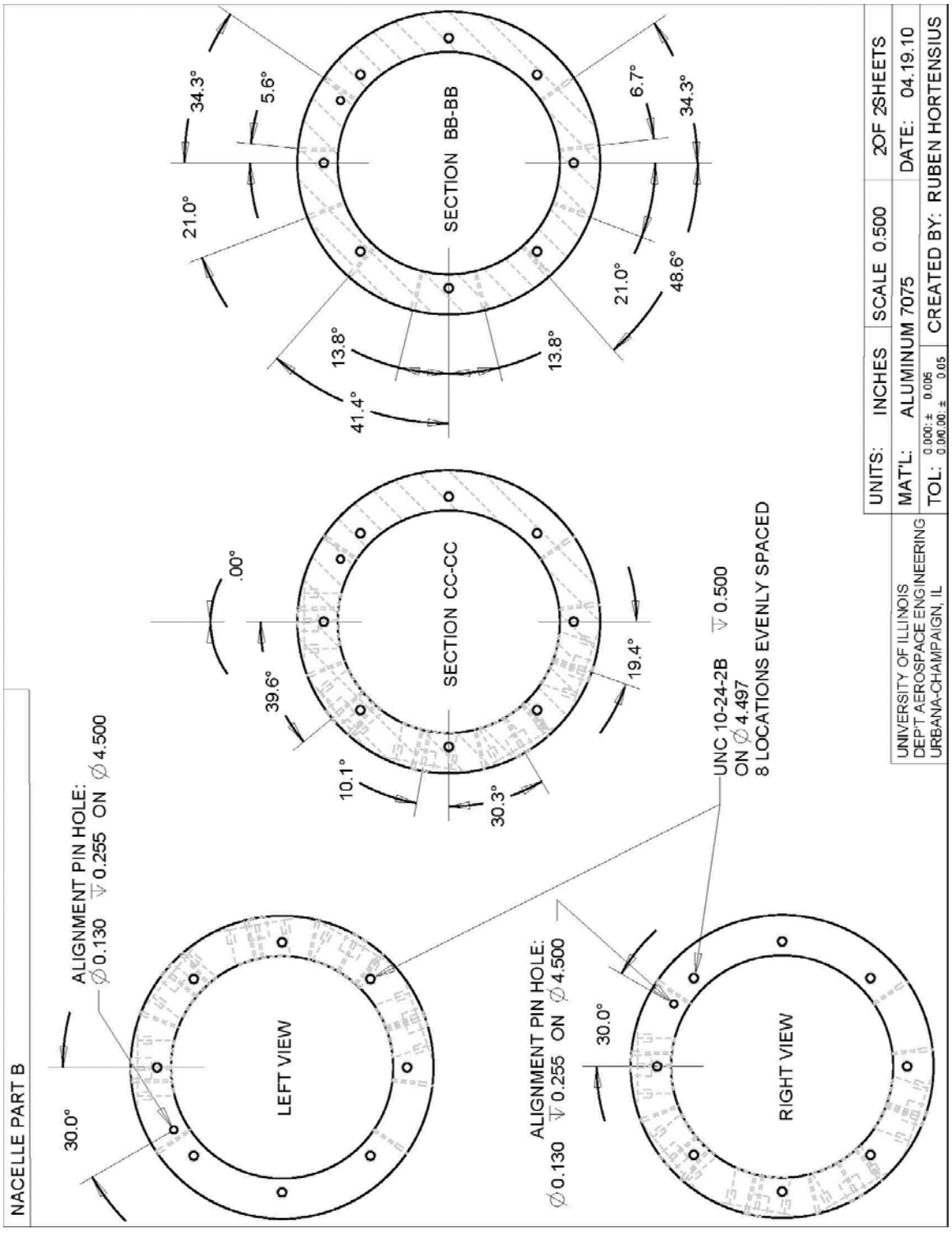

Fig. B.13 (cont.). Nacelle Part B Engineering Drawing.

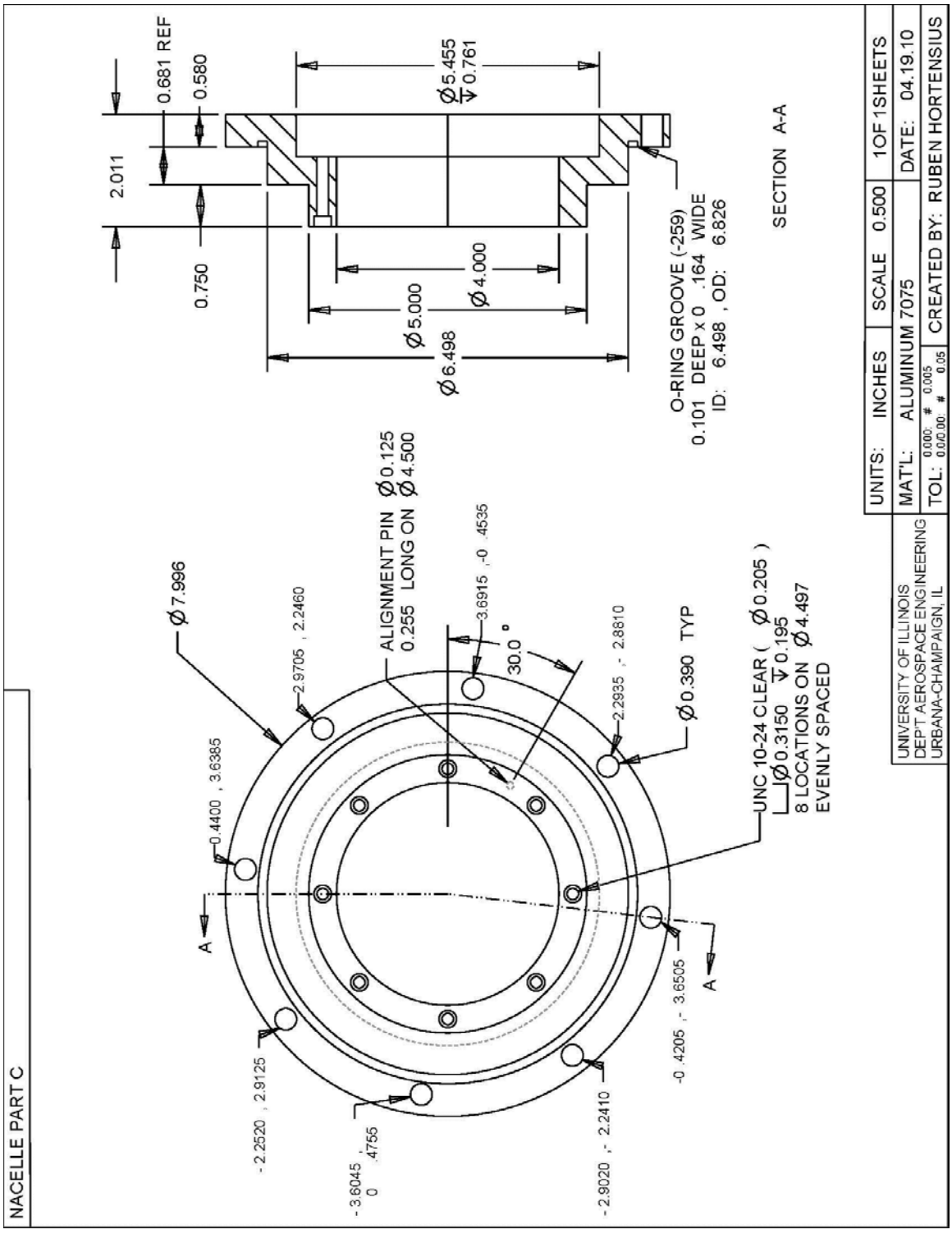

Fig. B.14. Nacelle Part C Engineering Drawing.

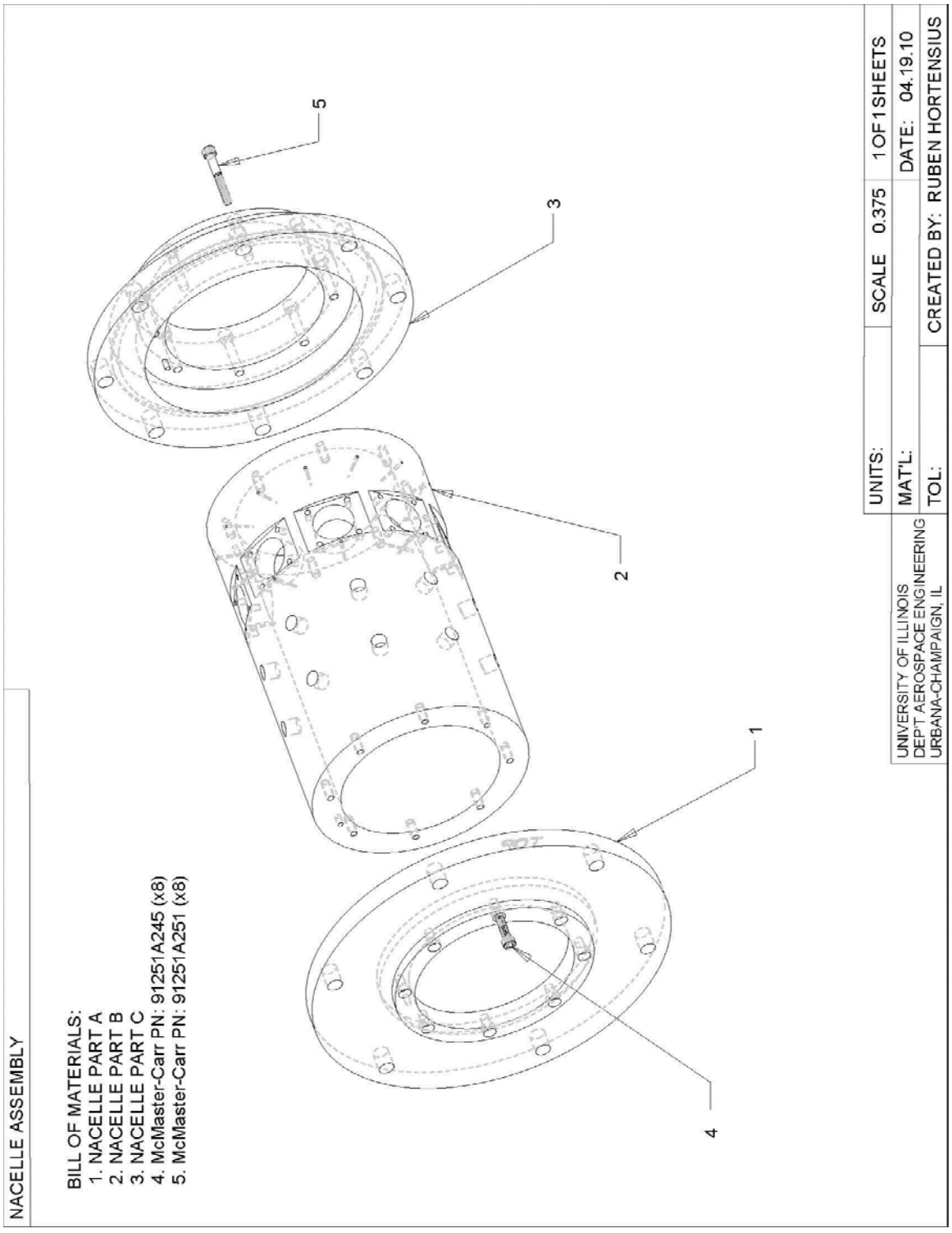

Fig. B.15. Nacelle Subassembly Drawing.

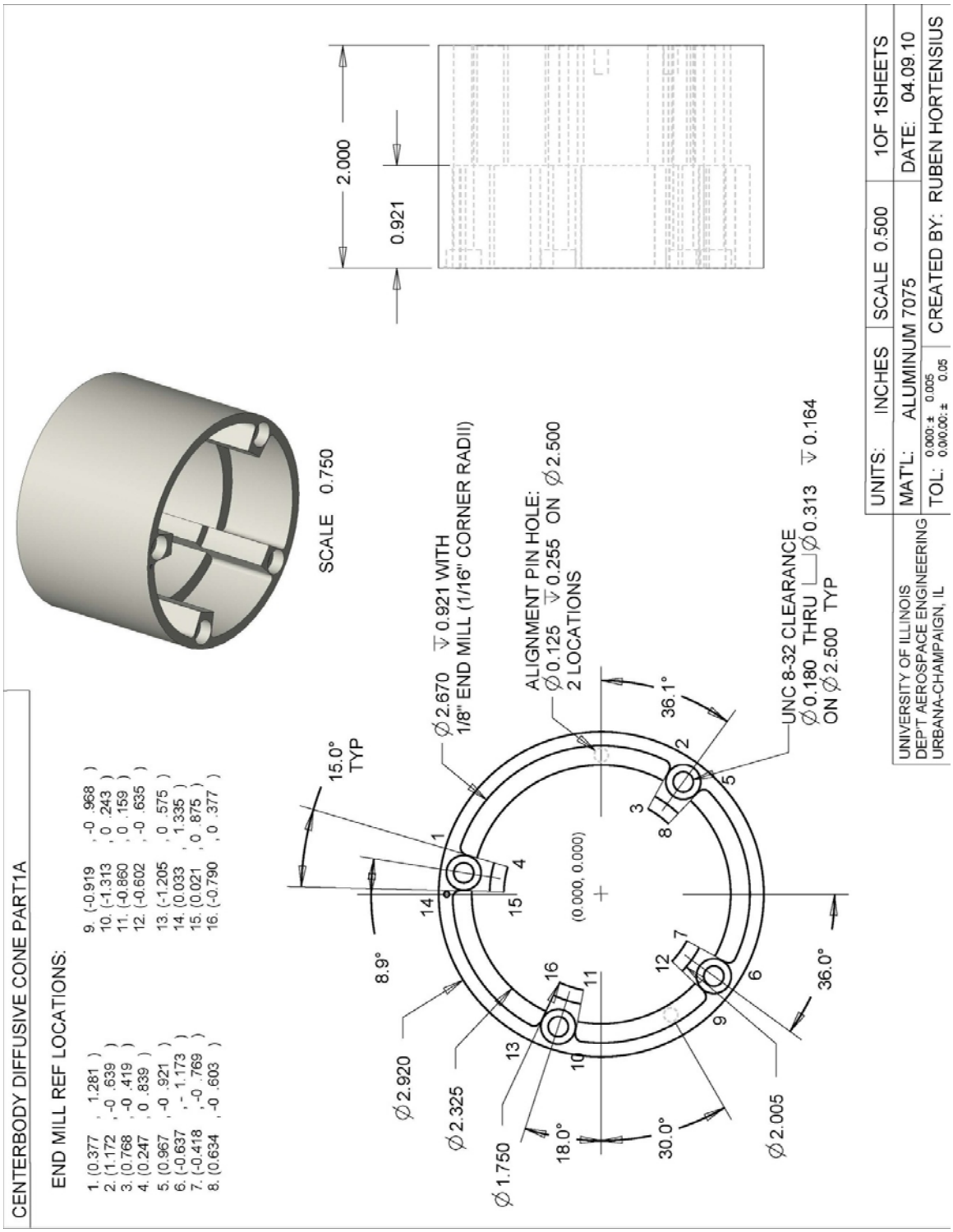

Fig. B.16. Pressure Line Reversal Cavity Reversal Cap Engineering Drawing.

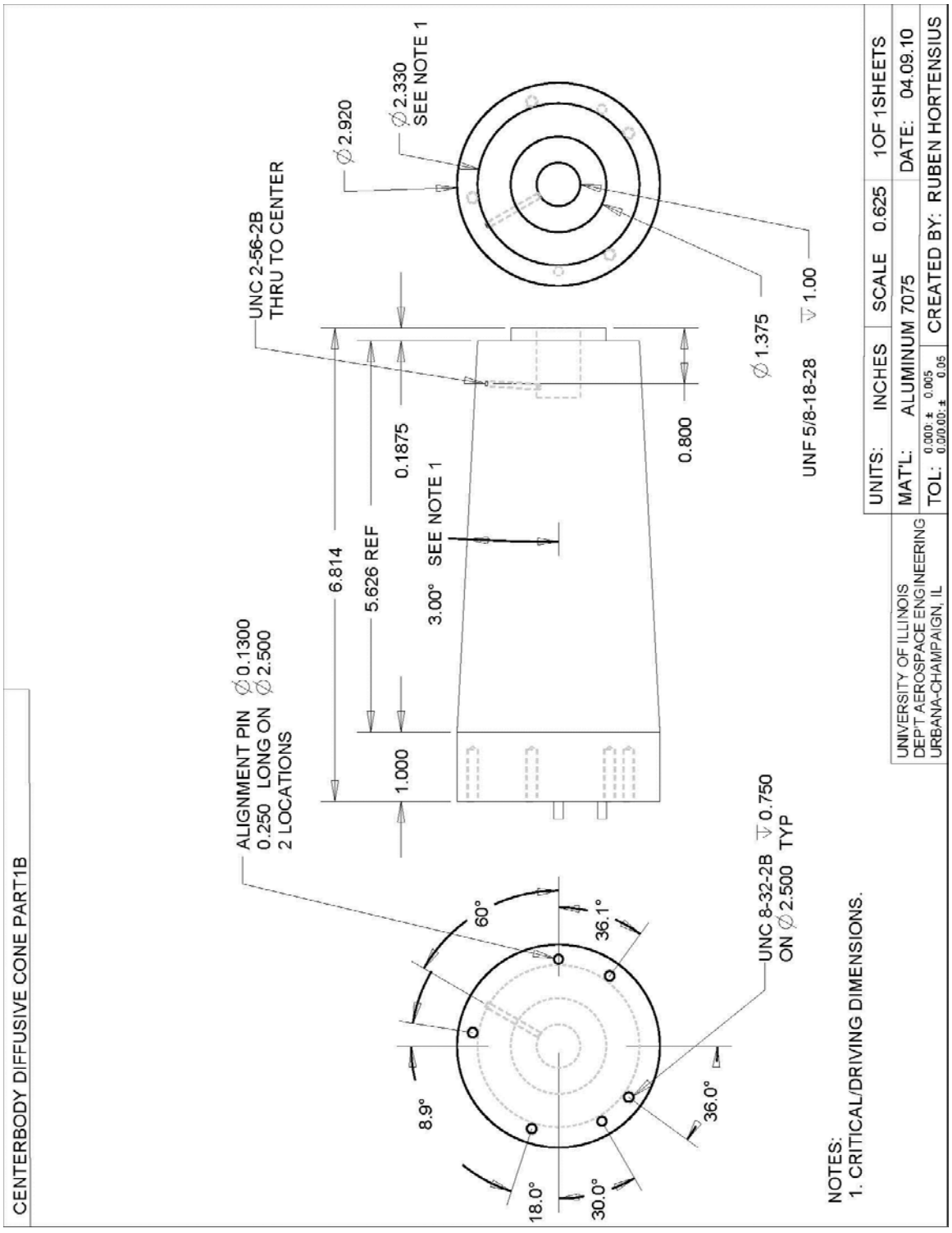

Fig. B.17. Centerbody Diffusive Cone Part A (forward segment) Engineering Drawing.

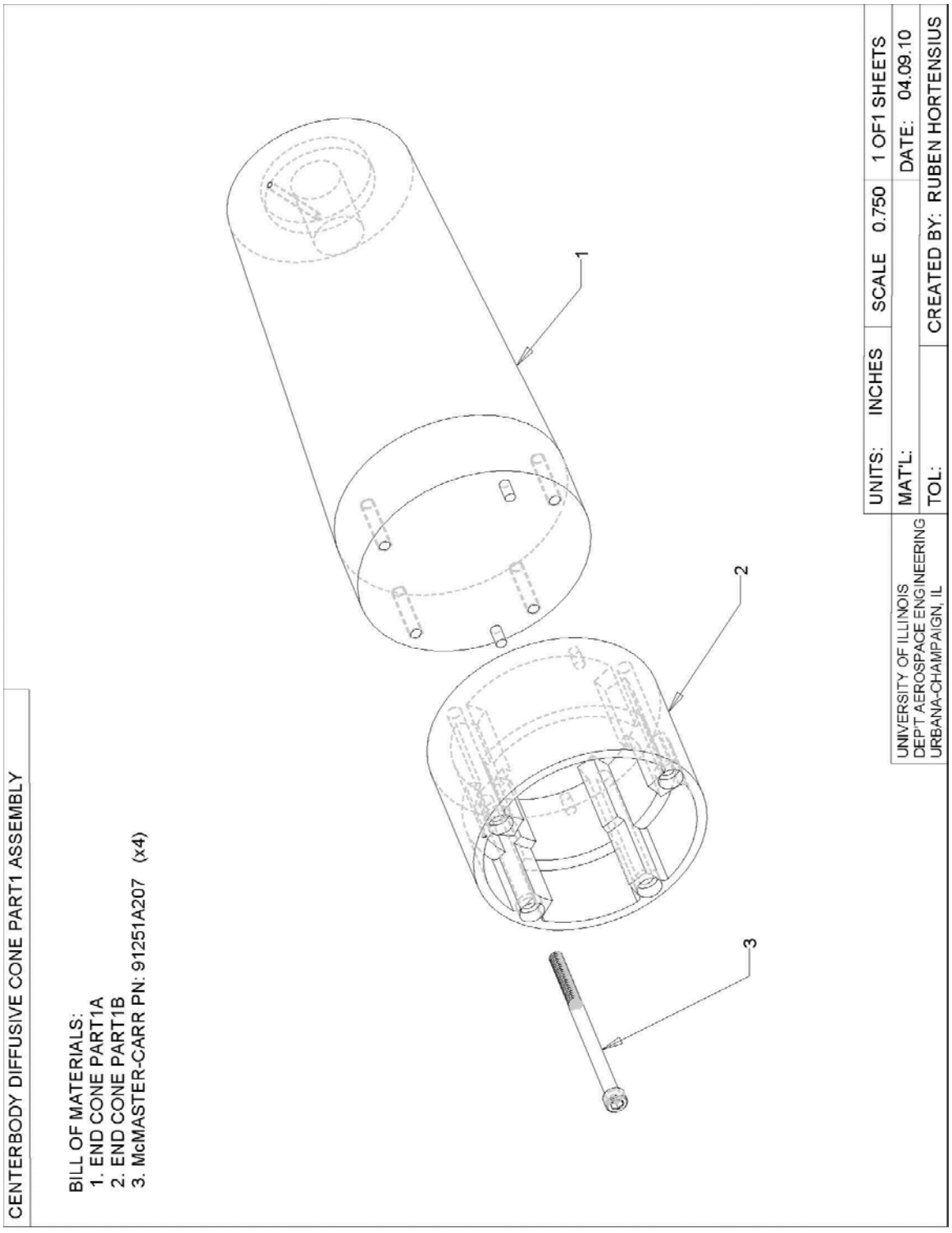

Fig. B.18. Forward Centerbody Subassembly Drawing.

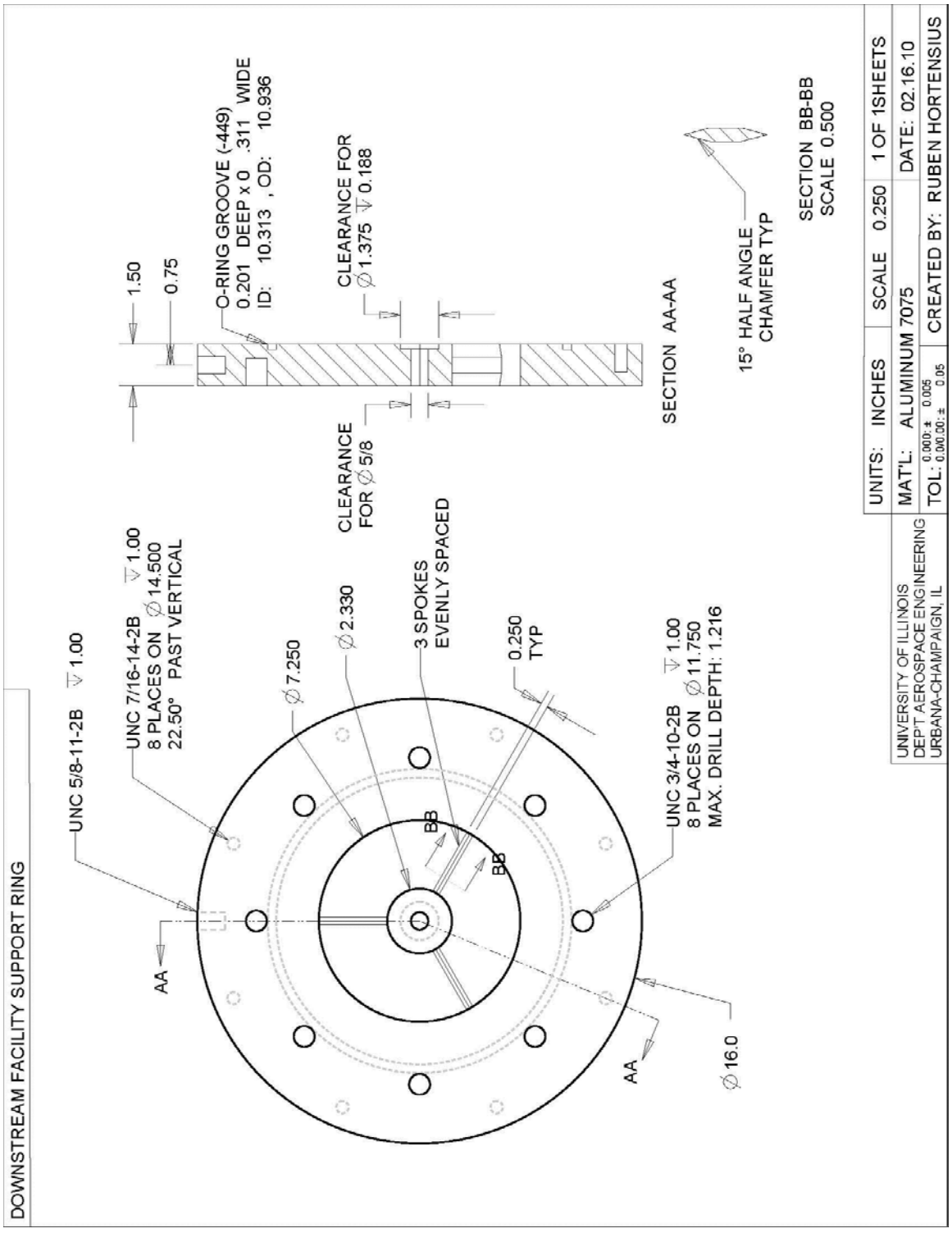

Fig. B.19. Downstream Facility Support Ring Engineering Drawing.

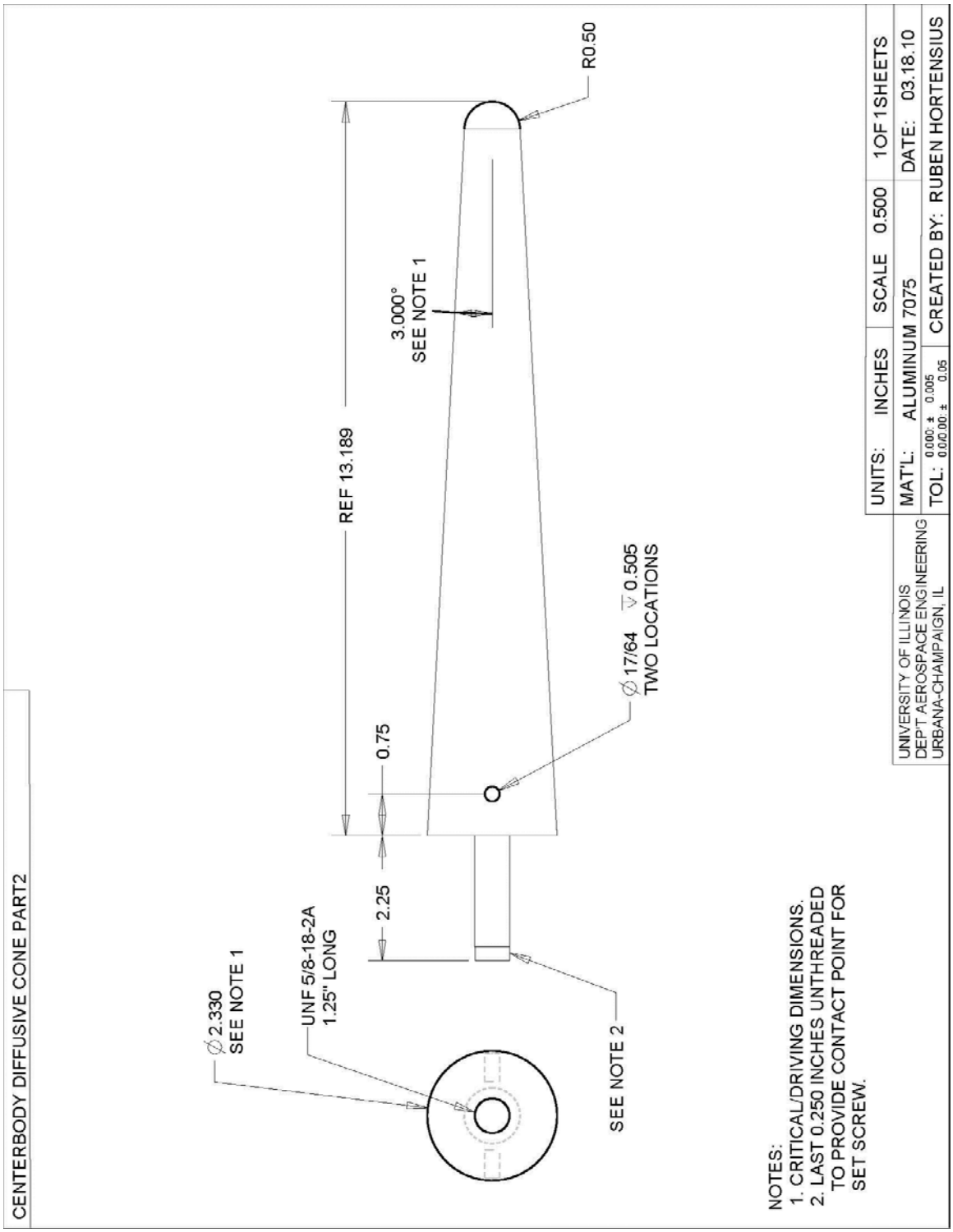

Fig. B.20. Centerbody Diffusive Cone Part B (aft segment) Engineering Drawing.

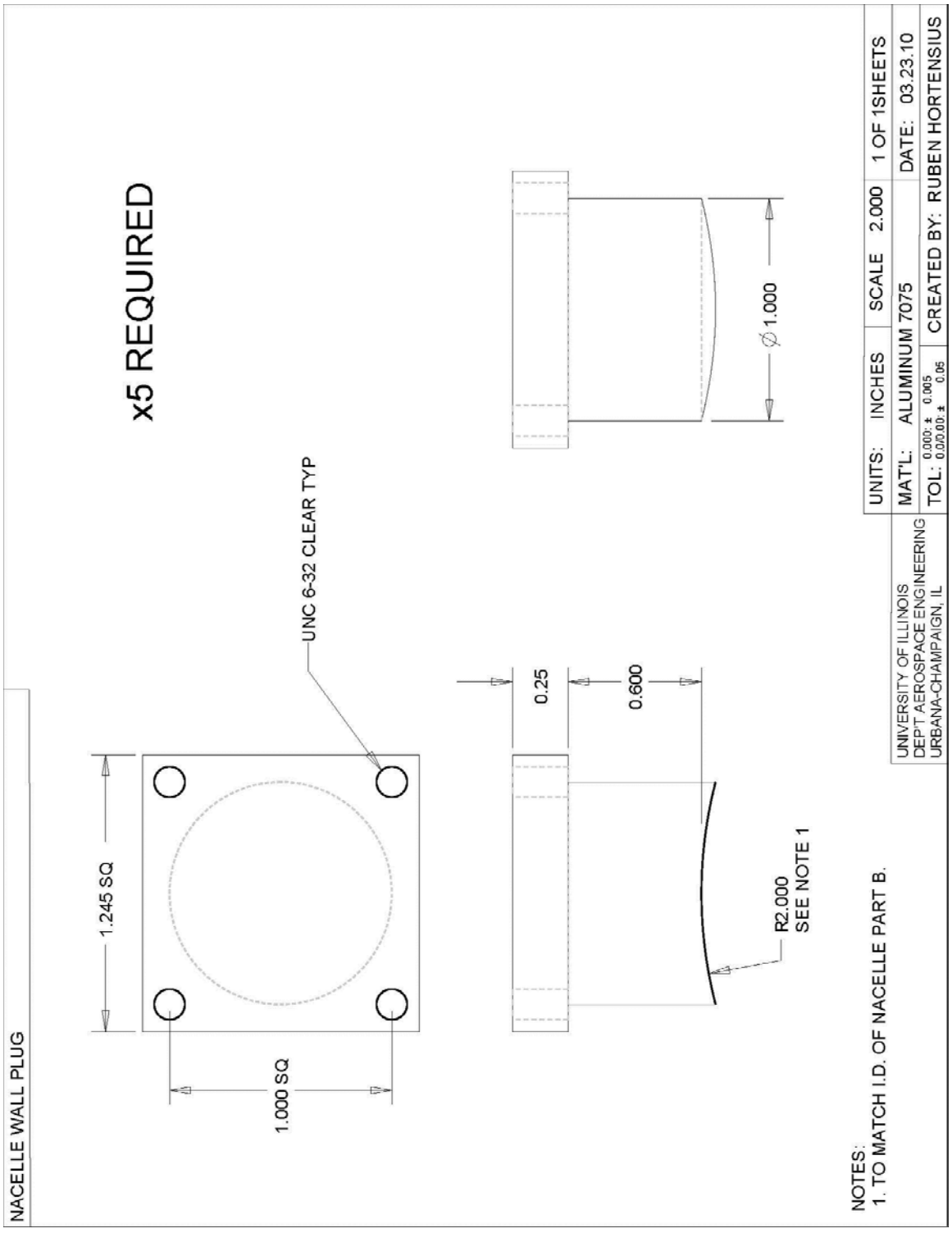

Fig. B.21. Nacelle Wall Plug Engineering Drawing.

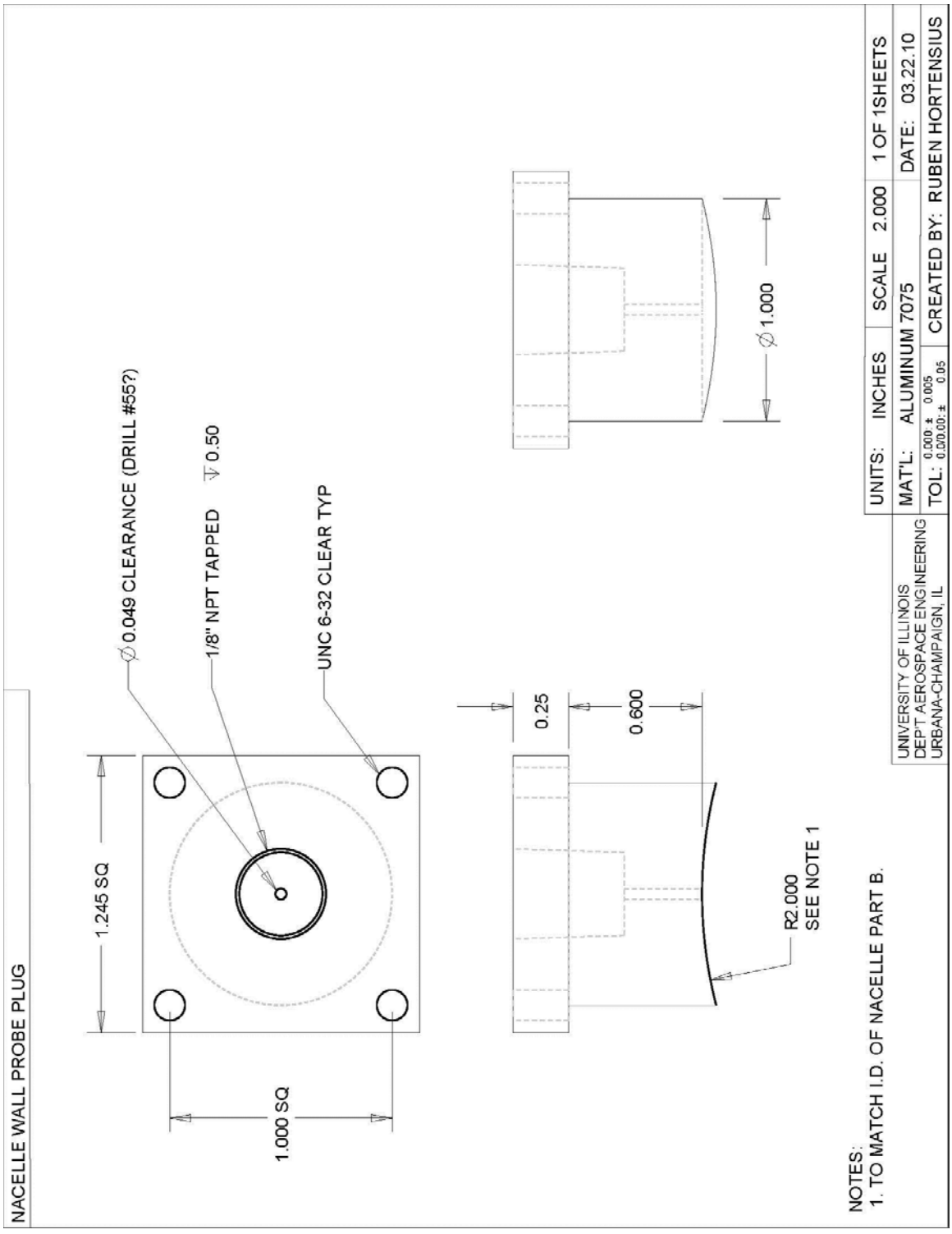

Fig. B.22. Nacelle Wall Probe Plug Engineering Drawing.

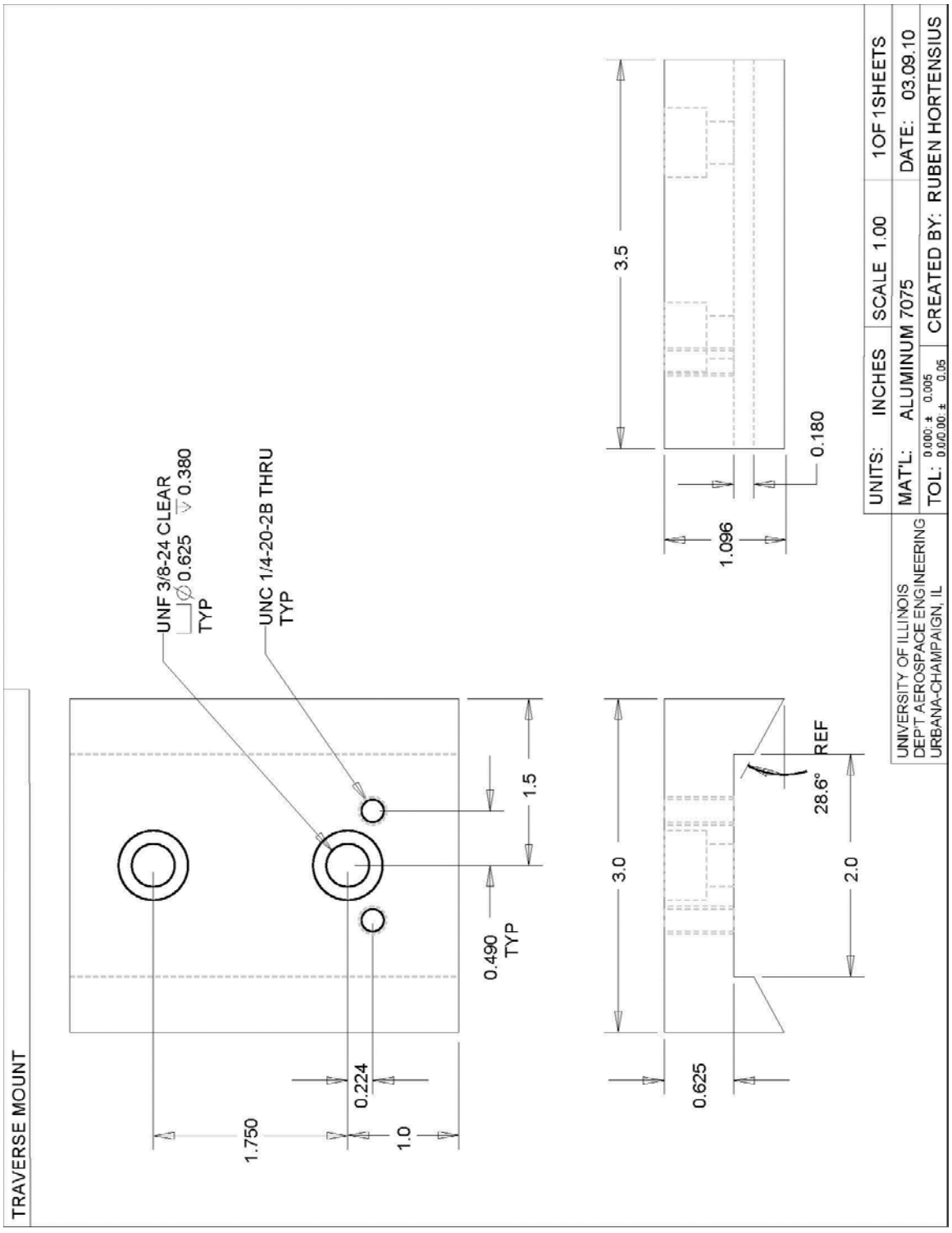

Fig. B.23. Traverse Mount Engineering Drawing.

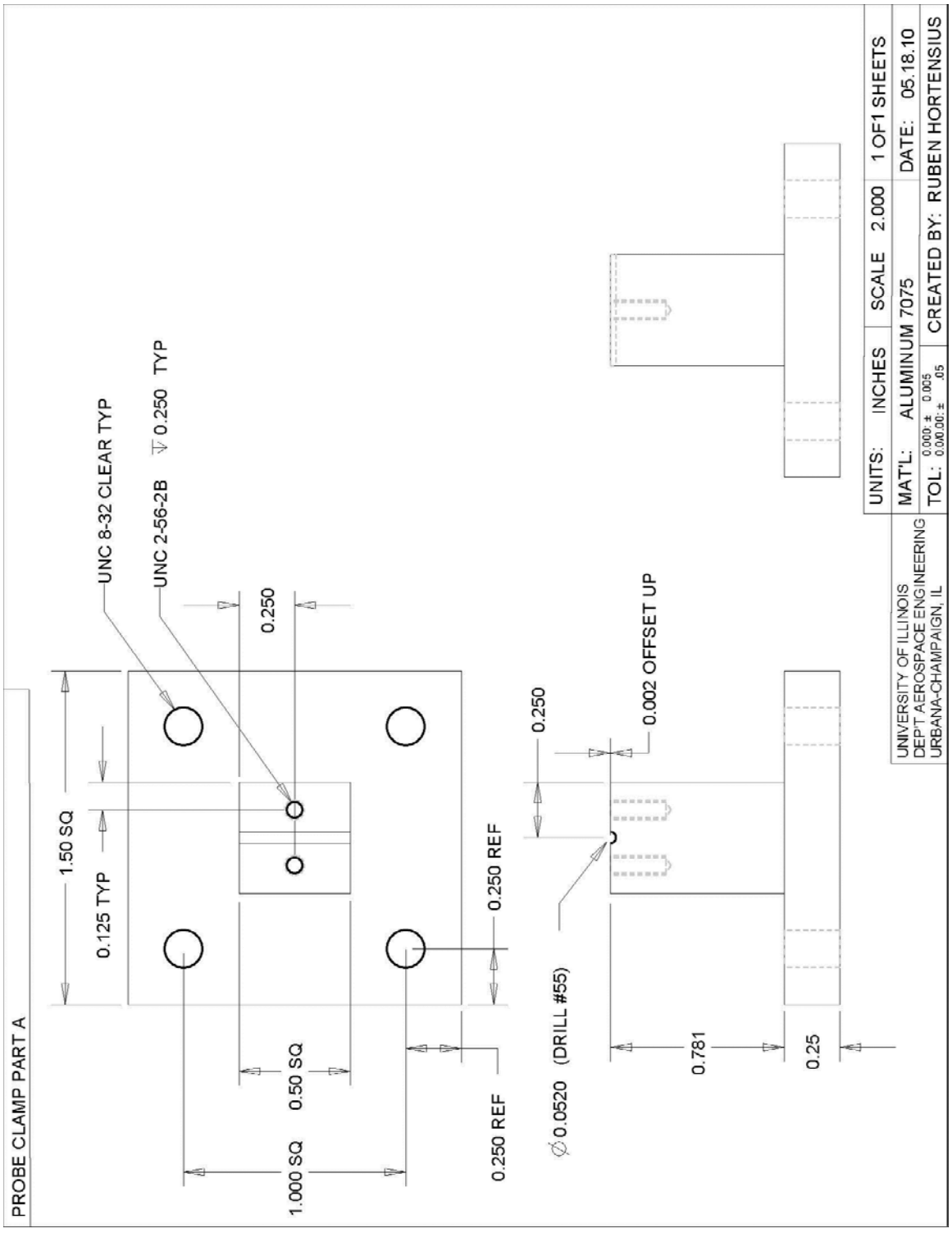

Fig. B.24. Probe Traverse Clamp Part A Engineering Drawing.

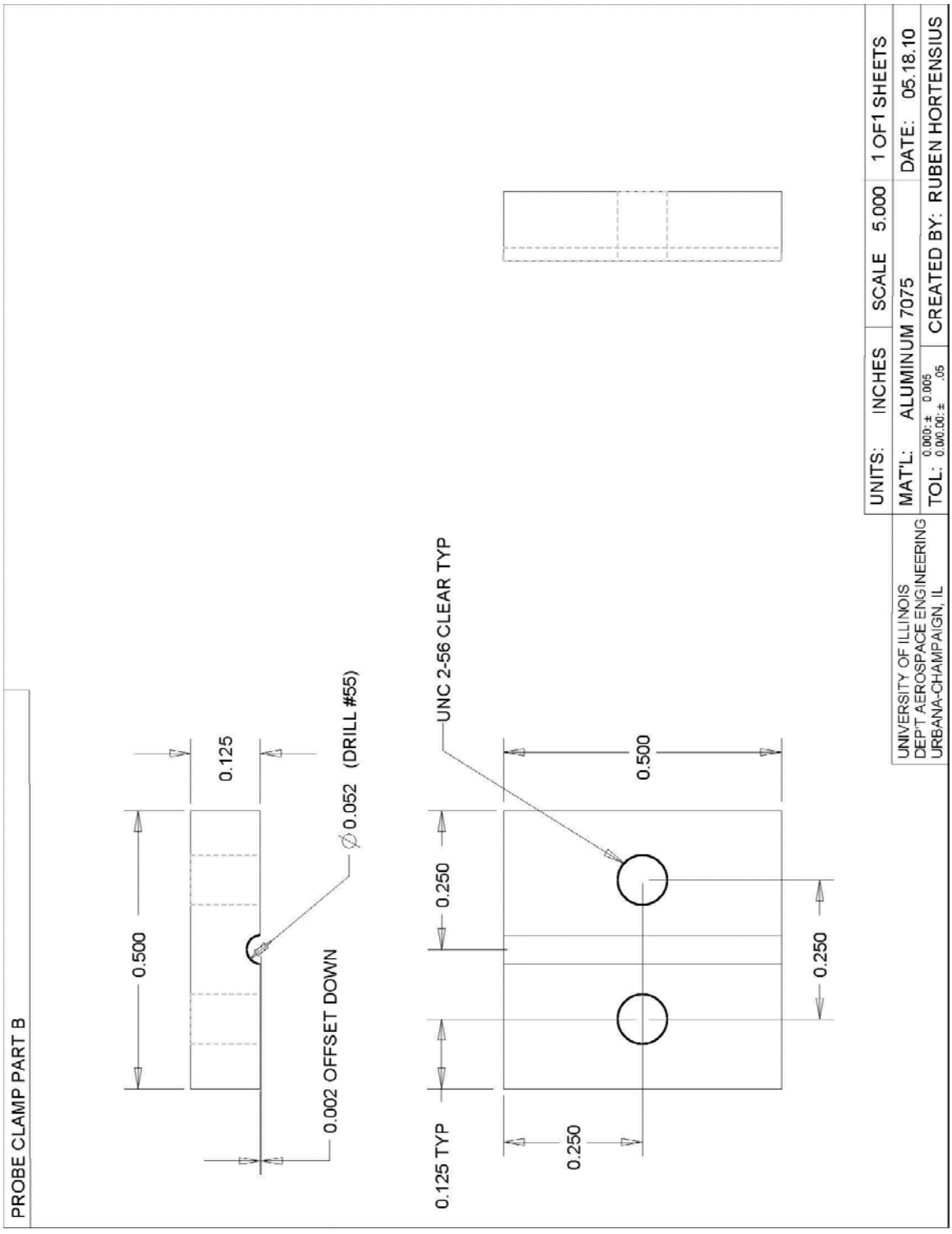

Fig. B.25. Probe Traverse Clamp Part B Engineering Drawing.

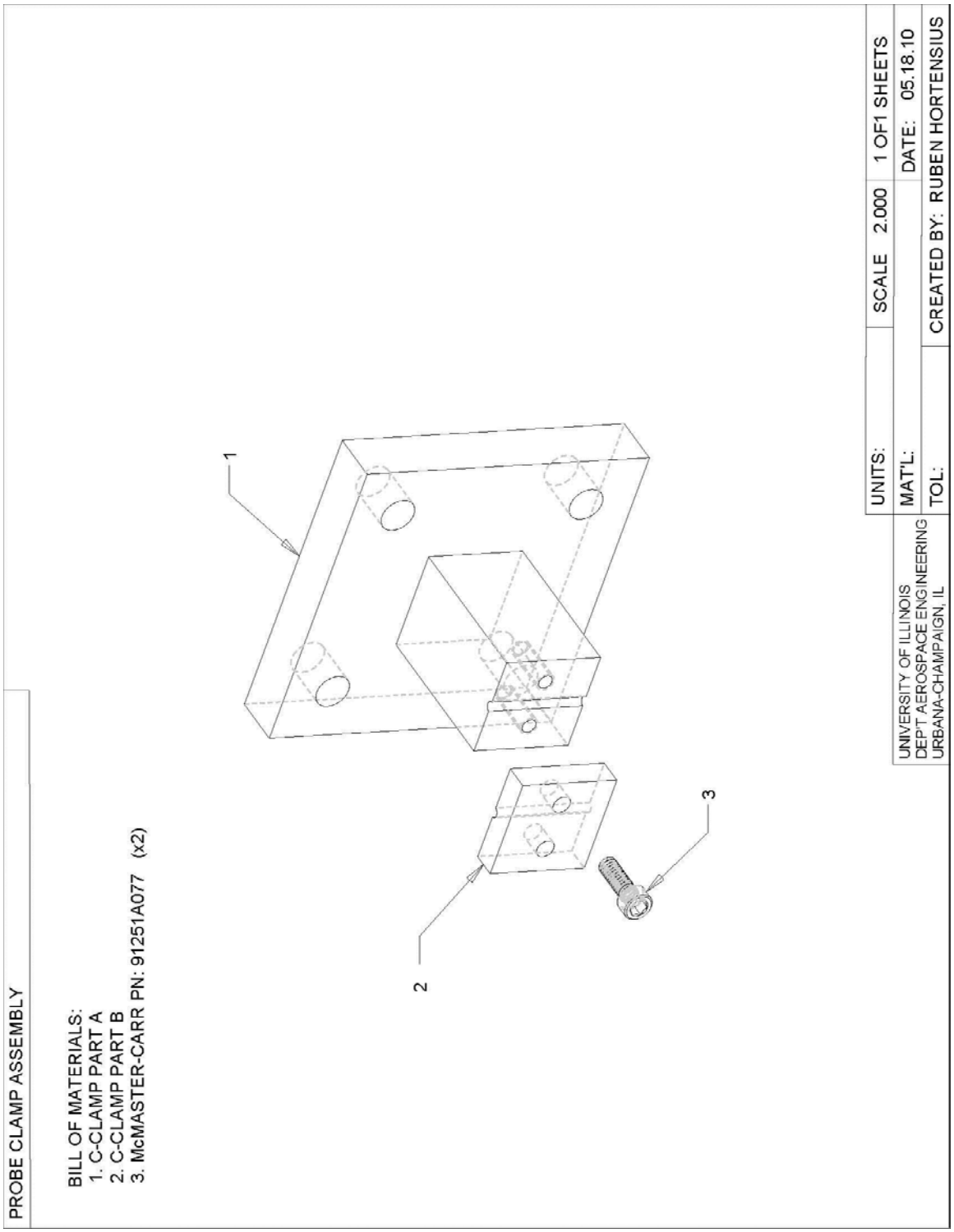

Fig. B.26. Probe Traverse Clamp Subassembly Drawing.

Appendix C

Nozzle Contours

The original wind tunnel construction included a two-part converging-diverging nozzle. For the purposes of this study, a new converging nozzle (with an identical countour) was machined. The diverging nozzle was removed and replaced with a constant area section which represented the outer cowling of the aft bypass. The contours of both original nozzles were measured and are presented in this appendix. A CAD representation of the original wind tunnel is shown in Fig. C.1. The converging and diverging nozzles are emphasized within the figure.

Nozzle coordinates are given in terms of axial and radial positions. The axial origin is located at the nozzle throat, that is, the plane that separates the two nozzle sections. Negative x is defined in the upstream direction (within the converging section) while positive x is in the downstream direction (diverging section). Since the nozzle is axisymmetric, radial position, measured from the wind tunnel centerline, fully defines the nozzle contours. Fig. C.2 provides the entire nozzle contour in coordinate form.

C.1 Converging Nozzle

The original brass converging nozzle contour was measured using a coordinate measuring machine located in the Metrology Lab of the Department of Mechanical Science and Engineering at UIUC. The coordinate measuring machine's radial measurements were spaced 0.10 inches apart (axial). When the aluminum 7075 nozzle was machined, the coordinate density was increased for the first inch (axial) using a 6^{th} order polynomial fit (R-squared = 0.9999) to an axial spacing of 0.033 inches. The remainder of the contour utilized the original 0.010 inch spacing. The radial coordinates are presented below:

Axial Position, x [in]	Radius [in]	Axial Position, x [in]	Radius [in]	Axial Position, x [in]	Radius [in]
0.000	4.717	-0.667	3.204	-2.000	2.356
-0.033	4.457	-0.700	3.175	-2.100	2.319
-0.067	4.261	-0.733	3.146	-2.200	2.284
-0.100	4.112	-0.767	3.117	-2.300	2.252
-0.133	3.998	-0.800	3.088	-2.400	2.222
-0.167	3.908	-0.833	3.058	-2.500	2.194
-0.200	3.834	-0.867	3.026	-2.600	2.167
-0.233	3.770	-0.900	2.994	-2.700	2.142
-0.267	3.713	-0.933	2.964	-2.800	2.120
-0.300	3.660	-0.967	2.937	-2.900	2.099
-0.333	3.610	-1.000	2.919	-3.000	2.081
-0.367	3.561	-1.100	2.844	-3.100	2.065
-0.400	3.513	-1.200	2.775	-3.200	2.051
-0.433	3.466	-1.300	2.711	-3.300	2.038
-0.467	3.422	-1.400	2.650	-3.400	2.026
-0.500	3.379	-1.500	2.592	-3.500	2.016
-0.533	3.339	-1.600	2.538	-3.600	2.009
-0.567	3.301	-1.700	2.488	-3.700	2.004
-0.600	3.267	-1.800	2.441	-3.800	2.001
-0.633	3.234	-1.900	2.397		

C.2 Diverging Nozzle

The original diverging nozzle contour was also measured using the coordinate measuring machine with a measurement axial spacing of 0.10 inches. Its contour is provided below for reference in unaltered form:

Axial Position, x [in]	Radius [in]	Axial Position, x [in]	Radius [in]	Axial Position, x [in]	Radius [in]
0.000	2.003	3.503	2.305	7.002	2.743
0.101	2.004	3.602	2.321	7.102	2.750
0.202	2.005	3.702	2.338	7.202	2.757
0.302	2.006	3.802	2.355	7.302	2.763
0.402	2.009	3.902	2.372	7.402	2.770
0.502	2.012	4.002	2.389	7.502	2.776
0.603	2.015	4.102	2.406	7.602	2.782
0.702	2.019	4.202	2.423	7.702	2.787
0.802	2.024	4.303	2.439	7.802	2.792
0.902	2.028	4.402	2.455	7.902	2.797
1.002	2.034	4.502	2.471	8.003	2.802
1.102	2.039	4.602	2.487	8.102	2.806
1.202	2.046	4.702	2.502	8.202	2.810
1.302	2.052	4.802	2.516	8.302	2.814
1.403	2.058	4.902	2.530	8.402	2.817
1.502	2.066	5.002	2.543	8.502	2.819
1.602	2.073	5.102	2.556	8.602	2.822
1.702	2.082	5.202	2.569	8.702	2.824
1.802	2.091	5.302	2.581	8.802	2.827
1.902	2.102	5.402	2.594	8.902	2.829
2.002	2.112	5.502	2.605	9.002	2.832
2.102	2.122	5.602	2.617	9.102	2.834
2.202	2.132	5.702	2.628	9.202	2.836
2.303	2.143	5.802	2.639	9.302	2.837
2.402	2.154	5.902	2.649	9.402	2.838
2.502	2.166	6.002	2.659	9.502	2.840
2.603	2.178	6.102	2.669	9.602	2.842
2.702	2.190	6.202	2.678	9.702	2.844
2.802	2.203	6.303	2.688	9.802	2.846
2.902	2.216	6.402	2.697	9.822	2.846
3.002	2.229	6.502	2.705		
3.102	2.243	6.602	2.714		
3.202	2.258	6.702	2.721		
3.302	2.273	6.802	2.729		
3.402	2.289	6.902	2.736		

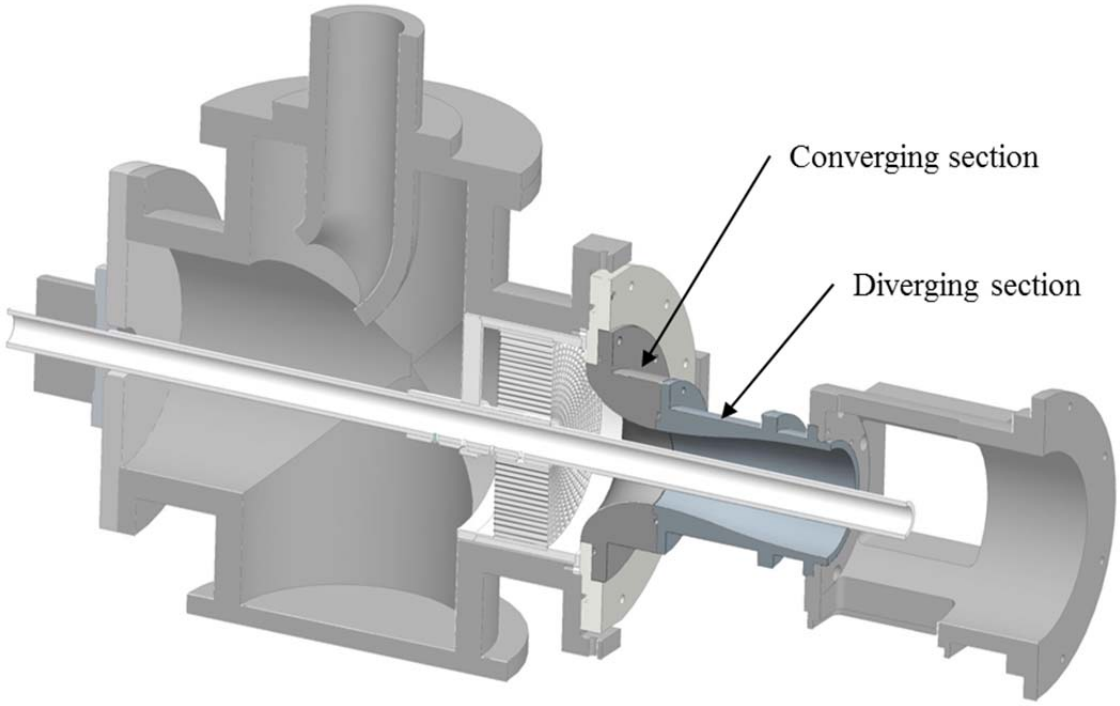

Fig. C.1. A CAD representation of the original wind tunnel configuration. The original converging and diverging sections of the nozzle are highlighted.

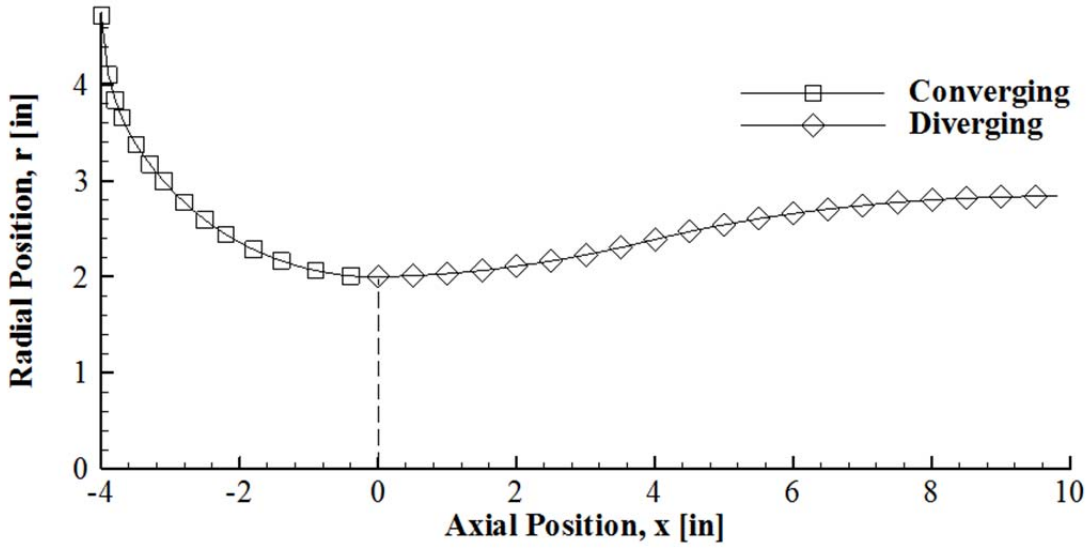

Fig. C.2. Original converging-diverging nozzle coordinates.

Appendix D

Uncertainty Analysis

Uncertainties in experimental data and derived values were determined in order to provide insight into the accuracy of the data. Uncertainties typically have two sources: bias and precision errors. Bias errors are attributed to calibration techniques and manufacturing errors. Precision errors are related to the accuracy of a measurement from a specific device. The sum of bias and precision represents the total error, which is propagated through any derived quantities.

Instead of calculating the errors due to bias and precision independently, the total error is calculated directly. The method used accounts for the errors associated with each of the inputs for a given measurement. It is called the propagation of uncertainties.[41] Using this method, the uncertainty in variable R is given by u_R, where R is a function of n measured experimental (or derived) variables, $x_1, x_2, \ldots, x_n$.

$$R = R(x_1, x_2, \ldots, x_n) \tag{D.1}$$

$$u_R = \sqrt{\sum_{i=1}^{n} \left(\frac{\partial R}{\partial x_i} u_{x_i} \right)^2} \tag{D.2}$$

In the calculation of uncertainties, it was assumed that constants, such as $\mathcal{R}$ and γ, had uncertainties equal to zero.

D.1 Stagnation Chamber Conditions

Stagnation chamber conditions were monitored during each experimental run. An Omega J-type thermocouple and DP26 Indicator recorded $T_{chamber}$ with a precision uncertainty of 0.9 °R. $P_{chamber}$ was measured in differential form using the NetScanner system (see Section D.2 for the definition of $u_{P_{chamber}}$). $T_{chamber}$ and $P_{chamber}$ were used to calculate the stagnation density, $\rho_{chamber}$ by the state equation ($P = \rho RT$). The

uncertainty in $\rho_{chamber}$ is given below, followed by the partial derivatives with respect to the variables of interest.

$$u_{\rho_{chamber}} = \sqrt{\left(\frac{\partial \rho_{chamber}}{\partial P_{chamber}} u_{P_{chamber}}\right)^2 + \left(\frac{\partial \rho_{chamber}}{\partial T_{chamber}} u_{T_{chamber}}\right)^2} \tag{D.3}$$

$$\frac{\partial \rho_{chamber}}{\partial P_{chamber}} = \frac{1}{RT_{chamber}} \tag{D.4}$$

$$\frac{\partial \rho_{chamber}}{\partial T_{chamber}} = -\frac{P_{chamber}}{RT_{chamber}^2} \tag{D.5}$$

D.2 Total Pressure

The data recorded by the pressure transducers were the relative (to ambient condition) pressures. Therefore, the total pressure is the sum of the ambient pressure and the differential pressure measured by the transducers, as shown in Eq. D.6. The ambient pressure, recorded by the NetScanner™ Model 9034, has a calibrated range of 45psia with ±0.05% FS uncertainty, which equates to a measurement uncertainty of 0.0225 psia.

$$P = dP + P_{amb} \tag{D.6}$$

The uncertainty in each *dP* was dependent on the full-scale (FS) range of the transducers utilized to measure that particular pressure. Table 2.2 displays the measurement uncertainty of each of the three different FS range transducers used in this experiment. $dP_{chamber}$ and dP_{total} were measured using the 0-100 psid transducers, leading to a measurement uncertainty of 0.05 psi. Nearly all of the remaining static pressure measurements, both on the model surface or on the outer (cowling) wall, were recorded using the ±30 psid transducers, leading to an uncertainty of 0.015 psi. The only exceptions were the four channel wall static pressure taps (described in Section 2.5.1.3.2) that used the ±15 psid transducers; these transducers had an uncertainty of 0.0075 psi.

Applying the propagation of uncertainties method (Eq. D.2) to the total pressure formulation, yields the results of Table D.1. Note that, for this case, the $\frac{\partial R}{\partial x_i}$ terms are all unity, greatly simplifying the calculation.

Table D.1. Uncertainties in Total Pressure Based on Transducer Range

Transducer Range	Uncertainty (psi)
±30 psid	0.027
±15 psid	0.024
0-100 psi	0.055

D.3 Mach Number

Several different Mach numbers are defined in this study. The formulation for each, however, is based on the isentropic relations characterized by Eq. 2.19. This isentropic relation allows for the direct calculation of Mach number based on experimentally recorded static and total pressures. M_{tunnel}, M_{inlet}, (and any other Mach numbers used in this study) all utilize a static and total pressure; therefore, the uncertainty in Mach number can be generalized in the manner given by Eq. D.7-9.

$$u_M = \sqrt{\left(\frac{\partial M}{\partial P_{total}} u_{P_{total}}\right)^2 + \left(\frac{\partial M}{\partial P_{st}} u_{P_{st}}\right)^2} \tag{D.7}$$

$$\frac{\partial M}{\partial P_{total}} = \frac{1}{\gamma P_{st}} \left(\frac{P_{total}}{P_{st}}\right)^{-1/\gamma} \left\{\frac{2}{\gamma - 1}\left[\left(\frac{P_{total}}{P_{st}}\right)^{\gamma-1/\gamma} - 1\right]\right\}^{-1/2} \tag{D.8}$$

$$\frac{\partial M}{\partial P_{st}} = -\frac{1}{\gamma P_{st}} \left(\frac{P_{total}}{P_{st}}\right)^{(\gamma-1)/\gamma} \left\{\frac{2}{\gamma - 1}\left[\left(\frac{P_{total}}{P_{st}}\right)^{\gamma-1/\gamma} - 1\right]\right\}^{-1/2} \tag{D.9}$$

D.4 Area Ratio

The Mach-area relation was used to determine the area ratio, and thereafter A^*, within each channel. The uncertainty in A/A^* (u_{AR}) is given by Eq. D.10-11. The uncertainty in A^* is given by Eq. D.12-14.

$$u_{AR} = \sqrt{\left(\frac{\partial (A/A^*)}{\partial M} u_M\right)^2} = \frac{\partial (A/A^*)}{\partial M} u_M \tag{D.10}$$

$$\frac{\partial(A/A^*)}{\partial M} = \frac{(M^2-1)\left(\frac{2+(\gamma-1)M^2}{\gamma+1}\right)^{\frac{\gamma+1}{2(\gamma-1)}}}{M^2\left(1+\frac{(\gamma-1)}{2}M^2\right)} \tag{D.11}$$

$$u_{A^*} = \sqrt{\left(\frac{\partial A^*}{\partial A_{st,tap1}}u_{A_{st,tap1}}\right)^2 + \left(\frac{\partial A^*}{\partial(A/A^*)}u_{AR}\right)^2} \tag{D.12}$$

$$\frac{\partial A^*}{\partial A_{st,tap1}} = \frac{1}{(A/A^*)} \tag{D.13}$$

$$\frac{\partial A^*}{\partial(A/A^*)} = -\frac{A_{st,tap1}}{(A/A^*)^2} \tag{D.14}$$

D.5 Local Temperature and Density

Just as Mach number could be calculated directly as a function of pressure data via isentropic relations, local temperature and density uncertainty calculations were also functions of experimental pressure (Eq. 2.22 and Eq. 2.23, respectively).

Uncertainty in local temperature is given by Eq. D.15-18.

$$u_T = \sqrt{\left(\frac{\partial T}{\partial T_{chamber}}u_{T_{chamber}}\right)^2 + \left(\frac{\partial T}{\partial P_{st}}u_{P_{st}}\right)^2 + \left(\frac{\partial T}{\partial P_{chamber}}u_{P_{chamber}}\right)^2} \tag{D.15}$$

$$\frac{\partial T}{\partial T_{chamber}} = \left(\frac{\mathrm{P}_{chamber}}{\mathrm{P}_{st}}\right)^{-1+\frac{1}{\gamma}} \tag{D.16}$$

$$\frac{\partial T}{\partial P_{st}} = \frac{\left(\frac{\mathrm{P}_{chamber}}{\mathrm{P}_{st}}\right)^{\frac{1}{\gamma}}\mathrm{T}_{chamber}(\gamma-1)}{\gamma \mathrm{P}_{chamber}} \tag{D.17}$$

$$\frac{\partial T}{\partial P_{chamber}} = -\frac{\left(\frac{\mathrm{P}_{chamber}}{\mathrm{P}_{st}}\right)^{\frac{1}{\gamma}}\mathrm{T}_{chamber}(\gamma-1)}{\gamma \mathrm{P}_{chamber}{}^2} \tag{D.18}$$

Uncertainty in local density is given by Eq. D.19-22.

$$u_\rho = \sqrt{\left(\frac{\partial \rho}{\partial \rho_{chamber}}u_{\rho_{chamber}}\right)^2 + \left(\frac{\partial \rho}{\partial P_{st}}u_{P_{st}}\right)^2 + \left(\frac{\partial \rho}{\partial P_{chamber}}u_{P_{chamber}}\right)^2} \tag{D.19}$$

$$\frac{\partial \rho}{\partial \rho_{chamber}} = \left(\frac{\mathrm{P}_{chamber}}{\mathrm{P}_{st}}\right)^{-1/\gamma} \tag{D.20}$$

$$\frac{\partial \rho}{\partial P_{st}} = \frac{\left(\frac{\mathrm{P}_{chamber}}{\mathrm{P}_{st}}\right)^{-1/\gamma} \rho_{chamber}}{\gamma \mathrm{P}_{st}} \tag{D.21}$$

$$\frac{\partial \rho}{\partial P_{chamber}} = -\frac{\left(\frac{\mathrm{P}_{chamber}}{\mathrm{P}_{st}}\right)^{-1/\gamma} \rho_{chamber}}{\gamma \mathrm{P}_{chamber}} \tag{D.22}$$

D.6 Velocity

The calculation of velocity is dependent on the speed of sound. The uncertainty in the speed of sound, c, is only a function of u_T since the uncertainties in γ and $\mathcal{R}$ are zero. The uncertainty is given by Eq. D. 23-24. The uncertainty in velocity, U, is given by Eq. D. 25-27.

$$u_c = \sqrt{\left(\frac{\partial c}{\partial T} u_T\right)^2} = \frac{\partial c}{\partial T} u_T \tag{D.23}$$

$$\frac{\partial c}{\partial T} = \frac{1}{2}\sqrt{\frac{\gamma \mathcal{R}}{T}} \tag{D.24}$$

$$u_U = \sqrt{\left(\frac{\partial U}{\partial M} u_M\right)^2 + \left(\frac{\partial U}{\partial c} u_c\right)^2} \tag{D.25}$$

$$\frac{\partial U}{\partial M} = c \tag{D.26}$$

$$\frac{\partial U}{\partial c} = M \tag{D.27}$$

D.7 Pressure Ratios, Factors, and Non-dimensionalizations

Several quantities are derived from pressure measurements in this study. These measurements serve several purposes. Pressure ratios aid in comparison of data, and provide insight into flow conditions via the isentropic relations. Factors, such as the pressure recovery factor (*PRF*), are intended to ensure that all experimental runs are

carried out at identical conditions. Factors lead to estimated quantities, such as P_0, which are ideally identical between all experimental runs of the same operating condition. Non-dimensionalization operations, such as that for $P_{t,\ non\text{-}dim}$, allow for the direct comparison of data from different operating conditions. In this section, the uncertainties in these quantities are shared.

The uncertainty in *PRF* is given by Eq. D.28-30.

$$u_{PRF} = \sqrt{\left(\frac{\partial(PRF)}{\partial P_{total}^{Ch\#1}} u_{P_{total}^{Ch\#1}}\right)^2 + \left(\frac{\partial(PRF)}{\partial P_{chamber}} u_{P_{chamber}}\right)^2} \tag{D.28}$$

$$\frac{\partial(PRF)}{\partial P_{total}^{Ch\#1}} = \frac{1}{P_{chamber}} \tag{D.29}$$

$$\frac{\partial(PRF)}{\partial P_{chamber}} = -\frac{P_{total}^{Ch\#1}}{{P_{chamber}}^2} \tag{D.30}$$

The uncertainty in P_0 is given by Eq. D.31-33.

$$u_{P_0} = \sqrt{\left(\frac{\partial P_0}{\partial(PRF)} u_{PRF}\right)^2 + \left(\frac{\partial P_0}{\partial P_{chamber}} u_{P_{chamber}}\right)^2} \tag{D.31}$$

$$\frac{\partial P_0}{\partial(PRF)} = P_{chamber} \tag{D.32}$$

$$\frac{\partial P_0}{\partial P_{chamber}} = PRF \tag{D.33}$$

The uncertainty in $P_{t,\ non\text{-}dim}$ is given by Eq. D.34-36.

$$u_{P_{t,non-dim}} = \sqrt{\left(\frac{\partial P_{t,non-dim}}{\partial P_{total}} u_{P_{total}}\right)^2 + \left(\frac{\partial P_{t,non-dim}}{\partial P_{chamber}} u_{P_{chamber}}\right)^2} \tag{D.34}$$

$$\frac{\partial P_{t,non-dim}}{\partial P_{total}} = \frac{1}{P_{chamber}} \tag{D.35}$$

$$\frac{\partial P_{t,non-dim}}{\partial P_{chamber}} = -\frac{P_{total}}{{P_{chamber}}^2} \tag{D.36}$$

The uncertainty in $P_{st,empty}^{*}$ is given by Eq. D.37-40. The uncertainty in $P_{chamber}$ is the same as that for $P_{chamber,empty}$, such that $u_{P_{chamber}} = u_{P_{chamber,empty}}$.

$$u_{P^*_{st,empty}} = \sqrt{\left(\frac{\partial P^*_{st,empty}}{\partial P_{chamber}} u_{P_{chamber}}\right)^2 + \left(\frac{\partial P^*_{st,empty}}{\partial P_{st}} u_{P_{st}}\right)^2 + \left(\frac{\partial P^*_{st,empty}}{\partial P_{chamber,empty}} u_{P_{chamber}}\right)^2} \quad \text{(D.37)}$$

$$\frac{\partial P^*_{st,empty}}{\partial P_{chamber}} = -\frac{\mathrm{P}_{st}\mathrm{P}_{chamber,empty}}{{P_{chamber}}^2} \quad \text{(D.38)}$$

$$\frac{\partial P^*_{st,empty}}{\partial P_{st}} = \frac{\mathrm{P}_{chamber,empty}}{\mathrm{P}_{chamber}} \quad \text{(D.39)}$$

$$\frac{\partial P^*_{st,empty}}{\partial P_{chamber,empty}} = \frac{\mathrm{P}_{st}}{\mathrm{P}_{chamber}} \quad \text{(D.40)}$$

The uncertainty in P/P_0 (represented by PR within the uncertainty equations) is given by Eq. D.41-43.

$$u_{PR} = \sqrt{\left(\frac{\partial (PR)}{\partial P_{st}} u_{P_{st}}\right)^2 + \left(\frac{\partial (PR)}{\partial P_0} u_{P_0}\right)^2} \quad \text{(D.41)}$$

$$\frac{\partial (PR)}{\partial P_{st}} = \frac{1}{P_0} \quad \text{(D.42)}$$

$$\frac{\partial (PR)}{\partial P_0} = -\frac{P_{st}}{{P_0}^2} \quad \text{(D.43)}$$

D.8 Viscosity

Viscosity was calculated using Sutherland's method. For purposes of uncertainty calculations, Sutherland's reference conditions and empirical constants were treated as having an uncertainty of zero. The result of this assumption is that the uncertainty of viscosity is only a function of the uncertainty in the local temperature, $u_\mu = u_\mu(u_T)$ since u_{C_1} and u_S are both equal to zero. The uncertainty in viscosity is given by Eq. D.44.

$$u_\mu = \sqrt{\left(\frac{C_1\sqrt{T}(3S+T)}{2(S+T)^2}\right)^2 {u_T}^2} = \frac{C_1\sqrt{T}(3S+T)}{2(S+T)^2} u_T \quad \text{(D.44)}$$

D.9 Reynolds Number

Reynolds number was used in part as a metric to evaluate the run-time variations in wind tunnel conditions. The length scale, d, is the difference between the inner and outer walls of the aft bypass (0.54 inches). The uncertainty, u_d, is equal to 0.005 inches. The uncertainty in Re is given by Eq. D.45-50.

$$u_{Re} = \sqrt{\left(\frac{\partial Re}{\partial M}u_M\right)^2 + \left(\frac{\partial Re}{\partial d}u_d\right)^2 + \left(\frac{\partial Re}{\partial \mu}u_\mu\right)^2 + \left(\frac{\partial Re}{\partial P_{st}}u_{P_{st}}\right)^2 + \left(\frac{\partial Re}{\partial T_{chamber}}u_{T_{chamber}}\right)^2} \tag{D.45}$$

$$\frac{\partial Re}{\partial M} = \frac{\sqrt{2}dP_{st}[1+(\gamma-1)M^2]\sqrt{\frac{\gamma}{R}}}{\mu T_{chamber}\sqrt{\frac{2+(\gamma-1)M^2}{T_{chamber}}}} \tag{D.46}$$

$$\frac{\partial Re}{\partial d} = \frac{MP_{st}\sqrt{\frac{1+\frac{(\gamma-1)}{2}M^2}{T_{chamber}}}\sqrt{\frac{\gamma}{R}}}{\mu} \tag{D.47}$$

$$\frac{\partial Re}{\partial \mu} = -\frac{dMP_{st}\sqrt{\frac{1+\frac{(\gamma-1)}{2}M^2}{T_{chamber}}}\sqrt{\frac{\gamma}{R}}}{\mu^2} \tag{D.48}$$

$$\frac{\partial Re}{\partial P_{st}} = \frac{dM\sqrt{\frac{1+\frac{(\gamma-1)}{2}M^2}{T_{chamber}}}\sqrt{\frac{\gamma}{R}}}{\mu} \tag{D.49}$$

$$\frac{\partial Re}{\partial T_{chamber}} = -\frac{dMP_{st}\sqrt{\frac{2+(\gamma-1)M^2}{T_{chamber}}}\sqrt{\frac{\gamma}{R}}}{2\sqrt{2}\mu T_{chamber}} \tag{D.50}$$

D.10 Kinematic Viscosity

The uncertainty in kinematic viscosity is given by Eq. D.51-53.

$$u_\nu = \sqrt{\left(\frac{\partial \nu}{\partial \mu}u_\mu\right)^2 + \left(\frac{\partial \nu}{\partial \rho}u_\rho\right)^2} \tag{D.51}$$

$$\frac{\partial \nu}{\partial \mu} = \frac{1}{\rho} \tag{D.52}$$

$$\frac{\partial \nu}{\partial \rho} = -\frac{\mu}{\rho^2} \tag{D.53}$$

D.11 Experimental-to-Isentropic Comparison

The calculation of uncertainty begins by calculating that for dependent variables such as λ, Θ_{Thw}, and $H(\lambda)$. Thwaites' method to estimate Θ_{Thw} contains a numerical integral. The integral, henceforth known as *int*, is calculated via a trapezoidal method, also contains an uncertainty. The integral uncertainty, u_{int}, can be estimated by

$$u_{int} = -\frac{(b-a)^3}{12n^2}\overline{f''} \tag{D.54}$$

$$\overline{f''} = \frac{\sum_{i=1}^{n} f''(\varepsilon_i)}{n} \tag{D.55}$$

where the integral of the function f(ε_i) is bounded by [a, b], and contains n intervals.[42]

The uncertainty in Θ_{Thw}, is given by Eq. D.56-59.

$$u_{\Theta_{Thw}} = \sqrt{\left(\frac{\partial \Theta_{Thw}}{\partial \nu_{local}} u_{\nu_{local}}\right)^2 + \left(\frac{\partial \Theta_{Thw}}{\partial int} u_{int}\right)^2 + \left(\frac{\partial \Theta_{Thw}}{\partial U} u_U\right)^2} \tag{D.56}$$

$$\frac{\partial \Theta_{Thw}}{\partial \nu_{local}} = 0.3354 \frac{\sqrt{\frac{\text{int}\,\nu_{local}}{U^6}}}{\nu_{local}} \tag{D.57}$$

$$\frac{\partial \Theta_{Thw}}{\partial int} = 0.3354 \frac{\sqrt{\frac{\text{int}\,\nu_{local}}{U^6}}}{\text{int}} \tag{D.58}$$

$$\frac{\partial \Theta_{Thw}}{\partial U} = -2.0125 \frac{\sqrt{\frac{\text{int}\,\nu_{local}}{U^6}}}{U} \tag{D.59}$$

In order to calculate the uncertainty in λ, the uncertainty of dU/dx is required. For a numerical derivative, the uncertainty in a function of a single variable is given by Eq. D.60.[43] When applied to the function dU/dx(x), Eq. D.61 results.

$$u_{f(x)} \approx f'(x) u_x \tag{D.60}$$

$$u_{dU/dx} \approx \frac{d^2U(x)}{dx^2} u_x \tag{D.61}$$

The uncertainty in λ is given by Eq. D.62-65.

$$u_\lambda = \sqrt{\left(\frac{\partial \lambda}{\partial \Theta_{Thw}} u_{\Theta_{Thw}}\right)^2 + \left(\frac{\partial \lambda}{\partial \left(dU/dx\right)} u_{dU/dx}\right)^2 + \left(\frac{\partial \lambda}{\partial \nu_{local}} u_{\nu_{local}}\right)^2} \tag{D.62}$$

$$\frac{\partial \lambda}{\partial \Theta_{Thw}} = \frac{2\Theta_{Thw}\left(dU/dx\right)}{\nu_{local}} \tag{D.63}$$

$$\frac{\partial \lambda}{\partial \left(dU/dx\right)} = \frac{{\Theta_{Thw}}^2}{\nu_{local}} \tag{D.64}$$

$$\frac{\partial \lambda}{\partial \nu_{local}} = -\frac{\left(dU/dx\right){\Theta_{Thw}}^2}{\nu_{local}^2} \tag{D.65}$$

Since Thwaites' empirical fit $H(\lambda)$ is only a function of λ, the calculation of the uncertainty in $H(\lambda)$ is simplified. Eq. D.66 presents the uncertainty in $H(\lambda)$.

$$u_H = u_\lambda(-3.3275 + 41.25\lambda - 1131\lambda^2 + 9532\lambda^3 - 22880\lambda^4) \tag{D.66}$$

The uncertainty in δ^*_{Thw} is given by Eq. D.67-69.

$$u_{\delta^*_{Thw}} = \sqrt{\left(\frac{\partial \delta^*_{Thw}}{\partial \Theta_{Thw}} u_{\Theta_{Thw}}\right)^2 + \left(\frac{\partial \delta^*_{Thw}}{\partial H} u_H\right)^2} \tag{D.67}$$

$$\frac{\partial \delta^*_{Thw}}{\partial \Theta_{Thw}} = H \tag{D.68}$$

$$\frac{\partial \delta^*_{Thw}}{\partial H} = \Theta_{Thw} \tag{D.69}$$

The Thwaites' method adjusted local normal area, A_{Thw}, was simply calculated by subtracting the quantity [$\delta^*(x)$]Perimeter(x) from A. The uncertainty in A_{Thw} is given by Eq. D.70-73.

$$u_{A_{Thw}} = \sqrt{\left(\frac{\partial A_{Thw}}{\partial \delta^*_{Thw}} u_{\delta^*_{Thw}}\right)^2 + \left(\frac{\partial A_{Thw}}{\partial Perimeter} u_{Perimeter}\right)^2 + \left(\frac{\partial A_{Thw}}{\partial A} u_A\right)^2} \quad \text{(D.70)}$$

$$\frac{\partial A_{Thw}}{\partial \delta^*_{Thw}} = -Per \quad \text{(D.71)}$$

$$\frac{\partial A_{Thw}}{\partial Perimeter} = -\delta^*_{Thw} \quad \text{(D.72)}$$

$$\frac{\partial A_{Thw}}{\partial A} = 1 \quad \text{(D.73)}$$

Once the Thwaites' method adjusted local normal area (A_{Thw}) had been calculated, a new A^* was determined so that $A/A^*|_{Thw}$ was defined. The calculation of the uncertainties within these quantities was carried out in an identical manner as that previously described in Section D.4.

$A/A^*|_{Thw}$ was used to determine a new Mach number, $M_{isen\ Thw}$, and thereafter a pressure ratio, $P/P_0|_{isen\ Thw}$. Since it is extremely difficult to write the Mach-Area relation as a function of Mach number, the method of propagation of uncertainties could not be used. Instead, the upper and lower bounds of $A/A^*|_{Thw}$ (defined by their uncertainty) were used to determine maximum and minimum values of $M_{isen\ Thw}$. The uncertainty of $M_{isen\ Thw}$ was defined as $\pm 0.5(M_{isen\ Thw|max} - M_{isen\ Thw|min})$.

$M_{isen\ Thw}$ was used to determine $P/P_0|_{isen\ Thw}$. The uncertainty is given by Eq. D.74-75.

$$u_{PR_{isen\ Thw}} = \sqrt{\left(\frac{\partial PR_{isen\ Thw}}{\partial M_{isen\ Thw}} u_{M_{isen\ Thw}}\right)^2} = abs\left(\frac{\partial PR_{isen\ Thw}}{\partial M_{isen\ Thw}}\right) u_{M_{isen\ Thw}} \quad \text{(D.74)}$$

$$\frac{\partial PR_{isen\ Thw}}{\partial M_{isen\ Thw}} = -\gamma M \left(1 + \frac{(\gamma - 1)}{2} M^2\right)^{\frac{1-2\gamma}{\gamma-1}} \quad \text{(D.75)}$$

Finally, the experimental pressure ratio could be compared to the isentropic pressure ratio. As described in Section 2.7.2.2.1, this comparison was conducted by calculating the percent difference between the two cases with respect to the experimental data. The uncertainty is given by Eq. D.76-78.

$$u_{\%\Delta} = \sqrt{\left(\frac{\partial(\%\Delta)}{\partial(PR_{Thw})}u_{PR_{Thw}}\right)^2 + \left(\frac{\partial(\%\Delta)}{\partial(PR_{\exp})}u_{(PR_{\exp}}\right)^2} \tag{D.76}$$

$$\frac{\partial(\%\Delta)}{\partial(PR_{Thw})} = -1 \tag{D.77}$$

$$\frac{\partial(\%\Delta)}{\partial(PR_{\exp})} = -\frac{PR_{Thw}}{PR_{\exp}{}^2} \tag{D.78}$$

D.12 Mass Flow Rate

The uncertainty in calculated mass flow rate is given by Eq. D.79-83.

$$u_{\dot{m}} = \sqrt{\left(\frac{\partial\dot{m}}{\partial A}u_A\right)^2 + \left(\frac{\partial\dot{m}}{\partial P_{total}}u_{P_{total}}\right)^2 + \left(\frac{\partial\dot{m}}{\partial T_{local}}u_{T_{total}}\right)^2 + \left(\frac{\partial\dot{m}}{\partial M}u_M\right)^2} \tag{D.79}$$

$$\frac{\partial\dot{m}}{\partial A} = \frac{MP_{total}\left(1+\frac{(\gamma-1)}{2}M^2\right)^{\frac{1+\gamma}{2-2\gamma}}\sqrt{\frac{\gamma}{R}}}{\sqrt{T_{local}}} \tag{D.80}$$

$$\frac{\partial\dot{m}}{\partial P_{total}} = \frac{AM\left(1+\frac{(\gamma-1)}{2}M^2\right)^{\frac{1+\gamma}{2-2\gamma}}\sqrt{\frac{\gamma}{R}}}{\sqrt{T_{local}}} \tag{D.81}$$

$$\frac{\partial\dot{m}}{\partial T_{local}} = -\frac{AMP_{total}\left(1+\frac{(\gamma-1)}{2}M^2\right)^{\frac{1+\gamma}{2-2\gamma}}\sqrt{\frac{\gamma}{R}}}{2T_{local}{}^{3/2}} \tag{D.82}$$

$$\frac{\partial\dot{m}}{\partial M} = -\frac{2A(M^2-1)P_{total}\left(1+\frac{(\gamma-1)}{2}M^2\right)^{\frac{1+\gamma}{2-2\gamma}}\sqrt{\frac{\gamma}{R}}}{\sqrt{T_{local}}(2+(\gamma-1)M^2)} \tag{D.83}$$

D.13 Boundary-Layer, Displacement, and Momentum Thicknesses

Calculation of uncertainty in boundary-layer thickness could not be conducted in the customary manner. Boundary-layer thickness is defined as the normal distance from

the wall at which the streamwise velocity reaches 99% of the core velocity. In order to calculate the reference value of δ, the velocities are surveyed to find the $0.99U_{core}$ velocity, and the corresponding distance from the wall is recorded. Since the function, $U(r)$, is undefined, the calculation of the uncertainty in this measurement was conducted in an alternative manner.

The reference value was calculated as described above. Then, known uncertainties in U were used to create extreme cases by calculating δ for $0.99(U_{core} + u_{U_{core}})$ and $0.99(U_{core} - u_{U_{core}})$. These vales represent the maximum and minimum calculable values in boundary-layer thickness. The uncertainty in δ was then defined as one half the difference between extreme cases.

In order to calculate the uncertainty in displacement and momentum thicknesses, an identical technique was employed. The equations were applied to attain the calculated values. Then, the integrals were calculated again at upper and lower limits (defined by uncertainties) to determine maximum and minimum values. For instance, the reference value of δ^* is determined by Eq. 2.17 evaluated at M_{inlet}/M_{core}. The integral was then evaluated again at the lower bound, that is, at $M_{inlet}/M_{core} - u_{M_{inlet/core}}$. The upper bound integral was then calculated (at $M_{inlet}/M_{core} + u_{M_{inlet/core}}$). The uncertainty in the calculated value was defined as half the difference between the upper and lower bounds.

D.14 Sample Uncertainties

Sample uncertainties of calculated values were calculated for the $M_{tunnel} = 0.531$ operating condition. In order to illustrate the magnitude of the uncertainties with respect to the calculated values, the relative uncertainty is also provided.

Table D.2 Sample Uncertainties of Stagnation Chamber Conditions.

Variable	Reference Value	Absolute Uncertainty	Relative Uncertainty (%)
$P_{chamber}$	19.052 psia	±0.055 psia	±0.289
$T_{chamber}$	503.5 °R	±0.9 °R	±0.179
$\rho_{chamber}$	0.00318 slug/ft^3	±1.078E-05 slug/ft^3	±0.340
$\mu_{chamber}$	3.699E-07 slug/(ft s)	±5.176E-10 slug/(ft s)	±0.140
$\nu_{chamber}$	1.165E-04 ft^2/s	±4.278E-07 ft^2/s	±0.367

Table D.3 Sample Uncertainties of Inlet Plane Data and Non-dimensional Quantities

Variable	Reference Value	Absolute Uncertainty	Relative Uncertainty (%)
$P_{total}^{Ch\#1\ core}$	18.994 psia	±0.055 psia	±0.290
PRF	0.997	±0.004	±0.409
P_0	18.994 psia	±0.095 psia	±0.501
P_{total}	18.905 psia	±0.055 psia	±0.291
$P_{t,\ non\text{-}dim}$	1.000	±0.006	±0.578
$P_{st,OP}$	15.677 psia	±0.027 psia	±0.172
P/P_0	0.825	±0.004	±0.529
M_{tunnel}	0.531	±0.004	±0.799
Re_{tunnel}	190763	±2405	±1.261

Table D.4 Sample Uncertainties of Ch #4 First Static Pressure Tap Conditions

Variable	Reference Value	Absolute Uncertainty	Relative Uncertainty (%)
P_{st}	11.586 psia	±0.027 psia	±0.233
T_{local}	449.8 °R	±0.8 °R	±0.174
ρ_{local}	0.00216 slug/ft^3	±6.859E-06 slug/ft^3	±0.317
ν_{local}	1.565E-04 ft^2/s	±5.773E-07 ft^2/s	±0.369
M_{local}	0.866	±0.003	±0.380
A/A^*	1.016	±0.001	±0.082
A^*	0.296	±0.004	±1.411
c	1039.6 ft/s	±0.9 ft/s	±0.087
U	900.8 ft/s	±3.5 ft/s	±0.390
$\dot{m}$	5.787E-03 slug/s	±7.770E-05 slug/s	±1.343

The uncertainty in boundary-layer thickness was found to be quite large. This is due to the fact that the method employed (see Section D.13) used the radial traverse data, which was recorded in 0.5 mm (0.0197 in) increments. The upper and lower thickness limits established to calculate uncertainty were therefore constrained to these specific probe-measurement locations. Often, this scheme resulted in overly conservative boundary-layer thickness limits. Since the boundary layers were already thin, the uncertainties tended to be of large relative magnitude.

Displacement and momentum thickness were not affected by this source of error since they are defined by integrations, which tend to dampen errors, and because their results were not required to be fixed to the locations of total pressure measurement.

Table D.5 Sample Uncertainties of Boundary-Layer Thickness at $M_{tunnel} = 0.531$

	Outer Wall		
	Reference Value	**Uncertainty**	**Relative Uncertainty (%)**
Ch #1	0.04921 in	2.46E-02 in	49.999
Ch #2	0.05905 in	1.97E-02 in	33.333
Ch #3	0.05905 in	1.97E-02 in	33.333
Ch #4	0.05905 in	2.46E-02 in	41.666
Ch #5	0.05905 in	1.48E-02 in	25.000

	Inner Wall		
	Reference Value	**Uncertainty**	**Relative Uncertainty (%)**
Ch #1	0.07611 in	1.97E-02 in	25.863
Ch #2	0.09580 in	9.84E-03 in	10.274
Ch #3	0.08596 in	9.84E-03 in	11.450
Ch #4	0.08596 in	1.48E-02 in	17.176
Ch #5	0.10564 in	2.46E-02 in	23.292

Table D.6 Sample Uncertainties of Displacement Thickness at $M_{tunnel} = 0.531$

	Outer Wall		
	Reference Value	**Uncertainty**	**Relative Uncertainty (%)**
Ch #1	0.00212 in	4.71E-06 in	0.222
Ch #2	0.00298 in	1.77E-06 in	0.059
Ch #3	0.00371 in	5.85E-07 in	0.016
Ch #4	0.00304 in	5.97E-06 in	0.197
Ch #5	0.00388 in	1.49E-05 in	0.383

	Inner Wall		
	Reference Value	**Uncertainty**	**Relative Uncertainty (%)**
Ch #1	0.00622 in	1.63E-05 in	0.262
Ch #2	0.01048 in	3.30E-05 in	0.314
Ch #3	0.00887 in	3.45E-05 in	0.389
Ch #4	0.00982 in	4.27E-05 in	0.435
Ch #5	0.01496 in	8.36E-05 in	0.558

Table D.7 Sample Uncertainties of Momentum Thickness at M_{tunnel} = 0.531

	Outer Wall		
	Reference Value	**Uncertainty**	**Relative Uncertainty (%)**
Ch #1	0.00203 in	3.34E-05 in	1.643
Ch #2	0.00283 in	3.67E-05 in	1.296
Ch #3	0.00346 in	5.09E-05 in	1.472
Ch #4	0.00287 in	4.74E-05 in	1.655
Ch #5	0.00357 in	9.33E-05 in	2.615

	Inner Wall		
	Reference Value	**Uncertainty**	**Relative Uncertainty (%)**
Ch #1	0.00558 in	4.53E-05 in	0.812
Ch #2	0.00895 in	8.96E-05 in	1.001
Ch #3	0.00761 in	9.46E-05 in	1.242
Ch #4	0.00826 in	1.17E-04 in	1.411
Ch #5	0.01204 in	2.21E-04 in	1.836

Table D.8 Sample Uncertainties of Isentropic-to-Experimental Comparison Quantities

Variable	**Reference Value**	**Absolute Uncertainty**	**Relative Uncertainty (%)**
$\int U^5 dx$	1.24E+13 ft^6/s^5	±5.60E+06 ft^6/s^5	±0.000
Θ_{Thw}	4.85E-04 in	±5.74E-06 in	±1.185
dU/dx	3966 1/s	±7	±0.173
λ	0.041	±0.001	±2.404
$H(\lambda)$	2.471	±0.003	±0.119
δ^*	1.20E-03 in	±1.43E-05 in	±1.190
A_{Thw}	0.299 in^2	±0.004 in^2	±1.421
A^*_{Thw}	0.294 in^2	±0.004 in^2	±1.423
$A/A^*\|_{Thw}$	1.016	±0.020	±2.011
$M_{isen\ Thw}$	0.867	±0.098	±11.321
$P/P_0\|_{isen\ Thw}$	0.613	±0.063	±10.347

Appendix E

Surface Oil Flow Visualization Images

The following appendix contains images of fluorescent surface oil flow visualization from three separate tested operating conditions. In all images, the flow is from left to right. A photograph was taken each time that the model was rotated several degrees.

E.1 $M_{tunnel} = 0.148$

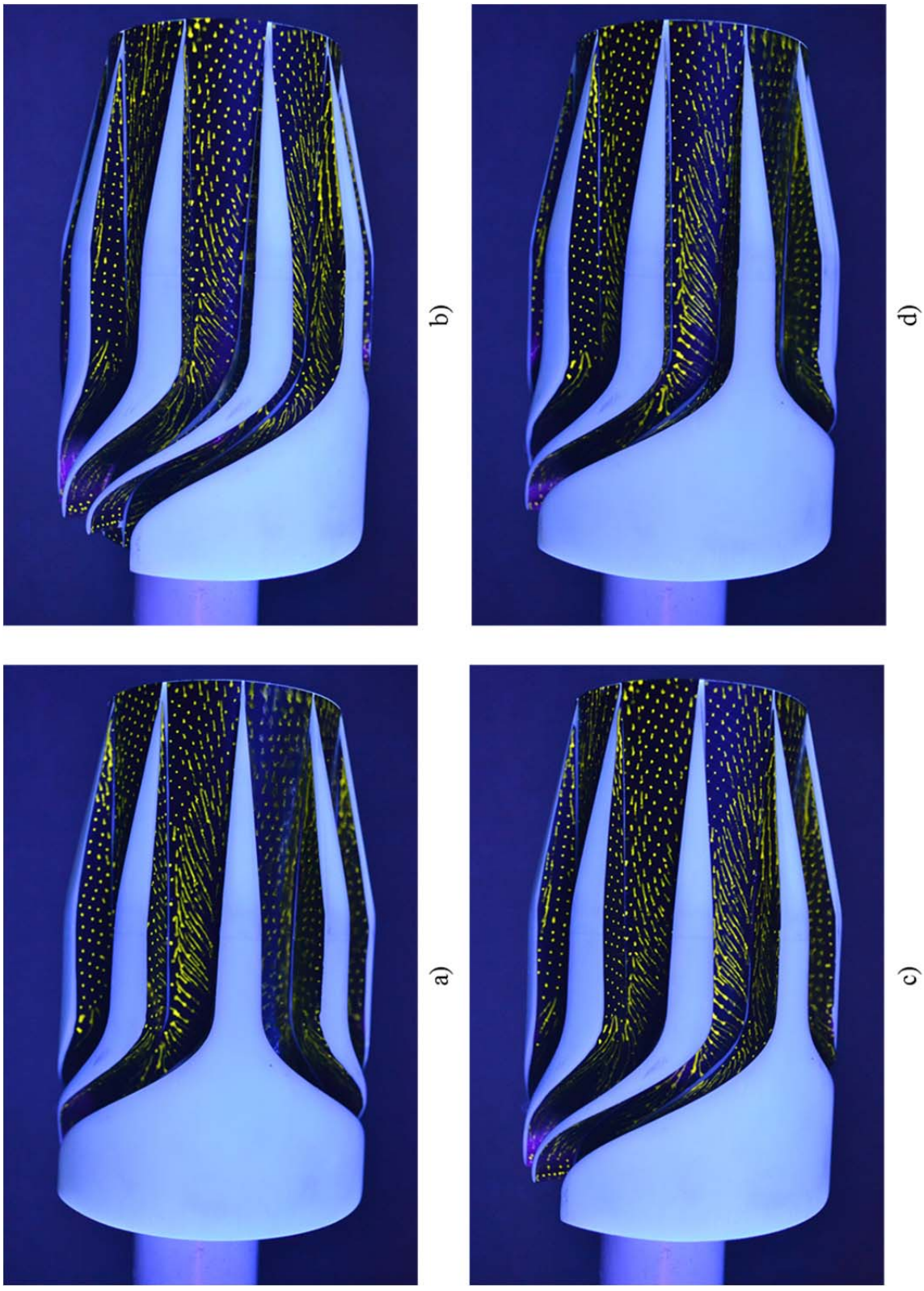

Fig. E.1. Vaned Model Fluorescent Oil Flow Visualization at $M_{tunnel} = 0.148$.

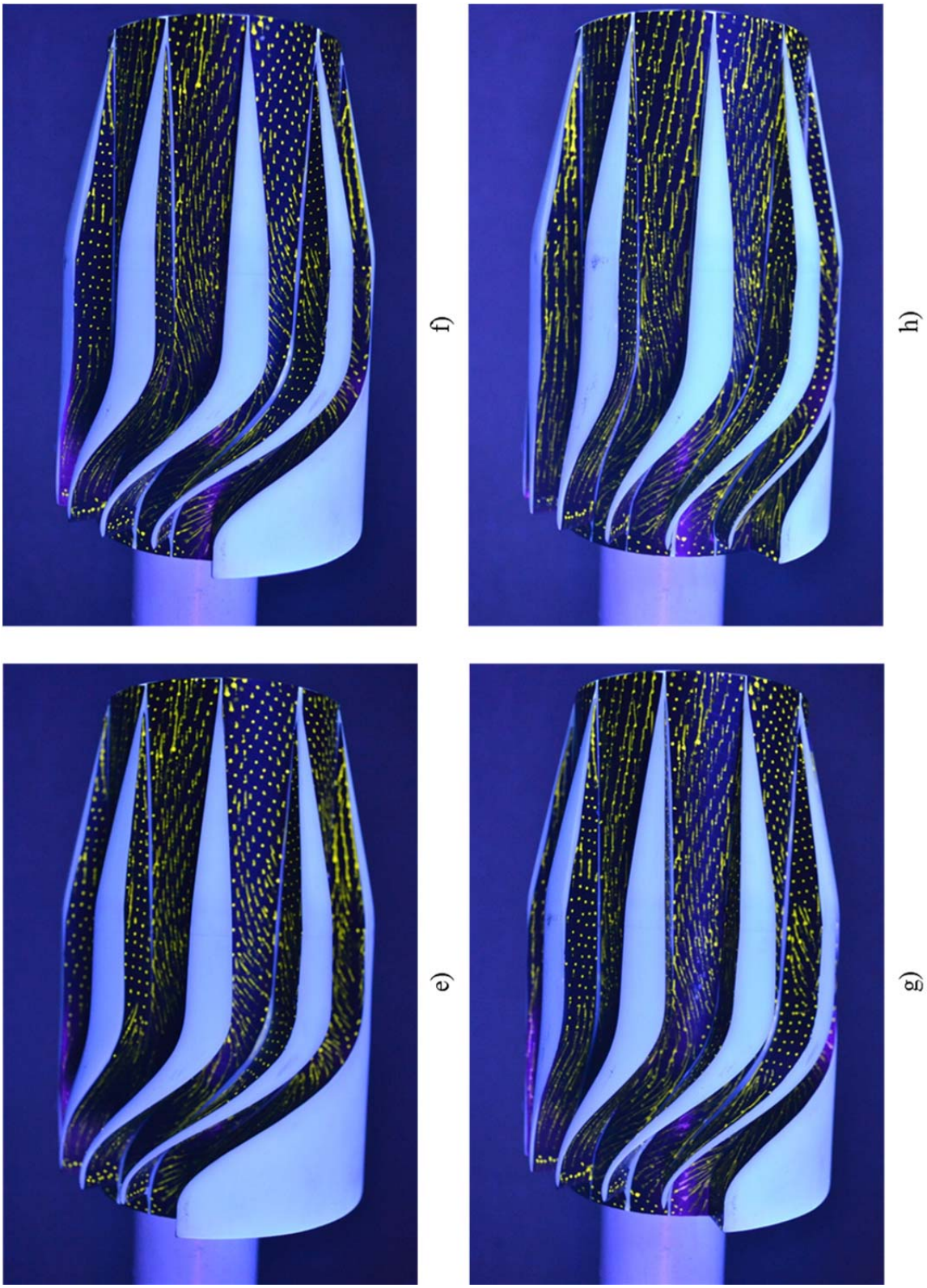

Fig. E.1 (cont.).

j)

i)

k)

Fig. E.1 (cont.).

E.2 $M_{tunnel} = 0.385$

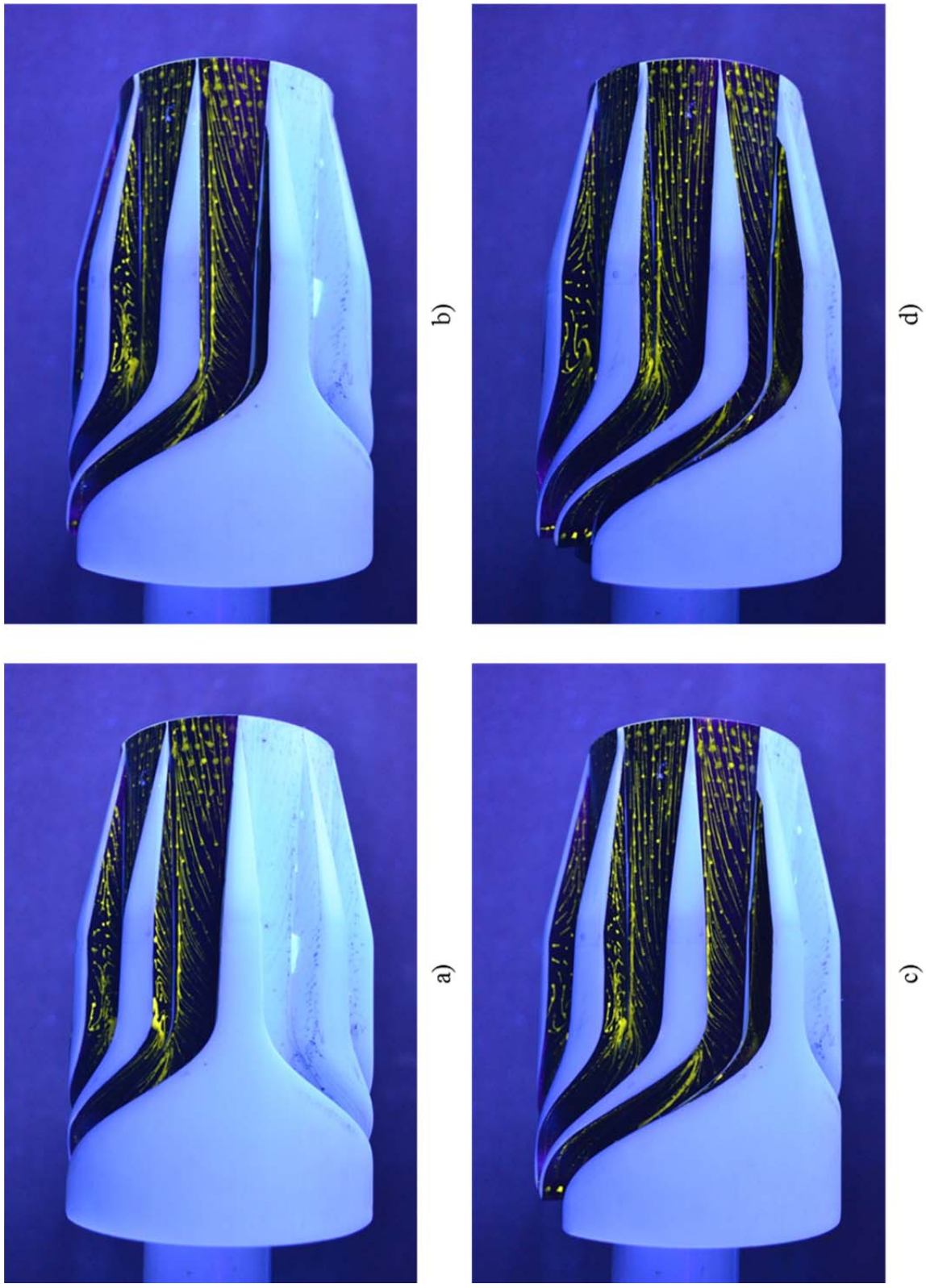

Fig. E.2. Vaned Model Fluorescent Oil Flow Visualization at $M_{tunnel} = 0.385$.

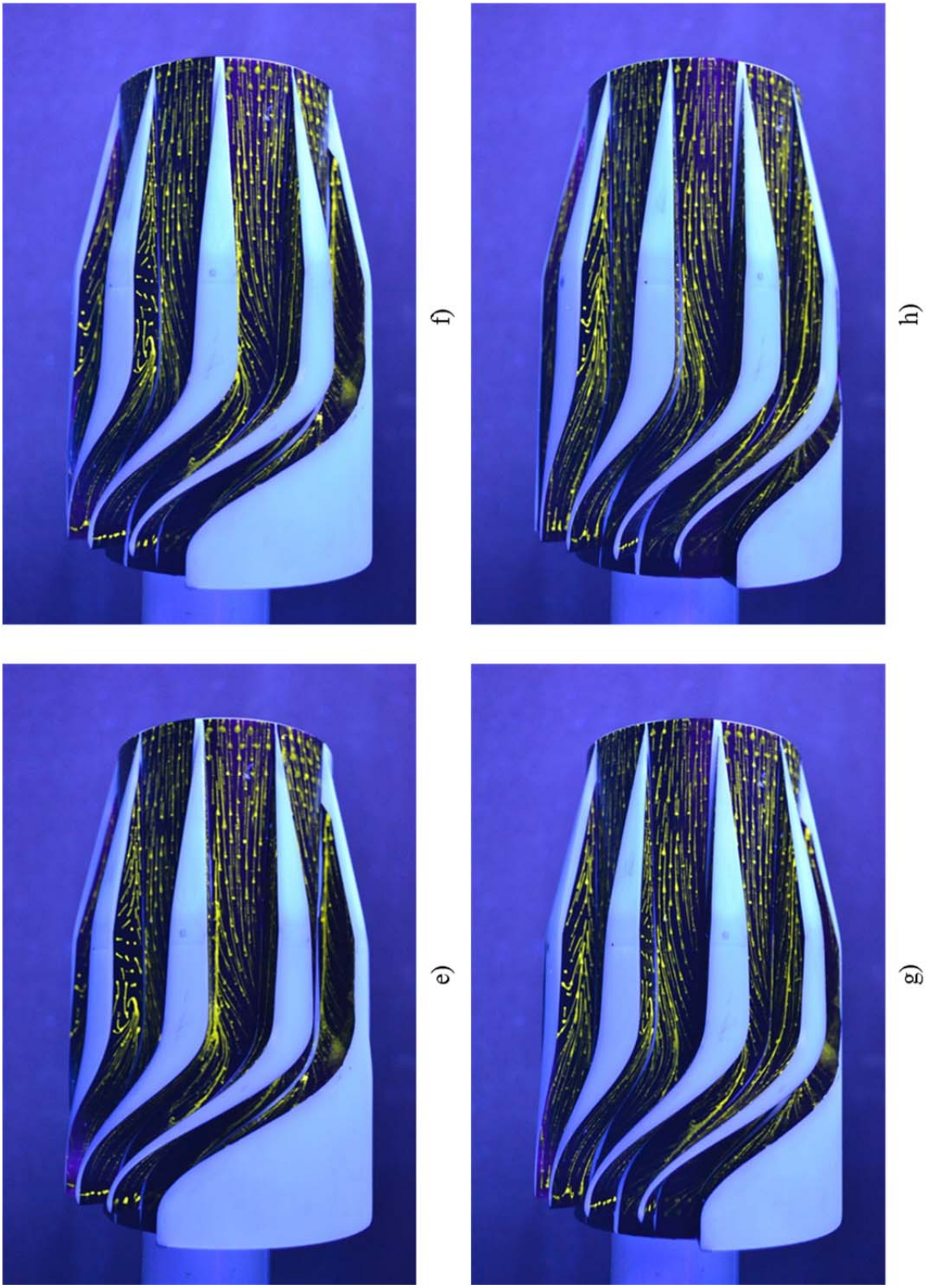

Fig. E.2 (cont.).

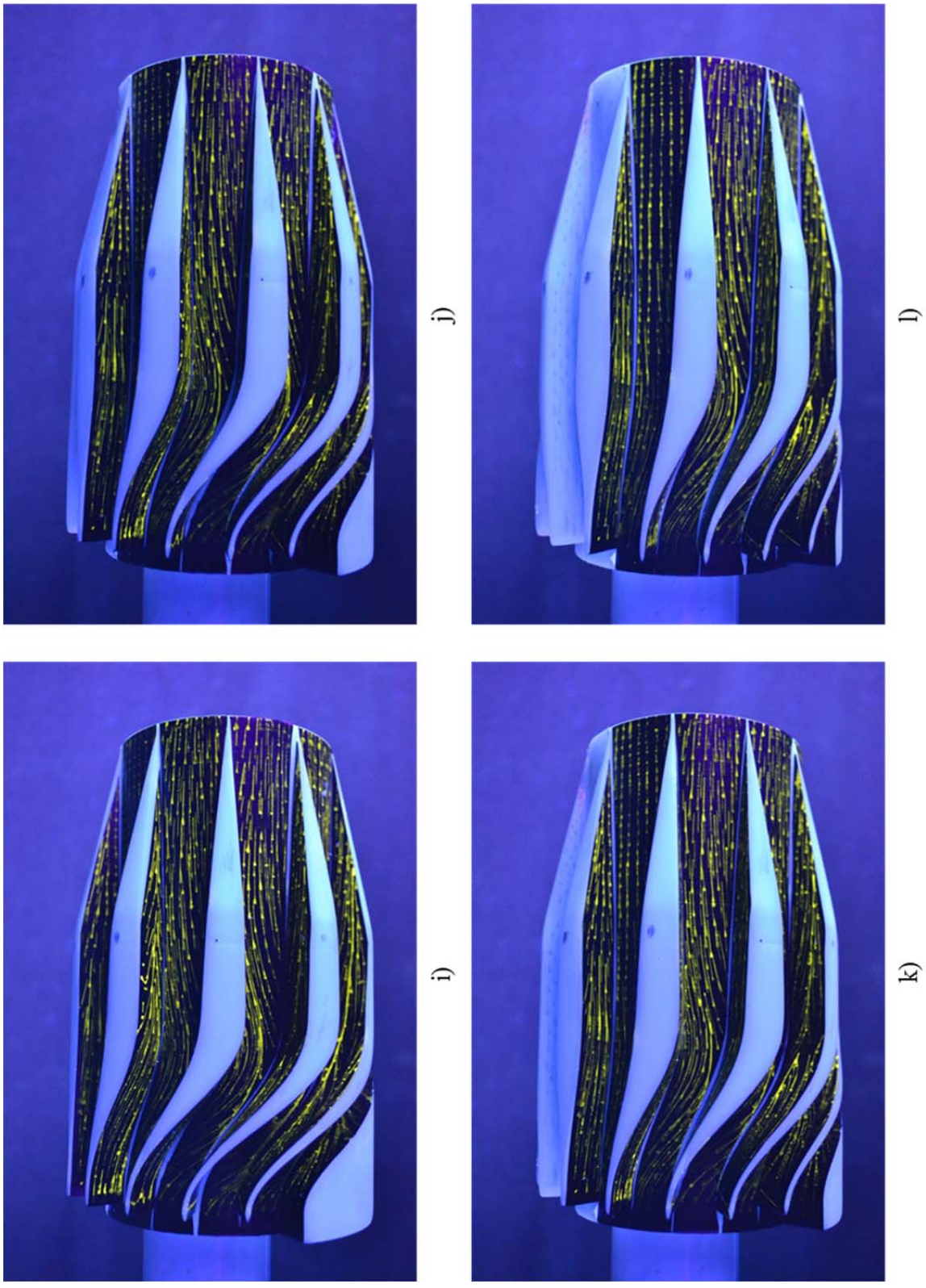

Fig. E.2 (cont.).

n)

m)

Fig. E.2 (cont.).

E.3 $M_{tunnel} = 0.538|_{21.00}$

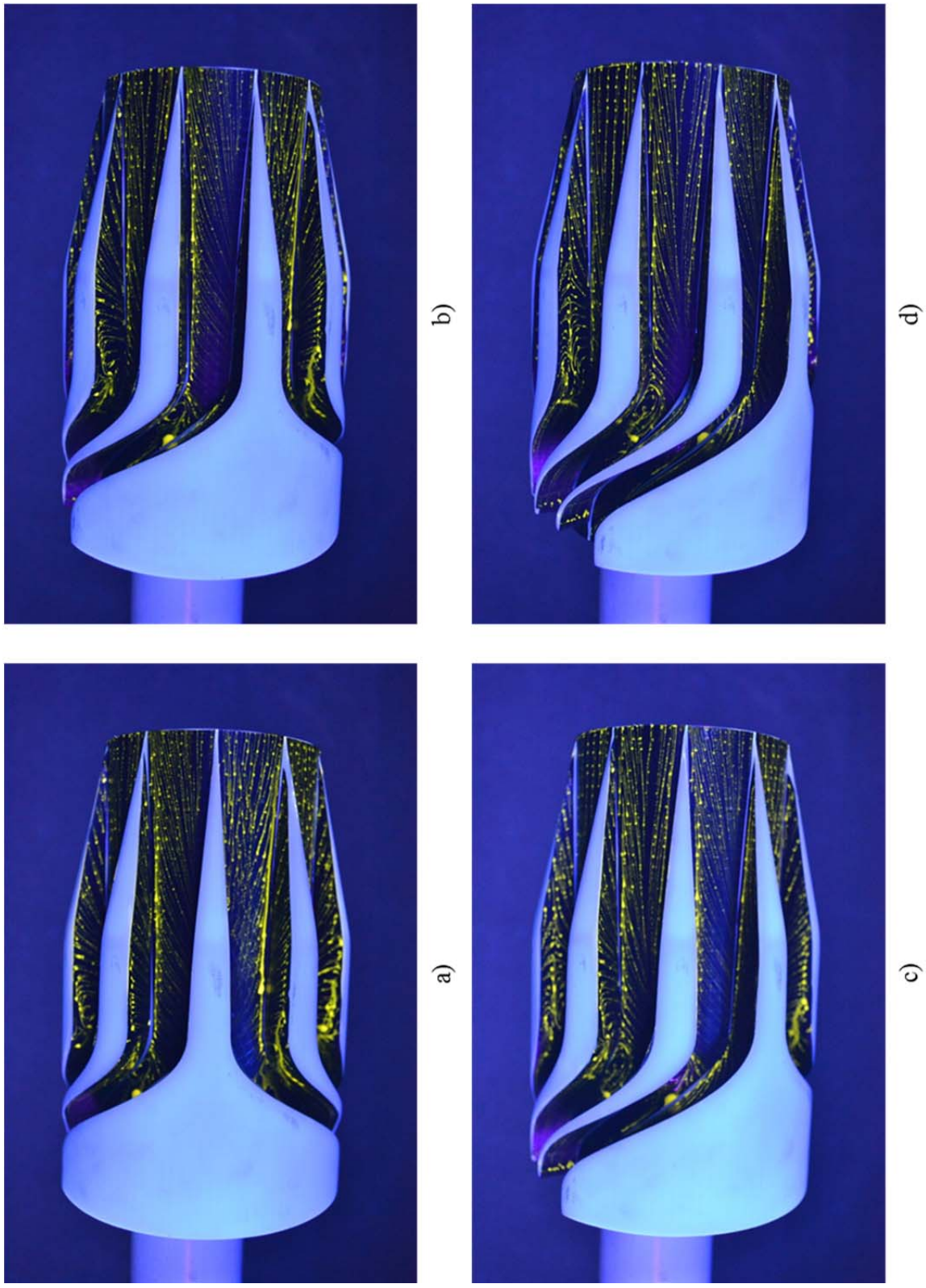

Fig. E.3. Vaned Model Fluorescent Oil Flow Visualization at $M_{tunnel} = 0.538|_{21.00}$.

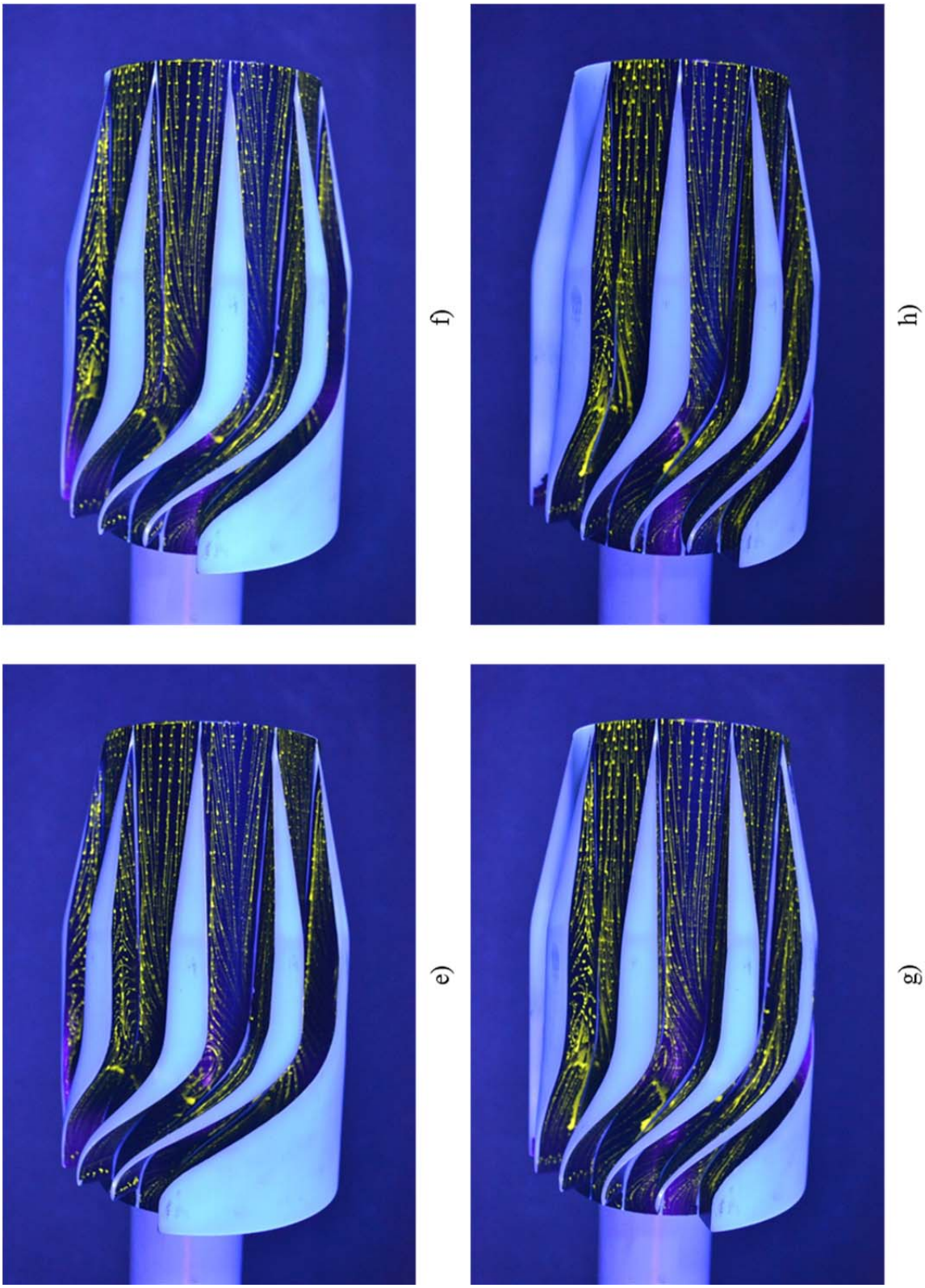

Fig. E.3 (cont.).

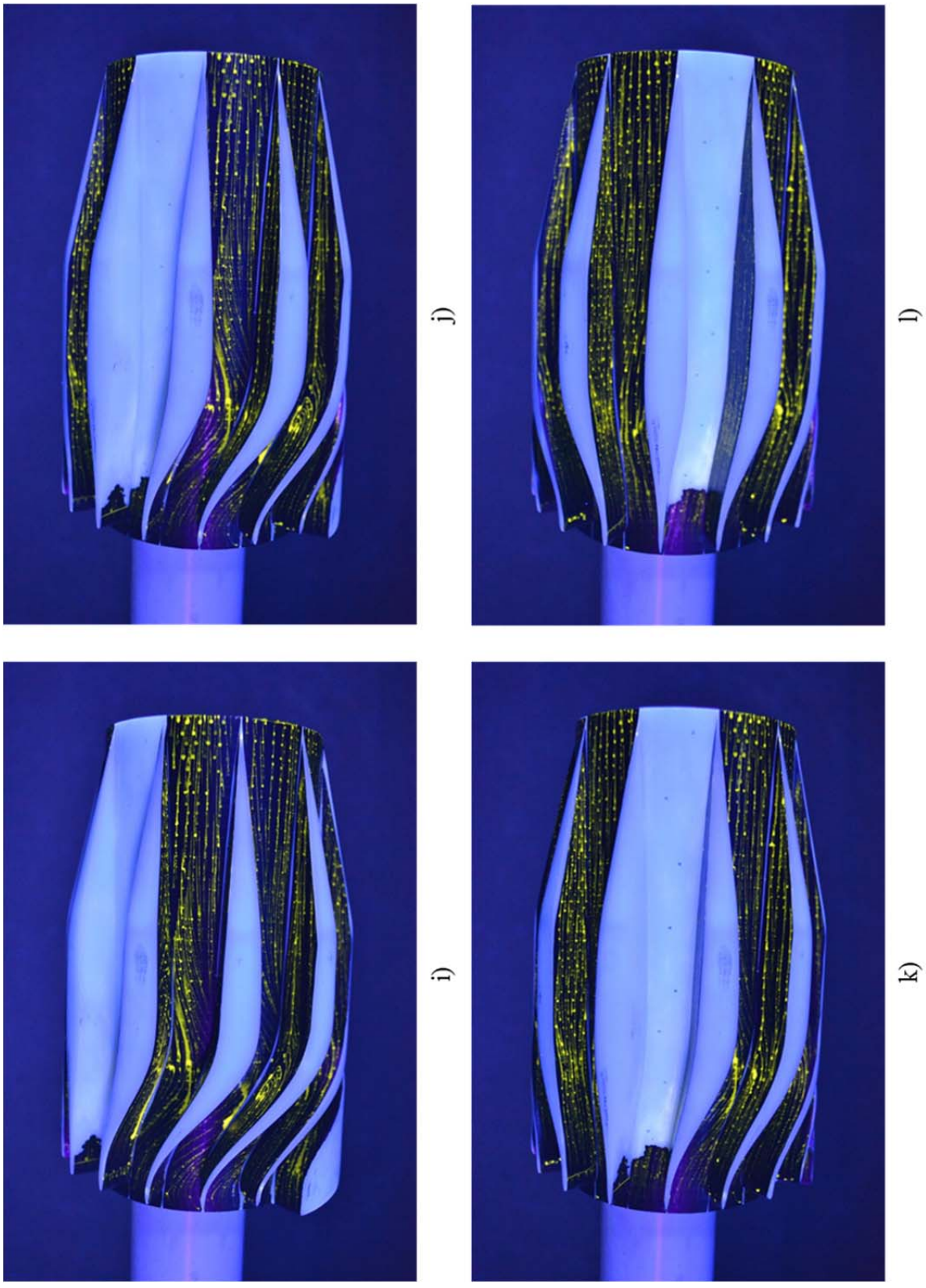

Fig. E.3 (cont.).

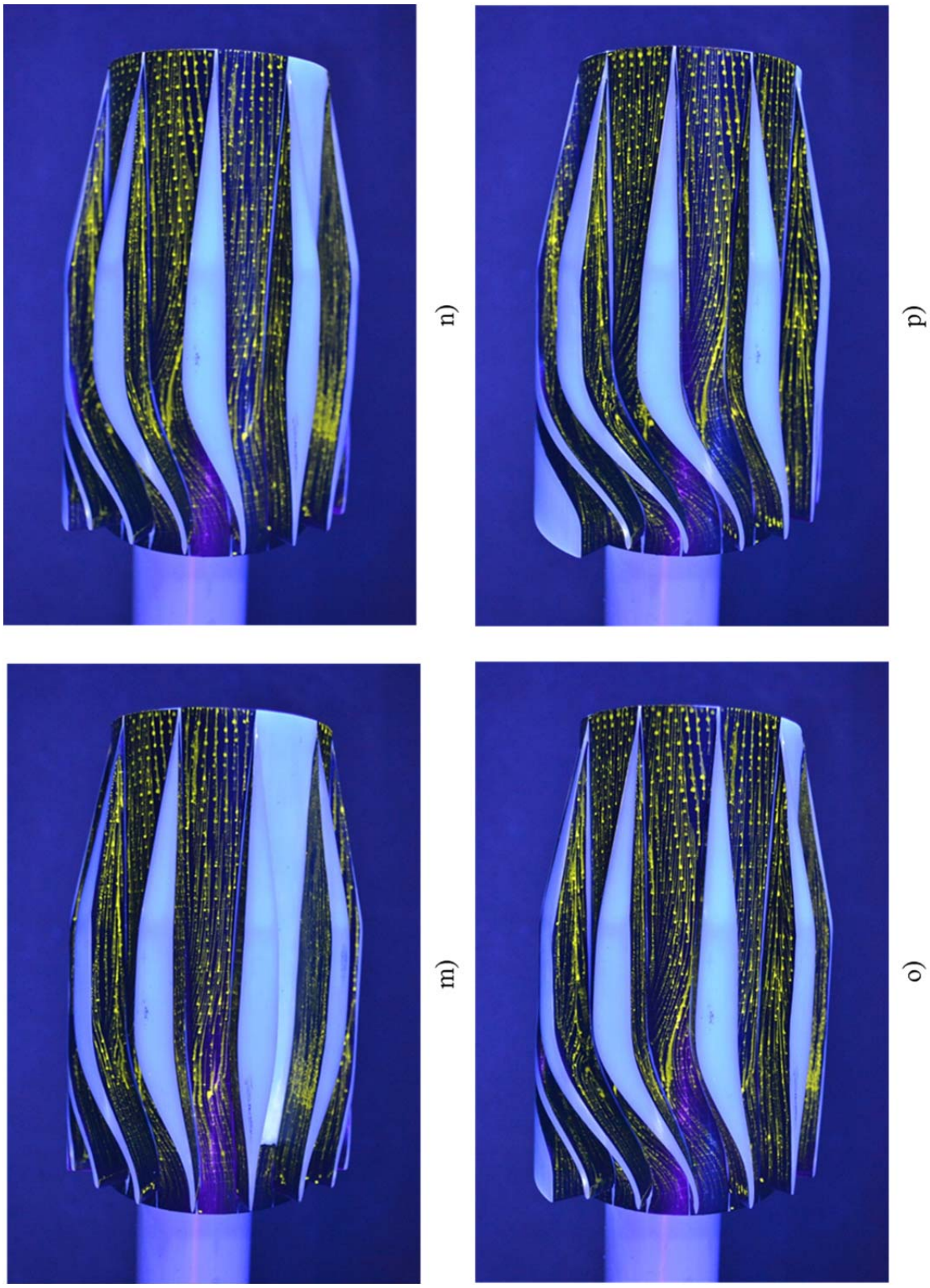

Fig. E.3 (cont.).

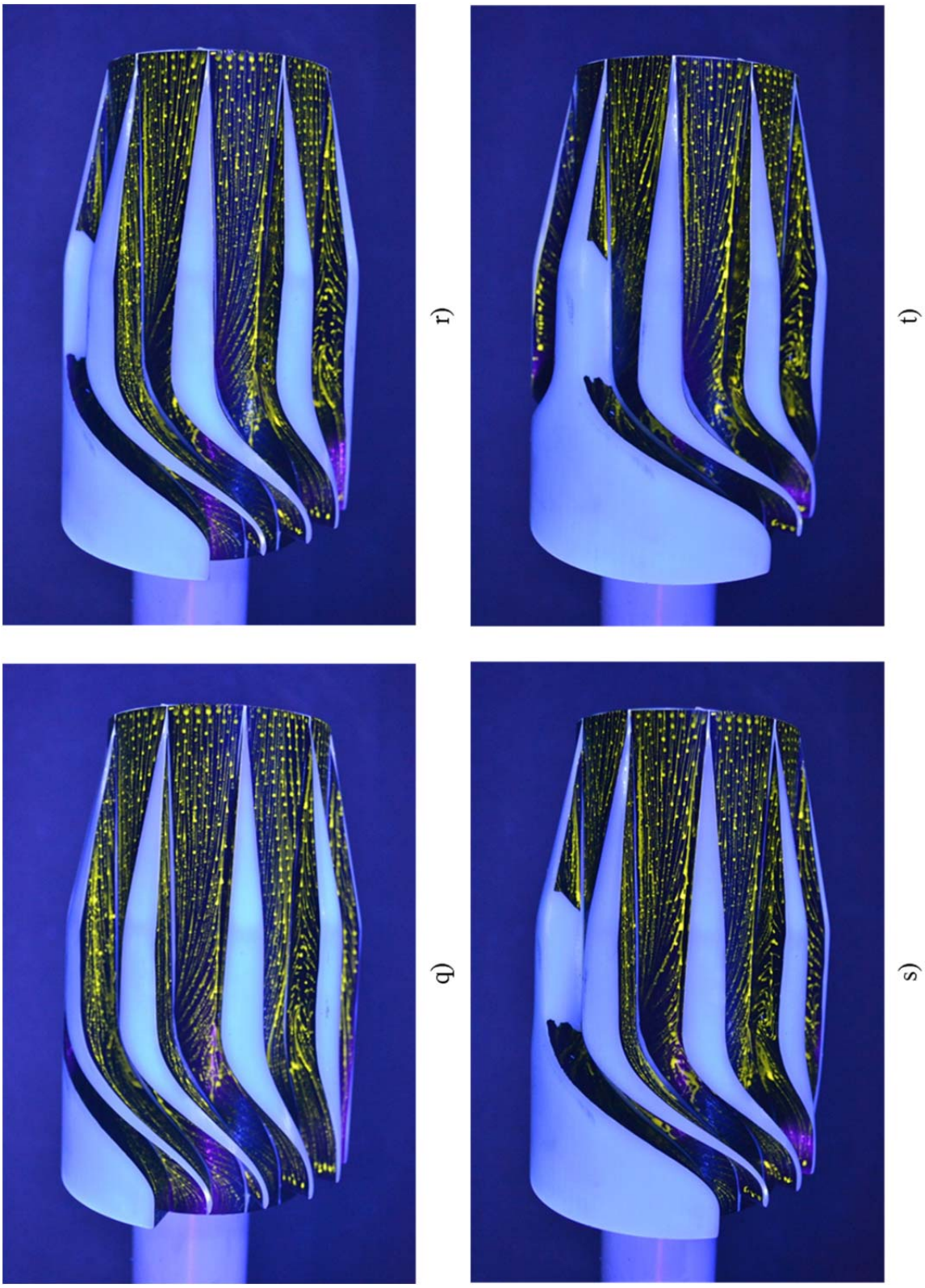

Fig. E.3 (cont.).

v)

u)

w)

Fig. E.3 (cont.).